A Structural and Developmental Study of the Posttrabecular Aqueous Outflow Pathway in the Mouse Eye

Elizabeth Lael van der Merwe

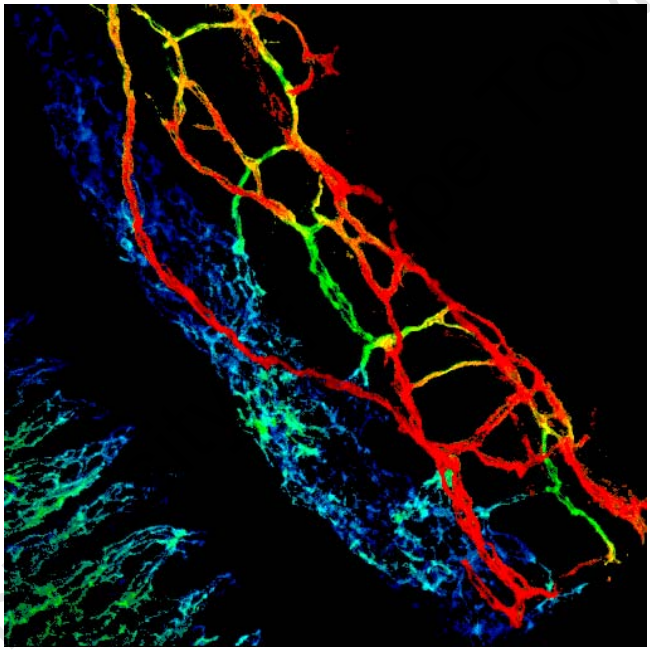

Thesis presented for the degree of

DOCTOR OF PHILOSOPHY

in the Department of Human Biology

Faculty of Health Sciences

UNIVERSITY OF CAPE TOWN

May 2009

CHAPTER 1

Literature review

Glaucoma is one of the leading causes of blindness worldwide and the second leading cause of blindness in South Africa (National Guideline for the Prevention of blindness in South Africa December 2002 (http://www.doh.gov.za/docs/factsheets/guidelines/blindness.pdf). A raised intraocular pressure (IOP) increases the risk of glaucoma which can arise from structural aberrations in the aqueous outflow pathway or in the tissues that regulate the IOP (Gould and John, 2002, Gould et al., 2004). Anterior segment dysgenesis (ASD) is a spectrum of ocular diseases that arises from developmental abnormalities that have their origin in different embryonic tissues such as those derived from the neural crest, neuroectoderm or mesoderm (Idrees et al., 2006). Absence or altered dosage of genes that play a pivotal role in anterior segment development leads to structural deformities that may lead to raised IOP and glaucoma (Kidson et al., 1999; Smith et al., 2000; Chang et al., 2001; Libby et al., 2003; Gould et al., 2004; Snowden, 2007). Although the pathogenesis of ASD is not fully elucidated, studies have identified genes common to both human and mouse which are implicated in the aetiology of ASD (Kume et al., 1998; Mears et al., 1998; Kidson et al., 1999; Smith et al., 2000; Chang et al., 2001; Gould and John, 2002; Gould et al., 2004). In all cases where a specific mutation in the causative gene is known, the severity of ASD (i.e. clinical phenotype) differs between individuals and between different strains. This anomaly is explained by different levels of penetrance of the clinical phenotype (or structural aberrations) which is thought to be influenced by multiple factors such as modifier genes and environment. Therefore in order to better understand these gene modifying and epigenetic influences, genes that mediate ocular development have been studied in mice on defined / pure bred genetic backgrounds which have been subjected to a stable environment.

1.1 Ocular anatomy.

The eye is one of the key sensory organs through which most animal species perceive their environment. It allows light to focus onto receptors in the retina which in turn respond by converting incoming photons to electrical impulses. These signals are conducted via the optic nerve to the visual cortex where they are interpreted. In humans, the loss or lack of sight is a major disability and diseases leading to loss of vision have been widely studied in order to understand their pathogenesis. In some conditions, early intervention treatments would help prevent vision loss. Mammalian eyes are located in bony sockets (orbital cavities) where they are secured by connective tissue ligaments, bands of tendons and skeletal muscles. In mice,

movement of the eyeball is accomplished by the attachment of four straight extra-ocular skeletal muscle bands (superior, inferior, medial and lateral recti), two oblique muscle bands (superior and inferior oblique extra-ocular muscles) and the retractor bulbi muscle, which encases the optic nerve (Smith et al., 2001b). The eye is formed from three tunics: 1) the outer fibrous tunic is comprised of the cornea, limbus and sclera, 2) the middle vascular tunic contains the choroid, ciliary body and iris, and, 3) the inner tunic (the retina) has an outer pigmented epithelial layer (retinal pigmented epithelium) and an inner neural layer. These three tunics enclose three internal chambers (the anterior, posterior chambers and the vitreous), and the eye is anatomically segregated into the anterior and posterior segments. The layout and anatomical relationships of the tunics, chambers and segments of the mouse eye are illustrated in Figure 1.1).

This thesis focuses on the limbus of the mouse eye with particular emphasis on the organisation of the blood and aqueous vessels, and the development of these vessels. Since the limbus is closely associated with the cornea and sclera, the essential structural differences between these regions are reviewed below.

The limbus is located at the periphery of the corneal bulge (see Figure 1.1). This region is rich in collagen fibres and forms a transition zone between the cornea and sclera. Unlike the sclera and cornea which are opaque and transparent respectively, the limbus is optically translucent. The differences in optical clarity of the sclera, limbus and cornea can be attributed to a number of structural features which are unique to each of these regions. These include the organisation and orientation of the collagen fibres and extracellular matrix, and, whether or not blood vessels are present.

The cornea is continuous with the limbus and its anterior and posterior surfaces interface directly with the external environment and anterior chamber respectively. The exterior surface of the cornea is lined by a stratified non-keratinized epithelium below which lies Bowman's capsule. The internal surface of the cornea, which lines the anterior chamber, is lined by a monolayer of corneal endothelium which lies on Descemet's membrane (see Figure 1.2). Bowman's membrane and Descemet's membrane are prominent acellular layers rich in basement membrane proteins. Located between these two layers is the corneal stroma. Within the stroma are flattened stellate-shaped keratocytes bone marrow-derived dentritic cells and macrophages (Hamrah et al., 2003). With the exception of the corneal arcades which are restricted to the outer stroma at the corneal periphery (see Figure 1.2), the cornea is avascular under normal conditions. The bulk of the corneal stroma is made up of overlapping lamellae arranged perpendicular to each other (Kidson

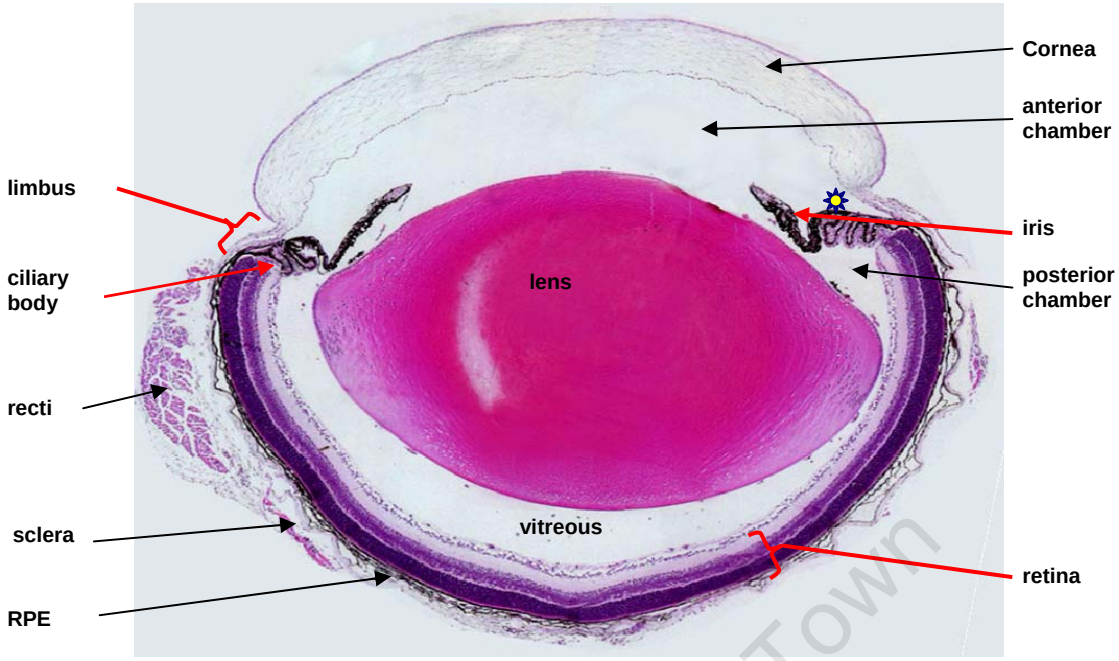

Figure 1.1 General histological organization of the mouse eye.

A composite image of histological section of the mouse eye, stained with haematoxylin and eosin, shows the different tunics and chambers that make up the eye. In this image, the choroid is not clearly visible as it forms a thin vascular layer between the retinal pigmented epithelium (RPE) and the sclera. A segment of the uveal layer comprising the ciliary body has torn away from the sclera in this section (star). The anterior segment comprises the cornea, the limbus, the iris, the lens, the ciliary body, and the internal anterior and posterior chambers filled with aqueous humour.

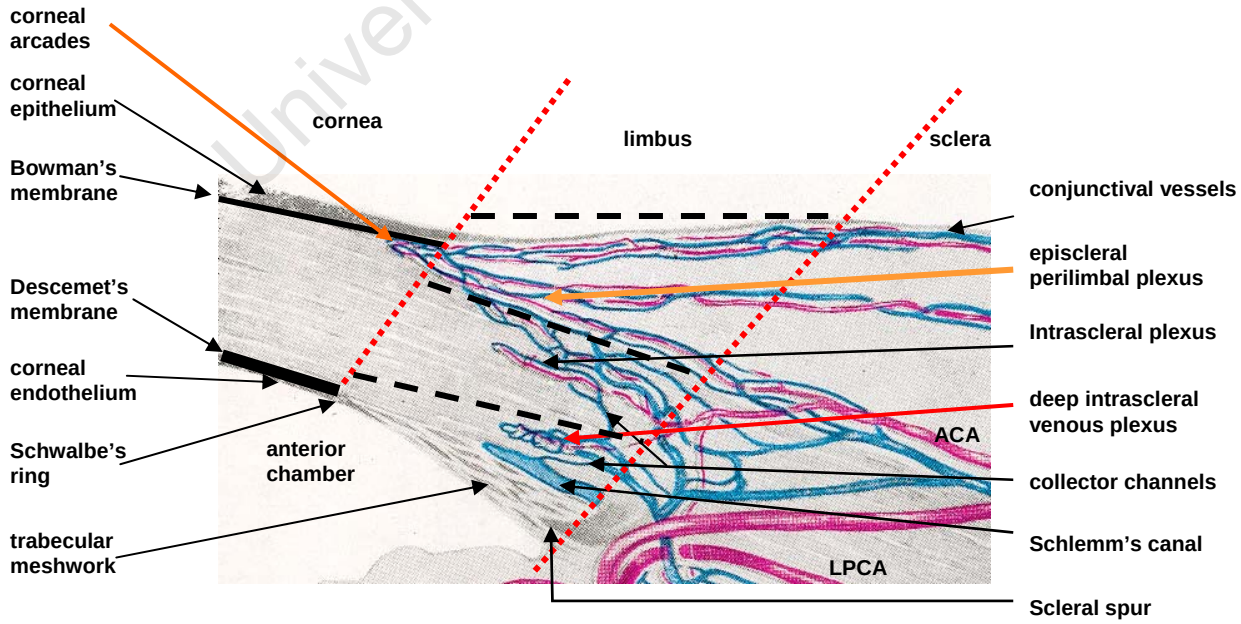

Figure 1.2 Anatomical location of the human limbus.

(Modified from Bron et al., 1997 - original drawing from Lauber H , after Maggiore, L. referenced in Bron et al, 1997 – Wolff's Anatomy of the eye).

et al., 1999). These lamellae are formed from closely packed fibres run across the full width of the cornea and curve at the limbus to form a pericorneal circle/annulus (Quantock et al., 2003). On the other hand, collagen fibrils of the sclera are randomly orientated have large variations in their diameter and are separated by large interfibrillar spaces (Komai and Ushiki, 1991; Austin et al., 2004). Covering the sclera is the episclera which is comprised of loose fibro-elastic tissue, blood vessels and lymphatic vessels (Bron et al., 1997). The sclera is essentially avascular with few blood vessels that communicate between the vascular beds of the choroid and episcleral vasculature that pass through it. In contrast to that of the cornea, the conjunctival stratified squamous epithelium has substantially more cells layers and forms rete-like ridges which penetrate the underlying connective tissue.

1.2 The limbus.

The limbus plays a pivotal role in the drainage of the major portion of aqueous humour from the anterior chamber. It contains tissues that are specialised for filtering the aqueous humour (the trabecular meshwork), and a complex set of aqueous vessels (Schlemm's canal, collector channels and aqueous veins) that transport the aqueous humour through to the circulatory system. One of the major functions of the trabecular meshwork and Schlemm's and surrounding extracellular matrix is to modulate the outflow resistance of the aqueous humour and this is critical in maintaining the intraocular pressure within the required range. The limbus is a narrow zone located at the periphery of the cornea and is defined by two anatomical boundaries. At the corneolimbal junction (inner boundary of the limbus), the limbus is demarcated by a line running from the terminal edge of Bowman's membrane through to the termination of Descemet's membrane of the cornea. In the human eye, the outer boundary of the limbus (the sclerolimbal junction) is demarcated by a line that passes through the deepest portion of the angle recess of the anterior chamber and the scleral spur, and runs parallel to the corneolimbal junction (Bron et al., 1997) (see Figure 1.2).

Since the terminology of some of the limbal anatomical structures varies in the literature, the following terms and location of the structures used in this thesis are presented below. There are three distinct layers of the limbus. In humans, the superficial limbus (the region between the upper and middle horizontal dashed lines - Figure 1.2) contains the epithelium of the limbal conjunctiva, and the underlying stroma and vasculature of the conjunctiva and episclera. Lymphatic vessels are also located in this layer. The circular plexus formed by the circular limbal artery and veins often referred to as the episcleral plexus will be referred to as the superficial perilimbal plexus in this thesis. Blood vessels that lie posterior to this perilimbal plexus are

referred to as the episcleral vessels. The mid limbus (the region between the middle and lowest horizontal dashed lines - Figure 1.2) contains the mid limbal intrascleral venous plexus (also called the mid scleral plexus by some authors), branches of the anterior ciliary and circular limbal arteries, and the aqueous vessels or collector channels that feed into the superficial perilimbal or episcleral veins. The mid limbus also contains a collagen rich stroma into which the dense transcorneal collagen fibres insert. This forms a perilimbal annulus (Quantock et al., 2003). The deep limbus (the region between the lowest horizontal dashed line and the anterior chamber) contains the deep intrascleral venous plexus, short collector channels, Schlemm's canal and the trabecular meshwork. Aqueous humour thus exits the anterior chamber at the iridocorneal angle and percolates through the trabecular meshwork, is transported into Schlemm's canal, then flows into the collector channels. In human and monkey eyes, a few collector channels called aqueous veins link directly to the superficial perilimbal or episcleral veins and the remaining channels feed into at the deep intrascleral venous plexus to enter the circulatory system. The outflow pathway of aqueous humour is simpler in the rat and mouse eye as there does not appear to be an intrascleral plexus. Collector channels (aqueous veins) pass through the sclera and drain directly into the aqueous veins in the episclera (Morrison et al., 1995, Smith et al., 2001a). The detail of these vessels and their organisation in the limbus is incompletely described.

The obvious question that arises when considering the complex limbal vasculature and aqueous drainage channels is how it functions and why this arrangement is necessary. For instance, why does the aqueous humour not enter directly into lymphatic vessels? One reason is that the intraocular pressure (IOP) needs to be maintained in order to preserve the shape of the globe which is essential for forming the optimal optical pathway. In order to maintain the IOP, but allow aqueous humour to drain from the eye, there must be resistance to flow between the anterior chamber and the circulatory system. This resistance is provided by the trabecular meshwork, Schlemm's canal, aqueous vessels and arterial-venous anastomoses in the episclera. However, it is important that the IOP is maintained within a narrow range of fluctuations (1-2 mm Hg) to prevent distortions in the optical pathway. In addition, large fluctuations of IOP in glaucoma patients are thought to increase the risk of progression of disease in patients with raised IOP (Lee et al., 2007; Simmons et al., 2008). In humans the normal IOP ranges from 10-21 mm Hg where individuals each have a distinct IOP (Ted M Montgomery at http://www.tedmontgomery.com/the_eye/optcnrve.html). In mice, each genetically distinct strain has a specific IOP which can range from 7-13.7 mm Hg depending on the strain (John et al., 1997; Savinova et al., 2001). Thus despite the specific normal IOP for the individual, the aqueous

outflow pathways play a pivotal role in maintaining the IOP within a narrow range. The different components of this pathway are reviewed below.

The first component of the conventional aqueous outflow pathway is the trabecular meshwork. It plays a major role in regulating the flow of aqueous humour through to Schlemm's canal. Permeability through the meshwork appears to be regulated by the alteration of cell volume of the trabecular cells, and by the contraction and relaxation of the ciliary muscle and myofibroblast-like cells in the trabecular beams (de Kater et al., 1992; Lütjen-Drecoll, 1998; Brandt and O' Donnell, 1999; Mitchell et al., 2002; Llobet et al., 2003). Although the trabecular meshwork was not studied in this thesis, its structure is briefly reviewed as this is closely associated with the structure and function of Schlemm's canal. The trabecular meshwork is a sponge-like tissue consisting of trabecular beams lined with an endothelium (trabecular cells) and intertrabecular spaces. The core of the trabecular beams consists of collagen and elastic fibres and myofibroblast-like cells. The trabecular meshwork extends from Schwalbe's ring anteriorly through to the insertion of the ciliary muscle in the sclera at the scleral spur in human eyes (Bron et al, 1997: Lütjen-Drecoll, 1998, Allingham et al., 2005) (Figure 1.2). Although a scleral spur is absent in mouse eyes the insertion of the ciliary muscle marks the posterior termination of the trabecular meshwork (Smith et al., 2001a). The aqueous fluid exits the anterior chamber, through the large intertrabecular spaces of the uveal meshwork. It then percolates through perforations in the trabecular sheets that make up the corneoscleral meshwork, then into the dense extracellular matrix of the juxtacanalicular meshwork before it is transported through the endothelium lining Schlemm's canal. The structure the trabecular beams is similar in humans, primates and mice except that the number of trabecular beams in mice is approximately $^1/_3$ - $^1/_2$ of that seen in human eyes. In mice, the number of trabecular beams ranges from 3-6 and 7-10 in the anterior and posterior regions of the meshwork respectively (John et al., 1999, Smith et al., 2001a). The juxtacanalicular region is prominent and smooth muscle cells from the ciliary muscle are located near the posterior border of the canal (Smith et al., 2001, 2001a). The trabecular meshwork accounts for 50 - 90% of the outflow resistance of aqueous humour in human and primate eyes (Lütjen-Drecoll, 1998). The endothelial cells lining the inner wall of Schlemm's canal are strongly attached to the juxtacanalicular meshwork (Ramos et al., 2007). Therefore movement of this region by the contraction or relaxation of the ciliary muscle and trabecular meshwork is thought to affect the shape of the canal (Moses, 1981).

Schlemm's canal forms a second barrier to the outflow of aqueous humour. Giant vacuoles, transcellular and paracellular pores, and aquaporins in the endothelium lining the inner wall of the

canal provide the route for the flow of aqueous humour from the trabecular meshwork into the canal. Since the three-dimensional architecture of the murine Schlemm's canal was studied in detail in the present study, the morphological characteristics of the canal are reviewed below. The canal is a wide circular vessel that is located next to the trabecular meshwork. Its inner wall faces the juxtacanalicular region of the trabecular meshwork and its outer wall faces the superficial limbus. The width of the canal is generally substantially broader than its height. In the human this ranges from 200-400 μm in width by 10-25 μm in height, and in mice the width of the canal varies from 43.4-75.6 μm (Bron et al., 1997; Smith et al., 2000). The canal is similar in several species and is irregular in shape, has a variable width that ranges from wide to very narrow segments. It also occurs as a single vessel that branches into a plexus of few anastomosing channels (Dvorak-Theobald, 1934, 1955; Ujie and Bill, 1984; Morrison et al., 1995; Bron et al., 1997). In humans, primates and mice, collagenous septae or beams span the inner and outer wall of the canal (Bill, 1993; Bron et al., 1997; Smith et al., 2001a; Johnstone, 2004, 2006). These beams which are often located near the openings of the collector channels are thought to provide structural support in preventing the collapse of the canal when the intraocular pressure is significantly raised (Johnstone and Grant, 1973; Johnson and Kamm, 1983; Ramos et al., 2007). Since the endothelium lining these beams is continuous with that of the canal, in cross section, the canal appears to be split into two or more smaller canals. Diverticuli extend from the canal into the surrounding tissue. Those that protrude from the inner wall of the canal penetrate the trabecular meshwork and are referred to as Sondermann's canals in humans and monkeys (Dvorak-Theobald, 1934. 1955; Ujie and Bill, 1984; Bron et al., 1997). Such diverticuli have not been reported in rats or mice. The canal which is also referred to as an angular aqueous plexus or sinus is also present in eyes of several lower mammalian species and also described in birds (Tripathi and Tripathi, 1972, 1973, 1973a; Richardson et al., 1985).

The endothelium lining the inner wall of the canal plays a role in controlling the flow of aqueous humour into the canal but appears to provide a relatively low resistance to flow (Sit et al., 1997). The morphology and functional properties of the inner wall endothelium are distinct from those lining the outer wall of the canal. The endothelial cells lining the canal are elongated with their longitudinal axes orientated along the length of the canal (Bron et al., 1997; Ethier, 2002; Johnson, 2006; Ramos et al., 2007). Endothelial cells that line the inner wall of the canal are generally longer and flatter than those that line the outer wall. The basal lamina of the inner wall is discontinuous whereas that lining the outer wall is prominent and continuous. In human eyes, cells containing smooth muscle actin and myosin are only located adjacent to the basal lamina of the outer wall of the canal (de Kater at al., 1990, 1992). Rat and mouse eyes also have a layer of

smooth muscle cells that reach the posterior juxtacanalicular region near the inner wall of the canal (Remé et al., 1983; Smith et al., 2001, 2001a). In the rat, smooth muscle cells of the ciliary muscle extend into the juxtacanalicular trabecular meshwork and lie adjacent and internal to the posterior region of the canal. However, it is not clear from the above reports whether the same occurs in mice. The endothelial cells lining the inner wall of Schlemm's canal in humans, primates, lower mammals and birds vary in size and possess unique giant vacuoles (Tripathi, 1968; Tripathi and Tripathi, 1972, 1973, 1973a; Remé et al., 1983; Bron et al., 1997; Smith et al., 2000, 2001, 2001a; Ethier, 2002; Ramos et al., 2007).

Giant vacuoles provide a mechanism for transcellular fluid and particulate transport across the inner wall endothelium that has filtered through the juxtacanalicular region of the trabecular meshwork (Tripathi, 1971; Tripathi and Tripathi, 1972, 1973a; Erickson-Lamy et al., 1991; Bron et al., 1997). When the intraocular pressure is raised, they increase in size and number (Johnstone and Grant, 1973; McMenamin and al-Shakarchi, 1989; Ye et al., 1997). Under raised IOP the giant vacuoles appear to concentrate near the ostea of collector channels in the outer wall of the canal (Parc et al., 2000). They are not true intracellular vacuoles but form on the basal side of the endothelial cells when the intraocular pressure is increased, thus bulging the endothelial cell into the canal (Johnson, 2006). Under these conditions, similar vacuoles or pseudovacuoles form between adjacent endothelial cells and provide a paracellular route for the outflow of aqueous humour (Epstein and Rohan, 1991; Ye et al., 1997). Small pores found on the distal portion of the giant vacuoles provide a transcellular route for passive flow between the juxtacanalicular extracellular matrix and the canal lumen.

Another mechanism of transfer of fluid into the canal is thought to occur via a mechanical pump which is coupled to the cardiac cycle. This has been proposed based on the presence of unusual features of the tissue beams in the canal (Johnstone, 2004; Johnson, 2006). The interior of the beams is continuous with the juxtacanalicular extracellular matrix and thus aqueous fluid accumulates here. During a transient rise in IOP with systole, aqueous fluid in the canal is forced out through collector channels by the deformation of the trabecular meshwork and outpouching of the inner wall endothelium. Fluid also enters the tissue beams causing them to stretch. Once the pressure is reduced, the trabecular meshwork and canal collapses and the fluid within the tissue beams moves into the canal (Johnstone, 2004).

Aqueous humour exits Schlemm's canal through collector channels or aqueous veins. Collector channels exit from several irregularly spaced points around the canal (Dvorak-Theobald, 1934,

1955; Ujie and Bill, 1984; Bron et al., 1997; Ramírez et al., 2004). In human eyes, they connect to the deep limbal, the mid intrascleral and superficial perilimbal or episcleral plexuses. Collector channels are also referred to as aqueous veins (Ashton, 1951; Jocson and Sears, 1969; Ujie and Bill, 1984; Bron et al., 1997), although some authors reserve this terminology for those collectors that directly link Schlemm's canal to the episcleral veins (Bron et al., 1997). In humans and primate eyes, collector channels number from 20-30 around the limbus, vary in width and length and are enclosed by cells expressing smooth muscle actin and myosin (de Kater et al., 1990, 1992). The number of channels is not known in the mouse eye. Most of the outflow through the inner wall of the canal is thought to occur in the region close to the collector channels as the number of giant vacuoles in the inner wall endothelium is greater near the ostea of the collector channels (Parc et al., 2000). The openings or ostea on the outer wall of Schlemm's canal are often funnel-shaped, elliptical or cylindrical (Dvorak-Theobald, 1934; Bron et al., 1997). During markedly raised IOP, the inner wall (and underlying juxtacanalicular meshwork) herniates and bulges into the canal and the collector channel ostea. Since the area of the canal near the collector channels essentially collapses, the aqueous humour entering the channels would therefore only originate from the portion of the canal that has herniated into the collector channel, thus effectively reducing the flow (Battista et al., 2008). Wholemount studies of the human eye show a different organisation of collector channels (Ramírez et al., 2004). These authors report that a collector channel runs parallel to Schlemm's canal along its exterior wall. It is linked to Schlemm's canal at numerous intervals by short aqueous vessels. Vessels that branch off the exterior wall of the collector channel then link to the intrascleral or episcleral veins.

In contrast to humans and primates, rat eyes do not appear to have a deep limbal or intrascleral limbal plexus. Collector channels arise directly from the outer wall of Schlemm's canal where they join the superficial perilimbal or episcleral venous plexus (Janes and Bounds, 1955; Morrison et al., 1995). Knowledge of the complete organisation of the limbal aqueous vessels and vasculature in the mouse eye is incomplete, but histological sections show that collector channels (aqueous veins) form a direct link between the canal and the superficial limbal/episcleral vessels (Smith et al., 2001a). This suggests that the mouse and rat eye are similar. Other images show small vessels near the outer wall of the canal in the adult mouse eye (see Figure 3E, G in Smith et al., 2001). However, it is not known whether these vessels are part of a deep intrascleral plexus or are cross sections of collector channels.

Although the major outflow pathway of the aqueous humour is via the trabecular meshwork, Schlemm's canal and aqueous vessels, outflow via the uveoscleral route has been shown in

humans, primates and mice (Ujie and Bill, 1984; Pederson and Toris, 1987; Toris et al., 1987; Bron et al., 1997; Krohn and Bertelsen, 1998; Lindsey and Weinreb, 2002; Aihara et al., 2003; Bernd et al., 2004).

1.3 The ocular vasculature.

Of paramount importance to tissue and organ function is an adequate blood supply. In most organs, the micro anatomical organisation of the vasculature is unique and regional differences in this organization are intricately associated with a specific and local microphysiology. The eye is comprised of many different histological regions, some of which (such as the choroid) are very heavily vascularised tissues, whilst others (such as the cornea, lens, anterior and posterior chambers and vitreous) are avascular. On the other hand the pericorneal limbus is vascularised, contains lymph vessels and a circumferential/circular aqueous vessel (Schlemm's canal) which connects to the superficial limbal vasculature via collector channels and aqueous veins.

The blood supply to the eye is via the ophthalmic artery. It branches near the optic stalk and supplies the inner and superficial regions of the globe. The anterior segment receives its supply via two long posterior arteries and the anterior ciliary arteries. The long posterior ciliary arteries penetrate the sclera near the optic stalk and traverse on the medial and lateral sides of the eyeball in the suprachoroidal space and branch to form the major arterial circle of the iris (MAC), or also referred to as the circulus arteriosus iridus major (Figure 1.3) (Morrison et al., 1995; Bron et al., 1997; Allingham at al, 2005). In rodents and hamsters this artery has been referred to as the iridociliary ring artery/circle or circular ciliary artery (Bhutto and Amemiya, 2001; Ninomiya and Inomata, 2005, 2006). The anterior ciliary arteries arise from the muscular branches of the ophthalmic artery. They travel with the arteries of the four external ocular muscles (recti), continue anteriorly and branch before they reach the corneoscleral junction (Figure 1.3) (Ashton and Smith, 1953; Jocson and Sears, 1968, 1969; Morrison et al., 1995; Bron et al., 1997: Allingham et al., 2005; Ninomiya and Inomata, 2005, 2006). In human and primate eyes, two anterior ciliary arteries feed from each extraocular muscle except the lateral muscle from which only one anterior ciliary artery arises. However, although anterior ciliary arteries are reported to be present in the rat and mouse eye, as far as can be established, the number of anterior ciliary arteries that supply the limbal vasculature in these species has not been reported. Scrutiny of Figure 7 in Morrison et al., (1995), suggests only two anterior ciliary arteries supply the limbal artery (circular limbal artery), with the other supply originating from a branch off the long posterior ciliary artery. Morrison et al. (1995) do not, however, comment on this.

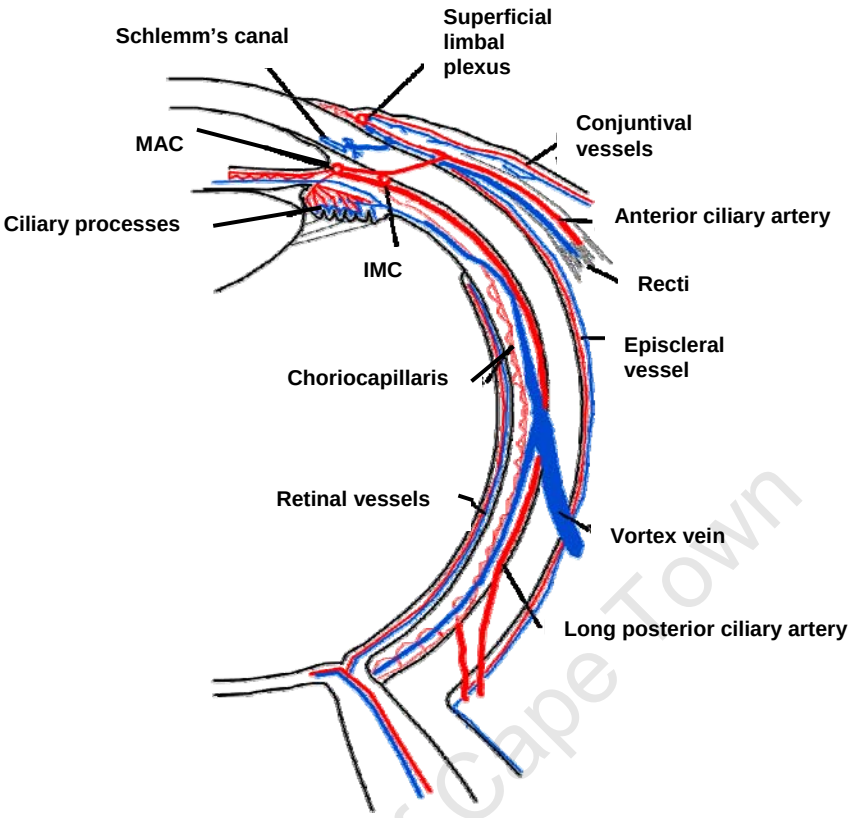

Figure 1.3: Vascular supply to the posterior and anterior ocular segments (redrawn from Bron et al., 1997).

After branching at the corneoscleral limbus, one branch of the anterior ciliary artery extends anteriorly to the episclera where it forms the episcleral arterial circle (circular limbal artery). This vessel directly supplies the sclera, limbus, conjunctiva, and indirectly supplies the iris via anastomoses with the major arterial circle of the iris. The other branch of the anterior ciliary artery penetrates the sclera just posterior to the limbus and reaches the ciliary muscle where it anastomoses with the vascular plexus in the ciliary muscle. In humans and primates, the ciliary intramuscular circle which is formed from anastomoses between vessels branching off from the anterior ciliary arteries and the long posterior arteries, is located within the ciliary muscle and lies posterior to the major arterial circle (Bron et al., 1997; Allingham et al., 2005). Within the ciliary muscle, terminal branches of the anterior ciliary arteries extend anteriorly to join with the major arterial circle (Ashton and Smith, 1953; Bron et al., 1997). In the rat, the anterior ciliary artery joins directly to the long posterior artery via an arteriole that perforates the sclera. This arteriole joins the long posterior artery at a site before the latter has split into the major arterial circle of the iris (Morrison et al., 1995). A different organisation of the vasculature has been reported in

hamsters where the anterior ciliary arteries branch off the long posterior ciliary arteries and branch to form the iridociliary ring (Ninomiya and Inomata, 2005).

At the limbus, the anterior ciliary arteries branch to form an incomplete arterial circle around the corneoscleral limbus, which in the human eye runs close to Schlemm's canal (Ashton and Smith, 1953). Other superficial branches of the anterior ciliary arteries give rise to the marginal corneal or limbal arcades that lie below the limbal epithelium and end at Bowman's membrane. In humans, arterioles that branch off the anterior ciliary arteries also form arcades that supply the palisades of Vogt (similar structures to rete ridges of the skin) (Bron et al., 1997). In rats, the vasculature of the corneal arcades is fed via short radial arterioles that branch off the circular limbal artery (Selbach et al., 1998).

Superficially, the anterior ciliary artery branches to form a single circular limbal artery which runs parallel with the superficial perilimbal venous plexus (Morrison et al., 1995). Others have reported that the circular limbal artery of the rat eye is formed by vessels that branch off the long posterior ciliary arteries. These arterioles reach the episclera and split to form the circular limbal artery that runs alongside two circular veins that interconnect with each other (Selbach et al., 1998; Bhutto and Amemiya, 2001). These authors do not report an association between the anterior ciliary arteries and the circular limbal arteries. The latter study used rats of a different strain to that reported by Morrison et al. (1995) and therefore this may account for the anatomical differences in the ocular vasculature – see Discussion). Others have reported an iridociliary ring artery (ciliary ring artery) in hamsters, mice and rats that arises from the anterior ciliary arteries. This ring artery supplies the ciliary body, the conjunctiva and the iris, with the latter also receiving blood from branches off the long posterior artery (Ninomiya and Kuno, 2001; Ninomiya and Inomata, 2005, 2006). According to these authors, this ring artery corresponds to the major arterial circle of the iris in humans and primates (Ninomiya and Inomata, 2005). Whilst these authors report that the conjunctiva is supplied via the anterior ciliary arteries, and also report the presence of an episcleral plexus, they do not report on the organisation of the limbal vasculature in rodents.

A superficial perilimbal venous plexus anastomoses with the corneal arcades and also receives aqueous humor from aqueous veins that arise either directly from Schlemm's canal or from deeper intrascleral venous plexus that connect with collector channels that arise from the canal (Figure 1.3) (Dvorak-Theobald, 1934, 1955; Ashton, 1951; Bron et al., 1997). In humans, the episcleral veins drain into the posterior ciliary veins and leave the eye via the inferior and superior

ophthalmic veins (Bron et al., 1997). In mice, the superficial perilimbal venous plexus drains into the ciliary veins in the episclera. These pass through the external ocular muscles where they link up to a well developed orbital venous sinus into which most of the venous drainage of the eye occurs (Yamashita et al., 1980).

1.4 Ocular development.

1.4.1 Formation of the optic cup, anterior and posterior segments.

The structure and development of the murine aqueous outflow pathway in the limbus is the focus of the present study. The limbus is derived from cells that have migrated from the periocular mesenchyme during prenatal development. To fully appreciate how the limbus develops, a brief overview of the prenatal development is provided. The vertebrate eye is composed of a variety of tissues that have their embryonic origins in the neural ectoderm, surface ectoderm, neural crest and paraxial mesoderm (Bron 1997; Creuzet et al., 2005; Gage et al., 2005). At the onset of morphogenesis of the murine eye shortly after 8.5 days post coitum (dpc), lateral outgrowths from the eye fields in the left and right walls of the forebrain give rise to optic vesicles that extend outward to the surface ectoderm (Pei and Rhodin, 1970; Hoar, 1982; Cvekl and Tamm, 2004). A reciprocal interaction between the surface ectoderm and neuroectoderm of the optic vesicle results in the formation of the lens and retinal placodes respectively. As the lens placode proliferates to form a lens pit, there is a concurrent invagination of the distal portion of the optic vesicle. With further growth, the lens vesicle forms and the invaginated optic vesicle forms the optic cup which is lined by a double layer of the neural epithelium. The inner and outer neural epithelial layers of the optic cup differentiate into the neural and the pigmented epithelial layers of the retina respectively. Surrounding the developing optic vesicle and optic cup is the periocular mesenchyme which contains mesenchymal cells that are derived from the cranial paraxial mesoderm and migrating cells from the neural crest (Creuzet et al., 2005; Gage et al., 2005; Iwao et al, 2008). Due to the asymmetrical development of the optic cup, a ventral fissure is formed (Figure 1.4a) which allows the entry of mesenchymal cells and the hyaloid artery to the presumptive posterior chamber (Figure 1.4b) (Cook and Sulik, 1986). The outer surface of the optic cup is continuous with the narrowed optic stalk which remains open to the cavity of the forebrain.

The surface ectodermal epithelium that remains after the detachment of the lens vesicle at 12.5 dpc in the mouse forms the primitive corneal epithelium consisting of two rows of cells resting on a basement membrane (Pei and Rhodin, 1970; Kidson et al., 1999; Saika et al., 2001; Gould et al.,

2004). Mesenchymal cells migrate from the periocular mesenchyme across the rim of the optic cup between the primitive corneal epithelium and lens epithelium to form the cornea and limbus. In the avian eye, the first influx of neural crest-derived mesenchymal cells forms the corneal endothelium. A second influx of neural crest-derived mesenchymal cells forms the corneal stroma (Creuzet et al., 2005). In humans and mice, the first wave of mesenchymal cells that migrate between the presumptive corneal epithelium and the lens vesicle originate from the neural crest and paraxial mesoderm, with the bulk of migrating cells arising from the neural crest (Cvekl and Tamm, 2004; Evans and Gage, 2005; Gage et al., 2005; Ittner et al., 2005). Migration occurs soon after the lens vesicle has detached from the overlying epithelium, and continues until several layers of mesenchymal cells are present. In mice, this takes place around 11-11.5 dpc. Between 13.5 and 14.5-15.5 dpc (in mice) and at 33 dpc (in humans), the inner layer of mesenchymal cells that faces the lenticular surface condenses and develops into the primitive corneal endothelium. This endothelium separates the cornea from the lens and results in the formation of a primitive anterior chamber (Pei and Rhodin, 1970; Bron et al., 1997; Kidson et al., 1999; Saika et al., 2001; Smith et al., 2001; Gould et al., 2004).

The iris and ciliary body develop from the anterior margin of the optic cup which continues to expand anteriorly and centrally by processes of proliferation and epithelial thinning. This causes the tip of the optic cup to markedly taper towards the centre (Pei and Rhodin, 1970, Bron et al., 1997; Napier and Kidson, 2005). However, prior to the outgrowth of the optical cup, a second wave of mesenchymal cells migrates from the periocular region near the rim of the optic cup across the anterior surface of the lens to form the pupillary membrane (Bron et al., 1997). This membrane is vascularised via vessels that branch off the major arterial circle and long posterior arteries (see section **1.3**). By 14-15 dpc the anterior portion of the murine embryonic iris is covered with a loose, vascularised mesenchymal tissue and the anterior margin of the optic cup continues to grow centrally between the pupillary membrane and the lens epithelium (Pei and Rhodin, 1970; Bron et al., 1997). By 16.5-17 dpc the cornea and iris become separated and an angular recess (iridocorneal angle) is formed between the cornea and iris root (Pei and Rhodin, 1970; Smith et al., 2001; Gould et al., 2004). The development of the iridocorneal angle is reviewed in more detail below (see section **1.4.3**). Between 18.5 dpc and birth (P0), the outer epithelium of the prospective ciliary body folds inwards eventually forming a well defined ciliary body by P4 (Napier and Kidson, 2005; Davis-Silberman and Ashery-Padan et al., 2007).

The primorida of the murine eye lids develop from shallow folds of the surface epithelium at 13 dpc and continue to grow centrally until they fuse at 15-16 dpc where they remain fused until

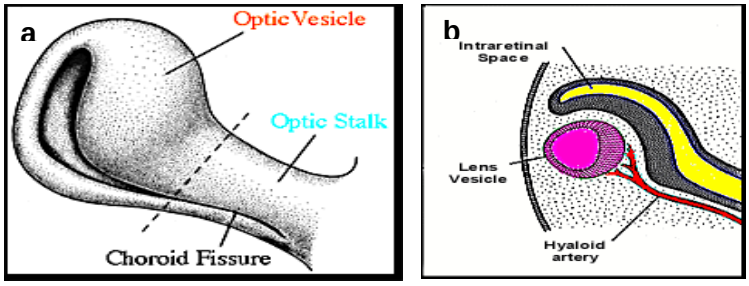

Figure 1.4: Development of the optic vesicle and stalk.
Assymetrical development of the optic vesicle forms the choroid fissure which allows mesenchyme and hyaloid artery to enter the presumptive posterior chamber. E12 mouse eye.
Adapted from: http://www.med.unc.edu/embryo_images/unit-eye/eye_htms/eye014a.htm

approximately eight to twelve days after birth (reviewed in Harris and Jurihoff, 1998; Saika et al., 2001).

1.4.2 Development of the murine ocular vasculature.

There are three general mechanisms by which blood vessels develop: 1) By d*e novo* formation (vasculogenesis) which occurs by coalescence of endothelial cell progenitors (angioblasts) which either migrate to or differentiate at the site of future blood vessels. These progenitors coalesce to form angiocysts or angiocords which further coalesce to form a primitive vascular network (Risau, 1997; Eichmann et al., 2002, 2005; Fruttiger 2002); 2) By the process of angiogenesis which occurs by the extension/sprouting of existing vasculature due to migration and proliferation of endothelial cells resident in the blood vessels (sprouting angiogenesis), or, by intussusception where a single vessel splits longitudinally to form two or more vessels (non-sprouting angiogenesis) (Risau,1997; Eichmann et al., 2002, 2005; Djonov et al., 2003); 3) By haemo-vasculogenesis where a common progenitor for haematopoietic and endothelial cells (the haemangioblast) gives rise to the simultaneous development of blood vessels and blood cells (Sequeira-Lopez et al., 2003; Hasegawa et al., 2007). Once the primary capillary vasculature is formed, a process of pruning, remodelling and vessel maturation takes place (Risau, 1997; Fruttiger, 2002).

All three mechanisms of vascular development are reported to occur in the human eye (Fruttiger, 2002; Chan-Ling et al., 2004; Saint-Geniez and D'Amore, 2004; McLeod et al., 2006; Hasegawa et al., 2007). However, relatively little is known about the early development of the blood vessels that supply the anterior segment in the mouse eye, and when the architecture of the mature limbal vasculature is formed. Since the limbal vessels are directly linked to the aqueous outflow pathway

and are supplied by the anterior ciliary and long posterior ciliary arteries, the following section reviews what is known of the early development of the mouse eye vasculature that is associated with the limbal vessels. The development of the aqueous outflow vessels which develops postnatally is reviewed in section **1.4.3**.

The earliest evidence of ocular blood vessels in the mouse eye is seen at 10-11 dpc. Randomly orientated, sinusoidal-like capillaries form in the periocular mesenchyme as the optic cup invaginates (Pei and Rhodin, 1970). At 10.5 -11.5 dpc, mesoderm-derived cells migrate between the developing lens vesicle and the tip of optic cup (See Figure 2a-c in Kidson et al., 1999; Smith et al., 2001; Gage et al., 2005; See Figure 2a in Iwao et al., 2008). It is thought that these mesoderm-derived cells contribute towards the development of the vasculature of the iris and ciliary body, the anterior portion of the vascular tunic surrounding the lens, and, to the hyaloid vascular system in the vitreous (Balazs et al., 1980 (abstract only) reviewed in Mitchell et al., 1998; Smith et al., 2001). Soon thereafter, primitive blood vessels form near the rim of the optic cup and between the lens and optic cup (Pei and Rhodin, 1970; Saint-Geniez et al., 2006). The primitive vessels in the periocular mesenchyme undergo reorganization and maturation to form a mature capillary network that becomes the choriocapillaris by 13-14 dpc in the mouse. At this stage, the only other blood vessels in the anterior segment are those that have formed a capillary network (pupillary membrane) around the anterior portion of the lens. Therefore, the episcleral vessels have not yet formed. By 11-13 dpc, the hyaloid artery, which enters the vitreous via the embryonic fissure posteriorly, branches and forms a vascular tunic around the posterior portion of the lens. The capillary beds that line the posterior and anterior parts of the lens anastomose and form the tunica vasculosa lentis (TVL) by 13-14 dpc. Accordingly, the supply to the TVL is via vessels that originate from the hyaloid artery and from the periocular vasculature. In the case of the latter source, it is not clear whether the anterior ciliary arteries contribute towards the formation of the TVL. Since the latter vessels may originate from the vascular supply to the extraocular muscles, these vessels are only likely to emerge after the muscles have started to form. Condensation of the mesenchyme that gives rise to the presumptive muscles appears 12 dpc (Sulik et al., 2001). Therefore by the time the TVL has formed, the anterior ciliary arteries may have reached the limbus, and sent a branch through the sclera to anastomose with the uveal vasculature and TVL. However, there is no evidence of vessels in the episclera in mice at this stage (see Plate 3 in Pei and Rhodin, 1970; see Figure 1b in Saint-Geniez at al., 2006). Furthermore, as far can be determined, there are no reports on the development of the episcleral and superficial perilimbal vasculature in mice, even during the early postnatal period. Since the choroid vasculature is well established by 15 dpc, the iris and ciliary body which are extensions of this uveal layer become

vascularised at the onset of their morphogenesis (Pei and Rhodin, 1970; Napier and Kidson, 2005).

With the exception of the retinal vessels, little is known of the mechanisms of vascular development in the mouse eye. However, support in favour of vasculogenesis comes from the presence of neural crest and mesoderm-derived cells in the primitive vitreous before the hyaloid vasculature has formed, and the subsequent presence of these cells in the more mature hyaloid vasculature (Evans and Gage, 2005; Gage et al., 2005). In the zebrafish, endothelial cells have been specifically identified in the posterior chamber before the hyaloid vascular network is evident (Alvarez et al., 2007), thus also indicating that the hyaloid vessels are formed by this process. However, nothing is known of how vessels are formed in the anterior segment.

On the other hand, there is more compelling evidence of vasculogenesis in other compartments of the human eye, thus this may also be true in the mouse eye. Early in ocular development, the primitive choroid vasculature and the embryonic annulus (vascular ring that encircles the lens) are formed before the anterior ciliary and long posterior ciliary arteries have developed (Bron et al., 1997). Therefore initially, neither the primitive choroid vasculature nor the embryonic annulus appears to be connected to the circulatory system. Others have used progenitor endothelial cell markers to show that the primary retinal vessels form by vasculogenesis (Chan-Ling et al., 2004; McLeod et al., 2006). Recently it has been reported that the primitive choroid vessels in the human form through haemo-vasculogenesis (Hasegawa et al., 2007).

By contrast, the secondary retinal vessels and larger vessels of the developing choroid (short and long posterior ciliary arteries and collecting channels that feed into the vortex veins) form by angiogenesis in the human eye (Chan-Ling et al., 2004; McLeod et al., 2006; Hasegawa et al., 2007). Angiogenesis also appears to be the only means by which primary and secondary retinal vessels develop in the mouse eye (Fruttiger et al., 2002).

1.4.3 Development of the iridocorneal angle, trabecular meshwork and Schlemm's canal.

The iridocorneal angle (anterior chamber angle) in the adult eye is the peripheral region of the anterior chamber that is formed between the iris and the cornea. The iris root lies at the apex of this angle. During its early development, the tissues that lie at this apex contain the mesenchymal tissues that will form the trabecular meshwork, the pericanalicular tissue of the inner wall of Schlemm's canal, and iris root. These tissues are derived from the periocular mesenchyme, which in mammals, originates mainly from the neural crest and from the paraxial mesoderm (Creuzet et

al., 2005; Gage et al., 2005; Iwao et al, 2008). The earliest signs of morphogenesis of the angle are observed during the late first trimester, or early second trimesters in humans, monkeys, cats, and rodents (Smelser and Ozanics, 1971; Remé et al., 1983; 1983a; Richardson et al., 1985; McMenamin, 1989; Hamanaka et al., 1992; Smith et al., 2001). The sequence of morphogenesis of the different components that make up the iridocorneal angle is remarkably conserved between vertebrate species (Barishak, 2003). However, definitive structural changes to the various components of the iridocorneal angle, such as the differentiation of the trabecular meshwork and development of Schlemm's canal or an aqueous plexus, occurs prenatally in humans and monkeys but postnatally in rodents and cats (Remé et al., 1983; 1983a; Richardson et al., 1985; Smith et al., 2001).

In order for the aqueous humour to exit the anterior chamber at the iridocorneal angle, the tissue in this region must provide a suitable passage through which the fluid can flow. This means that the undifferentiated, loosely arranged mesenchymal cells that form the anlagen of the aqueous outflow pathway have to undergo substantial differentiation. Importantly, the anterior chamber needs to first form to create the angle where aqueous humour will exit the eye. Before the anterior chamber is created, the mesenchyme that will form the aqueous outflow pathway is first seen as a loosely arranged group of undifferentiated cells lying close to the outer surface of the narrower rim of the optic cup (that will form the iris and ciliary body) (Smelser and Ozanics, 1971; Remé et al., 1983, 1983a; Richardson et al., 1985; McMenamin, 1989; Hamanaka et al., 1992; Smith et al., 2001). This is observed at 14.5 dpc in the mouse and before 7 weeks in human embryos (Pei and Rhodin, 1970; Bron et al., 1997; Smith et al., 2001). Initially, the primitive anterior chamber is formed by the anterior migration of mesenchymal cells concomitant with the advancing tip of the optic cup to create the chamber angle (iridocorneal angle). At this early stage of angle development, the corneal endothelium extends into the deep recess of the angle (Smelser and Ozanics, 1971; Richardson et al., 1985; Bron et al., 1997). At this stage, the mesenchyme in the angle and on the primitive iris becomes more densely packed but remains undifferentiated (Smith et al., 2001). In mice and rats, the angle is first observed at 16.5 dpc and 17 dpc respectively (early third trimester) whereas in the primate and humans, the angle has formed early during the late first or early second trimesters (Remé et al., 1983; Smelser and Ozanics, 1971; Pei and Rhodin, 1970; Bron et al., 1997; Smith et al., 2001). Although the present study examines the development of Schlemm's canal and the aqueous vessels, the early morphogenesis of the canal is associated with the development of the trabecular meshwork. Therefore the development of these structures is reviewed together.

The presumptive trabecular meshwork starts off as a strip of avascular, undifferentiated densely packed mesenchyme that accumulates between the differentiating ciliary body and sclera. This occurs when the cornea and sclera begin to differentiate and is observed at P4 in mice and at 14 weeks in humans (Smelser and Ozanics, 1971; Hamanaka et al., 1992; Bron et al., 1997; Smith et al., 2001). As cells in the presumptive trabecular meshwork start to differentiate, small vascular channels that form the precursor vessels of Schlemm's canal appear near the future trabecular meshwork. This occurs at P8 in mice, P5 in rats, and at 16 weeks in human fetuses (Remé et al., 1983; Hamanaka et al., 1992; Smith et al., 2001). The vascular channels increase in number as the future corneoscleral and uveal meshwork start differentiating into closely packed cells and a reticular-like meshwork respectively. At this stage of development, the alignment of the cells of the presumptive trabecular meshwork is regular whilst that of the surrounding mesenchymal cells remains randomly organised (Hamanaka et al., 1992). In the human eye, the cells of the presumptive corneoscleral trabecular meshwork are aligned with their longitudinal axes along the circumferential plane before the precursor vessels of Schlemm's canal are observed near the trabecular meshwork (Hamanaka et al., 1992). However, this preferential alignment along the circumferential plane is not seen in mice, rats and cats. By contrast, the cells forming the primitive corneoscleral meshwork have their longitudinal axes orientated in the meridional plane (i.e. aligned along the anterior-posterior axis) before blood vessels appear near the site of the future Schlemm's canal (Remé et al., 1983; Richardson et al., 1985; Smith et al., 2001).

In order to enable aqueous fluid to gain access to Schlemm's canal, the tissue in the angle recess deepens posteriorly by a process of rarefaction (i.e. opening up spaces between the cells) in the angle mesenchyme where intercellular spaces become apparent and "coalesce" to form large intercellular spaces (Smelser and Ozanics, 1971; Remé et al., 1983). With the exception of the rat, this process of rarefraction does not involve cell death (Smelser and Ozanics, 1971; Remé et al., 1983a; Smith et al., 2001). Prior to differentiation of the iridocorneal angle, the cells lining the angle recess posterior to the corneal endothelium form a continuous layer with the corneal endothelium. At the onset of differentiation of the angle, this cell lining becomes discontinuous thus allowing direct access of the aqueous humour to the intertrabecular spaces in the uveal trabecular meshwork. Communication between the anterior chamber and the uveal meshwork occurs shortly before birth in human fetuses and within a few days after birth in monkeys and cats (Smelser and Ozanics, 1971; Richardson et al., 1985). In rats, communication between the anterior chamber with the uveal meshwork starts relatively later at P10-20 (Remé et al., 1983). In the case of the mouse, it appears that this communication occurs at P14 (Smith et al., 2001). The trabecular meshwork continues to differentiate and both it and the iridocorneal angle reach

maturity between P35 and P42 in the mouse, between P60 and P100 in rats, and at 4 years in humans (Remé et al., 1983; Smith et al., 2001; Bron et al., 1997).

It is generally accepted that the primitive aqueous outflow vessels including Schlemm's canal function as blood vessels. Therefore, tracking the presence of blood vessels in the limbus during the early stages of development of the iridocorneal angle may provide evidence of how the canal is formed, i.e. by vasculogenesis or by angiogenesis from other limbal blood vessels. At the onset of the angle morphogenesis, it is clear that the canal has not yet formed. At this stage, the vessels that may give rise to the canal are not even present in the sclera or limbus near the presumptive chamber angle. However, at the onset of the formation of the iridocorneal angle, blood vessels that may form the presumptive episcleral vessels are present in the superficial sclera and reported to be only occasionally seen in the deep limbus by 14 weeks gestation (Hamanaka et al., 1972). Others report the presence of a vascular plexus lying anterior to the anlage of the trabecular meshwork in 70 mm embryos (i.e. between 11 to 12 weeks gestation), but do not indicate whether the plexus encircles the limbus (Sevel and Isaacs, 1988; also reviewed in Warwick, 1976; Rich et al., 1996, Bron et al., 1997). By 16-17 weeks gestation, blood vessels are frequently observed deeper in the limbus close to the region of the future Schlemm's canal, but have not reached the future corneoscleral portion of the trabecular meshwork (Hamanaka et al., 1992). By viewing sections cut in the circumferential plane, these authors show that blind-ending vessels branch off the deep limbal vessels. It is hypothesised that these vessels grow towards the trabecular meshwork. Arising from these vessels are vascular sprouts that are orientated along the circumferential plane to form a primitive but incomplete Schlemm's canal. Thus Schlemm's canal is thought to arise from angiogenesis from the deep intrascleral plexus. These authors also report that the canal is generally fully formed shortly before birth or shortly thereafter. On the other hand, at 16 weeks, Schlemm's canal is reported to consist of a plexus of blood vessels and it is hypothesised that these derive from the vascular plexus that is first observed in 70 mm embryos (Sevel and Isaacs, 1988; also reviewed Ramírez et al., 2004). The presence of vacuoles in the endothelium lining the canal indicate that aqueous humour is transported into the canal and that it becomes and aqueous vessel by 20 weeks gestation (Bron et al., 1997).

Morphogenesis of Schlemm's canal in the rat and mouse starts off as small vascular channels in the deep limbus at P5 and P8 respectively (Remé et al., 1983; Smith et al., 2001). By P10 and P24, a single canal-like vessel has formed in the rat and mouse eye respectively. Maturation of Schlemm's canal continues until P60 in the rat where numerous giant vacuoles are present in the endothelial lining of the canal. In the mouse, giant vacuoles are first seen at P14 and are more

numerous by P21 at which stage, the canal is fully mature (Smith et al., 2001). However, these authors do not show any evidence of the origin of the precursor vessels that form Schlemm's canal.

Although most studies report the presence of blood vessels, or endothelial lined channels before Schlemm's canal is formed, only that by Hamanaka et al. (1992) shows a direct relationship between the down growing scleral vessels and the presumptive Schlemm's canal. Based on these observations and the hypothesis of Smelser and Ozanics (1971), the favoured model of the development of Schlemm's canal is that the canal is formed from several blind-ending vessels that grow down from the deep scleral plexus and anastomose to form a the canal. A different relationship between Schlemm's canal and the development of the outflow pathway to the episcleral venous plexus has been reported by Ramírez et al. (2004). By cannulating Schlemm's canal and perfusing it with a pigmented polyester resin, the aqueous outflow was viewed in whole eyes from 24 week old human fetuses through to eyes from young children and adults. At 24 weeks gestation, Schlemm's canal was seen as complete but not connected to the outflow vessels in the mid limbus or in the episclera. Instead, short straight vessels are reported to radiate from the canal to link to collector channels which run superficial and parallel to the canal. Only after birth (as seen at 2 months) branches arising from the outer walls of the collector channels connect to segments of the intrascleral plexus and superficial perilimbal and episcleral plexuses. By eight years the intrascleral and superficial perilimbal plexuses were complete throughout the limbus. This finding suggests that Schlemm's canal is not derived by sprouting angiogenesis from the intrascleral vasculature, but may form *de novo* by vasculogenesis.

1.4.4 The role of developmental genes in ocular morphogenesis.

The morphogenesis of the anterior segment described above requires a series of coordinated events and interactions between different tissues, and is dependant on the timeous expression of several genes. These include key transcription factors, growth factors, receptors and cellular metabolites/enzymes that are expressed in the periocular mesenchyme, optic cup or lens prior to and during the development of the anterior segment. Genes encoding transcription factors, shown to be essential for normal development of the anterior segment are *Foxc1, Foxc2, Foxe3, Pitx2, Pitx3, Pax6, Lmx1b, Msx1,* and *Msx2* (Furuta and Hogan, 1998; Kidson et al., 1999; Smith et al., 2000; Gould and John, 2002; Zhao et al., 2002; Gould et al., 2004; Lang, 2004; Evans and Gage, 2005; Liu et al., 2006; Snowden, 2007).

1.4.4.1 Transcription factors that regulate morphogenesis of the anterior chamber and iridocorneal angle.

Foxc1, Foxc2, Lmx1b and Pitx2 are transcription factors that are expressed in a variety of tissues during the murine embryonic development. With respect to ocular development, *Foxc1, Foxc2, Lmx1b* and *Pitx2* are expressed in the periocular mesenchyme during the formation of the optic cup and lens vesicle and are essential for normal ocular development. *Foxc1* (formally *Mf1*) which encodes a forkhead/winged helix transcription factor is expressed in the periocular mesenchyme during the formation of the optic cup and invagination of the lens vesicle (10.5 - 11.5 dpc in the mouse) (Kidson et al., 1999; Berry et al., 2006). At this stage *Foxc1* is expressed mainly in the posterior ocular mesenchyme and to a lesser extent in anterior periocular and presumptive corneal mesenchyme (Gage et al., 2005; Berry et al., 2006; Snowden, 2007). ß-galactosidase lineage marking studies have shown that *Foxc1* is expressed predominantly in the neural crest-derived cells but is also expressed in a small proportion of mesoderm-derived cells in the periocular mesenchyme and in mesenchymal cells that have migrated between the lens and presumptive corneal epithelium (Gage et al., 2005). By contrast, *Foxc2* is expressed more anteriorly in the periocular mesenchyme (but not between the surface ectoderm and optic cup) and is only expressed in neural crest-derived cells (Gage et al., 2005).

Pitx2, which belongs to the homeodomain paired-box family of transcription factors, is more highly expressed in the anterior periocular mesenchyme and in cells migrating between the surface ectoderm and the lens (Gage et al., 2005; Berry et al., 2006). Initially *Pitx2* is expressed in neural crest-derived cells and later in larger portion of mesoderm-derived cells prior to their migration into the optic field (Gage et al., 2005). A proportion of the cells in the anterior ocular mesenchyme also co-express *Foxc1* and *Pitx2* and later this co-expression is seen in a subpopulation of cells in the corneal endothelium and future iridocorneal angle at 16.5 dpc (Berry et al., 2006). After detachment of the lens vesicle, *Foxc1* is expressed in the presumptive sclera and corneal mesenchyme and epithelium, but expression is markedly reduced in the cornea thereafter. After the anterior chamber has formed, *Foxc1* expression subsides and becomes restricted to the cells of the iridocorneal angle (presumptive trabecular meshwork) and the corneal endo- and epithelium from 15 to 18.5 dpc (Kidson et al., 1999; Ittner et al., 2005). The LIM homeodomain class transcription factor Limx1b is also expressed concomitantly with the above transcription factors in the periocular mesenchyme and primitive cornea. However, at birth, *Limx1b* is more widely expressed than *Foxc1* or *Foxc2* and is present in the mesenchyme of the iridocorneal angle, the iris and ciliary body, and cornea (Pressman et al., 2000 (abstract only) – reviewed in Gould et al., 2004).

The absence of Foxc1 caused by spontaneous mutation in the *Mf1* gene (*Mf1*^{ch}) or by ablation through a targeted gene strategy (see section **2.1.3** for details), results in mouse embryos dying perinatally with severe skeletal, cardiovascular, urogenital and haeomorrhagic hydrocephalus, and ocular defects (Kume et al., 1998; Hong et al., 1999; Kidson et al., 1999; Smith et al., 2000; Seo et al., 2006). *Foxc2* (formally *Mfh1*) has a similar pattern of embryonic expression to that of *Foxc1*, and homozygous mutants also die perinatally with abnormalities similar to those seen in *Foxc1*$^{-/-}$ mutants (Iida et al., 1997). Homozygous *Pitx2* mutants die at mid gestation with severe defects to the heart, asymmetry of the lungs, arrested development of the pituitary gland, and ocular defects (Kitamura et al., 1999; Gage et al., 1999). Complete absence of *Limx1b* expression results in smaller eyes with corneal abnormalities and a smaller anterior chamber. The effect of the null mutation on the development of the iridocorneal angle and aqueous outflow pathway is not known as these mice die shortly after birth (Pressman et al., 2000 (abstract only), reviewed in Gould et al., 2004).

Thus in *Foxc1, Foxc2* and *Pitx2* homozygous mutants, the corneal stroma is either abnormal or fails to develop and the corneal endothelium is absent (Gage et al., 1999; Kidson et al., 1999; Kitamura et al., 1999; Evans and Gage, 2005). The consequence of incomplete morphogenesis of the cornea is that the anterior chamber, the iridocorneal angle and the structures of the main aqueous outflow pathway are not formed (Gage et al., 1999; Kidson et al., 1999; Evans and Gage, 2005). On the other hand, heterozygous *Foxc1, Foxc2* and *Pitx2* mice survive until after birth or through to adulthood, but present with a variety of ocular defects. Heterozygous *Foxc1* (*ch/Mf1*) or *Foxc2* mice have ocular defects in the anterior segment (anterior segment dysgenesis) that include irregularly shaped pupils, corneal opacity with neovascularisation, corneal cataracts, iridocorneal adhesions (synechia), iris hypoplasia, (Hong et al., 1999; Smith et al., 2000). Histologically, the iris is attenuated, and there are a variety of defects in the iridocorneal angle which includes a small or absent Schlemm's canal, a poorly developed or absent trabecular meshwork, and the presence of vascular abnormalities (Smith et al., 2000). *Pitx2*$^{+/-}$ mice have a range of defects in the anterior chamber that show a marked hypercellularity or attenuation in the corneal stroma and epithelium in *Pitx2*$^{-/-}$and *Pitx2*$^{+/-}$ mice respectively (Gage et al., 1999; Asai-Coakwell et al., 2006). As mentioned in section **1.2**, the trabecular meshwork and Schlemm's canal play a pivotal role in maintaining the intraocular pressure by regulating the flow of aqueous humour. Thus structural abnormalities to these components of the aqueous outflow pathway in *Foxc1, Foxc2* or *Pitx2* heterozygous mice should cause a raised IOP. On the contrary, neither raised IOP nor glaucomatous damage to the optic disc has not been shown in *Foxc1*$^{+/-}$, *Foxc2*$^{+/-}$ or

Pit2x$^{+/-}$ mice. However, a small portion of patients who have mutations in the human homologue of *Foxc1* (FKHL7) develop raised IOP (Mears et al., 1998).

1.4.4.2 Bone morphogenetic protein-4 expression and signaling during ocular morphogenesis.

Bone morphogenetic proteins (BMPs) are a group of closely related polypeptides that form part of the transforming growth factor β (TGFβ) superfamily. These molecules have wide ranging functions that span the regulation of morphogenesis, cell proliferation, apoptosis, differentiation and the determination of cell fate. For the purpose of this review, only the role of BMPs (particularly BMP4) in ocular development will be reviewed below. BMPs are widely expressed from the earliest period of embryonic development, are key signaling molecules in organ development, and, are required for the maintenance and repair of adult tissues (Hogan, 1996, 1996a; Wordinger et al., 2002). BMP signaling occurs via trans-membrane serine-threonine kinase receptors BMPRIA, BMPRIB and BMPRII, through which the signal is transduced. BMP signal transduction through the type I receptors (BMPRIA (ALK3), BMPRIB (ALK6)) results in phosphorylation and activatation of the transcription factor Smad1 which complexes with Smad4. This complex translocates to the nucleus where it modulates the transcription of downstream genes (Attisano and Wrana, 2000).

The earliest expression of *Bmp4* in the developing mouse eye is detected in the distal portion of optic vesicle and in the surface ectoderm (14-16 somite stage (8 dpc) (Furuta and Hogan, 1998). After the lens placode has formed, *Bmp4* is no longer expressed in the surface ectoderm but becomes restricted to the dorsal segment of the optic vesicle at 10.5 dpc (Futura and Hogan, 1998). A similar expression pattern of *Bmp4* is seen in the chick eye during the same stages of eye development (Trousse et al., 2001). The genes for the receptors for Bmp4 (*Bmpr1A* (*Alk3*) and *Bmpr1B* (*Alk6*) are also differentially expressed in that *Alk3* is widely expressed throughout all ocular and periocular tissues from the earliest developmental stages during ocular development, and is still present at 11.5 dpc (Furuta and Hogan, 1998). Thus Bmp4 secreted from a restricted region of the dorsal optic cup is still able to exert its effect over a wide area. By contrast, *Alk6* expression is generally concentrated at the optic stalk and the posterior regions of the optic vesicle and optic cup. This pattern of *BmprIA* and *BmprIB* expression in the mouse eye has also been reported in the developing chick eyes (Trousse et al., 2001). In order for the lens to develop, signaling between the surface ectoderm and optic vesicle is required for the induction of the lens placode and subsequent lens formation. The expression and secretion of Bmp4 along with the expression of *Pax6* is thought to confer competency to the surface ectoderm by inducing the

expression of *Sox2*. Once competent, the surface ectoderm is thought to respond to signals which may be regulated by the local expression and secretion of Bmp4 (Furuta and Hogan., 1998)

After the optic cup has formed, *Bmp4* is expressed in the epithelial cells of the developing ciliary body, iris, and retinal pigment epithelium from 14.5 dpc, with increasing expression in these structures from birth through to P30 (Chang et al., 2001). However, others report that *Bmp4* transcripts are not detected in the epithelium of the iris during its morphogenesis from 18 dpc through to P7 but are expressed in the epithelium of the developing ciliary body during this period (Zhao et al., 2002). Other ocular tissues expressing *Bmp4* are the endothelial cells lining the blood vessels in the conjunctiva (possible episcleral vessels), retina, iris and orbit (Chang et al., 2001). However, none of the structures involved in the aqueous outflow pathway such as the trabecular meshwork, Schlemm's canal, or intrascleral limbal vasculature express *Bmp4*.

Although *Bmp4* expression is localised to the above regions, its putative signaling pathway is more widely spread throughout the ocular tissues. The transcription factor Smad1 becomes phosphorylated (pSmad1) in response to BMP signaling. Initially (at 12 dpc), pSmad1 is present in most of the ocular tissues. After birth, pSmad1 is present in the epithelium of the ciliary body, the lens and cornea as well as the corneal endothelium. Interestingly, pSmad1 is also present in the mesenchymal cells in the iridocorneal angle at P1 (prior to the differentiation of the trabecular meshwork), thus rendering these tissues receptive to Bmp signaling (Zhao et al., 2002).

Bmp4 is also transiently expressed by the lens epithelium during the initial stages of the regression of the pupillary membrane. In the rat eye this occurs during P6-P10 (Kiyono and Shibuya, 2008. The secretion of Bmp4 from the lens continues until 16 dpc by which time the pupillary membrane has regressed. The mechanism by which the pupillary vessels regress is that Bmp is secreted by the lens, and binds to Bmp4 receptors on the vascular endothelium. Bmp4 signaling in this case is via the Smad1/Smad5 pathway which induces apoptosis of the endothelial cells in the pupillary membrane (Kiyono and Shibuya, 2003). It is interesting to note that *Bmp4* is neither expressed in the trabecular meshwork, nor in the cornea of adult mouse eyes (Chang et al., 2001). By contrast, cells isolated from the trabecular meshwork in postnatal infants and adult humans express a number of BMPs including BMP4 and BMP receptors (Wordinger et al., 2002). BMPs and their receptors are also expressed in the adult cornea where they can either stimulate proliferation and/or apoptosis (the latter in the presence of actinomycin D) of the corneal fibroblasts (Mohan et al., 1998; You et al., 1999).

Bmp4 is expressed in mouse embryos from 6.5 dpc and homozygous *Bmp4* mutants usually do not develop beyond gastrulation. If they do develop further, the variety of severe defects are so severe that embryos do not survive beyond 10.5 dpc (Winnier et al., 1995; Furuta and Hogan., 1998). *Bmp4* mutant embryos that have survived until 10.5 dpc do not form a lens placode (Furuta and Hogan, 1998). The downstream effect of homozygous *Bmp* mutations is that the transcription factors *Sox2* and *Msx2* are not expressed in the surface ectoderm and in the distal portion of the optic vesicle prior to the period when the lens placode is formed. Several regulatory genes that are expressed in the optic vesicle and surface ectoderm during this period are unaffected in mutant *Bmp4* mice, hence the optic cup still forms but the lens does not develop (Furuta and Hogan, 1998).

Heterozygous *Bmp4* mice survive through to adulthood but present with ocular structural abnormalities similar to that seen in *Foxc1* and *Foxc2* mice. In particular, the iridocorneal angle is severely affected, and in places, the trabecular meshwork and Schlemm's canal are either poorly developed or even absent (Chang et al., 2001). BMP4 and its receptors are expressed in the human trabecular meshwork from the early postnatal period throughout life (Wordinger et al., 2002). Although the *Bmp4* geneis not expressed by the trabecular meshwork in mice, it is not known whether Bmp receptors (particularly Bmpr1a) are expressed in this region.

1.5 Imaging of ocular blood and aqueous vessels.

More than fifty years ago the aqueous outflow vessels and Schlemm's canal were studied by several groups but the relationship of Schlemm's canal with other vessels in the limbus and the exact origin of vessels in the aqueous outflow pathway remained unclear (Dvorak-Theobald, 1934; Ashton, 1951). The following section of this review examines the different approaches used since then to image blood vessels and how these have been used to examine the ocular vasculature and aqueous drainage vessels. Furthermore, insights into the origin of Schlemm's canal provided by these different imaging methods are reviewed.

One of the first ways that ocular vessels and aqueous outflow pathways were studied was by tracing vessels in serial sections cut through the meridonal or orthogonal planes of the eye (Dvorak-Theobald, 1934; Hamanaka et al., 1992; Krohn and Bertelsen, 1998;). In order to better visualise the aqueous outflow routes and ocular vessels, some investigators injected coloured dyes or India ink into the vascular system or outflow pathway, then fixed and processed the eyes for histology (reviewed in Dvorak-Theobald, 1934; Ashton, 1951; Krohn and Bertelsen, 1998). In this way "stained" vessels could then be traced in serial sections of eyes cut along the meridonial

or orthogonal planes. Three-dimensional reconstructions were made from wax models built on tracings of the vessels (Dvorak-Theobald, 1934, 1955). These approaches however, proved to be extremely tedious and the accuracy of the traced vasculature was deemed questionable due to distortions created by the histological processing (reviewed in Ashton, 1951). Furthermore, the curved shape of the eye is not conducive to accurately constructing the anatomical vascular organisation from sectioned material (reviewed in Burger et al., 1987).

1.5.1 Microvascular perfusion with plastics and corrosion casting.

A more successful technique of viewing the three-dimensional organisaton of the ocular vessels is microcorrosion vascular casting. Vascular casts are produced by injecting unpolymerised plastics (monomers) such as methyl methacrylate resins with or without Mercox (van Buskirk et al., 1979; Risco and Nopanitaya, 1980; Morrison et al., 1995; Majji et al., 2000; Bhutto and Amemiya, 2001; Ninomiya and Kuno, 2001; Ninomiya et al., 2005, Ninomiya and Inomata 2005, 2006,), Microphil or neoprene latex (Ashton, 1951, Ashton, 1952; Ashton and Smith 1953) directly into blood vessels or Schlemm's canal. The liquefied resin/plastic/neoprene is allowed to polymerize *in situ*, after which the surrounding tissue is digested away leaving the plastic cast representing the lumen of the vascular system. Casts can be viewed and photographed under a dissecting microscope and higher resolution images can be obtained by viewing with a scanning electron microscope (Lametschwandtner and Lametschwandtner, 1992).

Microcorrosion vascular casting has considerably improved the understanding of the spatial organisation of the ocular vasculature. Additional benefits of this technique are that arteries, veins and capillaries can be distinguished from each other by noting the characteristic surface features of the cast left by the "footprints" of the endothelial cells showing the shape and orientation of their nuclei (Burger et al., 1987; Selbach et al., 1998). The three-dimensional organisation of the Schlemm's canal, and its relationship to the aqueous outflow vessels and the limbal blood vessels in the human eye was first shown in microvascular casts by administering neoprene into the ophthalmic artery and into Schlemm's canal (Ashton, 1951, 1952; Ashton and Smith, 1953). In later studies, coloured silicone injected into Schlemm's canal or anterior chamber was used to reveal the limbal vessels in primate eyes. Instead of digesting the tissues, the aqueous outflow vessels were viewed in the intact eye by clearing the tissue with methyl salicylate (Jocson and Sears, 1968, 1969; Gaasterland et al., 1970). By injecting the silicone into specific limbal vessels or into the anterior chamber, these studies report that the organisation of collector channels and deep intrascleral aqueous plexus of the primate eye is similar to that seen in the human eye.

Importantly, they show that the deep intrascleral plexus is not connected to the uveal vasculature and that aqueous humour exits the limbus via the episcleral veins (Gaasterland et al., 1970).

Microcorrosion vascular casts have also been used to reveal the ocular vasculature of the anterior segment in small animals such as cats, guinea pigs hamsters , mice, raccoons, rats, rabbits, (Morrison et al., 1987 (cats, guinea pigs, rats); Selbach et al., 1998 (rabbit & rat); Ninomiya and Kuno, 2001 (rat) Ninomyia et al., 2005 (raccoon); Ninomiya and Inomata, 2005 (hamster); Ninomiya and Inomata, 2006 (mouse)). However, despite the wide use of this technique in studying the ocular vasculature, there is only one study that reports the association of canal with collector channels which link to the superficial limbal plexus (Morrison et al., 1995). Importantly, these authors also emphasise the fragile nature of corrosion casts that results in incomplete segments of the the aqueous outflow pathway.

A limitation in microcorrosion vascular casting is that filling defects arise during perfusion of the plastics with loss of information of vessel architecture. Polymerized casts are often fragile and are easily damaged during specimen handling. Administration of the liquefied plastic monomers under non-physiological pressures also increases the risk of creating artefacts of non-existing vascular space/linkages between microvascular systems (Lametschwandtner et al., 1984; Hamid et al., 2006). Blind-ending vascular outgrowths may not be filled so visualising recent angiogenic events is often not reproducible (Lametschwandtner and Lametschwandtner, 1992). Furthermore, visualisation of lymphatic vessels generally requires separate perfusion into the lymphatic system.

A modification of the vascular casting approach is that of diaphanization. Here vessels are perfused using a liquid polyester resin containing a dye. After the resin has polymerised, the fixed tissue is bleached in hydrogen peroxide, and dehydrated in ethanol and benzyol. The final process of diaphanization includes “clarifying” the tissue in a mixture of methyl salicylate and benzyol peroxide. Ramírez et al. (2004) used this approach to view the development of Schlemm’s canal and collector channels of the human eye. By introducing the liquid resin directly into Schlemm’s canal, these authors were able to show that Schlemm’s canal was already formed at 24 weeks gestation, with the presence of outer collector vessels running in parallel to the canal. Short straight vessels arising from the outer wall of the canal formed links to the outer collector vessel. These authors also show that connection of the outer collector vessels to the intrascleral plexus occurs later in development (36 weeks gestation) and the connection to the episcleral vascular plexus appears even later. Their study thus suggests that Schlemm’s canal does not develop from downgrowths off the deep limbal vessels as previously reported (Hamanaka et al., 1992).

1.5.2 In vivo imaging of ocular vessels.

1.5.2.1 Fluorescein angiography.

Fluorescein angiography (administration of fluorescein via intravenous injection) was first used in 1961 to observe retinal vasculature and blood flow in the living human eye (Novotny and Alvis, 1961). Due to its low molecular weight it also has the additional benefit of determining whether tight junctions of the vascular endothelium of the ocular microvasculature are intact or leaky (Meyer and Watson, 1987). Whilst a high level of junction integrity is present between cells of the vascular endothelium of normal retinal vessels, scleral and conjunctival vessels are leaky to molecules smaller than albumin (Meyer and Watson, 1987). Application of low doses of fluorescein and rapid slit-lamp photography has revealed the episcleral and conjunctival vessels with similar architecture to that of the corrosion casts of described by Ashton (1951, 1952) (Meyer and Watson, 1987).

Fluorescein isothiocyanate linked to dextran does not leak through the vessels of the anterior segment and has been used to view the limbal vessels and retinal vessels in living mice (Hawes et al., 1999; Lahvis et al., 2000; Ritter et al., 2005) and iris vessels in rats (Burns-Belhorn et al., 1978) after injecting the dye into the vascular system. Others have traced the limbal vessels by injecting fluorescent dextrans into the anterior chamber and viewing its flow through the limbal vessels (Morrison et al., 1995). With the exception of Ritter et al. (2005) who used confocal microscopy to capture images of the labelled vessels, most fluorescein angiography studies use slit-lamp cameras to capture images.

1.5.2.2 Transgenic mice expression GFP-vascular endothelium fusion proteins.

The ocular vasculature in living mice expressing green fluorescent protein (GFP) under the promoter for Tie2 (which is exclusively expressed by vascular endothelium) has been imaged using laser scanning confocal microscopy (Ritter et al., 2005). Because ocular vessels of the same animal can be imaged at different time points, this model is ideal for studying ocular vascular development. In this regard regression of hyaloid vessels and the morphogenesis of the retinal vasculature have been revealed in postnatal mice (Ritter et al., 2005). Although the limbal vasculature was also noted in this study, these authors have not examined Schlemm's canal nor associated aqueous vessels. In addition, it is not certain as to whether or not angiopoeitin receptors are present in the endothelium lining Schlemm's canal.

1.5.2.3 In vivo microscopy of fluorescent-labelled antibodies.

Fluorescent-labelled antibodies specific for vascular endothelial cell adhesion molecules such as PECAM-1, VCAM-1 and E-selectin which is injected into vascular system of mice and allowed to circulate allows the above antibodies to bind *in vivo* to the adluminal endothelial plasma membranes. Using this approach and imaging with two-photon microscopy, conjunctival, choroid and retinal vessels have been revealed in living animals (Runnels et al., 2006). The advantage of this approach is that the effects of experimental treatments on the vasculature over time, as well as observing developmental processes can be traced in the same animal.

1.5.2.4 In vivo imaging of the limbal vasculature.

One of the well known methods of viewing the limbal vasculature *in vivo* in small animals is by slit- lamp microscopy and photography (Kure et al., 2003; Cursiefen et al, 2005). Slit-lamp microscopy or photography is particularly useful in detecting corneal neovascularisation where the vascular networks are revealed by the presence of blood in the vessel lumens. However, aqueous vessels are not readily revealed by this approach. A goniolens is able to view inside the anterior chamber and the iridocorneal angle which is not visible by conventional stereo/surgical microscopy. Using this approach, Schlemm's canal, however, is only visible if filled with blood (Smith et al., 2002).

1.5.3 Vascular Endothelial cell labelling.

Improved optical systems, the increased availability of antibodies recognising vascular endothelium, vascular tracers such as fluorescent-labelled or histochemically stained lectins and endothelial cell-specific histochemical stains have paved the way for imaging the ocular vasculature in wholemount preparations or *in situ.* The advantage of these applications over vascular casting methods is that multiple labelling can be combined with vascular perfusion in the same material.

A solution of silver nitrate administered via the intravascular route, fixed *in situ* and reduced to silver halide by exposure to bright light has been used to view limbal vessels in wholemounts of the monkey eye (Gaasterland et al., 1970). This method also produces high definition of endothelial cell borders and can be viewed in wholemounts using Nomarski optics (Murphy et al., 1999; Ezaki et al., 2001). As far as can be established, this method has not been used to view lymphatic vessels and Schlemm's canal.

1.5.3.1 Lectins.

The use of lectins to detect specific glycogongugates in tissues is well established and has been applied to study the limbus of the mouse eye (Vanden Hoek et al., 1987). The endothelium lining Schlemm's canal has been detected with several lectins (*Concanavalia ensiformis* (ConA), *Tricicum vulgaris* agglutinin (WGA), *Ricinus communis* agglutinin (RCA) and *Limulus polyphemus* agglutinin (LPA). In addition, these lectins also stain the corneal scleral stroma and other components of the anterior segment, therefore, are not suitable for tracing the vasculature in wholemount applications. Lectins such as *Concanavalia ensiformis* (ConA), *Griffonia simplicifolia* (Isolectin IB4), *Lycopersicon esculentum* (LEA) and *Ulex Europeaus agglutinin-1* (UEA-1) bind to the surface of vascular endothelial cells in rodents (ConA, Isolectin IB4, LEA) and in humans (UEA). They are often used in intravascular perfusions to trace perfused vessels (Murphy et al., 1999; Moromizato et al., 2000; Thurston et al., 2000; Ezaki et al., 2001; Joussen et al., 2001; Thurston, 2002; Baluk et al., 2004, 2004a; Matsumoto et al., 2004; Babu et al., 2007) but can also be applied to whole-mounts or tissue sections (van Wijngaarden et al., 2005; Campos et al., 2006; Hamid et al., 2006; Ritter et al., 2006). Lectins are also useful for distinguishing between the anatomical vascular bed and that which is perfused. Here fluorescently-labelled lectins or dextrans are injected into the vascular system after which the excised material is immunostained as whole mounts with vascular endothelium specific antibodies (such as PECAM-1(CD31) or stained with fluorescent lectins. The perfused (functional) or anatomical vascular beds can then be compared (Campos et al, 2006; O'Ceallaigh et al., 2006; Babu et al., 2007;). Staining vascular endothelium with lectins yields a generalised surface stain, but borders of the endothelial cells are not clearly defined (Figure 2a, b in Murphy et al., 1999; Figure 2 in Thurston et al., 2000; Figure 1 in Ezaki et al., 2001; Figure 3 in Joussen et al., 2001). Lymphatic vessels in rodents are not detected with lectins that stain vascular endothelium (Baluk and McDonald, 2008).

1.5.3.2 Immunostaining of vascular endothelium.

1.5.3.2.1 Intracellular and cell surface molecules.

Numerous intracellular and cell surface markers expressed by endothelia lining blood and lymphatic vessels have been identified, with some such as PECAM-1 (CD31), VE-Cadherin, VEGFR-2, Von Willibrand factor expressed by both vessel types. On the other hand, Prox-1 and LYVE-1 are more specific to lymphatic endothelium (Baluk and McDonald, 2008). Using a combination of lymphatic-specific markers with a marker common to blood and lymphatic vessels, each vessel type can be distinguished in the same specimen. The rest of this review will focus on the various approaches to viewing vascular and lymphatic vessels, and comment on the

potential use of these approaches in imaging Schlemm's canal. Von Willibrand factor (vWF or Factor VIII), is a secreted protein produced by endothelial cells of vascular origin. For instance, the corneal endothelium does not produce von Willibrand factor (Hyldahl, 1985; Ramos et al., 2007). Weibel-pallade bodies, unique to endothelium of vascular origin, are recognized by antisera raised against vWF (Wagner et al., 1982). Weibel-pallade bodies are less abundant in the endothelial cells lining Schlemm's canal compared to vascular endothelium, with much of the endothelium lining the inner wall devoid of these structures (Hamanaka et al., 1992). Vascular endothelium is readily detected with vWF antisera but lymphatic vessels stain relatively weaker and show patchy staining (Erhard et al., 1996; Ramos et al., 2007). Where limbal vessels and collector channels are readily detected with vWF antisera, lymphatic vessels and Schlemm's canal stain poorly with this antibody, with large segments of the canal remaining unstained (Hamanaka et al., 1992; Krohn, 1999; Ramos et al., 2007).

Receptors to vascular endothelial growth factors (VEGF1, -2, and -3) are present on the surface of endothelial cells in blood vessels. Lymphatic vessels express VEGFR-2 and VEGFR-3 and have been detected in wholemounts of the corneolimbus (Hamrah et al., 2004; Ramos et al., 2007). However, it is not known whether these growth factor receptors are expressed by the endothelium of Schlemm's canal.

1.5.3.2.2 Cell adhesion molecules.

Vascular and lymphatic endothelial cells express numerous surface proteins against which antibodies have been raised and which have been used in imunolabelling procedures to detect blood vessels. Cell surface molecules such as endothelial-leukocyte adhesion molecule (E-selectin), intercellular adhesion molecule-1 (ICAM-1), vascular cell adhesion molecule-1 (VCAM-1 or CD54), and platelet-endothelial cell adhesion molecule (PECAM-1 or CD31) are present on human vascular endothelial cells (Ayalon et al., 1994; Erhard., et al., 1996). It is generally accepted that this endothelium demonstrates both structural and functional heterogeneity in different organs and sometimes within different regions of the same organ (Craig et al., 1998). Similarly, ocular vessels are also reported to show site-specific functional heterogeneity, specifically involving extravasation of inflammatory leukocytes that occurs mainly in the iris and ciliary body. By contrast, retinal, scleral and choroid vessels appear to be less "permeable" to transcytosis of inflammatory cells (Silverman et al., 2001). These differences are thought to be due to the differential expression of cell adhesion molecules in particularly those associated with the cellular junctions (Silverman et al., 2001). Endothelial cells express numerous cell surface proteins such as ICAM-1, ICAM-2, VCAM-1, PECAM-1, E-selectin and VE-cadherin. However,

not all of the above cell surface antigens are expressed at consistent and detectable levels (Silverman et al., 2001). This possibly limits their use as a general vascular endothelial cell specific marker. Of these adhesion molecules, PECAM-1 appears to be the most consistent in its level of expression in the general vasculature in several organs (Vallien et al., 2000). VE cadherin and PECAM-1 are expressed by the endothelia of Schlemm's canal and collector aqueous channels in the human eye (Heimark et al., 2002; Read et al., 2007), and PECAM-1 is also expressed by endothelial cells lining lymphatic vessels (Cursiefen et al., 2002; Hamrah et al., 2004; Morisada et al., 2005). Whilst some authors report that lymphatic vessels are not detected with antibodies raised against PAL-E, E-selectin, ICAM-1 and VCAM-1 (Erhard et al., 1996), others report that ICAM-1 is expressed by endothelia of blood and lymphatic vessels and Schlemm's canal (Ramos et al., 2007).

Lymphatic vessels express Hyaluronan-binding receptors (LYVE-1). These receptors are not found on vascular endothelium in normal blood vessels but have been detected in endothelia lining the liver sinusoids and in a subpopulation of bone marrow-derived cells in the cornea (Banerji et al., 1999; Mouta Carrera et al., 2001; Chen et al., 2005). Developing lymphatic vessels express the homeobox gene *Prox-1*, a master gene that specifies the lymphatic cell fate (Hong et al., 2002; Oliver et al., 2002). Once the lymphatic vessels have formed, this gene is no longer expressed. VE-cadherins are also expressed by lymphatic vessel endothelia, but their expression is markedly less compared to PECAM-1 (Murfee et al., 2007). Podoplanin and Desmoplakin are also exclusively expressed by lymphatic endothelia (Cursiefen et al., 2002; Hong et al., 2002; Ramos et al., 2007) and CD11b positive macrophages involved in lymphangiogenesis (Maruyama et al., 2005). Of the above-mentioned endothelial cell-specific molecules, PECAM-1 is expressed not only by the endothelium lining blood and lymphatic vessels, but also by the endothelial cells lining Schlemm's canal in humans (Heimark et al., 2002). As far as can be ascertained, there are as yet, no published reports of detecting the murine Schlemm's canal with antibodies to PECAM-1. A more indepth review of this molecule is given below.

1.5.3.2.3 PECAM-1 (CD 31).

Platelet Endothelial Cell Adhesion Molecule- 1 (PECAM-1)/CD31 was first identified as a glycoprotein of MW 110-140 kD on platelets, monocytes, neutrophils and a subset of lymphoblasts (Ohto et al., 1985). An independent study in the same year reported that a glycoprotein of similar size range (145kD) was common to platelets and vascular endothelial cells (van Mourik et al., 1985). Subsequently a 130kD glycoprotein called EndoCAM was identified on bovine and human endothelial cells and this study also showed that this molecule was related to

CD31/ PECAM-1 in human endothelial cells (Newman et al., 1990). The general consensus put forth was that the above glycoproteins, which were common to endothelial cells and the above leukocytes, were the same molecule (Albelda at al., 1991). Since then PECAM-1 (CD31) has been used as a panendothelial cell marker to detect vascular endothelium in immunostained tissue sections and in wholemounts. In the mouse eye, it has been used to examine the superficial perilimbal vasculature in corneal angiogenic assays and to examine the choroid and retinal vasculature (Ambati et al., 2002; Cursiefen et al., 2002, 2005; Kure et al., 2003; Hamrah et al., 2004; Chen et al., 2005; Marneros et al., 2005; Dell et al., 2006; Saint-Geniez et al., 2006).

PECAM-1 is expressed on circulating platelets, monocytes, neutrophils, some subsets of T cells and endothelial cells, with the latter cells containing highest density of molecules on their plasma membranes (DeLisser et al., 1994; Galkina et al 2007;). PECAM-1 is expressed in peripheral cells lining blood islands of the yolk sac and in the embryonic vessels forming cardiovascular system and other organ systems (Baldwin et al 1994; Vecchi et al., 1994)).

PECAM-1 is generally localised at the lateral borders of adjacent endothelial cells at points of cell-cell contact where they form a strong homophilic binding with PECAM-1 molecules on the adjacent cell (Albelda et al., 1990; Ayalon et al., 1994; DeLisser et al., 1994; Vecchi et al., 1994; Erhard et al., 1996; Newman, 1997; Wong et al., 2000; Graesser et al., 2002; Moseley and Jackson, 2004). PECAM-1 is also reported to be located in subluminal pinocytotic-like vesicles, in deep invaginations of the plasma membranes and in parajunctional vesiculo-vacuolar organelles which are open to the lumen of the blood vessel (Erhard et al., 1996; Mamdouh et al., 2003; Feng et al., 2004). These vesicles provide a ready supply of the molecule in the plasma membrane for homophilic binding with leucocytes during their transmigration through the endothelium. Localisation to the cell periphery only occurs when the extracellular and transcellular domains of the molecule are intact (Sun et al., 2000; Wong et al., 2000). Loss of the entire cytoplasmic domain causes dispersed localisation of the molecule over the plasma membrane (DeLisser et al., 1994a). The extracellular Ig II domain of this molecule is essential for directing it to the cell borders where its main purpose is to form cell-cell contacts (homophilic interactions) (Sun et al., 2000; Wong et al., 2000).

Interpretation of PECAM-1 distribution depends on the epitopes of the molecule to which antibodies are targeted (Erhard et al., 1996; Feng et al., 2004). Depending on whether antibodies to PECAM-1 recognise the intracytoplasmic or extracellular domains, PECAM-1 is either evenly distributed across the cell membrane or concentrated at the lateral cell borders respectively (Feng

et al., 2004). Different sources for the antibodies to PECAM-1 and the epitopes recognised by these antibodies have led to reports that show variations in the distribution of PECAM-1 in vascular and lymphatic endothelium. In some cases, PECAM-1 is reported to be present on the luminal and abluminal cell surfaces of vascular endothelium whilst in others, the molecule is only located on the luminal surface (Erhard et al., 1996; Sauter et al., 1998; Ebata et al., 2001). On the hand, lymphatic vessels less intensely with little staining of PECAM-1 on the abluminal surface. In lymphatic vessels, PECAM-1 is more concentrated at the junctions between endothelial cells (Erhard et al., 1996).

1.6 Aims and Objectives.

Abnormalities in the development and structure of the posttrabecular aqueous outflow pathway are a significant risk factor for glaucoma. The broad aim of this thesis is to advance the understanding of the murine outflow pathway and its development

Specific objectives.

1) To develop a novel, effective and practical method for visualization and analysis of the entire outflow pathway including the Schlemm's canal, the collector channels and their relationship to the superficial limbal vasculature.

2) To develop an immunostaining methodology that allows accurate discrimination between the different components of this pathway.

3) To describe in detail the entire outflow pathway of the normal adult C57BL/6Jx129 and ICR mouse strains.

4) To elucidate in detail the postnatal development of the posttrabecular aqueous outflow pathway in ICR mice from day 2-14.

5) To describe the effects of *Foxc1* and *Bmp4* haploinsufficiency on the posttrabecular aqueous outflow pathway in C57BL/6Jx129 and ICR mouse strains.

CHAPTER 2

Materials and Methods

2.1 Animals and Genotyping.

Use and breeding of mice for this project was approved by the UCT Animal Ethics Committee (License number 01/11). *Bmp4*^{lacZ} (Lawson et al., 1999) and *FoxC1*^{lacZ} (Kume et al., 1998) mice were generously donated by Prof Brigid Hogan (Duke University). The *Bmp4*^{lacZ} mice were maintained on an ICR background and the *Foxc1*^{lacZ} mice were maintained on the C57BL/6Jx129 and ICR backgrounds at the UCT animal unit. New breeding pairs were established every 6 months from young mice positively identified by genotyping as carrying the *Bmp4*^{lacZ} or *Foxc1*^{lacZ} cassettes. Animals were fed *ad libitum* and had free access to fresh water. Ambient temperature was maintained at 21^{o}C, and mice were exposed to twelve hour day and night cycles. Most of the adult *Bmp4*^{lacZ} and *Foxc1*^{lacZ} mice used in the present study were older breeders that were no longer used in the breeding programme. The genotyping of most of these breeders had been established by others who required litters produced by these breeders for their research (Napier, 2005; Napier and Kidson, 2005; Sommer et al., 2006). The remaining animals used in the present study were genotyped according to the protocols established by Napier (2005) in our laboratory.

2.1.1 DNA extraction.

Genomic DNA was extracted from mouse tail cuts according to a protocol based on that of (Sambrook et al., 1989) or (Miller et al., 1988). The latter is referenced on the Transgenic Animal Web at http://www.med.umich.edu/tamc/tDNA.html. Briefly, tail cuts were digested overnight at 56^{o}C in 1 or 0.5 mg/ml Proteinase K (Roche Diagnostics) in buffer containing 100 mM or 400 mM NaCl, 100 mM Tris-HCl pH 7.5-8.0, 100 mM EDTA and 0.5% SDS. DNA was extracted with phenol:chloroform, and precipitated from the aqueous phase by the addition of an equal volume of isopropanol to the upper aqueous phase, followed by centrifugation at 14,000g for 10-15 minutes. An alternative DNA extraction method (i.e. that of Miller et al., 1988) was to add a 1/3 volume of warmed 6 M NaCl to the tail digests to first precipitate the proteins followed by centrifugation at 14,000g for 10-15 minutes. An equal volume of ice cold 95% ethanol was added to the supernatant and centrifuged as above. The supernatant was drained and the remaining pellet of DNA was washed in 70% ethanol, dried and resuspended in 20 µl double distilled water.

2.1.2 *Bmp4*^{lacZ} genotyping.

The murine *Bmp4* gene has five exons *viz* I, II, III, IV, and V (Kurihara et al., 1993) which was later referred to as exons 1A, 1B, 2, 3 and 4 (Feng et al., 1995; Lawson et al, 1999). The gene has two different transcripts with one that includes exons 1A, 2, 3, and 4 and the other comprising exons 1B, 2, 3 and 4 (Feng et al., 1995). Exons 1A, 1B and 2 are untranslated and the ATG start site of the protein-coding region is located at the 5' end of exon 3 (Feng et al., 1995). The protein coding portion of the gene spans exons 3 and 4 and there is an untranslated flanking region at the 3' end of exon 4 (Feng et al., 1995). The gene targeting strategy used to generate the original *Bmp4*^{lacZ} mice was the replacement of nucleotides 6807-7178 in exon 3 of the *Bmp4* gene with a *lacZ* reporter cassette (Figure 2.1), thus the normal regulatory function of the *Bmp4* gene was retained with this construct (Lawson et al., 1999).

There were two approaches established in our laboratory that were used for genotyping the mice (Napier, 2005). The first was to amplify by PCR the 479 bp region that flanked the insertion site of the *lacZ* cassette with an initial denaturation of the DNA at 94 ^{o}C for 5 minutes, followed by 30 cycles consisting of DNA denaturation for 30 seconds at 94 ^{o}C, annealing for 45 seconds at 55 ^{o}C and extension for 55 seconds at 72 ^{o}C. After 30 cycles, a final extension for a further 7 minutes was done at 72 ^{o}C before cooling to 4^{o}C (Napier, 2005).

During the latter part of the current study, PCR products using this approach became inconsistent and the alternate approach used below yielded good quality PCR products. Here a 279 bp region of the *β-galactosidase* gene incorporated into the *lacZ* cassette was amplified by PCR. The PCR reaction was similar to that used above with the exception that annealing and extension periods were extended to 60 seconds and the annealing temperature was performed at 58^{o} C (Napier, 2005). Since postnatal and adult mice were used in this study, genotyping was used to distinguish between *Bmp4* heterozygous and wildtype animals. Homozygous *Bmp4* mutants die during the early embryonic period between 6.5-9.5 days *post coitum* (dpc) (Winnier et al., 1995). Since only the early formation of optic vesicles occurs during this period, homozygous mice were not considered for the present study.

2.1.3 *Foxc1*^{lacZ} genotyping.

The *Foxc1* gene has a single exon flanked by 5' and 3' untranslated regions (Hiemisch et al., 1998). The gene targeting strategy used to generate the original *Foxc1*^{lacZ} mice was the replacement of the sequences encoding the 90-553 amino acids of the *Mf1* (*Foxc1*) gene with a *lacZ/*^{PGneo} cassette (Figure 2.2) (Kume et al., 1998). The normal regulatory elements of the *Foxc1*

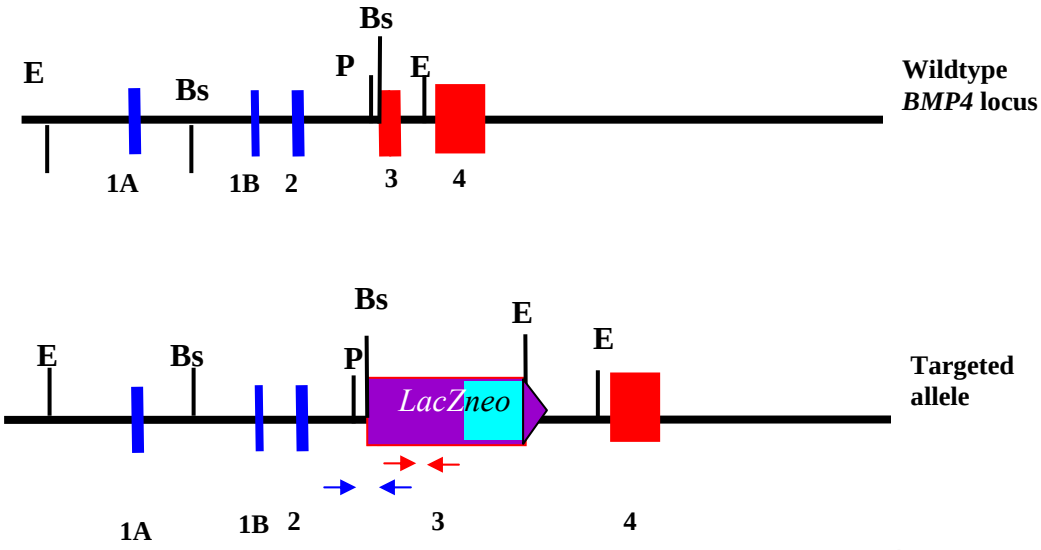

Figure 2.1: Disruption of the *Bmp4* gene by targeted insertion of the *LacZ* cassette.

Modified from Lawson et al. (1999) and Napier, (2005). There are five exons in the *Bmp4* gene with exons 1A and 1B each having a transcription start site. Both exons 1A and 1B with exon 2 are non-protein-coding regions (blue boxes). The protein-coding region spans exons 3 and 4 (red boxes). The *β-galactosidase* gene (purple box) with *neo* cassette has been inserted into the BsmI (Bs) and EcoRI (E) sites to replace exon 3 and a portion of the 3' intronic sequences to create the reporter construct that will be transcribed and translated with activation of *Bmp4* transcription. Forward and reverse $Bmp4^{LacZ}$ primers (5' acccaacttaatcgccttgc 3' and 5' aacaaacggcggattgacc 3' respectively) are indicated with the red arrows. Forward and reverse *Bmp4* flanking primers (5' agaagccacgctgagatcat 3' and 5' gtttcccagtcgacgtt 3' respectively) are indicated with the blue arrows.

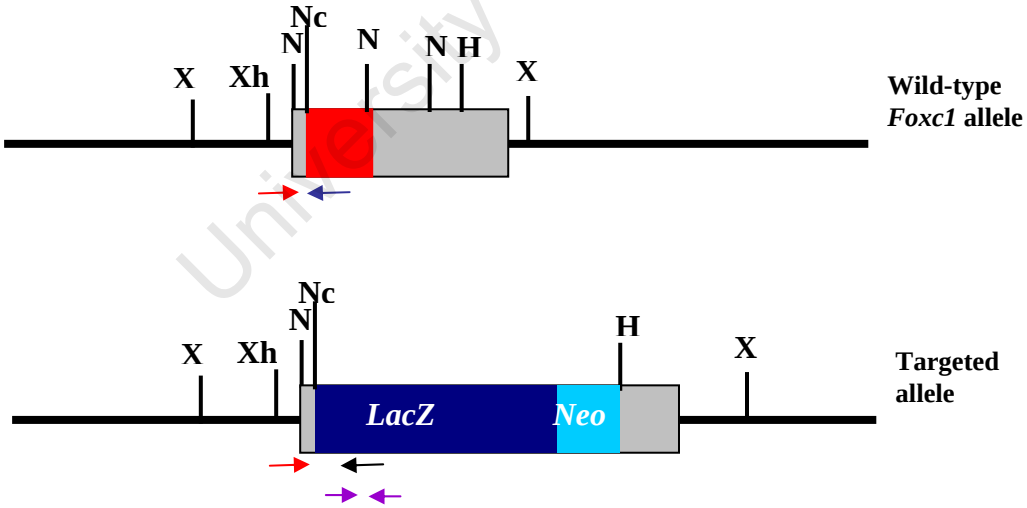

Figure 2.2: Disruption of the *Foxc1* gene by targeted insertion of the *LacZ* cassette.

A single exon contains the protein-coding region (red box) of *Foxc1* and is flanked by untranslated 5' and 3' untranslated regions (gray boxes). The *β-galactosidase* gene (blue box) together with the neomycin resistance gene (turquoise box) was inserted into the NcoI (Nc) and HindIII (H) restriction sites to disrupt the transcription of *Foxc1*. For the multiplex PCR reaction, the forward primer (5' gccctacagctacatcgctcttatc 3' indicated by the red arrow) is targeted to the 3' untranslated region whilst the first reverse primer (5' ccctgcttattgtcccgatagaa 3' indicated by blue arrow) is targeted to the *Foxc1* gene. The second reverse primer (5' accgtgcatctgccagtttgag 3' indicated by the black arrow) would anneal with its complementary sequences in the *β-galactosidase* gene. For PCR detection of the *β-galactosidase* gene, forward and reverse $Foxc1^{LacZ}$ primers (5' acccaacttaatcgccttgc 3' and 5' aacaaacggcggattgacc 3' respectively) are both targeted to the *β-galactosidase* gene indicated with the purple arrows.

gene remained intact as the 5' untranslated regions containing the *Foxc1* promoter were not affected by the homologous recombination. A multiplex PCR reaction was used to distinguish heterozygous and wild-type mice by using a single forward primer in the 5' region upstream of the insertion site of the *lacZ* reporter gene, and two reverse primers (Napier, 2005). One of the reverse primers was specific to the *β-galactosidase* gene, whilst the other was specific to the *Foxc1* gene (Napier, 2005). The PCR reaction comprised an initial DNA denaturation step of 90 seconds at 94^{o} C followed by 35 cycles consisting of denaturation at 94^{o}C for 30 seconds, annealing at 62^{o}C for 30 seconds and extension at 72^{o}C for 90 seconds. A final extension step at 72^{o}C for 10 minutes was done before cooling to 4^{o} C (Napier, 2005). DNA from Wild-type mice ($Foxc1^{+/+}$) produces amplified PCR products of 124 bp whilst that from heterozygous mice ($Foxc1^{+/-}$) produces 124 bp and 370 bp PCR products (Figure 2.3). Genotyping of *Foxc1* mice was also done by PCR amplification of the same 279 bp region lying within the *β-galactosidase* gene as used for genotyping $Bmp4^{lacZ}$ mice above (Napier, 2005).

2.2 Specimen preparation.

2.2.1 Fixation.

Mice were euthanised according to the agreement of standard practice of the Animal Unit at UCT. Adult and early postnatal mice were euthanized by rapid cervical dislocation or rapid decapitation respectively was performed with the assistance of experienced animal technical staff of the UCT Animal Unit. Adult mouse eyes were removed immediately after euthanasia and placed in ice-cold Phosphate buffered saline (PBS) (pH 7.4) briefly before fixing with 100% ice cold methanol which was injected via a 29 gauge hypodermic syringe needle through the cornea into the anterior chamber (intracameral injection). This was to ensure rapid delivery of fixative to the tissue structures close to the interior margins of the anterior chamber. To relieve excess intraocular pressure during delivery of methanol, the sclera was perforated in the posterior segment just prior to delivery of the fixative. Fixative was delivered via the anterior chamber for 60 seconds until the corneas became opaque, after which the eyes were immersed in 100% methanol for a further 15-30 minutes to allow the ocular tissues to harden. The anterior segment of each eye was separated by an equatorial incision through the posterior chamber, the lens was removed, and the remaining tissue was further fixed in 100% methanol for another 30-60 minutes with continuous agitation. Anterior ocular segments were bathed in cold PBS and transferred to a dissecting microscope. In order to flatten the curvature of the anterior segment for later viewing, four to five radial incisions were made leaving the centre portion of the cornea intact (Figure 2.4). The irises and ciliary body of adult mouse eyes were carefully removed leaving the intact corneoscleral layer

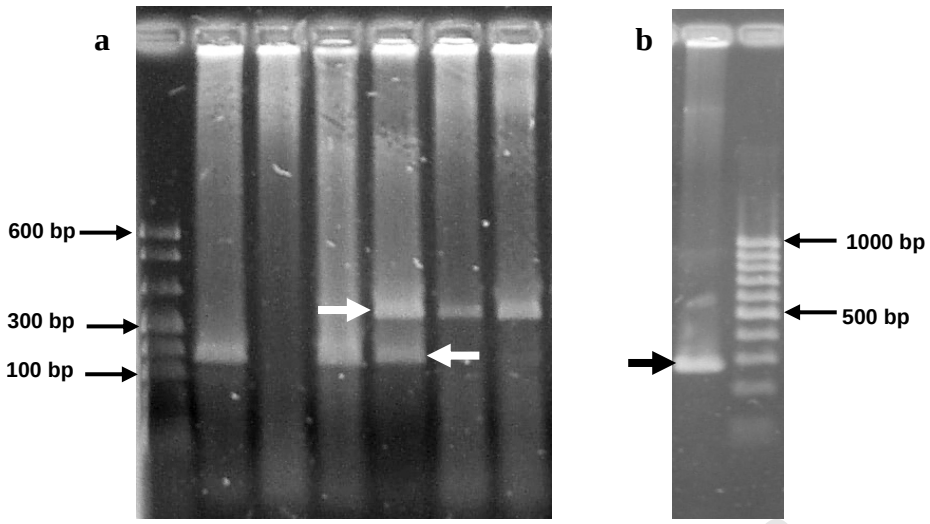

Figure 2.3: Gel electrophoresis of PCR products to determine *Foxc1* and *Bmp4* heterozygous genotypes.

a) PCR products from a multiplex PCR reaction using primers to detect *Foxc*1 mutants, heterozygous and wildtype mice (see Figure 2.2). Heterozygous mice have two PCR products (white arrows) of 129 and 370 bp amplified fragments. The other lanes show wildtype mice with a single DNA band of 124 bp and homozygous mutant mice with a single DNA band of 370 bp.

b) PCR product of the PCR reaction using primers targeting the *β-galactosidase* gene (see Figure 2.1 and 2.2). *Foxc1* or *Bmp4* heterozygous mice show a single PCR product of 270 bp (arrow).

containing the Schlemm's canal, the aqueous drainage vessels and superficial limbal vessels. Eyes from early postnatal mice were dissected from their orbits as the eyelids were still closed at these ages. Eyes were immersed into ice cold 100% methanol for 15-30 minutes to harden the ocular tissues before cutting through the equatorial plane. The lens was gently removed and the ciliary body and iris were retained. Anterior segments were further fixed for 30-60 minutes.

A few adult mouse eyes were also fixed whole in buffered 4% paraformaldehyde (pH 7.4) overnight and processed to wax. Others were fixed in 4% paraformaldehyde and 2.5% glutaraldehyde in 0.1 M phosphate buffer for 1-2 hours to harden, trimmed to thin tissue slices (0.5-1 mm thick) across the corneolimbal junction, fixed for a further 60 minutes, rinsed in buffer, post-fixed in 1% osmium tetroxide, dehydrated in ethanol and propylene oxide and embedded in Epon/araldite resin. Wax sections of 5 µm thick were stained with Haematoxylin and Eosin (H&E) and 0.5-1 µm thick resin sections stained with toluidine blue were examined for general histology and orientation of the anterior ocular structures.

2.2.2 PECAM-1 immunolabelling.

Since there are no reports to date that show that Schlemm's canal in the mouse eye can be detected using anti-murine PECAM-1, it was necessary to first test this antibody on sectioned eyes and then compare the anatomical location of PECAM-1 stained structures to the known location of blood vessels and Schlemm's canal in either H&E-stained or toluidine blue-stained wax or resin sections respectively. Therefore, before embarking on immunostaining wholemounts, a pilot study was performed on 10 µm thick frozen sections of adult mouse eyes. Cryosections were fixed in 4% paraformaldehyde or 100% methanol for 15-30 minutes, rinsed in PBS, immersed in 50mM NH_4Cl for 30 minutes (see below), blocked in 1% BSA in PBS for 30 minutes followed by incubation in 4µg/ml (1:250) dilution of rat anti-mouse CD313 (PECAM-1) (PharMingen, International) overnight at 4^o C. Sections were rinsed in PBS (3 times) and incubated in 1:2000 of anti-rat Alexa 488 (Molecular Probes, Invitrogen, USA) for 90-120 minutes. After three rinses in PBS, sections were mounted in PBS glycerol containing antifade (see below), and viewed on a Zeiss Axiovert microscope. In order to establish the optimal concentration of anti-PECAM-1 on wholemount preparations, a dilution series ranging from 1:100 to 1:1000 dilution of anti-PECAM-1 was carried out on anterior segments according to the protocol stated below. These preliminary studies were performed by Karen Verster who was an Honours student under my supervision.

For wholemount preparations, washes and immunostaining steps were performed with continuous agitation on a nutator (Clay Adams). After fixation and microdissection of the anterior segment, wholemounts were washed three times in PBS (10 minutes for each wash) followed by incubation in 50mM ammonium chloride (NH_4Cl) for 1-2 hours to reduce background fluorescence (http://www.bcm.edu/microscopy/?PMID=2855 and http://www.biotech.ufl.edu/EM/data/iempretreatments.html). Biochemical sources of autofluorescence in tissue can arise from Flavins, NAD(P)H, Lipofuscins, advanced glycation end products found in human cornea, collagen and elastin (Billinton and Knight, 2001). Formaldehyde fixatives leave free aldehyde groups which autofluoresce when excited at the wavelengths used to detect common fluorophores (Billinton and Knight, 2001). Sodium borohydrate, glycine and ammonium chloride (NH_4Cl) have been used to reduce autofluorescence generated by free aldehydes in paraformaldehyde fixed tissues (Billinton and Knight, 2001; J.A.; Kiernan – comment at http://www.histosearch.com/histonet/JulooA/RE.QuenchingautofluoresceC.html). Although aldehydes were not used to fix the anterior segments, preliminary studies in our laboratory showed lower fluorescent background levels in mouse ocular wholemounts after exposure to 50 mM NH_4Cl. Although not previously shown in mouse cornea and sclera, arterial collagen is known to

autofluoresce (emission above 515 nm) when excited at 476 nm. These excitation and emission wavelengths fall within the range used to detect Alexa 488.

After exposure to NH_4Cl, anterior segments were incubated in 1% bovine serum albumin (BSA) in PBS (pH 7.4) containing 0.01% DMSO for 2-3 hours to prevent non-specific binding of antibodies and to improve antibody penetration of the tissue. Anterior segments were immunolabelled in 4µg/ml (1:250 dilution) of the purified rat anti-mouse PECAM-1 (PharMingen International) in the above BSA solution at 4^oC overnight after which they were washed three times in PBS (1 hour for each wash). A few anterior segments were also co-incubated with the above PECAM-1 antibody and rabbit anti-mouse LYVE-1 (Abcam Inc.) to detect lymphatic vessels. Anterior segments were then incubated in anti-rat IgG conjugated to Alexa 488 (Molecular Probes, Invitrogen, USA) and anti-rat IgG conjugated to C3 (Jackson Laboratories, USA) (1:2000 dilutions in 1% BSA in PBS) at 4^oC overnight followed by three washes in PBS in 2 hours. Anterior segments were flatmounted in PBS/glycerol containing antifade (50 mg/ml n-propylgallate or 1,4 diazobizlyclo[2.2.2]octane - DABCO) with the exterior ocular surface facing the coverslip (Figure 2.4a).

2.3 Image capture.

Examination and image capture for most of the adult mouse eyes was done using a Zeiss Axiovert 200W fluorescence microscope (Carl Zeiss AG, Germany). A Zeiss Pascal confocal microscope fitted with onto an Axiovert microscope (Carl Zeiss AG, Germany) was used to view and capture images of the postnatal mouse eyes. Towards the final stages of this study, a Zeiss 510 Meta confocal microscope was available to capture high quality optical sections of adult mouse eyes. Viewing and imaging on the Zeiss axiovert 200W fluorescence microscope fitted with a 100 watt mercury vapour lamp was done using a dichroic filter fitted with an excitation filter of wavelength 488nm and a short-pass emission filter of bandwidth 510-540 nm. Detection of the Cy3-labelled secondary anibodies bound to LYVE-1 antibodies in double immunostained anterior segments was possible using the dichroic filter set with excitation wavelength of 546nm and long-pass emission filter ranging from (590-700 nm). Images were captured with the Zeiss HR Axiocam fitted to the microscope using Axiovision 3.1, 4.5 or 4.6 versions of the software.

The optical configuration used to detect the Alexa 488-stained PECAM-1 on the Zeiss Pascal or LSM 510 meta confocal microscopes was an excitation wavelength of 488 nm using the Argon laser and emission bandwidth of 505-530 nm. The pinhole was set to 180 µm (approximately 1.8 Airy units). This increased the thickness of the optical section sufficiently in order to capture a

slightly broader region of the Z axis on either side of the focal plane which allowed better visual continuity of the limbal vessels in optical stacks and also required fewer optical sections.

In order to capture images of the whole limbus, the first image field was taken at the cut edge of the first segment (blue arrow - Figure 2.4b). Following the direction of the arrow, consecutive fields were captured until the entire limbal circumference was recorded. Images of the PECAM-1-stained superficial limbal plexus were captured using a 10x objective lens (Zeiss Neofluor - NA 0.4mm). In most cases the entire volume (i.e. depth) of the superficial plexus could be captured in a single optical section or in rare cases, two optical sections. This was because the depth of field of this is greater and fluorescent-stained structures from a wider range of optical planes are clearly visible in the focal plane of the lens. Images of Schlemm's canal were captured using a 20x objective lens (Neofluor, NA 0.5mm) in a series of optical sections (Z-stacks) each section separated by 3 microns. The poorer depth of field of this lens compared to that of the 10x objective lens and small variations in depth of the canal required viewing and capturing images at different focal planes to detect clear PECAM-1 signals on the epithelial cells of Schlemm's canal.

Each image field (circles - in Figure 2.4b) was also examined for the presence of collector channels linking Schlemm's canal to the overlying intrascleral and superficial perilimbal or episcleral plexus. In order to visualize these channels, the objective lens was first focused onto the superficial limbal plexus and defocused into the deeper limbus to track the penetrating vessels until Schlemm's canal was reached. The total number of collector channels was only recorded in adult the study on adult mouse eyes. Collector channels of interest were captured as Z stacks starting at the superficial perilimbal plexus and progressing through the limbus to include Schlemm's canal and in postnatal mice, the uveal vasculature. Images were generally separated by an interval of 3-5 µm steps. The superficial limbal and episcleral vessels were viewed through different focal planes (Z sectioning) in both widefield and confocal microscopy, and images of the superficial limbal and episcleral vessels were captured using a 10x objective lens. Conditions used in wide-field fluorescence and confocal microscopy (e.g. dichroic filter sets and pinhole settings) were similar to that used for capturing images of Schlemm's canal.

2.4 Image Processing.

In some instances, images captured using the widefield fluorescence microscope (Zeiss Axiovert), demonstrated a higher level of background (noise) that was generated from the glare of structures from optical planes above or below that of the focal plane. This in addition to some endogenous low level autofluorescence of the wholemounts at times required various forms of image

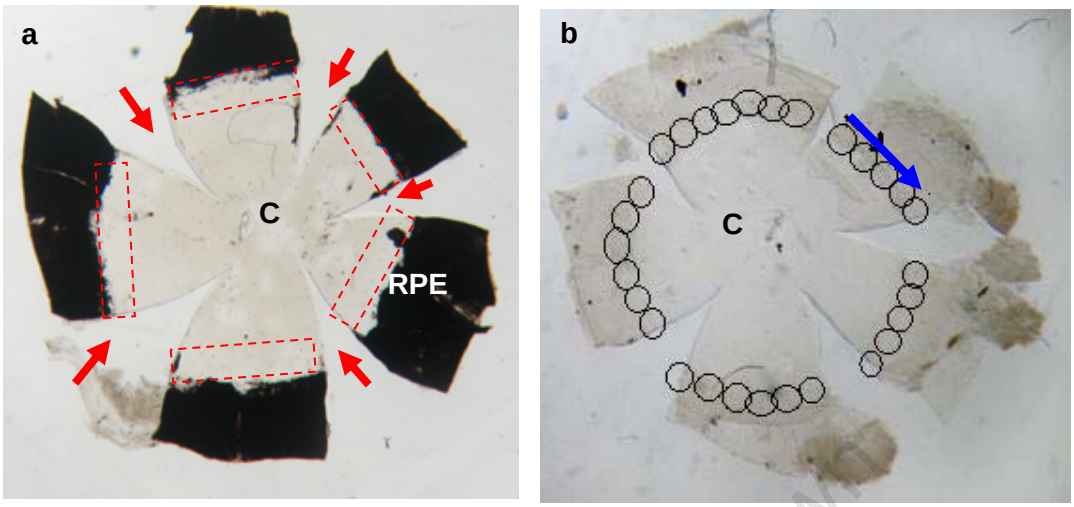

Figure 2.4: Flatmounts of the anterior segments of pigmented C57BL/6Jx129 (a) and non-pigmented ICR mice (b).

a) Flatmounts of the anterior segments were achieved by making radial incisions (red arrows) leaving the centre portion of the cornea (C) intact. The irises and ciliary body have been removed. The remaining black pigmented region in this anterior segment is the retinal pigmented epithelium (RPE). The limbus is the region indicated by the red dotted line.

b) The circles represent the consecutive fields imaged to cover the entire limbus. The blue arrow indicates the start and direction of image capture.

processing. This was to enhance the PECAM-1 signals lying in the deeper regions of the tissue below the more brightly stained blood vessels of the superficial limbus. Contrast was enhanced by compressing the grayscale by raising the black level (minimum slider in right inset of Figure 2.5) and reducing the white levels (maximum slider in right inset of Figure 2.5) Extended focus images (a flat image that represents the combination of all images in the optical stack) were generated from Z-stacks captured on the wide-field or confocal microscope using NIH ImageJ (Rasband W at http://rsb.info.nih.gov.info//ij/) (Figure 2.5) or the LSM Pascal or LSM 510 meta software respectively to produce a clear image of Schlemm's canal.

2.5 Image analysis.

Image analysis was performed using Photoshop 5.5 or 9 (CS2) (Adobe Systems), or NIH ImageJ. A morphometric grid overlay (with lines drawn at 2 cm intervals along the x and Y axes) was overlaid onto the images. The images taken on the wide-field fluorescence microscope measured 22 cm in width by 17 cm in length (1300 x 1018 pixels) (Figure 2.5). Images taken on the confocal microscope measured 18.05 by 18.05 cm (512 x 512 pixels). In order to ensure randomization of measurements, the width of Schlemm's canal (SC width) was measured in a

systematic way by starting at the point where the horizontal grid lines of the grid overlay intersected with one lateral edge of the canal (white arrows - Figure 2.5). If Schlemm's canal was orientated along the horizontal axis, then the measurements were taken where the vertical axes of the grid overlay intersected with the lateral edge of the canal. Measurements were made using the measuring tool to draw a perpendicular line from the edge of the canal that intersected with the grid overlay to the opposite border of the canal (Figure 2.5). Measurements were taken at 4 cm intervals (every second line) of the overlay a (see left insert in Figure 2.5 for an example of the measurement ("Length" column)). The angle column indicates the angle of the red lines and was not used in this study. This 4 cm interval corresponded to approximately 100µm in actual distance on the tissue in images captured using the 20 x objective lens.

In addition to measuring the width of the Schlemm's canal, a qualitative analysis was done at the same regions where the width of the canal was determined. Structural features of Schlemm's canal were categorized as follows: the presence of a single canal, the presence of a bifurcation (split into two parallel canals), formation of a plexus (canal split into more than two channels), absence or fragmentation of the canal, and, the distribution of the PECAM-1 signal. In regions of the limbus where the canal was absent (fragmented), a value of zero was given at the grid lines that would have intersected with the canal. Although PECAM-1 is generally concentrated at the endothelial cell lateral borders, it has been shown to stain more diffusely and less intensely in endothelial cells of lymphatic vessels (Erhard et al., 1996; Sauter et al., 1998; Ebata et al., 2001). Since Schlemm's canal is reported to have characteristics of vascular and lymphatic vessels, the distribution of PECAM-1 (i.e. whether it was concentrated at the cell borders or spread more diffusely across the endothelial cells) was also noted at the points of analysis. Each of the aforementioned structural features was counted and represented as a proportion (percentage) of the total number of points counted per eye.

The perilimbal corneal arcades were assessed in terms of their complexity and distance of penetration into the cornea from the perilimbal veins. Images were overlaid with a 2 cm grid as for Schlemm's canal and the penetration of the corneal arcades into the cornea (CA length) was measured in the following way. Measurements were taken from the point where the vertical or horizontal grid axes intercepted the most anterior capillary loop of the arcade (yellow arrows in Figure 2.6) to the inner vessel of the perilimbal vein (arrowheads - Figure 2.6). Although this measurement did not necessarily reflect the longest distance of corneal penetration, the systematic measurement using the regular intervals along the grid ensured randomization. The complexity of the corneal arcades plexus was determined by counting the total number of "loops" (white stars -

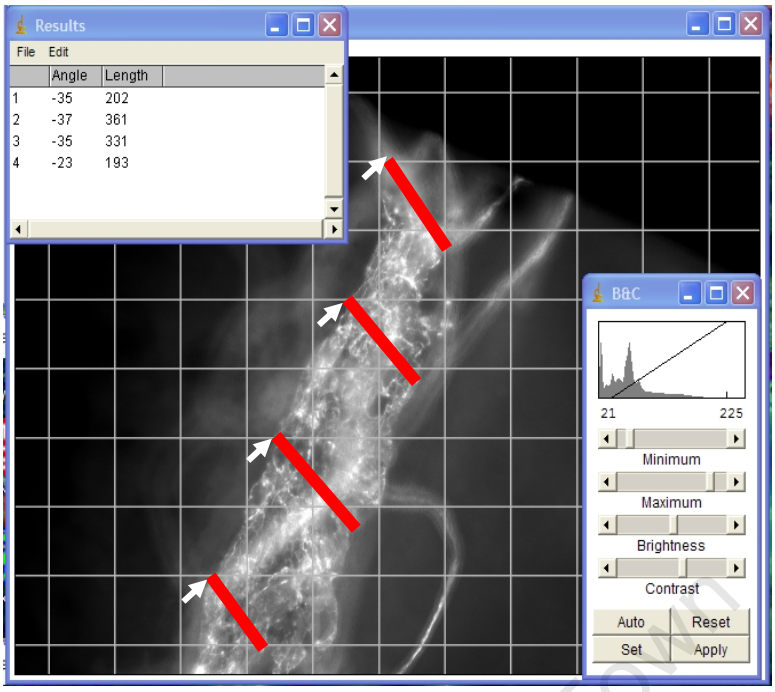

Figure 2.5: Method of image analysis of Schlemm's canal.

The contrast was improved by altering the black and white levels when necessary (inset box on the right). The diagonal line across the histogram denotes the contrast correction. A 2 cm grid is overlaid on the image. The starting point (white arrows) of measuring the width of the canal is indicated where the horizontal lines of the grid overlay intersect with the edge of the canal. The red bars indicate the region measured and the values are recorded in the "Length" column in the left inset box)

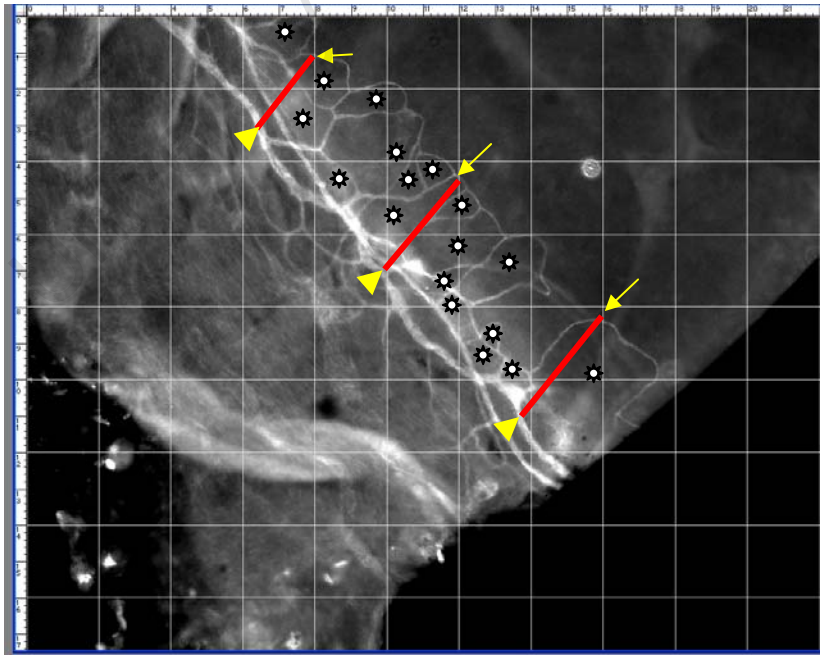

Figure 2.6: Assessment of the perilimbal corneal arcades.

A 2 cm grid is overlaid on the image. The starting point of measuring the penetration of the capillaries into the cornea is located where the vertical lines of the grid overlay intersect with capillary of the most anterior (distal) loop of the corneal arcade (yellow arrows). The red bars indicate the distance measured from his point to the perilimbal vein (arrowheads). Each loop (white stars) of the arcade plexus was counted to determine the total number of capillary loops per eye.

Figure 2.6) lying anterior/ distal (i.e. on the corneal side) to the perilimbal circumferential venous plexus in each micrograph.

2.6 Data processing and Statistics.

Data was managed and bar charts were generated in Excel version 2003 (Microsoft Corp). **R** (Gentleman R. and Ihaka, R. - free-ware at http://www.r-project.org) was used to perform the statistical analysis (see below) on the raw data from measurements of the width of Schlemm's canal (SC width), the depth of penetration of the corneal arcades into the cornea (CA length), the complexity of the corneal arcade plexus, and the number of collector channels. The Shapiro-Wilk's normality test was used to determine whether the data followed a normal distribution. In order to test for significance, an analysis of variance (ANOVA) was performed on the entire data set where all coefficients of effects were taken into account. These included different strains (ICR and C57BL/6Jx129), WT (normal), *Foxc1*$^{+/-}$ and *Bmp4*$^{+/-}$ genotypes, different age groups (6-8 months; 10-12 months, and 15 months), left and right eyes and gender. ANOVA was used to test for significance within the following subgroups:

- age and genotype within the C57BL/6Jx129 strain (pink cells - Tables 1-3 in sections **3.5.1.1**, **3.5.1.4, 3.5.2.1,** and **3.5.2.3**)
- age within the C57BL/6Jx129 strain and *Foxc1*$^{+/-}$ genotype (dark green cells - Tables 1-3)
- genotype within the 10-12 month age group of the ICR strain (blue cells - Tables 1-3)
- age (excluding the 15 month age group) and strain within the wild type (WT) genotype (yellow cells - Tables 1-3), and,
- strain and genotype (*Foxc1*$^{+/-}$) within the 10-12 month age group (pale green cells - Tables 1-3).

If ANOVA showed significant effects, a linear regression model was used to estimate the direction of the effects. In the case of only one effect examined (e.g. genotype), where significance was not shown in the ANOVA but strongly indicated in the linear regression model, the non-parametric Kruskal-Wallis rank sum test was used to test for significance.

For the morphological analysis of Schlemm's canal, the mean percentage of the individual morphological features (single canal, absent or fragmented canal, presence of bifurcations and plexuses) per group is represented in a bar chart (see Figure 3.32). Statistical analysis was not performed on these data.

CHAPTER 3

Results

3.1. Establishing PECAM-1 as an appropriate marker for Schlemm's canal in the mouse eye. In order to carry out an analysis of the microanatomy and development of Schlemm's canal, it was first essential to ensure that Schlemm's canal could be detected with an appropriate antibody that targeted its endothelium. . In addition, it was necessary to ensure that both vascular and lymphatic endothelia would be identified so that the anatomical relationship between these vessels and Schlemm's canal could be uncovered. It is well known that vascular endothelium expresses several intracellular and cell surface markers (see section **1.5.3**). However, the expression levels of most of these molecules is variable (Silverman et al., 2001), and some are expressed in vascular but not lymphatic endothelium (Erhard et al., 1996; Baluk and McDonald, 2008). The panendothelial cell marker PECAM-1 is expressed in vascular and lymphatic endothelium, and has been previously used to visualize the limbal vasculature in the mouse eye (see section **1.5.3.2.3**). Furthermore, the endothelium of Schlemm's canal in the human eye has been previously detected with antibodies to PECAM-1 (Heimark et al., 2002; Read et al., 2007). Thus, for the present study, the antibody to PECAM-1 seemed to be suitable to use for the detection of the limbal vasculature. However, it is not known whether PECAM-1 was expressed by endothelial cells lining the murine Schlemm's canal. To establish whether this antibody might be suitable, a pilot study using PECAM-1 was undertaken on frozen sections and then wholemounts of the wildtype mouse eye.

The manufacturer of the PECAM-1 antibody recommends that a zinc-based fixative be used for fixation of tissues that would be processed to wax. Others have used paraformaldehyde fixation (personal communication) for light microscopy using enzyme-based amplification detection systems such as alkaline phosphatase or diaminobenzidine. These fixatives were tested on frozen sections and wholemounts (see section **2.2.2**) to determine their suitability for PECAM-1 immunostaining. Due to high levels of background fluorescence and poor PECAM-1 signals in these preparations (data not shown) it was concluded that these fixation protocols were unsuitable for the present study. After exploring a variety of other options, methanol fixation was shown to be the most ideal because it yielded high levels of PECAM-1 staining with low levels of background fluorescence.

The next step was to establish whether it was possible to identify Schlemm's canal in frozen sections of mouse eyes fixed in methanol. A large number of PECAM-1 positively stained vascular structures were seen in the frozen section (Figure 3.1b). In order to become familiarised with the identity of the limbal blood vessels and Schlemm's canal in these PECAM-1 immunostained sections, the location of fluorescent PECAM-1 stained vessels was compared to the corresponding location in toluidine blue stained resin sections where the histological features of the various vessels were recognisable (Figure 3.1a). In cross section, Schlemm's canal is a wide vessel located deep in the limbus (SC - Figure 3.1a) and is located posterior to the iridocorneal angle (arrowhead - Figure 3.1a). The superficial limbal vessels, which included the superficial perilimbal plexus and episcleral vessels (black arrows), and capillaries of the corneal arcades (red arrows) are located below the corneal epithelium (Figure 3.1a). In frozen sections (Figure 3.1b), PECAM-1 staining was identified in structures that corresponded to the superficial perilimbal and episcleral vessels (Epi), corneal arcades (red arrows) and Schlemm's canal (SC) seen in Figure 3.1a. The putative Schlemm's canal was seen in cross section as a wide vessel (approximately 130 μm wide) lying deep in the limbus approximately 50 μm below the superficial limbal vessels. In addition, PECAM-1 staining was also observed in the iris vessels and in the region where the choroid vessels would be located. A small vessel or putative collector channel was also detected in the limbus between the superficial limbal vessels and the putative canal (Figure 3.1b). Frozen sections subjected to the same immunostaining protocol but excluding anti-PECAM-1 served as negative controls. In these sections fluorescent signals were undetectable (Figure 3.1c) thus confirming the specificity of PECAM-1 in the fluorescent stained structures in Figure 3.1b.

The above pilot study on frozen sections confirmed that PECAM-1 was detectable in the limbal vessels and in the putative Schlemm's canal of the mouse eye. This antibody was then further tested on wholemount preparations of the anterior segment (see section **2.2.2**) to determine whether the three dimensional architecture of all the limbal blood vessels, aqueous vessels and Schlemm's canal could be revealed. In these wholemounts, complex networks of interconnecting vessels of varying sizes in the superficial limbus were seen (Figure 3.2a). Here even the smallest capillaries of the perilimbal vascular plexus and corneal arcades were visible. This image, taken at low magnification using widefield fluorescence microscopy, was focused on the superficial limbal vasculature. In this focal plane, lying posterior to the perilimbal episcleral plexus, were vessels of larger diameter and less intense staining (L in Figure 3.2a) than those of the superficial perilimbal plexus. Some of these vessels terminated as blind-ends (yellow arrows) suggesting that

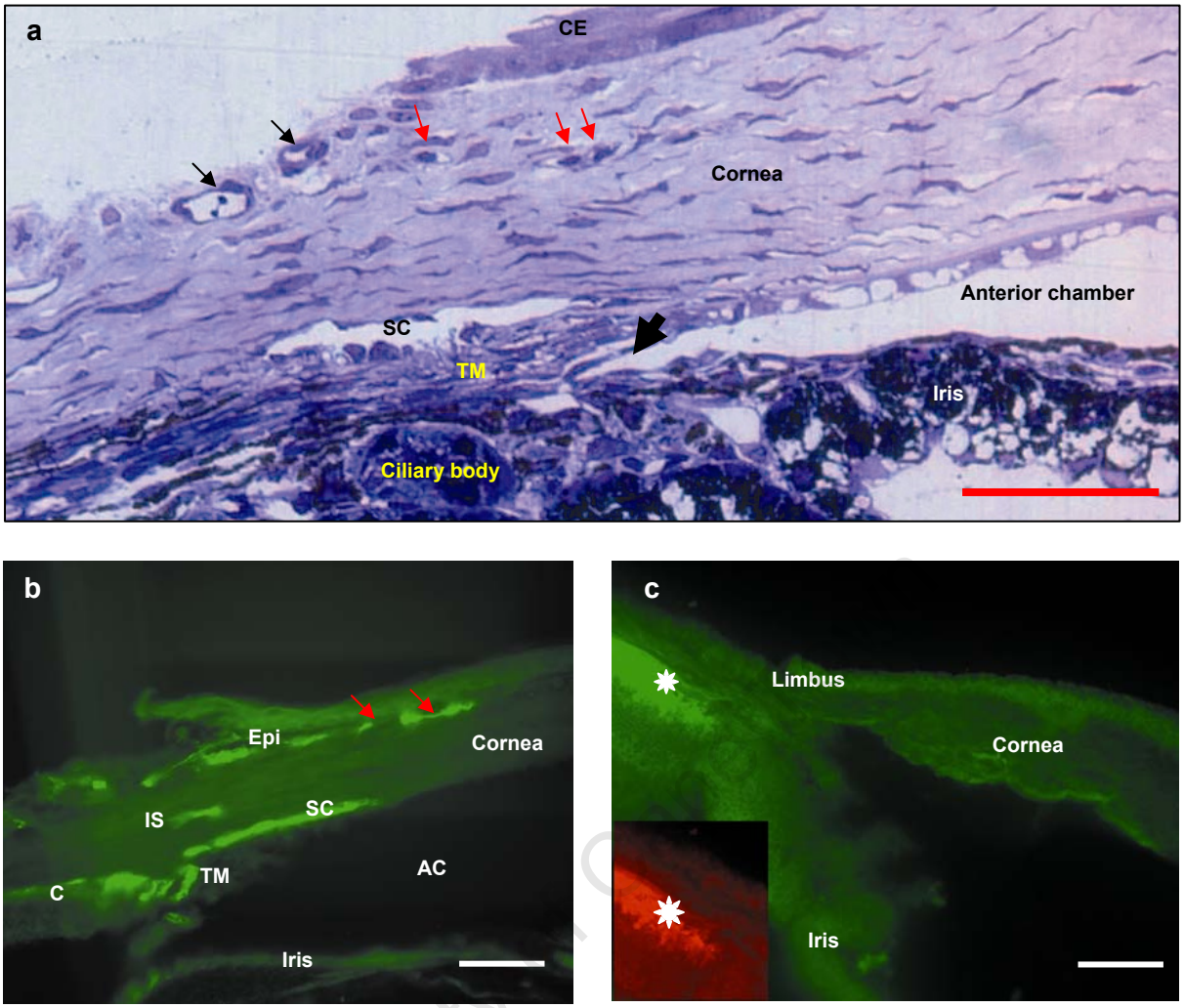

Figure 3.1: Histological sections and immunostained frozen sections of the mouse eye showing the comparative anatomical location of the limbal vessels and PECAM-1 stained structures in the limbus.

a) A resin section (0.5 mm thick) stained with toluidine blue, shows the limbus, cornea, iris and ciliary body of an adult mouse eye. The relative locations of the superficial limbal/episcleral vessels (black arrows); capillaries of the corneal arcades (red arrows) and Schlemm's canal (SC) are shown. Intrascleral vessels or collector channels are not visible in this section. Bar = 100 µm.

b) A frozen section cut along the sagittal plane of an adult mouse eye shows a number of structures stained for PECAM-1 that correspond anatomically to the superficial limbal/episcleral vessels, corneal arcades and Schlemm's canal seen in Figure 3.1a. Endothelial cells of the choroid vessels (C) and iris are also stained. Due to some damage during sectioning the iris has pulled away from its root at the iridocorneal angle (IR). AC = anterior chamber, Epi = superficial limbal/episcleral vessels, IS = intrascleral vessel or collector channel, SC = Schlemm's canal, TM = trabecular meshwork. Red arrows indicate the capillaries of the corneal arcades. Original image is courtesy of Karen Verster. Bar = 100 µm

c) A frozen section cut along the sagittal plane of an adult mouse eye where anti-PECAM-1 was omitted from the staining protocol serves as a negative control. The apparent signal seen in the region of the retina (white star) is due to autofluorescence which persists when imaged in the "red" channel (568 nm excitation and 650 nm long-pass filters) (inset). Original image is courtesy of Karen Verster. Bar = 100 µm

these may be lymphatic vessels. Cusp-shaped densities which correspond to putative valves (red arrows) were spaced at regular intervals along the vessels and were often located at bifurcations (Figure 3.2a). A larger PECAM-1 stained vessel was seen deeper in the limbus (white arrow) but was obscured by the overlying perilimbal plexus (Figure 3.2a). In regions of the limbus where the perilimbal vascular plexus was sparse, this deeper limbal vessel was more clearly observed (Figure 3.2b). Since the width of this vessel was similar to that seen in cross section (Figure 3.1b) it could be reasonably deduced that this was the putative Schlemm's canal.

The image in Figure 3.2a was captured in a single focal plane and does not indicate the depth relationship between the putative Schlemm's canal and the superficial limbal vessels. In order to determine the depth of the putative Schlemm's canal in the limbus, the Z-value of the microscope stage was noted at the focal planes of the perilimbal/episcleral vessels and the putative Schlemm's canal. The distance between these focal planes varied between 45 and 65 μm. A composite pseudocoloured image, indicating the relative depths of the vessels in the limbus, was generated from a series of optical sections through the limbus (Figure 3.2c). In this image the putative Schlemm's canal (red-orange structure - Figure 3.2c) is 60-65 μm below the outermost episcleral vessels (blue vessels). Several vessels (putative collector channels) (arrows - Figure 3.2c) emerging from the perilimbal plexus were seen to penetrate the limbus and terminate at the canal. The change in colour from blue to pale orange of these vessels is evidence of their changing depth in the limbus (Figure 3.2c). In wholemounts serving as negative controls, fluorescent signals were not detected where anti-PECAM-1 was omitted from the staining protocol (Figure 3.2d).

The above results from the optical sectioning of wholemounts thus corroborated the results of the studies done on frozen sections. Together they strongly suggest that the broad circular channel located 60-65 μm below the perilimbal plexus is indeed Schlemm's canal. Further strengthening this deduction was the detection of vessels linking this canal to the overlying perilimbal plexus. This strongly suggested that these are the collector channels of the aqueous outflow pathway. A movie of a Z-stack where the putative collector channels can be tracked from the superficial limbus through to the putative Schlemm's canal is attached in the supplementary CD ("Collector channel movie"). In summary, this pilot study showed that PECAM-1 is a suitable marker for studying Schlemm's canal in wholemounts preparations of the mouse eye anterior segment. The next stage was to use this antibody to elucidate the anatomical and morphological features of the limbal vessels in detail.

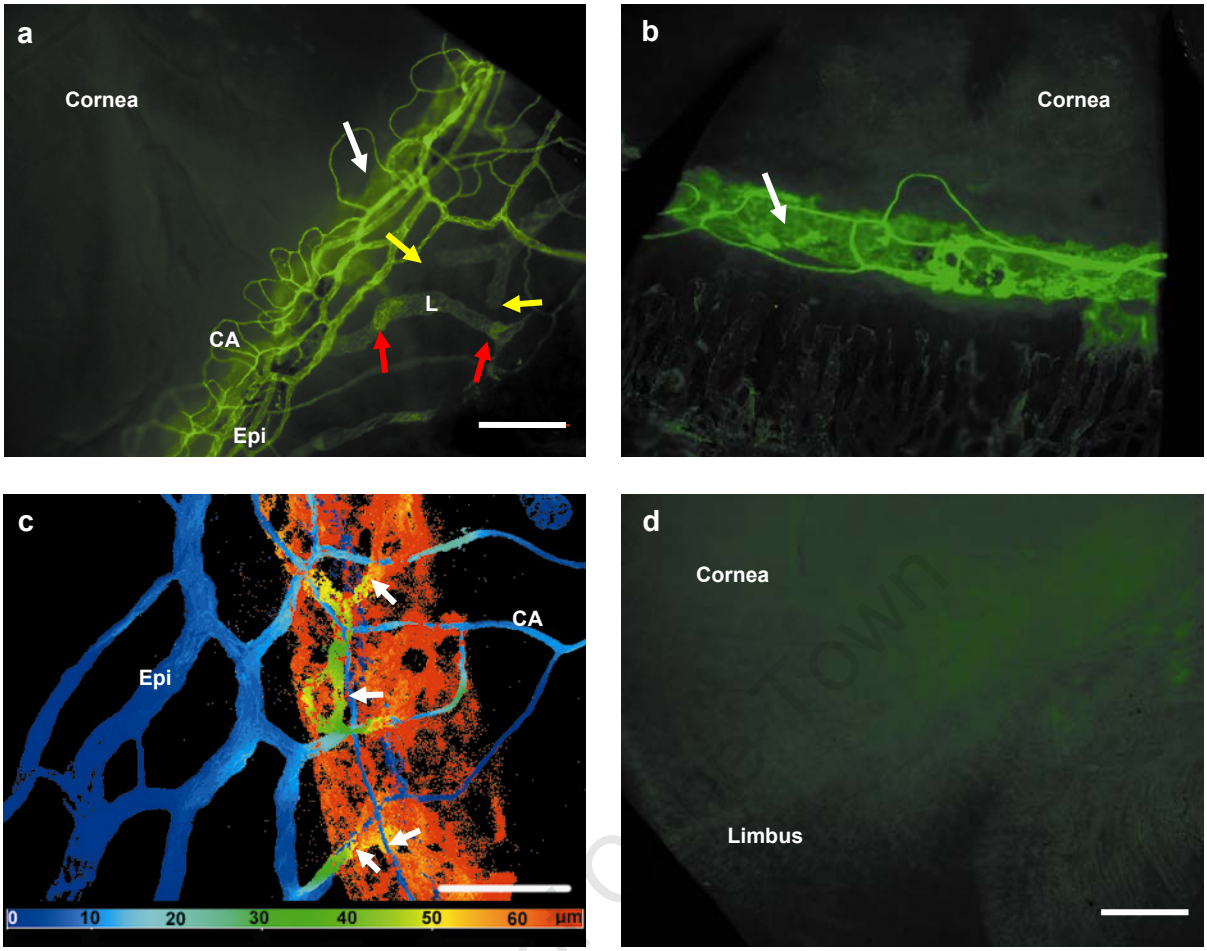

Figure 3.2: Wholemounts of the anterior segment of the adult mouse eye immunostained to detect PECAM-1.

a) This image (captured on a widefield fluorescence microscope) is focused on the external surface of the limbus. It shows an elaborate network of PECAM-1 stained capillaries of the corneal arcades (CA) and the perilimbal episcleral vascular plexus (Epi). Larger vascular structures (L) show blind-ended terminals (yellow arrows) which were confirmed by Z-plane sectioning, and have cusp-shaped densities (red arrows) resembling valves. Located deeper in the limbus (and out of focus) is a wide PECAM-1 stained structure (white arrow) that lies beneath the perilimbal plexus. Bar = 200 µm

b) A large PECAM-1 stained vessel (white arrow) is visible where the overlying perilimbal plexus and corneal arcades are less elaborate. The width of this vessel is similar to that of Schlemm's canal shown in Figures 3.1a and b. The image was captured on a widefield fluorescence microscope. Bar = 200 µm

c) A pseudocoloured image, generated from a Z-stack of twenty one optical sections captured on a confocal microscope, indicates the relative depths of the vasculature in the limbus. The different colours correspond to the distances indicated on the colour bar. Each optical section is separated by 3 microns. The wide vessel (orange) (seen in the deeper limbus in Figures 3.2a, b) is approximately 60 µm deeper in the limbus than the superficial perilimbal and episcleral vessels (dark blue). Putative collector channels (white arrows) that branch off the superficial limbal vessels penetrate the limbus and appear to link to the large canal-like vessels below. CA = capillaries of the corneal arcades. Bar = 100 µm

d) A wholemount preparation where anti-PECAM-1 was omitted from the staining protocol serves as a negative control and shows no staining of any structures. Bar = 200 µm

3.2 The anatomical features of the limbal vessels as revealed by imaging wholemount preparations.

Whilst the anatomical relationships of the limbal vessels are well described in humans (Ashton, 1951, 1952; Ashton and Smith, 1953), primates (Ujiie and Bill, 1984; Selbach, 2005), dogs (van Buskirk, 1979), rabbits (Selbach, 1998) and rats (Morrison, 1995; Selbach 1998; Bhutto and Amemiya, 2001), such three-dimensional studies have not been reported on the posttrabecular outflow vessels in mice. In particular, the detailed anatomy of Schlemm's canal in its entirety and its relationship to the limbal vessels in *Foxc1*$^{+/-}$ or *Bmp4*$^{+/-}$ mice has not been reported in this way. In order to understand the relationships between the different limbal vessels and Schlemm's canal in normal mouse eyes, the first undertaking was to differentiate between the limbal vascular and lymphatic vessels. The more tortuous shape and paler staining intensity of the larger PECAM-1 stained vessels in the superficial limbus (L in Figure 3.2a) compared to the other vessels of the perilimbal plexus seen in Figure 3.2a suggested that they may be lymphatic vessels. LYVE-1 has been used to detect lymphatic vessels in the mouse eye (Hamrah et al., 2004; Cursiefen et al., 2005). Therefore, in order to confirm whether the above vessels were indeed lymphatic vessels, wholemounts of anterior segments were double-immunostained with antibodies to PECAM-1 and LYVE-1. Signals were detected with Alexa 488-labelled (green signal) and Cy3-labelled (red signal) secondary antibodies for PECAM-1 and LYVE-1 respectively. Whereas PECAM-1 was observed in all superficial limbal vessels (Figure 3.3a), LYVE-1 was only detected in a subset of these vessels, thus confirming their lymphatic phenotype (Figure 3.3b). As seen in Figure 3.3a, a relatively wide lymphatic vessel (star) is obscured by the intensely stained PECAM-1 signals in the perilimbal plexus in Figure 3.3a. This same vessel is also stained with LYVE-1 (star – Figure 3.3b), and blind-ending vessels that branch off this lymphatic vessel penetrate the cornea (yellow arrows Figure 3.3b). This circumferentially-aligned lymphatic vessel was also linked to the episcleral lymphatic vessels which displayed the valve-like structures seen in Figure 3.2a (See below and Figure 3.9 for further description of these vessels). LYVE-1 was also detected in numerous cells in the superficial limbus posterior to the cornea (short white arrow – Figure 3.2b).

It has been suggested that the endothelium lining the inner wall of Schlemm's canal displays properties of both vascular and lymphatic endothelia (reviewed in Ramos et al., 2007). However, there are no reports as to whether or not Schlemm's canal expresses LYVE-1. In wholemounts immunostained to reveal both PECAM-1 and LYVE-1, only PECAM-1 was detected in Schlemm's canal (SC - Figure 3.3c). In a focal plane deeper than Schlemm's canal, LYVE-1 was detected in a vascular-like structure (yellow arrows – Figure 3.3c). A clearer view of the deep limbus was obtained by confocal microscopy where an extended image of optical sections of the

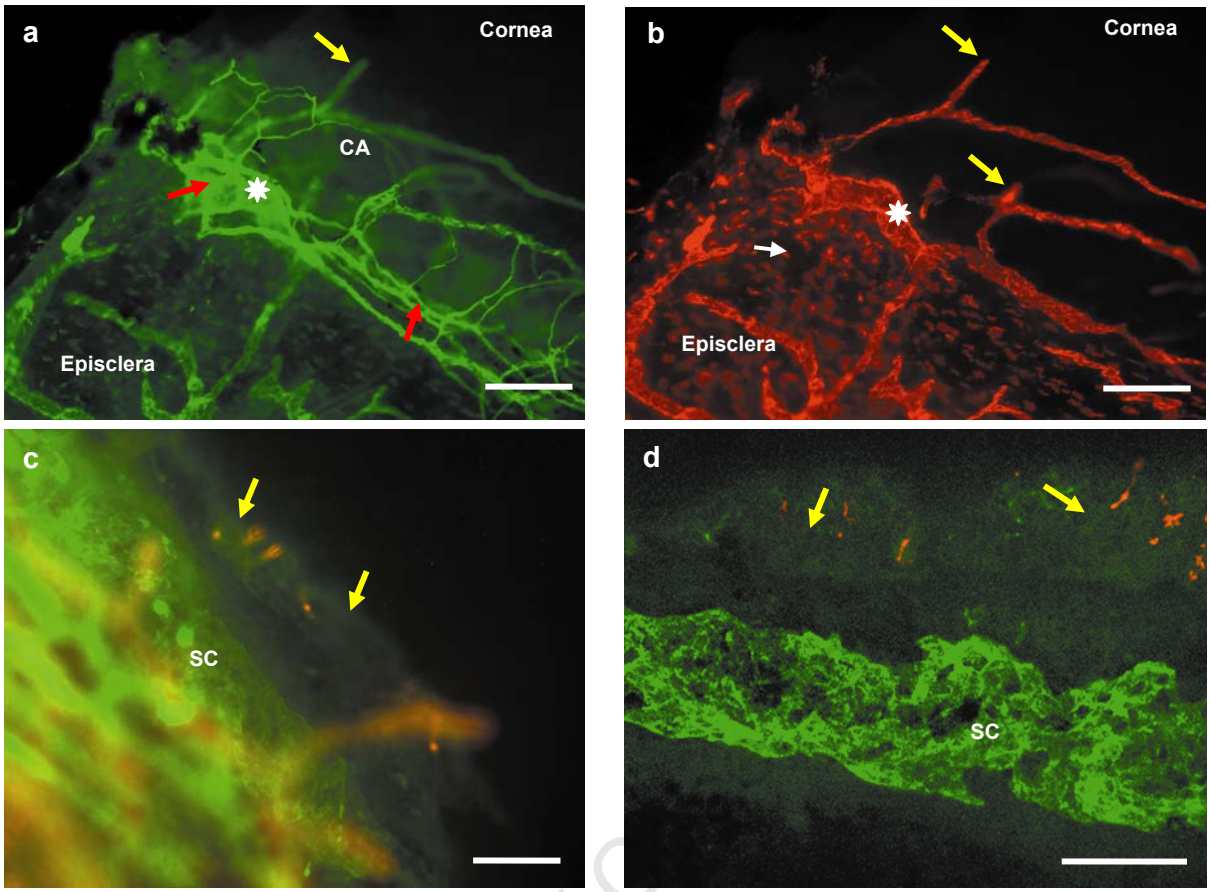

Figure 3.3: Comparative PECAM-1 and LYVE-1 staining of limbal vessels in wholemounts of the anterior segment of the adult mouse eye.

Whole mounts were double immunostained with anti-PECAM-1 and anti-LYVE-1 (see section 2.2.2) and viewed at 488 nm and 568 nm excitation wavelengths to reveal PECAM-1 (a), and LYVE-1 (b) respectively.

a) PECAM-1 is detected in the perilimbal vascular plexus (red arrows) and putative lymphatic vessels (star) in the episclera. Blind-ending vessels (yellow arrows) penetrate the cornea. Bar = 200 µm

b) LYVE-1 is detected in a subset of limbal vessels and numerous cells in the episclera. The LYVE-1 stained network of vessels appears to be independent of the other PECAM-1 stained vessels in Figure 3.3a. A large perilimbal vessel (star), obscured by the strongly PECAM-stained perilimbal plexus in Figure 3.3a gives rise to vessels that penetrate the cornea, some of which are blind-ending (yellow arrows), and also linked directly to the vessel network in the episclera. Bar = 200 µm

c) The putative Schlemm's canal (SC) is located approximately 45-65 µm below the superficial limbal blood vessels and is partially obscured by the overlying brighter fluorescence signals of vessels (out of focus). Image was captured by widefield fluorescence microscopy. LYVE-1 is absent in the putative Schlemm's canal but detected in a segment of tissue (yellow arrows) in an optical plane several microns below the putative Schlemm's canal, hence is out of focus in this image. Bar = 100 µm

d) An extended image (merged) was generated from several of optical sections captured by confocal microscopy starting in the upper plane of the putative Schlemm's canal and ending some distance below the canal. Episcleral vessels are thus excluded in this image whilst the putative Schlemm's canal (SC) and lower tissue segment (yellow arrows) seen in Figure 3.3c are all in focus. The putative Schlemm's canal does not stain with LYVE-1. Bar = 100 µm

deep limbus revealed small LYVE-1 and PECAM-stained capillary-like shapes in the structure indicated (yellow arrows - Figure 3.3d). Since the wholemounts in these preparations could still include parts of the iris and ciliary body that were not completely dissected away, and both of which are located below Schlemm's canal, it was likely that the LYVE-1 stained structures and small PECAM-1 fragments seen in these images were located in the iris or ciliary body. To date, lymphatic vessels have not been reported in these structures. Since Chen et al. (2005) have reported that monocytic-derived conjunctival cells express LYVE-1, it may be possible that a similar cell type is found in the iris and ciliary body. Further investigation may elucidate this, but were not addressed in the present study. The image shown in Figure 3.3 was of a wholemount of the C57BL/6Jx129 mouse eye where the blood vessels in the iris and ciliary body and choroid may be obscured in places by the pigmented epithelium where the tissue is folded. This would explain the fragmented staining seen in these regions in Figures 3.3c, d.

In summary, this study established that the large and less intensely stained superficial perilimbal and episcleral vessels observed in PECAM-1 stained wholemounts were lymphatic vessels. It also confirmed that these vessels were not linked to the blood vessels in the perilimbal vasculature. Furthermore this study revealed that the murine Schlemm's canal does not express LYVE-1.

3.2.1 Identification of vessel phenotypes in the limbus.

The anatomical morphology (phenotypes) of arteries, veins and capillaries.

The limbal vasculature consists of vascular and aqueous veins, arteries, capillaries, lymphatic vessels and Schlemm's canal. Of these, the above study had identified Schlemm's canal, lymphatic vessels and putative collector channels (aqueous veins). Capillaries were easily identified by their narrow width as seen in the corneal arcades (Figures 3.2a and 3.4a). In order to further elucidate the vascular architecture of the limbus, it was necessary to identify veins, arteries and collector channels. Arteries and arterioles tend to have uniform diameters and form straight unwavering/rigid vessels, whereas veins and venules have a larger diameter than arteries and display an uneven width and more tortuous morphology in wholemounts (Ezaki et al., 2001; Gale et al., 2002; Baluk et al., 2004, 2004a; Murfee et al., 2007). Using the above anatomical features, arterial (long arrow - Figures 3.2c, and 3.6a) and venous (Epi - Figures 3.2a, c and 3.6g) phenotypes were easily identified in the perilimbal vasculature.

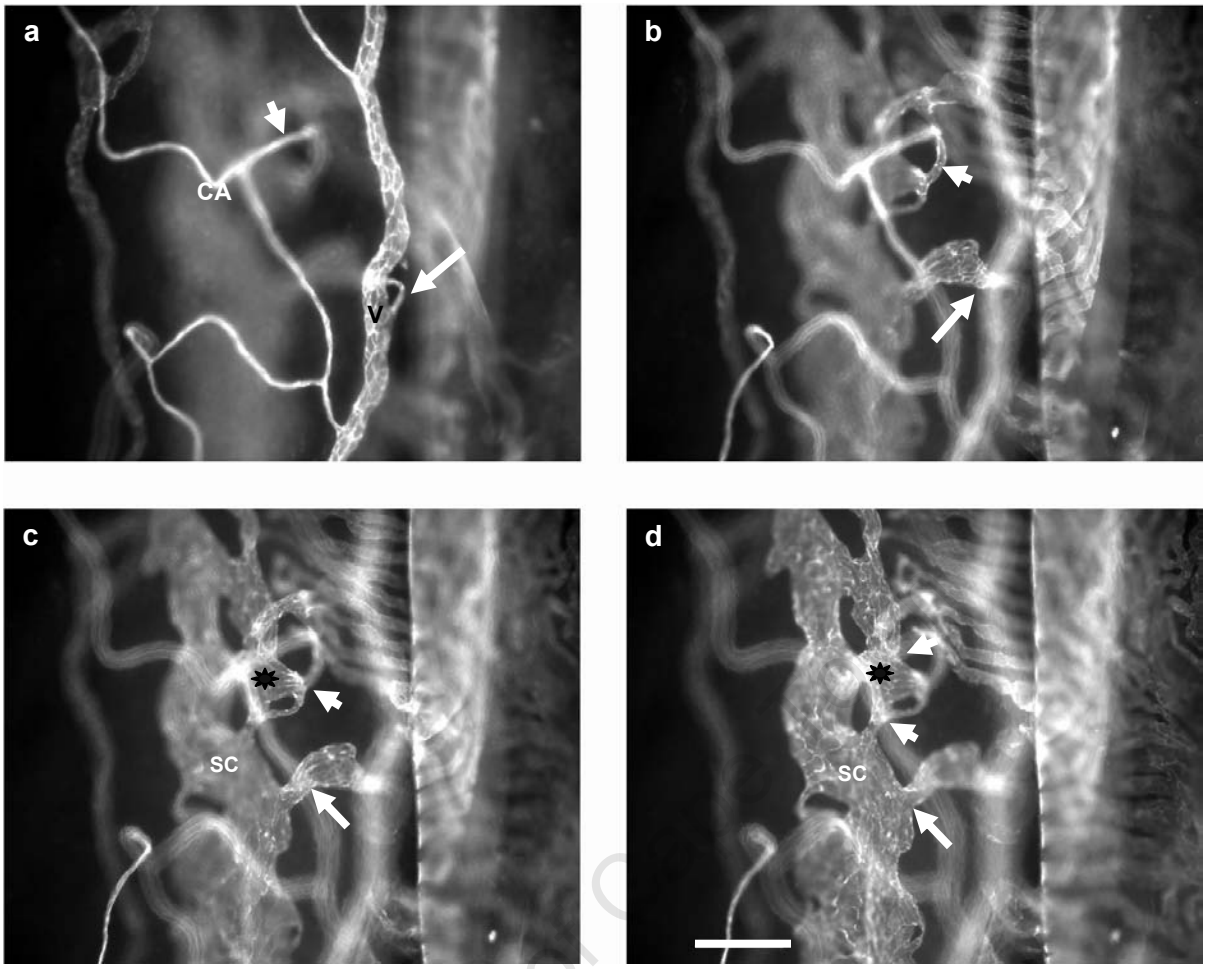

Figure 3.4: Optical sections of PECAM-1 stained limbal vessels captured by widefield fluorescence microscopy.

a-d) A series of optical sections starting in the focal plane of the superficial limbal vessels (a) and ending in the plane of Schlemm's canal (d) shows two putative collector channels (short and long arrows) arising from the corneal arcade (CA) and larger perilimbal vein (V) penetrating the limbus (a). These vessels are tracked through the limbus (b) where they anastomose with Schlemm's canal or with a plexus (star) that is linked to the canal (d). Bar = 100 μm.

The anatomical morphology of collector channels.

Putative collector channels were identified as vessels that branched off the superficial perilimbal vessels and penetrated into the limbus. This is shown in a pseudocoloured image that illustrates the relative depth of vessels in the limbus (Figure 3.2c). Here, collector channels that penetrate the limbus show a colour gradient from blue to yellow. Collector channels could also be tracked in wholemounts viewed by widefield fluorescence microscopy starting at the exterior ocular surface and focusing through the limbus (Figure 3.4). The PECAM-1 stained vessels in optical planes above and below the plane of focus also made it easier to see the anatomical relationship between the collector channel and the perilimbal plexus or Schlemm's canal. In a series of images captured at different depths of the limbus, two putative collector channels (long and short arrows – Figure 3.4a) branch off a perilimbal vein (V) and a segment of the corneal arcades (CA)

respectively. Deeper in the limbus, one putative collector channel (short arrow) continues as a thin vessel that anastomoses with a plexus (star) near Schlemm's canal (SC) (Figure 3.4b-d). The other collector channel (long arrow) becomes more bulbous in its morphology before it joins directly to the canal (Figure 3.4b-d). In cases where the perilimbal plexus was more densely packed with vessels, images of the vessels in the deep limbus were not as clear as those shown in Figure 3.4, and it was more difficult to track collector channels. Therefore, confocal microscopy was used to image the limbal vessels where collector channels (curly brackets in Figure 3.5) could be tracked through the limbus. Three-dimensional reconstructions of the optical sections were generated and collector channels were viewed in Z-plane images between the perilimbal plexus (long arrow) and Schlemm's canal (short arrow) (inset - Figure 3.5). In this image, collector channels showed two forms, one as a short vessel and the other as a long flexed vessel which appears to run close to and parallel to the canal for some distance before linking to it.

PECAM-1 distribution in the endothelium of the limbal vasculature.

Figure 3.6 shows the distinguishing endothelial cell morphology and staining characteristics found in arteries, veins, lymphatic vessels and Schlemm's canal. PECAM-1 was generally located at the peripheral borders of endothelial cells. Because all vascular structures were preserved in the wholemount preparations, the relative sizes and shapes of the endothelial cells were clearly demonstrated.

Arteries were of even width and displayed a rigid shape and generally had long and unbranched segments (Figures 3.2c and 3.6a, e). They typically displayed fusiform-shaped endothelial cells (Figures 3.6a, e), and the peripheral borders of these cells were more intensely stained than the peripheral borders of the endothelium in lymphatic vessels (Figures 3.6b, f), Schlemm's canal (Figures 3.6c, e) or veins (Figures 3.6d, g). At higher magnifications the cell borders were straight and showed regions of increased levels of punctate staining of PECAM-1 (arrow - Figure 3.6 e). By contrast, lymphatic vessels displayed a variable width, and a flexed and frequently branching morphology (Figure 3.6b - see also Figures 3.2a and 3.3a, b). Endothelial cells were less intensely stained at the peripheral borders than that seen in arteries or veins and also displayed a light diffuse staining. These vessels were the only type that displayed cusp-like structures that were regularly spaced along the vessel, particularly at points of bifurcation (Figure 3.6b - also see Figures 3.2a and 3.9c). These features are similar to the secondary valves reported in lymphatic vessels (Murfee et al., 2007). When viewed at higher magnifications, the endothelial cell borders were scalloped (Figures 3.6f, j). Lymphatic endothelial cells were substantially larger than those in arteries or veins and were polygonal in shape. These putative secondary valves consisted of

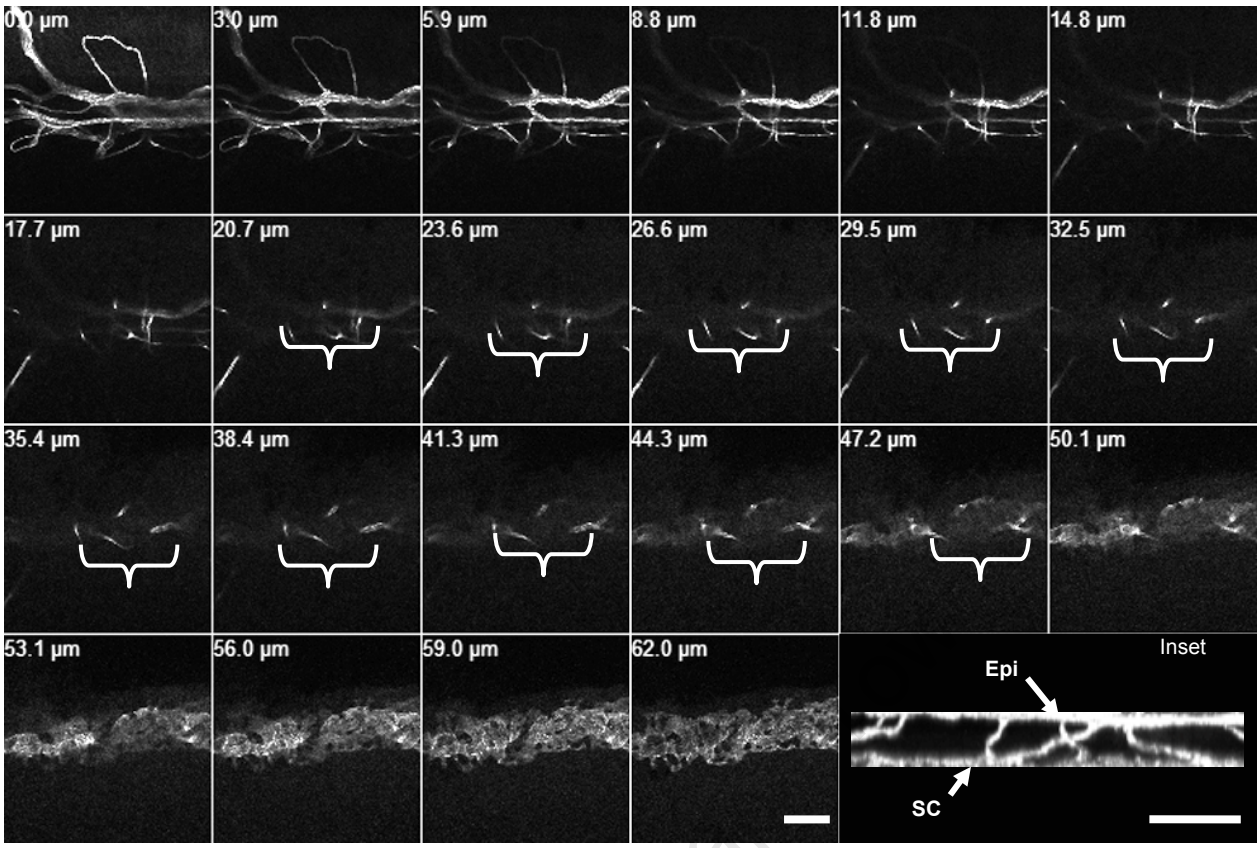

Figure 3.5: Optical sections of PECAM-1 stained limbal vessels captured by confocal microscopy.

A series of optical sections were imaged at three micron intervals through the depth of the limbus. The series starts at the level of the superficial limbal/episcleral vessels (0.0 µm) and ends at the base of Schlemm's canal which is 62.0 µm deeper in the limbus. A group of collector channels (curly bracket) can be tracked through the limbus from the episcleral vessels to Schlemm's canal. A three dimensional reconstruction of the Z-stack is viewed in the Z-plane (inset) and shows short and long forms of collector channels linking Schlemm's canal (SC) to the superficial limbal vessels (Epi). Bar = 100 µm

smaller endothelial cells (Figures 3.6f, j).

Limbal veins were generally more uniform in width, and displayed a flexed and branching morphology (Figure 3.6d). The polygonal-shaped endothelial cells in veins were smaller than those in lymphatic vessels but wider than those in arteries (compare figures 3.6g-f). In the endothelium lining veins or venules, PECAM-1 was concentrated at the cell periphery and was generally less intensely stained than in arteries.

Of all the vessels in the limbus, Schlemm's canal was generally the broadest and most commonly seen as an unbranched, canal-like structure (Figures 3.2b, c; 3.3c, d; 3.5, 3.6e, h, i, and 3.7d). Schlemm's canal also displayed other features such splitting into two segments (bifurcations)

Figure 3.6: Morphology of the limbal vessels and their associated endothelial cells in PECAM-1 immunostained wholemounts of the ocular anterior segment of wildtype adult mice.

a) Arteries display intense PECAM-1 staining and show a uniform width and a rigid linear morphology. This image is of the major arterial circle of the iris. Bar = 100 µm

b) Lymphatic vessels are less intensely stained than arteries or veins and the vessel displays a variable width and a more flexuous linear morphology. Regularly spaced cup-like structures thought to be secondary valves are more intensely stained (arrows). Bar = 100 µm

c) Schlemm's canal is generally the largest vessel in the limbus but its width and shape can vary substantially (compare with Figure 3.6e and Figures 3.7). The intensity of PECAM-1 staining was generally the lowest compared to the other limbal vessels. Bar = 100 µm

d) Limbal veins display a uniform width and a flexuous linear morphology. Collector channels (arrows) are similar to capillaries but also display variable width along a segment (see Figure 3.4 b-d). Bar = 100 µm

e) Fusiform-shaped endothelial cells (short arrow) of the long posterior artery are aligned with their longitudinal axis in the direction of the blood flow. Endothelial cells of Schlemm's canal are large and angular in shape, and have relatively smooth cell borders (long arrow) compared to the lymphatic endothelial cells (see (f) below). Bar = 50 µm

f) The endothelial cells of lymphatic vessels are large and their cells borders show a scalloped pattern (short arrow). The cup-like structure (long arrow) consists of smaller endothelial cells and is formed from additional layers of cells internally. This extended focus image was generated from a series of optical sections. Bar = 50 µm

g) Endothelial cells lining veins are larger than those in arteries but are substantially smaller than those seen in lymphatic vessels or Schlemm's canal. Although elongated along the longitudinal axis of the vein, these cells are not typically fusiform (arrow). Bar = 50 µm

h) Enlarged view of Schlemm's canal focused on the endothelial cells lining the external wall. These cells are substantially larger than those lining the internal wall of the canal (compare with Figure 3.6i). Bar = 50 µm

i) Enlarged view of Schlemm's canal focused on the endothelial cells lining the internal wall of the canal. The cells are generally smaller than those lining the external wall and there are numerous small round structures at the periphery of the endothelial cells (arrows). Bar = 50 µm

j) Enlarged view of Figure 3.6f showing the scalloped endothelial cell cell borders (arrow). Bar = 50 µm

(a, f, g and j) are confocal images and the remaining images were captured using widefield fluorescence microscopy.

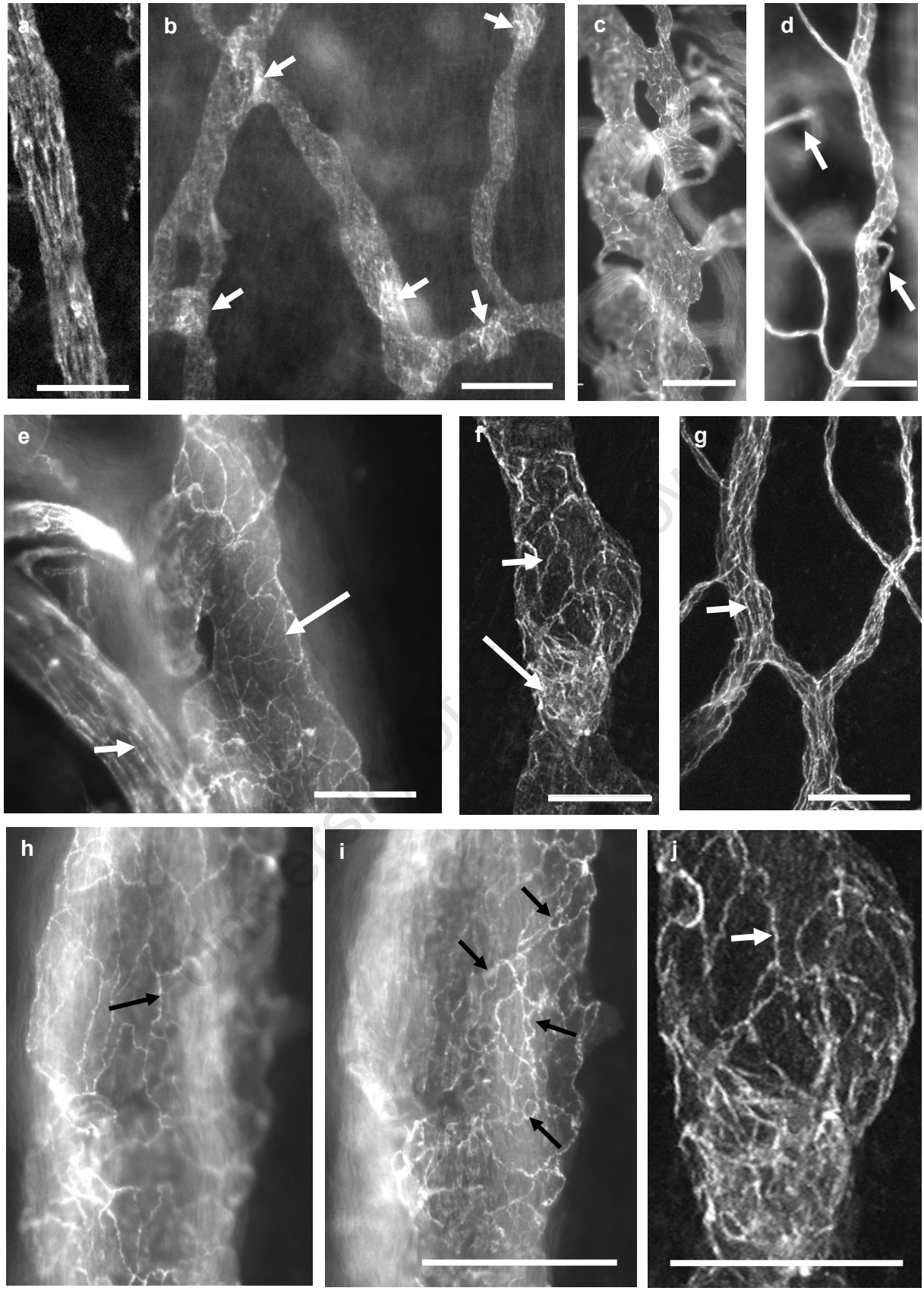

Figure 3.6: Morphology of the limbal vessels and their associated endothelial cells in PECAM-1 immunostained wholemounts of the ocular anterior segment of wildtype adult mice.

(arrows - Figure 3.6c) or into a simple plexus of narrow vessels (short arrow - Figure 3.7c). Short narrow bridges connecting the broader canal-like segments (arrow - Figure 3.7b) were also observed. In many cases these connecting segments were only visible at focal planes above the Schlemm's canal. By changing the focus, these segments were found to be linked to the broader segments of the canal thus showing continuity of the canal. In regions where the canal formed a plexus, this plexus was sometimes observed in focal planes above Schlemm's canal. By focusing through several optical planes, these vessels were traced to show that they linked to the canal thereby showing continuity of the canal around the limbus. Small blind-ending sprouts (diverticuli) (arrow - Figure 3.7a) were often seen on the lateral wall facing the cornea (anterior wall). Even when the diverticuli were absent, the anterior wall of the canal was uneven compared to the posterior wall on the scleral side of the canal (Figures 3.7b, d).

The endothelial cells lining the canal were large and were polygonal and triangular in shape (Figures 3.6e, h, i). In general, PECAM-1 staining was less intense at the cell borders compared to the endothelial cells on the other vessels. In addition, some diffuse staining of PECAM-1 was distributed within or on the surface of the endothelial cells similar to that seen in lymphatic vessels (Figures 3.6b, e, h, i). By changing the focal plane, the endothelium lining the outer and inner walls of Schlemm's canal were revealed in places (Figures 3.6h, i). Endothelial cells lining the outer wall showed large cells with punctate intensities along smooth cell borders (arrow - Figure 3.6h). At a focal plane slightly deeper in the limbus, the endothelial cells lining the inner wall of the canal could be seen. They appeared smaller, had variable shapes, and displayed numerous small ring-like structures outlined with PECAM-1 (arrows - Figure 3.6i). These structures considered to be collector channels (Figure 3.6d), were easily observed in PECAM-1 immunostained wholemounts (Figures 3.6d, and 3.4). These vessels formed anastomoses with the capillaries of the corneal arcades or with the perilimbal veins (Figures 3.6 d and 3.4). Their width and lengths varied, forming either short links to the canal or a more tortuous path through the limbus (Figure 3.5 inset; see also Figures 3.4 and 3.2c).

3.3 The anatomical organization of the limbal vessels of the normal mouse eye revealed in PECAM-1 immunostained wholemounts.

The next aim of this study was to elucidate the anatomical relationship between the vessels in the superficial perilimbal vasculature in normal mouse eyes. When this work was initiated, a confocal microscope was not available and wholemounts were studied using widefield fluorescence microscopy. However, because the vessels of the iris and ciliary body are located below the limbus, the out-of-focus glare from the numerous blood vessels in these structures interfered with

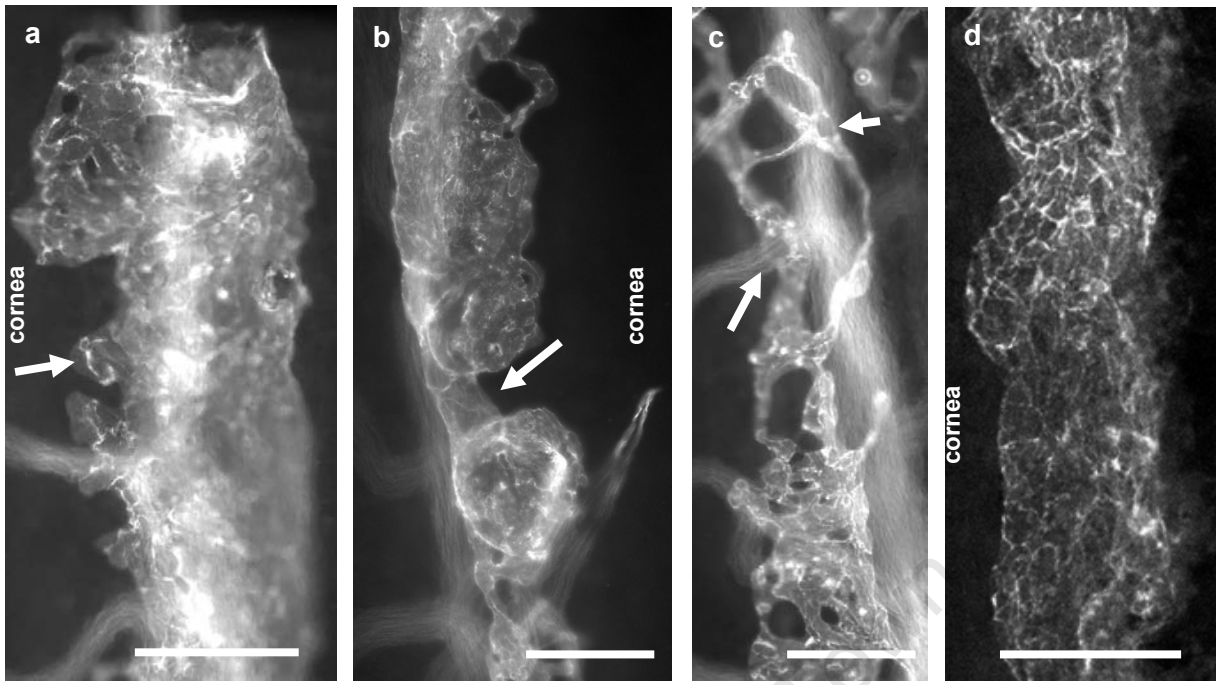

Figure 3.7: The morphology of Schlemm's canal revealed in PECAM-1 immunostained wholemounts of the mouse eye anterior segment.

a-c: ICR strain. d: C57BL/6Jx129 strain

a) A wide canal shows blind-ending diverticuli (arrow) arising only from the anterior edge of the canal.

b) A merged image of several optical sections over Schlemm's canal reveals an irregular shape with large bulbous segments. The narrow segment (long arrow) that joins the bulbous regions is at a focal plane higher in the limbus than the rest of the canal. The bulbous shape gives way to a short narrow segment (short arrow).

c) A single wide canal branches to form a plexus (short arrow). An out-of-focus collector channel (long arrow) arises from the plexus.

d) The lateral walls of the canal show less prominent anterior bulges and the canal is generally of even width. This feature was more typically seen in the normal C57BL/6Jx129 strain.

Bar = 100 μm for all images.

the fluorescence from the limbal vessels thus severely limiting the resolution of the limbal vessels (data not shown). Therefore, the iris and ciliary body were carefully dissected away from the rest of the anterior segment, leaving the limbal, episcleral and choroid vasculature intact. This work was carried out on non-pigmented ICR mice because slight undulations in the tissue caused the pigmented epithelium underlying the choroid vessels of the C57BL/6Jx129 strain to mask some of the PECAM-1 fluorescent signals in blood vessels that may approach the limbus via the choroid.

In the mouse eye, the anterior ciliary artery (ACA) was identified as a fairly rigid single vessel that approached the perilimbal vessels from the vascular plexus of the external ocular muscles

(ACA and arrowhead respectively in Figures 3.8a, e). Two long posterior arteries reported to be the lateral and medial long posterior arteries (Ninomiya and Inomata, 2006) were observed as wide rigid vessels traversing the choroid vasculature and branching before reaching the iridocorneal junction (LPCA in Figure 3.8c). There were two anterior ciliary arteries, each derived from the vasculature of the superior and inferior external ocular muscles. This was deduced from the absence of the ACAs in the superficial limbus overlying the lateral and medial long posterior arteries. At the limbus, the anterior ciliary arteries, and a branch off each of the long posterior ciliary arteries splits into two vessels which together form one of the four segments that make up the circular limbal artery (CLA, long arrows, white stars in Figures 3.8a, b and c respectively). At the distal end of each CLA segment, the venous end often formed hairpin-bended loops and anastomosed with the perilimbal vein at points where the two segments of the CLA approached each other from opposite directions (long arrows - Figure 3.8b). At focal planes which captured the choroid vessels, the long posterior artery (LPCA) was observed approaching the limbus (Figure 3.8c). Here, an artery (arrowhead) that branches off the LPCA bifurcates in thedeeper planes to form one segment of the circular limbal artery (stars - Figure 3.8c). Long arrows indicate the points at which the CLA penetrates the limbus. Thus the above findings show that the blood supply to the limbus is via the long posterior ciliary arteries and two anterior ciliary arteries. Direct association of the circular limbal artery with Schlemm's canal was not seen in any of the wholemounts. The circular limbal artery did not branch to form a plexus but anastomosed with the corneal arcades (short arrow - Figure 3.8b) and episcleral capillary plexus lying posterior to the artery (not shown). The distal end of the corneal arcades and episcleral capillaries anastomosed with the perilimbal venous plexus (PLV - Figures 3.8a-c). Corneal arcades were simple and relatively few in ICR mouse eyes (CA -Figures 3.8b, c, e) whereas they were more complex in C57BL/6Jx129 mice (CA - Figures 3.8d, f). Detailed analysis of the penetration of the corneal arcades into the cornea and the complexity of this plexus in the normal ICR and C57BL/6Jx129 mouse strains is presented in Section **3.5.2**.

The perilimbal vein (PLV) was observed as either a single large vein (PLV - Figures 3.8a-c; long arrows in Figure 3.8e) or as two parallel veins which anastomosed with each other (long arrows in Figures 3.8d, f). The distal portions of the capillaries of the episclera and corneal arcades formed anastomoses with the perilimbal veins (long arrows - Figure 3.8d). The single perilimbal vein was generally more prevalent in ICR mouse eyes whereas the split configuration was seen more frequently in the C57BL/6Jx129 strain (long arrows - Figures 3.8d, f). Several episcleral veins that branch off the perilimbal vein or plexus (open arrows and long arrows in Figures 3.8a and e respectively) lead to the exterior ocular muscle vascular plexus. The width of some of these

efferent veins was substantially wider than that of the incoming anterior ciliary artery (white triangle - Figure 3.8a). Occasionally, the efferent episcleral veins anastomosed with the anterior ciliary artery (curved arrow) forming possible arteriovenous anastomoses (Figure 3.8a).

At the focal plane of the superficial limbus, vessels assumed to be collector channels were observed penetrating the limbus (stars - Figure 3.8a) to join to Schlemm's canal in the deeper focal plane (SC - Figure 3.8a). Collector channels are seen in Figures 3.2c (short arrows), 3.4 and 3.5). These vessels were either joined directly to the larger perilimbal vein (double white arrows - Figure 3.8a, long arrow in Figure 3.4a), or anastomosed with the radial segments of the corneal arcades (short arrow - Figure 3.4a). A hook-shaped collector channel resembling a similarly shaped aqueous vein reported in the human eye (Dvorak-Theobald, 1943; Ashton, 1951) was also observed in the mouse eye (white-rimmed star - Figure 3.8a).

The episcleral lymphatic vessels were less conspicuous in the ICR strain than in the C57BL/6Jx129 strain. Perilimbal lymphatic vessels often extended short blind-ending sprouts (short arrow – Figure 3.8f) into the cornea. The location of these lymphatic vessels appeared to be deeper in the limbus than the perilimbal artery and veins (Figures 3.3a and 3.8f). In order to confirm this, images of wholemounts double-immunostained with anti-PECAM-1 and anti-LYVE-1 were imaged at different focal planes (Figure 3.9). In all cases, the lymphatic vessels were located deeper in the limbus than the episcleral and perilimbal blood vessels as seen in Figure 3.9a (which is focused on the most exterior surface) and in Figure 3.9b (which is focused deeper into the limbus). An extended focus confocal image of a series of optical sections of the outer limbus revealed that the secondary valve-like structures stain more intensely for PECAM-1 than for LYVE-1 (yellow arrows - Figure 3.9c). These secondary valves were not observed in the large perilimbal lymphatic vessel and in the blind-ending lymphatic vessels penetrating the cornea. In this image the perilimbal vascular plexus is clearly seen to be more superficial than the lymphatic vessels. As mentioned before and reported previously (Chen et al., 2005), numerous LYVE-1 stained cells were present in the episclera and were always located in the same plane as the lymphatic vessels (compare Figures 3.9a, b). These cells were also restricted to the episcleral zone posterior to the perilimbal lymphatic vessel.

Figure 3.8: Figure 3.8: The spatial organisation of the limbal vessels in PECAM-1 immunostained wholemounts of the ocular anterior segment of wildtype adult mice.

(a-c, e) ICR strain; (d, f) C57BL/6Jx129 strain

a) Various vessels in the superficial limbus are shown. The anterior ciliary artery (ACA), identified by the typical fusiform shape of the endothelial cells at higher magnification (not shown), approaches the limbus from the vascular plexus of the exterior ocular muscles (EOM). It branches at the limbus to form the circular limbal artery (CLA). Three collector channels (white and open stars) arising from Schlemm's canal (SC - out of focus structure) join the perilimbal circular vein (PLV). The collector channel on the extreme right (open star) has a hook-shape whilst the other two form straight channels through the limbus. Triangle shows an episcleral vein. Open arrows indicate episcleral veins that communicate with the anterior ciliary artery (ACA). Curved arrow indicates arteriovenous anastomoses between the episcleral vein (open arrow) and the anterior ciliary artery (ACA).

b) Two segments of the CLA (long arrows) join the limbal venous plexus at hairpin-bend looped capillaries. Unlike the perilimbal vein (PLV) the CLA does not form a complete circle around the limbus. Two capillaries of the corneal arcades (CA) anastomose with the CLA at one end (short arrow) and with the PLV at the other end (star).

c) Two segments of the CLA (white stars) penetrate the limbus (long arrows) to join to a branch (arrowhead) of the long posterior ciliary artery (LPCA). CA = corneal arcades; PLV = perilimbal vein.

d) The circular limbal artery (short arrow) is single whilst the perilimbal vein has branched into two vessels (long arrows) which are linked to each other via short vessels to form a loose plexus.

e) The perilimbal veins (short arrows) leave the limbus via a few episcleral veins (long arrows) that join the vasculature of the exterior ocular muscles (EOM). Arrowhead indicates the circular limbal artery.

f) The superficial periimbal plexus (arrows) and corneal arcades (CA) are more elaborate in the C57BL/6Jx129 strain. CA = corneal arcades; star = circular limbal artery

Bar = 100µm for all images

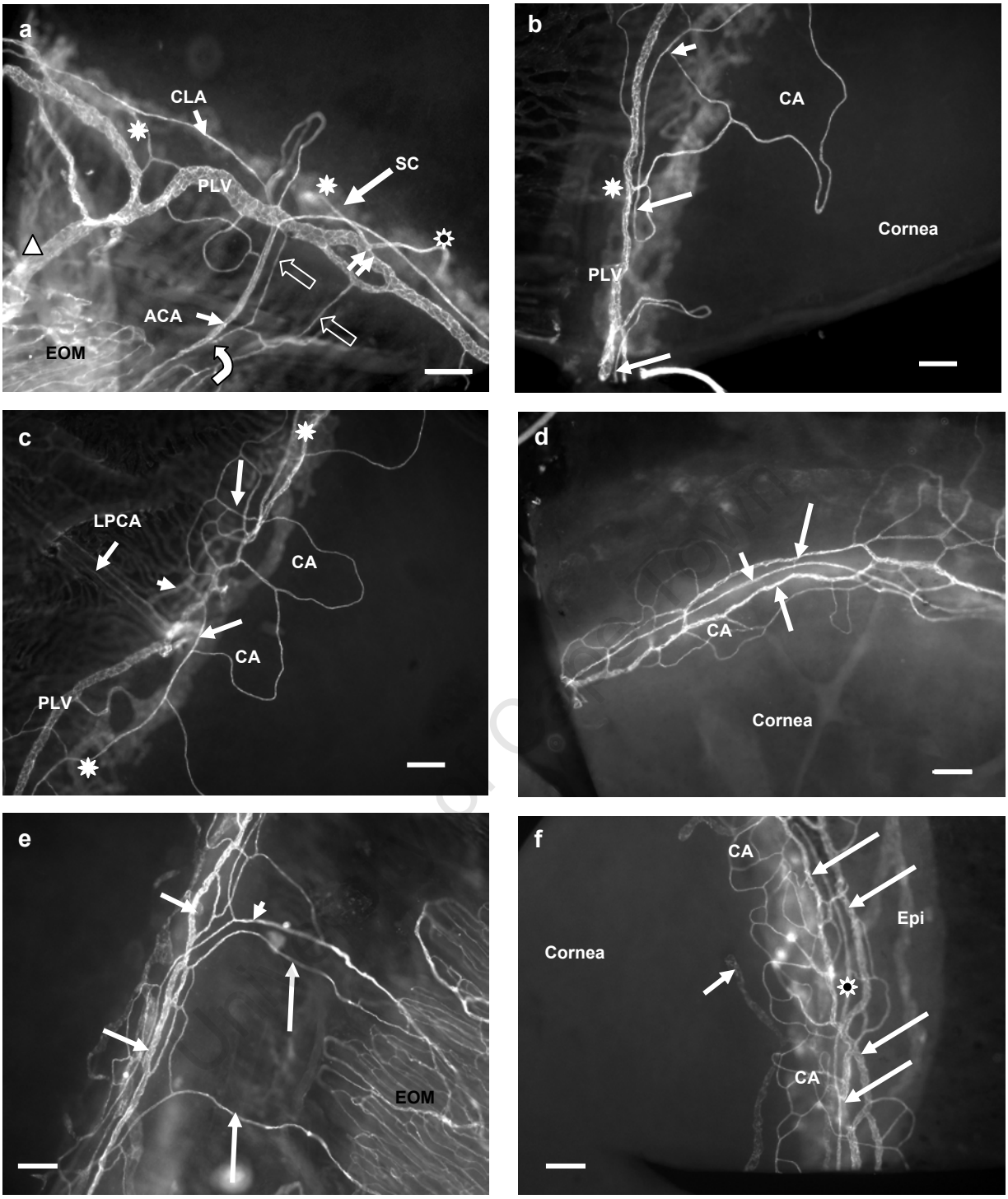

Figure 3.8: The spatial organisation of the limbal vessels in PECAM-1 immunostained wholemounts of the ocular anterior segment of wildtype adult mice.

(a-c, e) ICR strain; (d, f) C57BL/6Jx129 strain

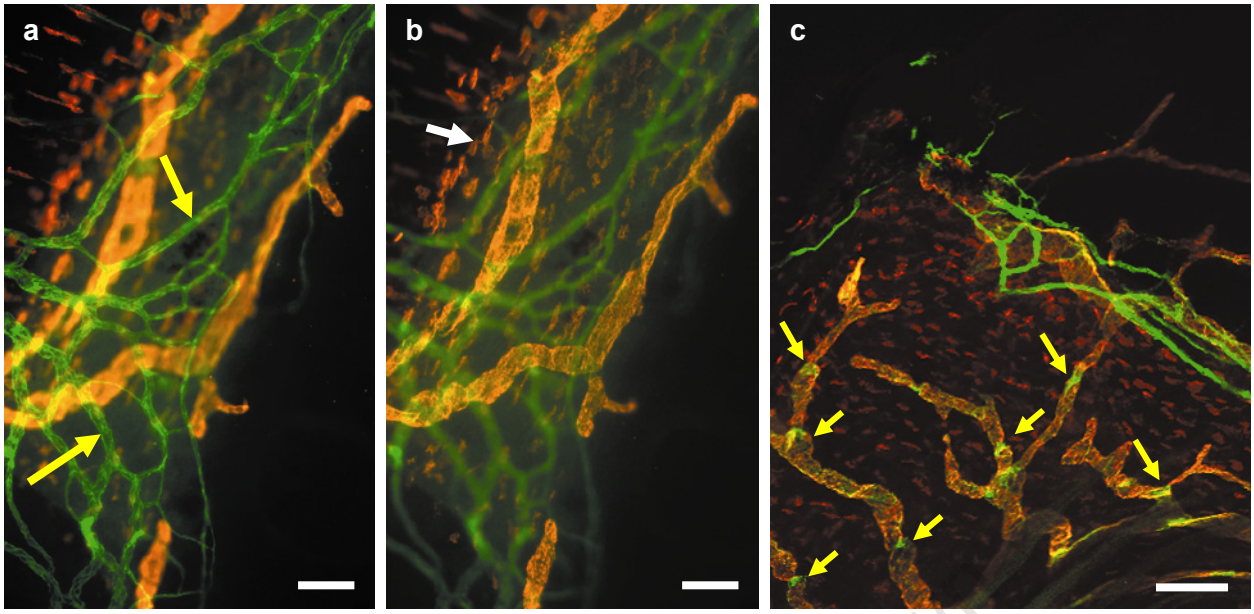

Figure 3.9: Organisation of LYVE-1 immunostained limbal lymphatic vessels.

a) Double immunostained wholemounts show limbal blood vessels staining only for PECAM-1 (green vessels) and lymphatic vessels showing dual staining for LYVE-1 and PECAM-1 (orange vessels). This image was taken with widefield fluorescence and focused on the superficial (exterior) limbus where the vascular plexus (yellow arrows) is in sharp focus. The lymphatic vessels (orange) are out of focus in this image plane. Bar = 100 µm

b) This image of the same field as in Figure 3.9a was captured at a focal plane deeper in the limbus to that in (a) and confirms that the lymphatic network in the episclera and limbus lie beneath the vascular system in this region. The numerous cells in the episcleral region (arrow) staining for LYVE-1 are also located in the same plane as the lymphatic vessels. Bar = 100 µm

c) An extended focused (merged) image of a Z-stack of optical sections through the superficial limbus was captured by confocal microscopy. The perilimbal PECAM-1 stained vascular plexus (green vessels) clearly lies superficial to the perilimbal lymphatic vessel (orange). Yellow arrows indicate the putative secondary lymphatic valves which are more strongly stained for PECAM-1 than LYVE-1. The numerous LYVE-1 stained cells in the episclera are only located posterior to the large perilimbal lymphatic vessel (yellow arrow). Bar = 100 µm

3.4 Morphogenesis of Schlemm's canal and the limbal vasculature in normal mice.

Although studies have elucidated the temporal development of the trabecular meshwork and Schlemm's canal in humans and mice, there is little information on the relationship of the developing canal to the surrounding vessels of the limbus (Hamanaka et al., 1992; Ramírez et al., 2004; Smith et al 2001). There are no reports on how the posttrabecular vessels develop in the mouse, although it has been reported that small blood vessels are located in the region of the presumptive canal prior to the emergence of the canal-like morphology (Smith et al., 2001). Thus the aim in this section was to make use of developmental stages to answer the following questions: 1) Does Schlemm's canal form *de novo* or by angiogenesis? 2) If the canal forms from angiogenic outgrowths from existing vessels, then from which vessels does the canal arise? 3) Does Schlemm's canal form from a precursor vessel which remodels and how and when does this happen?

In order to address the above questions, the appropriate ages/stages need to be identified. Because Smith et al., (2001) reported that small blood vessels and a small canal-like structure were present in some regions of the limbus at day 8 (P8) and 10 (P10) respectively, it was reasoned that the present study should focus on the time points prior to and just after P10. Fortunately for the purposes of this study, the development of the iridocorneal angle occurs postnatally in mouse whereas in humans where it occurs prenatally (Pei and Rhodin, 1972; Smith et al., 2001; Tripathi et al., 1996). The time points of P2, P3, P4, P6, P8, P10, P12 and P14 were studied since these would cover the stages (prior to P8) that could elucidate the possible source of the vessels of the presumptive canal, and to cover the stages (P8-14) in order to observe the growth of the canal to its mature form.

In contrast to the studies of adult mouse eyes described in the previous sections, the iris and ciliary body were not dissected away from the anterior segments of the postnatal mouse eyes. This was to ensure that all blood vessels of the anterior segment were intact in order to image the vascular system at the various ages. Procedures of fixation and immunostaining were carried out as described before (see sections **2.2.1** and **2.2.2**) on 8-16 eyes per age group. It was important that the albino ICR strain was used for this study, since it is not pigmented. This lack of pigment allowed a clear view of the entire wholemount that would not have been seen in the pigmented C57BL/6Jx129 strain. Procedures of fixation and immunostaining to detect PECAM-1 were carried out as described before (see sections **2.2.1** and **2.2.2**) on 8-16 eyes per age group, and wholemounts were viewed by confocal microscopy.

One of the challenges at the outset was to locate and recognise, with certainty, the various limbal vessels including Schlemm's canal. Fortunately, at all postnatal ages examined, a superficial perilimbal plexus was present (Figures 3.10a, b, 3.16c, d, 3.20, 3.22, 3.24, 3.25b and 3.26g, h). This served as an ideal starting point or landmark for identifying vessels that penetrated the limbus. From this landmark, vessels arising from the superficial plexus that penetrated the limbus were then tracked through the deeper planes of the limbus (Z-plane tracking) to determine whether they formed anastomoses with other vessels or gave rise to blind-ending outgrowths. Since it was probable that the primitive form of Schlemm's canal would not be present throughout the limbus, Z-plane tracking and image capture was done in sequential fields of view as described in section **2.3** (see Figure 2.3). In order to reveal the complete morphology of the putative Schlemm's canal, and show in the same "flat" image possible connections to the underlying uveal vasculature, extended focus images (merged images produced from several individual optical sections from a Z-stack) were generated, and are presented in some of the figures in this section. In order to show any vascular connections between the primitive Schlemm's to the perilimbal plexus, galleries of individual optical sections are presented in some figures in this section.

3.4.1 The limbal vasculature at postnatal day 2 (P2).

The superficial limbal vasculature:

At P2, the superficial limbal vasculature was present and formed a complex perilimbal plexus (SP - Figure 3.10a, b). In contrast to that seen in adult mouse eyes, arterial and venous vessel phenotypes were not morphologically distinguishable. The perilimbal plexus was linked to the vasculature of the exterior ocular muscles via numerous radial vessels in the episclera (Epi - Figure 3.10b). Several arched capillary-like vessels arising from the plexus were seen penetrating the limbus (long arrows - Figure 3.10a, b). Lymphatic-like vessels that were somewhat larger in width and paler staining compared to those in the superficial plexus, were located deeper in the limbus just below the superficial vascular plexus (white star and short arrow in Figures 3.10a and b respectively). The endothelial cells within these vessels appeared to be larger than those seen in the superficial vascular plexus. The perilimbal lymphatic vessels were intertwined and formed anastomoses with one another. Interestingly, they formed long segments but not a complete circle around the circumference of the limbus (not shown). Arising from these vessels were short blind-ending outgrowths that penetrated the cornea (open arrow - Figure 3.10b). In addition, branches from these lymphatic-like vessels (short arrow - Figure 3.10a) joined the circumferential vessels in the episclera (stars in Figure 3.10a, b). The secondary valve-like structures seen in adult episcleral lymphatic vessels (Figures 3.6b and 3.9c) were not observed at this age. When viewed at 488 nm

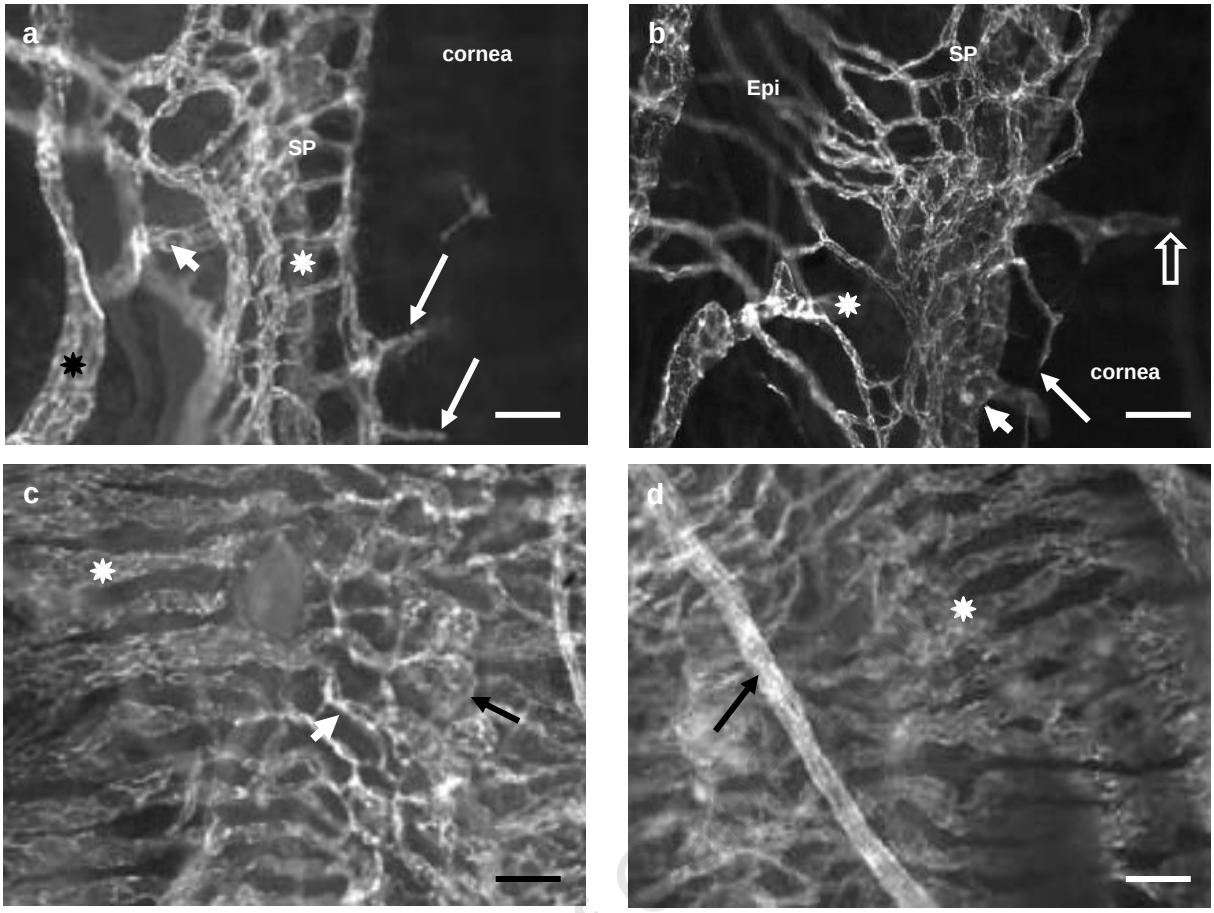

Figure 3.10: Confocal images of the superficial limbal and uveal vasculature at P2.

Figures a and c are different optical sections of the same region in the limbus

a) An optical section focussed on the superficial perilimbal plexus (SP) reveals a complex network of vessels. Vascular outgrowths from the perilimbal plexus (presumptive collector channels) are seen penetrating the limbus (long arrows). A larger flexuous lymphatic-like vessel (black star) is located in the episclera. A vessel (short arrow) links this to a larger lymphatic vessel (white star) located below the perilimbal vasculature). Bar = 50 µm

b) A large lymphatic vessel (short arrow) with short blind-ending outgrowths (open arrow) into the cornea is located beneath the superficial perilimbal plexus (SP). The lymphatic-like vessel (star) in the episclera is seen approaching the large lymphatic-like vessels below the superficial plexus. Long arrow indicates limbal penetrating vessels. The secondary valves were not detected in these vessels at this age.
Bar = 50 µm

c) An optical section focussed deep into the wholemount below the region shown in Figure 3.10a, shows a well-formed uveal vasculature. The vessels of the pars plana of the choroid (PP) link directly to the sinusoidal-like vessels of the ciliary processes (long black arrow) via narrow vascular segments (short white arrow). Iris vessels are at the extreme right of the image. Bar = 50 µm

d) The major arterial circle of the iris (black arrow), is located in optical plane above the choroid (white star) and ciliary body vasculature. The uveal vessels are slightly out of focus and there are segments that are masked by the overlying continuous circular artery of the iris. Bar = 50 µm

and 546 nm excitation wavelengths, autofluorescent erythrocytes (detected with 568 nm excitation) were present in the perilimbal plexus (long arrow - Figure 3.11a) but were not observed in the episcleral lymphatic-like vessels (short arrows - Figure 3.11a). Although LYVE-1 immuostaining was not performed on these eyes, the anatomical location and the absence of erythrocytes in these vessels provides strong support that these are indeed lymphatic vessels.

The uveal vasculature.

The PECAM-1 stained uveal vasculature was identified in the deepest part of the wholemount of the anterior segments where the iris and ciliary body were located. At this stage, the vessels of the choroid, ciliary body and iris were well developed (Figure 3.10c, d). The blood vessels of the pars plana were arranged in single layer (PP - Figure 3.10c) and formed anastomoses with the blood vessels of the ciliary processes (long arrow - Figure 3.10c) via narrow vascular segments (short arrow - Figure 3.10c). The major arterial circle of the iris (long arrow - Figure 3.10d) was located in the focal plane slightly above the choroid and ciliary body vessels (star – Figure 3.10d).

The deep limbal vasculature.

In order to search for evidence of a primitive Schlemm's canal, optical sections were taken from the superficial plexus to the uveal vasculature (shown in Figure 3.12). At this postnatal age (P2), there was no evidence of a circular canal-like vessel in the deep limbus. However, short disconnected vascular segments seen in focus at 21-27 µm (dotted line boxes - Figure 3.12) were orientated in the circumferential plane. A graphic outline of these vascular segments is shown in the inset of Figure 3.12. These vascular segments are at a higher focal plane in the limbus that of the uveal vasculature (in focus at levels 30-36 µm - Figure 3.12), which shows the major arterial circle of the iris and the long posterior ciliary artery (black and white star, and, white star respectively - Figure 3.12). In order to determine if this deep limbal vascular segment was linked to other vessels, observations were made at all the focal planes (Z-plane) throughout the wholemounts. Starting at the superficial plexus, there were numerous vessels that branched off this plexus, some of which terminated as blind ending, unbranched vessels at various depths in the limbus (small arrows - Figure 3.12). Other penetrating vessels (putative collector channels) (long arrow - Figure 3.13a) could be tracked all the way down to the short circumferentially orientated vascular segments (short arrows - Figure 3.13a) (open arrow, long arrow and arrowhead - 3.14a-d). The orientation of the vascular sprout in the circumferential plane (right short arrow - Figure 3.13a) suggested that the other vascular segments (dotted line boxes and dotted line in Figures 3.12 and 3.13b respectively) may also have formed from similar outgrowths from the penetrating vessels. Longer vascular segments such as that shown in Figure 3.13b were not straight but

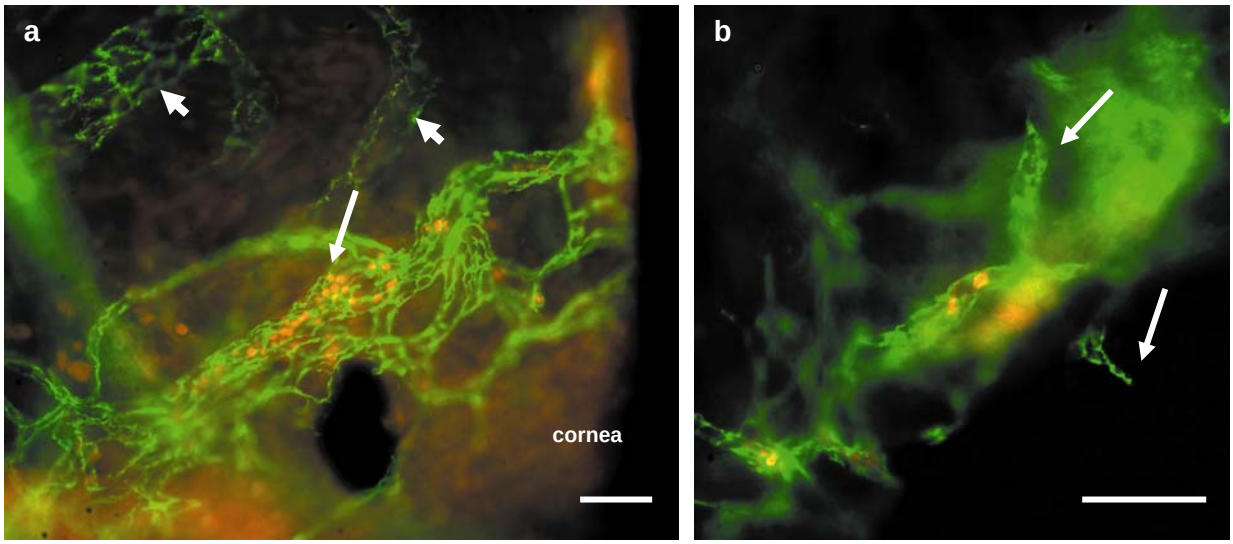

Figure 3.11: Merged images showing PECAM-1 stained vessels (green) and autofluorescence of erythrocytes (red) in the limbal vessels in mouse eyes at P2.

a) The superficial limbal plexus (long arrow) is well perfused with blood. The large, unperfused vessel (short arrows) corresponds to the episcleral lymphatic vessels.
Bar = 50 µm

b) The deep rudimentary limbal plexus of the presumptive Schlemm's canal contains erythrocytes (red cells). Sprouts (arrows) arising from these vessels do not contain erythrocytes. Bar = 50 µm

appeared warped and formed from the fusion of smaller vascular segments (dotted lines - Figure 3.13b). Several short sprouts (diamonds - Figure 3.13b) arose from what appears to be a coalesced single vessel (short arrows - Figure 3.13b). In all cases, these circumferentially orientated vascular segments were linked to the superficial plexus via connecting vessels (Figure 3.14a-d). Here, two putative collector channels (arrowhead and long arrow) that are linked to the superficial plexus in Figure 3.14a can be tracked through deeper optical planes (Figures 3.14b-d) to where they join the vascular segment (right dotted line box - Figure 3.14c, d). A putative collector channel (open arrow) joins the superficial plexus to the vascular segment in the left box (see Figures 3.14a-e). In some cases, a vascular segment was linked to the choroid vessels by a short vessel (follow short arrows from Figure 3.14d-h). This shows that the same vascular segment is linked to both the superficial plexus and the uveal vasculature. Connections between the vascular segments and the choroid vessels were, however, less frequently observed than connections to the superficial perilimbal vasculature.

These vascular segments, all of which were connected to the superficial plexus, were only seen in the deep limbus, were always superficial to the uveal vasculature, and, were orientated along the circumferential plane. It was thus likely that these segments were the most primitive form of the

Figure 3.12: Gallery of optical sections of the limbus at P2.

Optical sections were captured at 3 µm intervals through the limbus starting at the superficial limbal plexus (0.0 µm) and ending at the choroid vasculature (36.0 µm). Blind-ending vessels arising from the superficial plexus terminate at different depths in the limbus (short arrows). Vascular segments (dotted lines) located between 21 and 27 µm below the superficial plexus are orientated in the circumferential plane. An outline of showing the complete structure of these two vascular segments is shown in the inset. The choroid vasculature of the pars plana (PP), the branching long posterior ciliary artery (white star), major arterial circle of the iris (black & white star) and the ciliary body plexus (CB) are in sharp focus at 33 and 36 µm below the superficial limbal plexus. Bar = 50 µm.

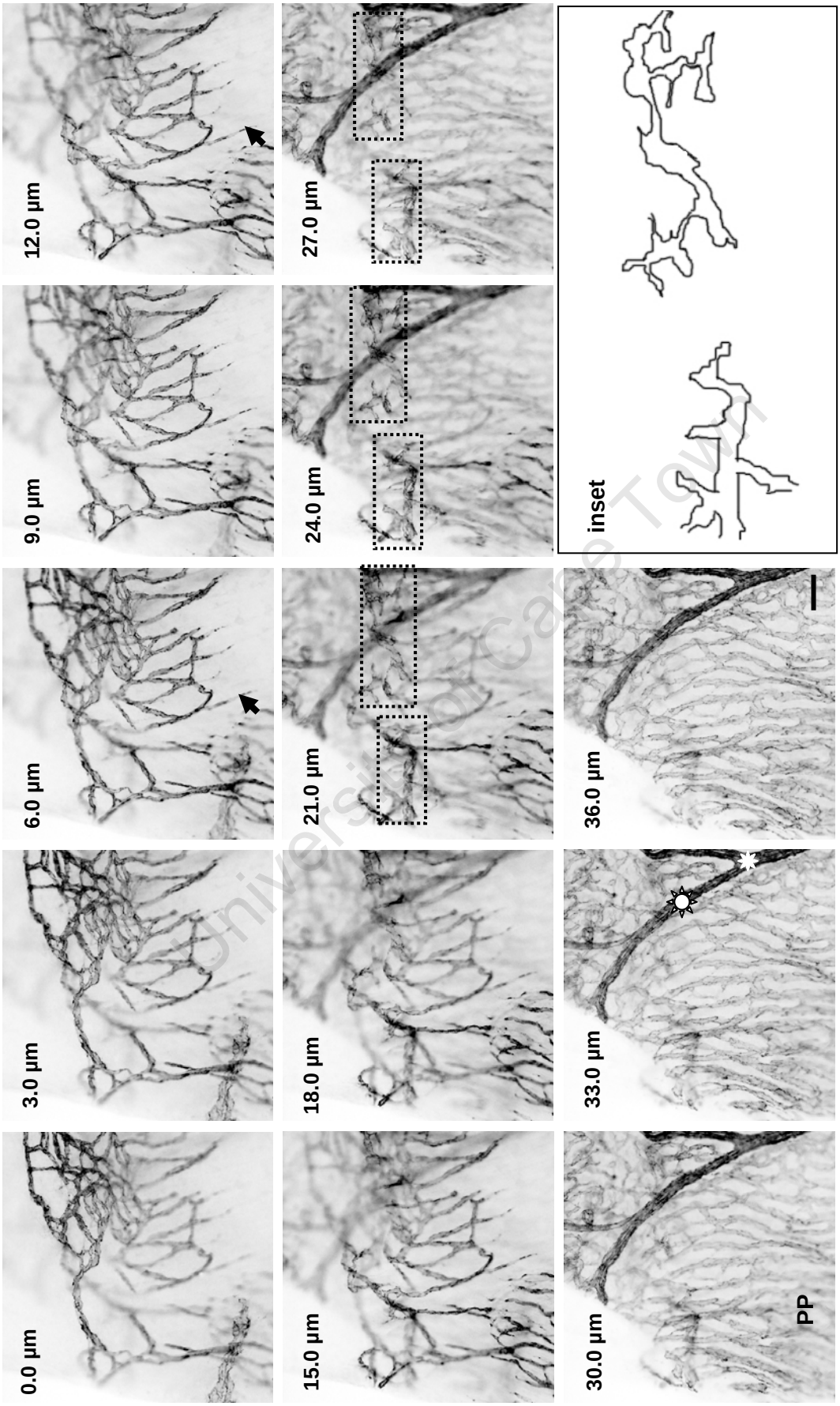

Figure 3.12: Gallery of optical sections of the limbus at P2.

putative Schlemm's canal. These segments were also always located posterior to the vasculature of the ciliary body. The location of the primitive Schlemm's canal (dotted line box) relative to the vessels in the minor processes of the ciliary body (long arrow) is shown in Figure 3.15a. In the deeper optical plane, the relative location of the canal (out of focus in this optical plane) indicated by the dotted line box, is clearly on the posterior side of the ciliary body vasculature (long arrow) and major arterial circle of the iris (star). As seen in Figures 3.13 and 3.14, the vasculature of the pars plana of the choroid (PP) is located in the in an optical planes below the primitive Schlemm's canal and also anastomoses (arrowhead) with the ciliary body vasculature (long arrow - Figure 3.15b).

Since the above findings confirmed a direct association between the rudimentary deep limbal plexus of the presumptive Schlemm's canal with the superficial limbal plexus and choroid vessels, it was thus likely that this forming plexus would be perfused with blood, further confirming its origin from the above vessels. In order to detect erythrocytes, wholemounts were viewed at 546 nm excitation wavelength which detected autofluorescence emitted by these cells. Erythrocytes were detected in the superficial plexus (red signal - Figure 3.11a) and in the short segments of the rudimentary plexus (red signal in Figure 3.11b) which were connected to the superficial limbal plexus by two or more putative collector channels. In contrast, erythrocytes were not seen in the short blind-ending sprouts arising from the rudimentary plexus (arrows - Figure 3.11b).

3.4.2 The limbal vasculature at postnatal day 3 (P3).

Schlemm's canal.

The morphology of the putative Schlemm's canal ranged from a rudimentary loose plexus (Figure 3.16a) to one displaying a greater complexity. These plexuses had numerous sprouting and looping vessels (arrowheads and short arrows respectively - Figure 3.16 a, b) and showed evidence of longitudinal coalescence and increased vessel density in the centre of the plexus (long arrow - Figure 3.16b). The general architecture of the plexus was reminiscent of a linked chain forming a loose spiral around its longitudinal axis. The segments of coalesced vessels were longer and more frequent than those seen at P2. Few connections between this plexus to the underlying pars plana were observed (not shown). There were, however, numerous connections to the superficial perilimbal vascular plexus. The diameter of the spiral plexus of the primitive canal in many places was approximately 50 µm at this stage (Figure 3.16a, b).

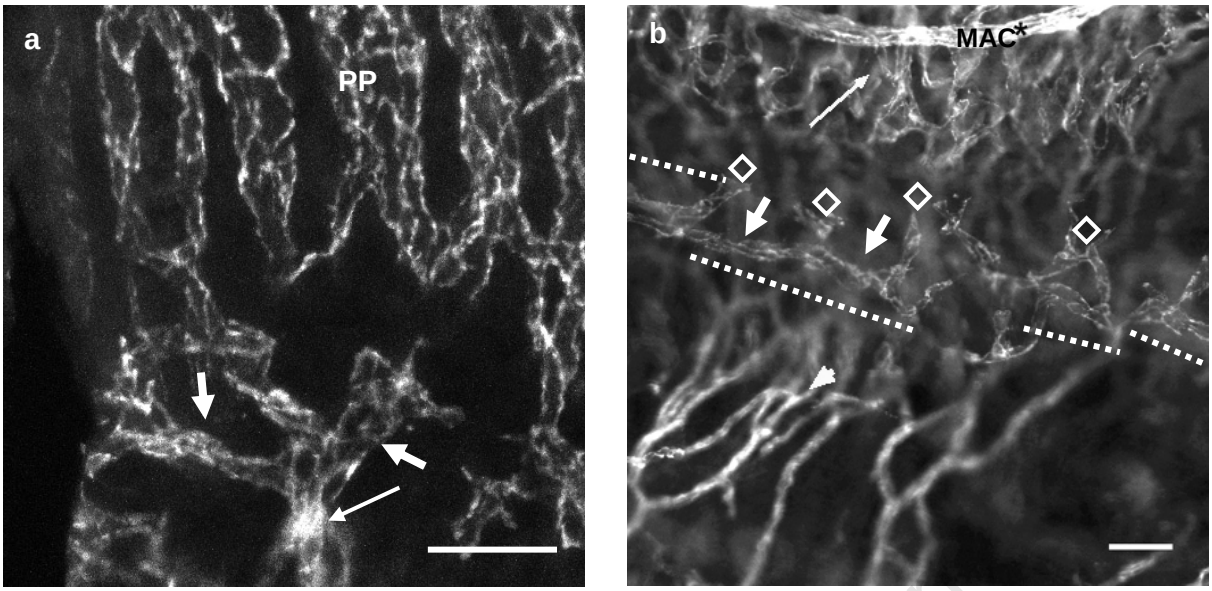

Figure 3.13: Early morphogenesis of Schlemm's canal at P2.

a) An extended focus image of the deep limbus shows vascular sprouts (short arrows) arising from a vessel that is linked to the perilimbal plexus (long arrow). The vascular sprouts are orientated in the circumferential plane at of the limbus and are actually located in a more superficial optical plane than that of the pars plana vessels (PP) (not evident because several optical sections have been merged into a flat image). Thus the branched sprout of the putative canal (arrow head) is not linked to the choroidal vasculature. Bar = 50 µm

b) Several vascular sprouts (diamonds) extend from vascular segments comprising a single vessel (short arrow) in the deep limbus. The arrowhead indicates the vessels of the superficial limbal plexus which are penetrating the limbus. The major arterial circle of the iris (MAC) and ciliary body vessels (long arrow) are located in optical planes below the putative forming Schlemm's canal. Bar = 50 µm

The superficial limbal vasculature.

The superficial plexus was similar to that at P2 with no distinctive arterial and venous phenotypes observed. The plexus appeared to be slightly broader than that seen at P2 (compare Figures 3.10a, b and 3.16c, d). A single, large vessel (long arrow Figure 3.16c) and several narrow vessels (region indicated by curly brackets - Figure 3.16d) linked the superficial perilimbal plexus with the extraocular muscle vascular plexus. The major arterial circle of the iris was deeper in the limbus (white star - Figure 3.16c, d), located anterior to the plexus and ran around the entire circumference of the eye. In certain segments around the limbus, the episcleral plexus of lymphatic vessels showed a few intensely stained secondary valve-like structures at points where the vessel branched (short arrows - Figure 3.16c).

3.4.3 The limbal vasculature at postnatal day 4 (P4).

Schlemm's canal.

By the fourth postnatal day, the presumptive Schlemm's canal was seen as a continuous ring around the limbus. The plexus was more complex than that observed at P3 and there were numerous short intertwining and coalescing vascular loops (short arrows - Figure 3.17a). A greater proportion of the presumptive canal was seen as a wider core vessel from which smaller vascular sprouts and loops projected (arrowheads and short arrows respectively- Figures 3.17a, b). These sprouts and loops emerged mainly from the lateral and superficial face of the wider core vessel (compare Figures 3.16a, b with c). These sprouts generally emanated from the corneal side of the "canal" (long arrows - Figure 3.17a-c). In some sections, the putative canal was similar to that seen at P3. The putative collector channels connected to the primitive canal in two ways. They would link to the outer capillary loops of the "canal" (follow the short arrows from 18 µm - 30 µm in Figure 3.18), or directly to the central canal-like vessel (follow the long arrows from 30 µm - 45 µm in Figure 3.18; see also short arrow in Figure 3.19a). The presumptive Schlemm's canal was also deeper in the limbus than at P2 (compare Figures 3.18 to 3.12). Anastomosis between the presumptive Schlemm's canal and the underlying vasculature of the choroid was not readily observed in any of the mouse eyes in this age group. At this stage, erythrocytes were still seen in the primitive Schlemm's canal (Figure 3.19a) but these cells were sparse compared to their distribution in vessels of the choroid (Figure 3.19b).

The superficial limbal vasculature.

The superficial limbal plexus was generally similar to that seen at earlier time points with the exception of a very complex superficial perilimbal and episcleral plexuses in some regions (long arrow - Figure 3.20a) and the presence of vessels with less branching morphology than the rest of the plexus (arrowhead - Figure 3.20b). These latter vessels had a uniform width (arrowhead - Figure 3.20b) and were lined with fusiform shaped cells (not seen at this magnification). Although showing a branching morphology, their features were similar to that generally seen in the circular limbal artery in adult mice (Figure 3.8). The episcleral lymphatic-like vessels anastomosed with those below the superficial plexus (long arrow - Figure 3.20b). Here for the first time, few putative secondary valves were observed at both the branching points and the linear segments of these vessels (double arrowhead - Figure 3.20b).

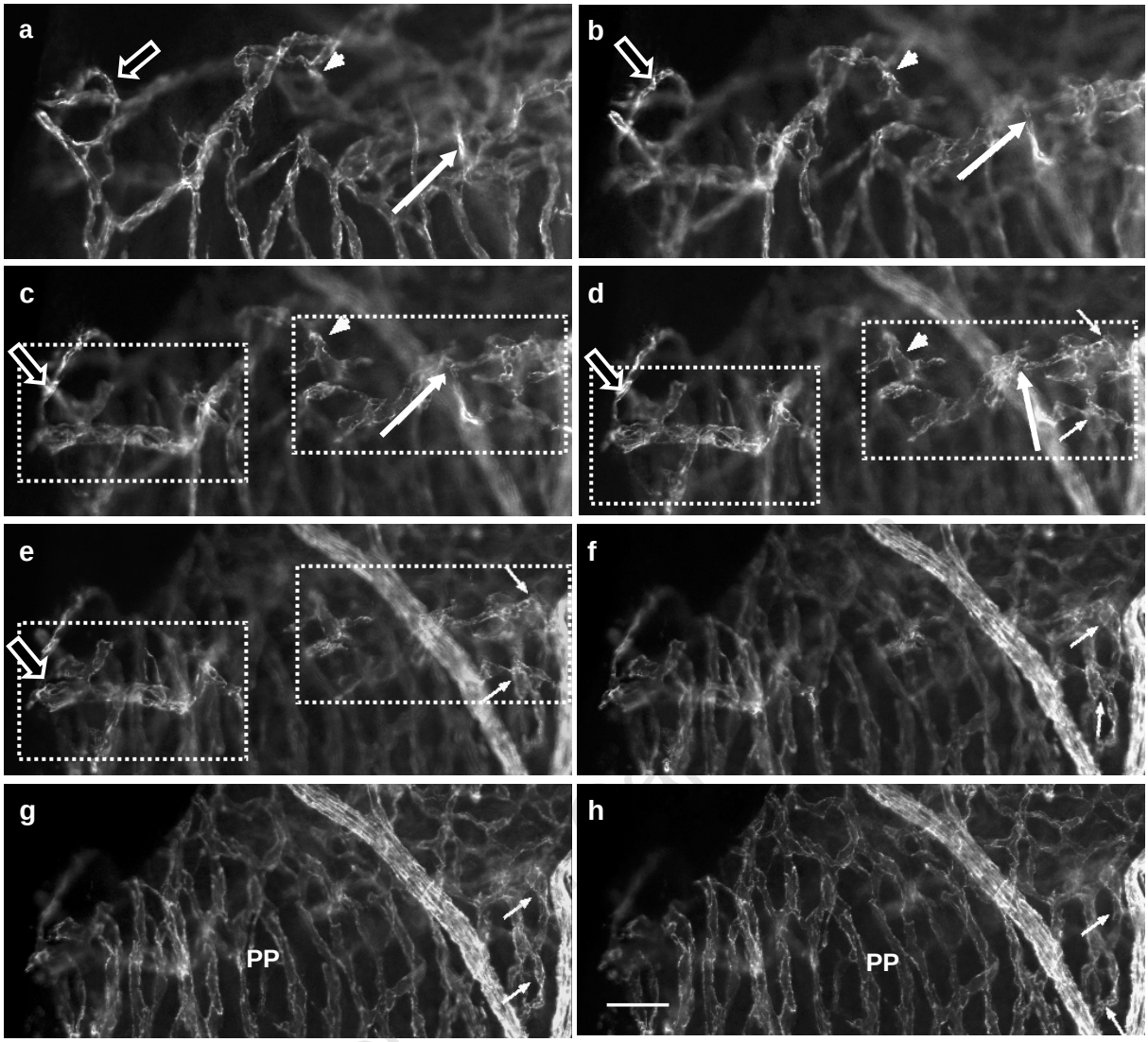

Figure 3.14: Optical sections showing the anatomical association between penetrating limbal vessels and the presumptive Schlemm's canal in the mouse eye at P2.

a-h: Optical sections taken at different depths show different segments of the three-dimensional vascular organisation of the limbus. Bar = 50 µm

a) From the superficial plexus, arched vessels penetrate the limbus at these points (open arrow, long arrow and arrowhead).

b) Vascular segments (dotted line boxes) are located deeper in the limbus. Open arrow, long arrow and arrowhead show the continuation of the penetrating vessels in (a).

c) This optical plane shows that the vascular segment (right box) is connected to two putative collector channels.

d) The two vascular segment (boxes) show a corkscrew-like morphology in the circumferential plane. Small arrows indicate the points from which outgrowths to the deeper limbus arise.

e– h). Small arrows mark the vessels connecting the vascular segment in (d) through a series of optical sections deeper in the limbus than the plane shown in (d). Small arrows in g and h indicate where the connecting vessels link to the vasculature of the pars plana (PP).

3.4.4 The limbal vasculature at postnatal day 6 (6).

Schlemm's canal.

In P6 mice the plexus of the putative Schlemm's canal was wider than seen in the previous postnatal stages. Its morphology varied from a typical canal-like structure to that of a complex plexus surrounding a core vessel (compare Figure 3.21a, b). Numerous blind-ending vascular sprouts (short arrows) were observed on the corneal side of the plexus, whereas closed vascular loops (long arrows) were more prevalent on the posterior side of the plexus (Figure 3.21a). In many regions of the putative canal the plexus had coalesced and had longer segments showing smoother lateral walls (short arrows - Figure 3.21b). The width was variable and ranged from 30-70 µm.

The superficial limbal vasculature:

At this age, parts of the superficial plexus showed a less complex morphology than that seen at earlier postnatal ages (Figure 3.22a). Putative perilimbal veins were more evident (short arrows - Figure 3.22a) and the capillaries of the plexus anastomosed with these veins and putative circular limbal artery (long arrow - Figure 3.22a). The circular limbal artery did not show branching morphology and was lined with fusiform shaped cells (not seen at this magnification). Blind-ending capillaries were also frequently seen in the most anterior regions of the superficial plexus (arrowheads - Figure 3.22a, b). This morphological feature suggests that these vessels could be undergoing regression or sprouting angiogenesis. The episcleral lymphatic-like vessels showed numerous and regularly spaced secondary valve-like structures at points of branching (Figure 3.22b). These valve-like structures were also present in the linear portion of the vessels (arrows - Figure 3.22b) and were similar to that seen in adult mouse eyes.

3.4.5 The limbal vasculature at postnatal day 8 (P8).

Schlemm's canal.

In all mouse eyes, a wide canal-like vessel was seen in the deep limbus and showed features similar to Schlemm's canal seen in adult mouse eyes. The small plexus-like loops seen at the earlier ages were no longer present (Figure 3.23). The width of the canal was generally between 60-75 µm and was more even in width with smoother lateral walls than seen at earlier time points. In optical planes just superficial to the canal, deep intrascleral penetrating vessels were curved and formed a loose spiral-like form before joining to the canal (arrows - Figure 3.23a). Occasionally, segments of the canal split into two smaller vessels (arrowheads - Figures 3.23b) or branched into

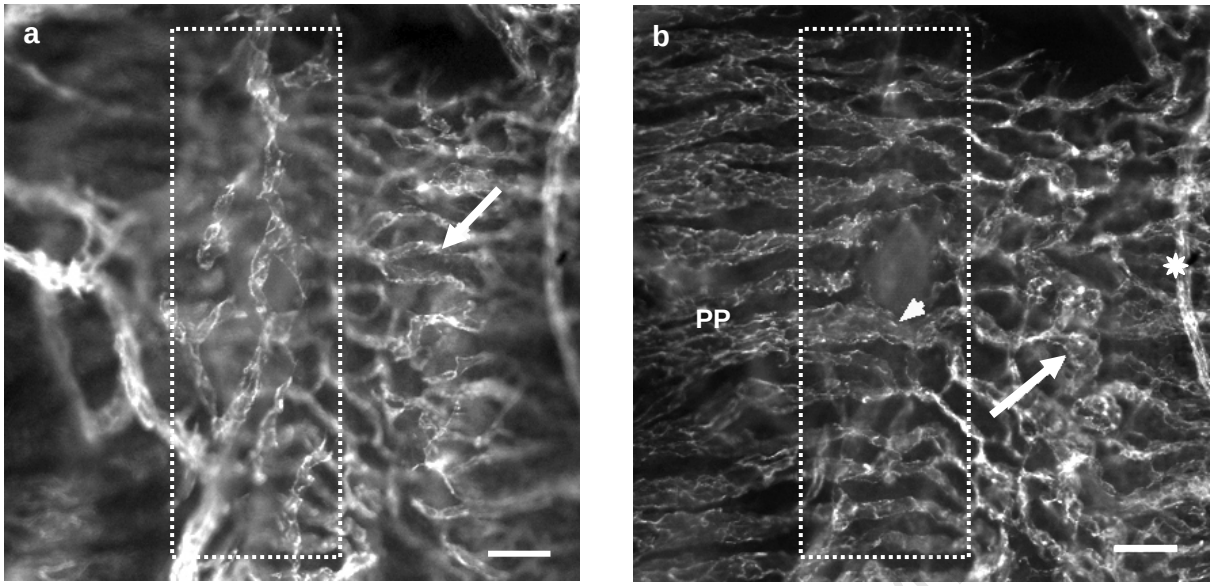

Figure 3.15: The vascular relations of the ciliary body and primitive Schlemm's canal at P2.

a) An extended focus image of a few optical sections of the deep limbus shows s rudimentary plexus of the presumptive Schlemm's canal (dotted line box) is located close to but superficial to the vasculature of the pars plana (PP) (seen in Figure 3.14b). The plexus is located posterior to the blood vessels in the basal region of the ciliary body (long arrow).

b) The deepest optical plane of the same segment of the limbus shows palisade -like vessels of the pars plana (PP) which link (arrowhead) to the sinusoidal-like vessels in the processes of the ciliary body (long arrow). The major circular artery of the iris is visible to the right of the image (star). Bar = 50 µm

a short plexus (short arrows – Figures 3.23c, d). Optical sections imaged at different planes through the canal in Figure 3.23, showed that a canal-like morphology was consistent the deeper optical planes shown in Figures 3.23b-c, thus verifying that the structure of the canal was a generally single broad channel. Anastomosis between Schlemm's canal and the choroid vasculature was detected in only one of the twelve mouse eyes studied in this age group (not shown).

The superficial limbal vasculature.

The vasculature of the superficial limbal plexus showed a clearer morphological distinction between arteries and veins than seen in earlier postnatal ages (Figure 3.24a, b). For example the anterior ciliary artery (ACA), circular limbal artery (short arrows) and perilimbal veins (long arrows) are clearly distinguishable from the large veins (Epi) draining the limbal plexus (Figure 3.24a). The anterior ciliary artery branches in the episclera just anterior to the vascular plexus of the external ocular muscles (arrowhead - Figure 3.24a) to give rise to one segment of the narrow circular limbal artery (short arrow - Figure 3.24a), the width of which remains constant around the

limbus. At this stage, the first evidence of an association between the circular limbal artery and the long posterior ciliary arteries was seen (not shown for P8 but similar to P10 - see Figure 3.25b). The endothelial cells were typically fusiform in shape (not shown). As in the adult mouse, radial branches (long arrows) off the perilimbal vein (short arrow) and circular limbal arteries (arrowhead) give rise to the plexus of the corneal arcades (Figure 3.24b). Posterior episcleral vessels (Epi - Figure 3.24b), connecting to the perilimbal veins, were generally observed near regions where the vasculature of the external ocular muscles were located. Although the superficial limbal plexus was still complex, the most anterior or distal region (i.e. corneal side) had a more defined arcade-like morphology (stars - Figure 3.24b). Similar to that seen at P6, short blind-ending vessels (diamonds – Figure 3.24a, b) of the most anterior arcades were present, and most likely indicating regression of these vessels. The morphology of the episcleral lymphatic vessels was similar to that seen in P6 mice (stars - Figure 3.24a).

3.4.6 The limbal vasculature at postnatal day 10 (P10).

Schlemm's canal.

At P10, Schlemm's canal showed a morphology similar to that seen P8 (Figure 3.25a). The canal was located approximately 50 µm below the superficial limbal plexus (not shown). The lateral walls of the canal were smooth in most segments of the canal and the morphology of the canal was similar to that seen in adult mice. There were wide segments of width 80-90 um with occasional narrowing (arrow - Figure 3.25a), bifurcations and plexus formations (not shown). As seen at P8, this morphology was also associated at times with a deep simple limbal plexus on its superficial surface (not shown). Similar to that seen in adult mice, the single channel would occasionally give way to a small plexus which was organised in a loose spiral arrangement (not shown).

The superficial limbal vasculature.

The superficial limbal plexus at this stage was unmistakably less complex than postnatal periods in that the number of loops was fewer (Figure 3.25b). Signs of possible vessel regression (arrows-Figure 3.25b) at the anterior/corneal edge were still evident. The circular limbal artery (long arrow) was seen as penetrating the limbus to join to a branch of the long posterior ciliary artery (arrowhead) (Figure 3.25b).

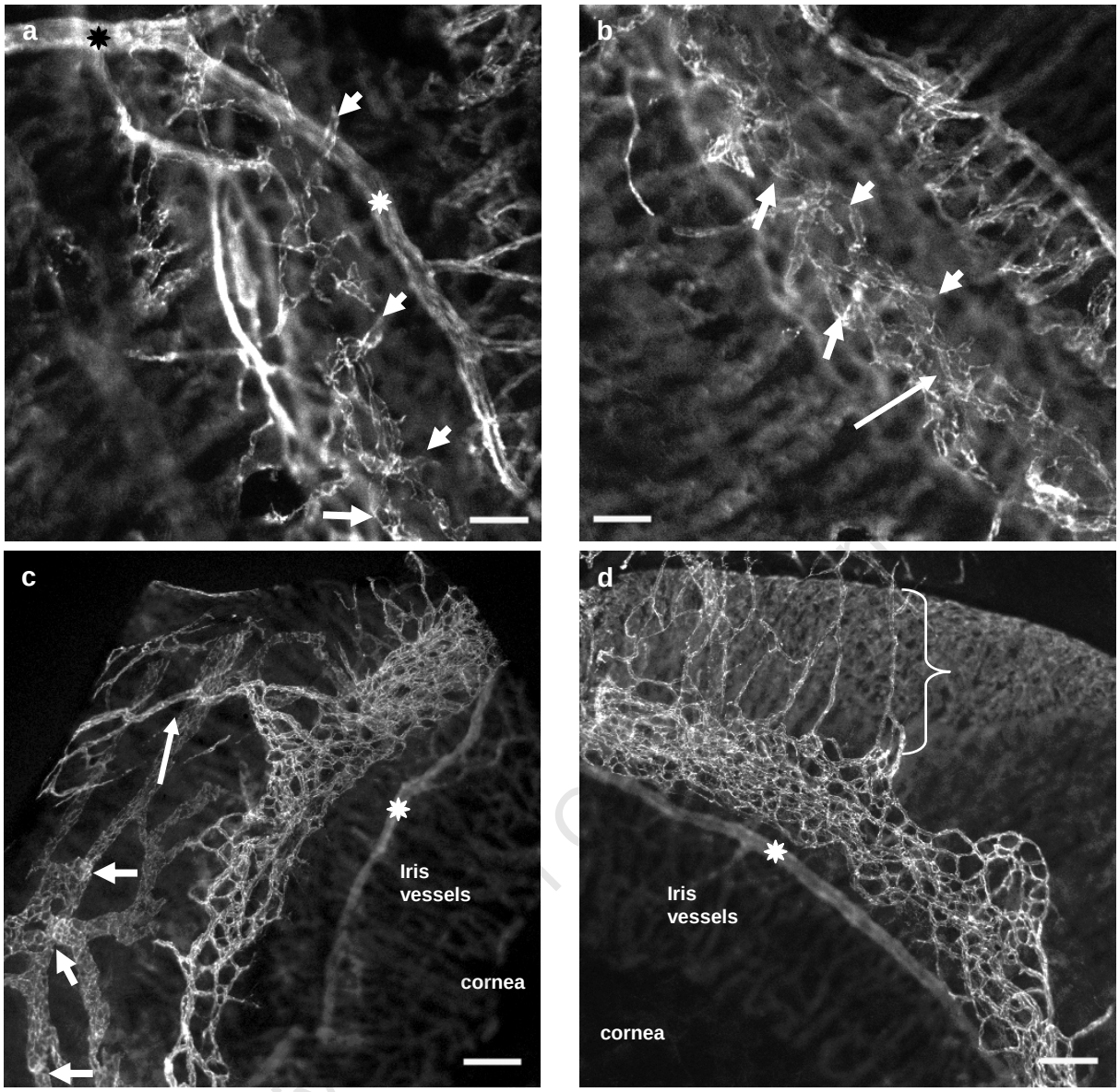

Figure 3.16: The limbal vasculature at P3.

a) An optical section of the deep limbus shows short vascular segments located above and posterior to the major circular artery of the iris (white star) and the long posterior artery (black star). Arrow indicates a penetrating limbal vessel linking to the forming plexus. Bar = 50 µm

b) The deep limbal plexus of the putative Schlemm's canal shows more developed segments of simple anastomosing vessels with evident of coalescence (arrow). Bar = 50 µm

c) The superficial plexus is dense, complex and is broad. It is linked to the vasculature of the exterior ocular muscles by a large tortuous vessel (long arrow). Large episcleral lymphatic-like vessels showing a few densely stained segments that resemble secondary valves (short arrows) seen in the adult mouse eye, are present at the points of branching. White star = major circular artery of the iris. Iris vessels are in the deepest plane of the wholemount. Bar = 100 µm

d) A broad superficial plexus with undifferentiated vasculature has numerous radial episcleral vessels associated with the exterior ocular muscles (bracketed region). White star = major circular artery of the iris. Iris vessels are seen in the deepest plane of the wholemount. Bar = 100 µm

3.4.7 The limbal vasculature at postnatal days 12 (P12) and 14 (P14).

Schlemm's canal.

At P12, Schlemm's canal was a distinctive single canal in most sections of the limbus. It was generally wider than the canal seen at earlier time-points with a diameter of about 90-100 µm (Figures 3.26a-c). In some mouse eyes, its width remained constant throughout most of the limbus. In other eyes, the morphology was more variable, ranging from a wide even canal to a twisted narrow vessel and a small capillary-like plexus. A few diverticuli (short arrow - Figure 3.26a) emerged from the anterior (corneal side) wall of the canal. In all of the twelve eyes studied at P12, there was at least one section of the canal that gave way to a short segment containing a capillary-like plexus. Of note at this stage were the large endothelial cells in some regions of the canal as indicated by the peripheral distribution of PECAM-1 (Figure 3.26b). These large cells were not necessarily present at regions of the canal where collector channels (arrows - Figure 3.26c) emerged from the canal to link to the overlying plexus (arrowheads - Figure 3.26c). At P14, the morphology of Schlemm's canal was similar to that seen at P12 (Figure 3.26d). Collector channels were still numerous and often emerged from raised sections of the outer wall of the canal (Figure 3.26e) and traversed parallel to the canal for some distance (Figure 3.26f) before rising through the limbus to anastomose with the superficial perilimbal plexus. These long collector channels are similar to those seen in the adult mouse eye (see inset - Figure 3.5).

The superficial limbal vasculature.

The morphology of the circular limbal veins and artery in the superficial limbal plexus in P12 and P14 mice was similar to that seen in the adult mouse eye. There was a single circular limbal artery (star in Figure 3.27a, b) that supplied the corneal arcades via radial branches. As seen in adult mice, the circular limbal artery was not a continuous perilimbal vessel, but made up of segments. Occasionally the circular limbal artery terminated in the episcleral plexus (open star - Figure 3.27b). The perilimbal veins (mainly one, and occasionally two) were more clearly defined than at earlier time points (PLV - Figure 3.27a, b). The corneal arcades were less complex than those observed at P10 but still more complex than those seen in the normal adult ICR mouse eye (See Figures 3.2 and 3.8). The arcades were more pronounced and formed longer loops (short arrows – Figure 3.27a, b). The arcades anastomosed with the circular limbal artery and the perilimbal veins. In some regions around the limbus very few blind-ending vessels were observe (Figure 3.27a). In other regions, blind-ending vessels (grey arrows - Figure 3.27a), indicating vessel regression, were present. Interestingly, signs of vessels regression were not observed in the plexus lying posterior to the perilimbal veins (Epi - Figure 3.27a, b). Episcleral lymphatic vessels were

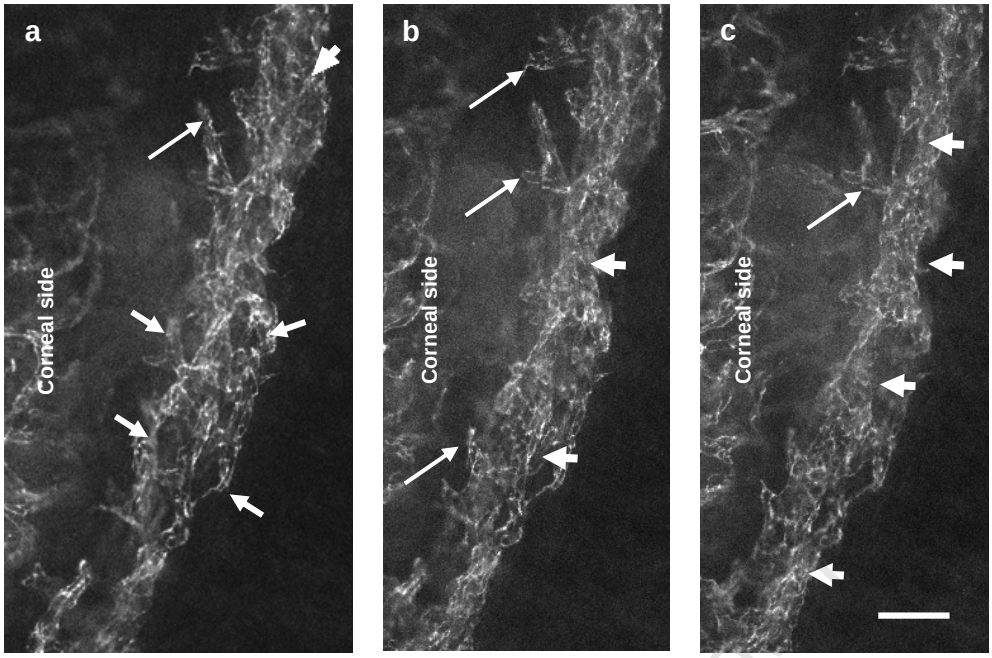

Figure 3.17: Optical sections showing different planes of the primitive Schlemm's canal plexus in mice at P4.

a) The most superficial plane of the deep limbal plexus (putative Schlemm's canal) shows several loops (short arrows) sprouts (long arrows) and a fused wider core (arrowhead).

b) A deeper optical plane show the central region of the plexus has fused forming a continuous vessel from which several lateral sprouts emerge.

c) The deepest optical plane of the deep limbal plexus shows a wider core (arrow) and no plexus formation as seen in Figure 3.17a.

Bar = 50 µm

similar to those observed in P6 –P10 mouse eyes. As noted previously, the perilimbal lymphatic vessel was broad and located below the corneal arcades (open arrow - Figure 3.27a). Arising from this vessel were prominent arcades (double arrowhead - Figure 3.27a) and blind-ending vessels (arrowheads - Figure 3.27b) that penetrated the cornea. Putative secondary valves were observed at regular intervals only along the episcleral lymphatic vessels at points of branching and straight sections of the vessels (long arrows - Figure 3.27a, b).

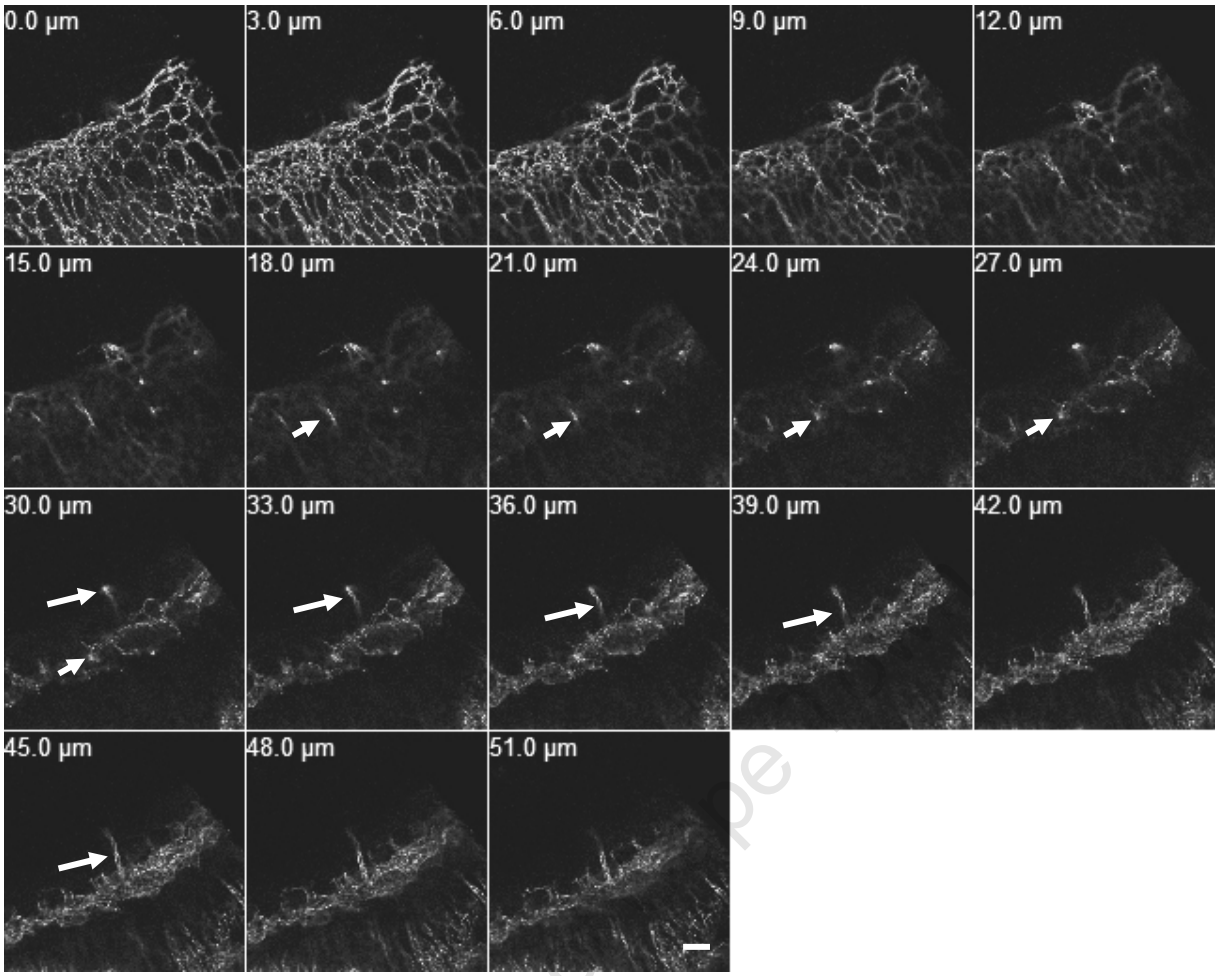

Figure 3.18: Gallery of optical sections of the limbus at P4.

Optical sections were captured at 3 µm intervals through the limbus starting the superficial perilimbal plexus (0.00 µm) and ending at the deepest segment of the deep limbus plexus (51.0 µm). Short arrow indicates a putative collector channel which eventually anastomoses with a looped vessel associated with the outer portion of the primitive Schlemm's canal (seen at 30.0 µm). Long arrow indicates a putative collector channel that joins the fused segment of the putative Schlemm's canal at 45-51.0 µm.

Bar = 50 µm

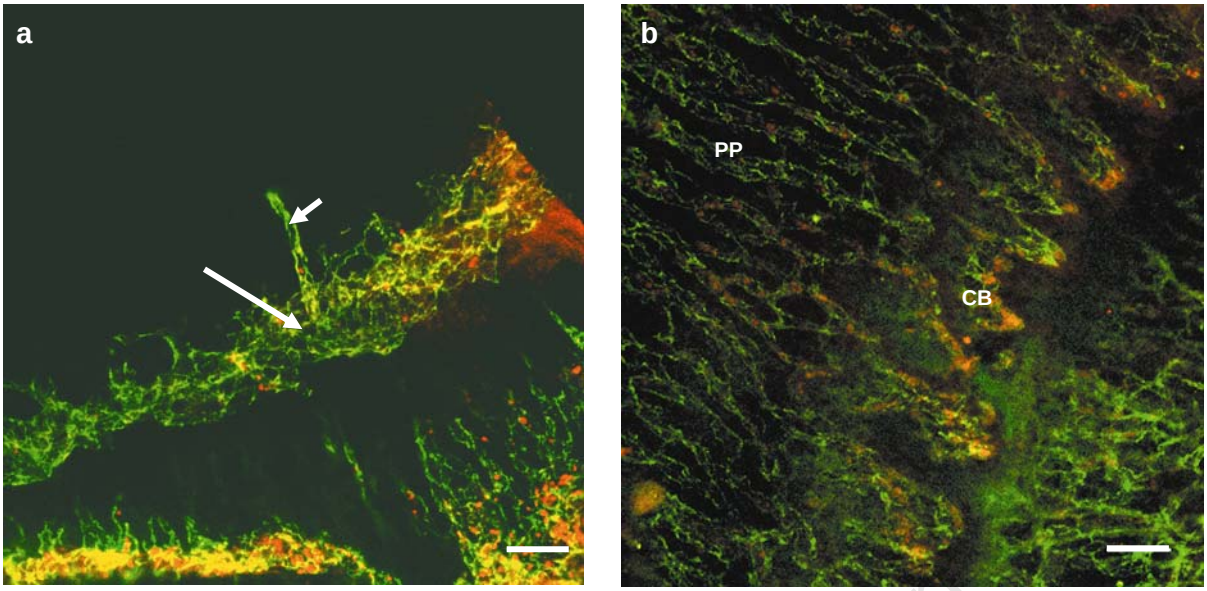

Figure 3.19: Merged image showing PECAM-1 stained vessels (green) and autofluorescence of erythrocytes (red) in the limbal vessels at P4.

a) The deep limbal plexus and core vessel of the putative Schlemm's canal (long arrow) contains few erythrocytes (red structures). A putative collector channel (short arrow) is seen linking to the core of the "canal"
Bar = 50 µm

b) The choroid vessels of the pars plana (PP) and ciliary body processes (CB) contain numerous erythrocytes (red signal). Bar = 50 µm

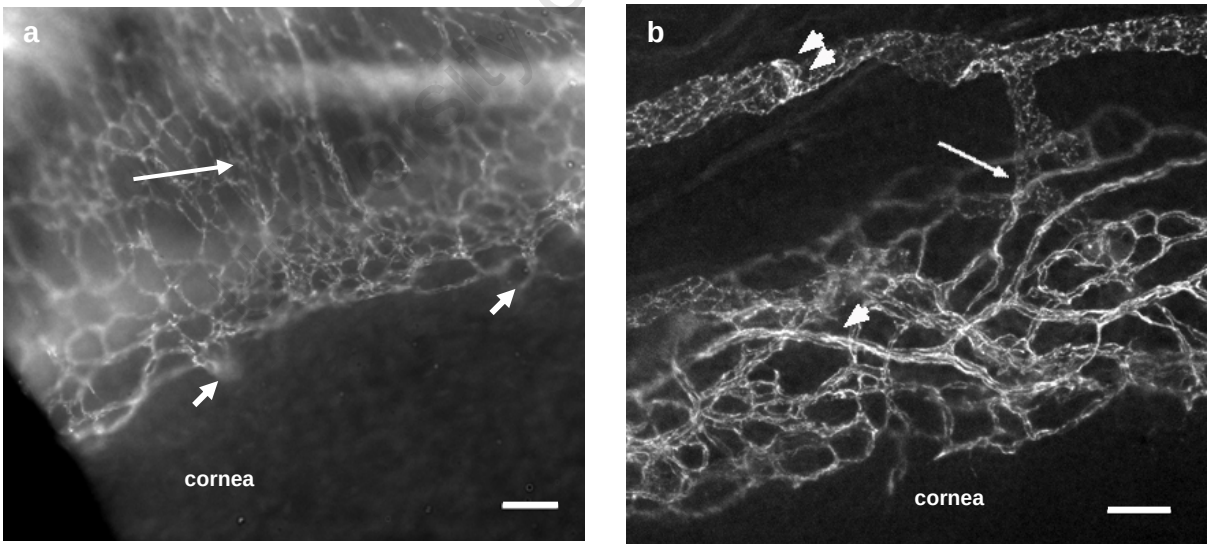

Figure 3.20: The superficial limbal plexus at P4.

a) The superficial limbal plexus is still complex, and vasculature phenotypes are morphologically undifferentiated in the superficial limbal plexus. Putative collector channels (arrows) are seen penetrating the limbus.
Bar = 100 µm

b) Thin branched vessels of regular width show fusiform shaped endothelial cells (arrowhead). An episcleral lymphatic-like vessel showing secondary valve-like regions in an unbranched region of the vessel (double arrowhead) is linked to large vessels underlying the superficial vascular plexus.
Bar = 50 µm

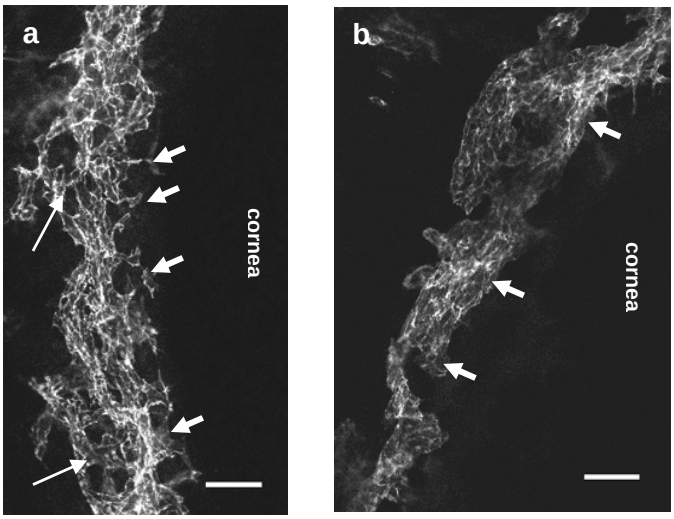

Figure 3.21: The primitive Schlemm's canal at P6.

a) A central fused vessel shows several outgrowths/sprouts (short arrows) and closed vascular loops (long arrows). Bar = 50 µm

b) Fused segments of the canal show variations in width and have fewer sprouts (short arrows).
Bar = 50 µm

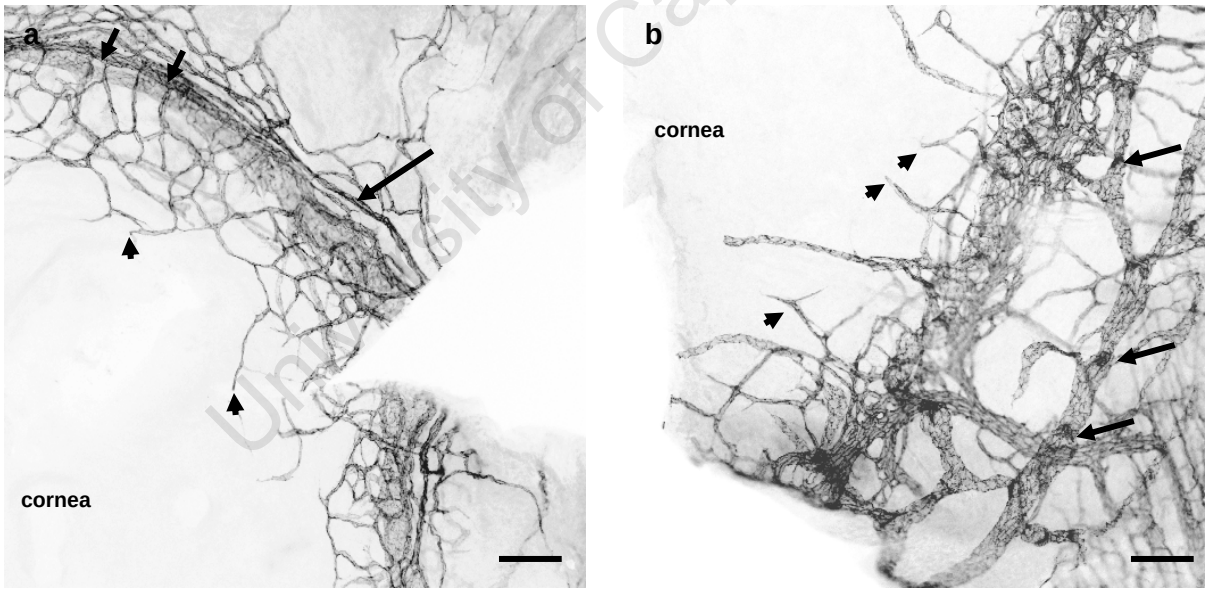

Figure 3.22: The superficial limbal plexus at P6.

Images have been inverted to illustrate a better contrast of the vasculature (dark) against a light background.

a) The superficial limbal plexus is has fewer capillary loops compared to Figure 3.16c, d and 3.20. Short arrows indicate the putative perilimbal vein and sites of anastomoses with the limbal capillaries. A thinner vessel (long arrow) has a similar morphology to the circular limbal artery seen in adult mouse eyes. Blind-ending blood vessels penetrate the cornea (arrowheads). Bar = 100 µm

b) The episcleral lymphatic vessels show numerous secondary valves along the linear segments of the vessel (short arrows). Numerous blind-ending vascular sprouts are seen in the cornea (arrowheads).
Bar = 100 µm

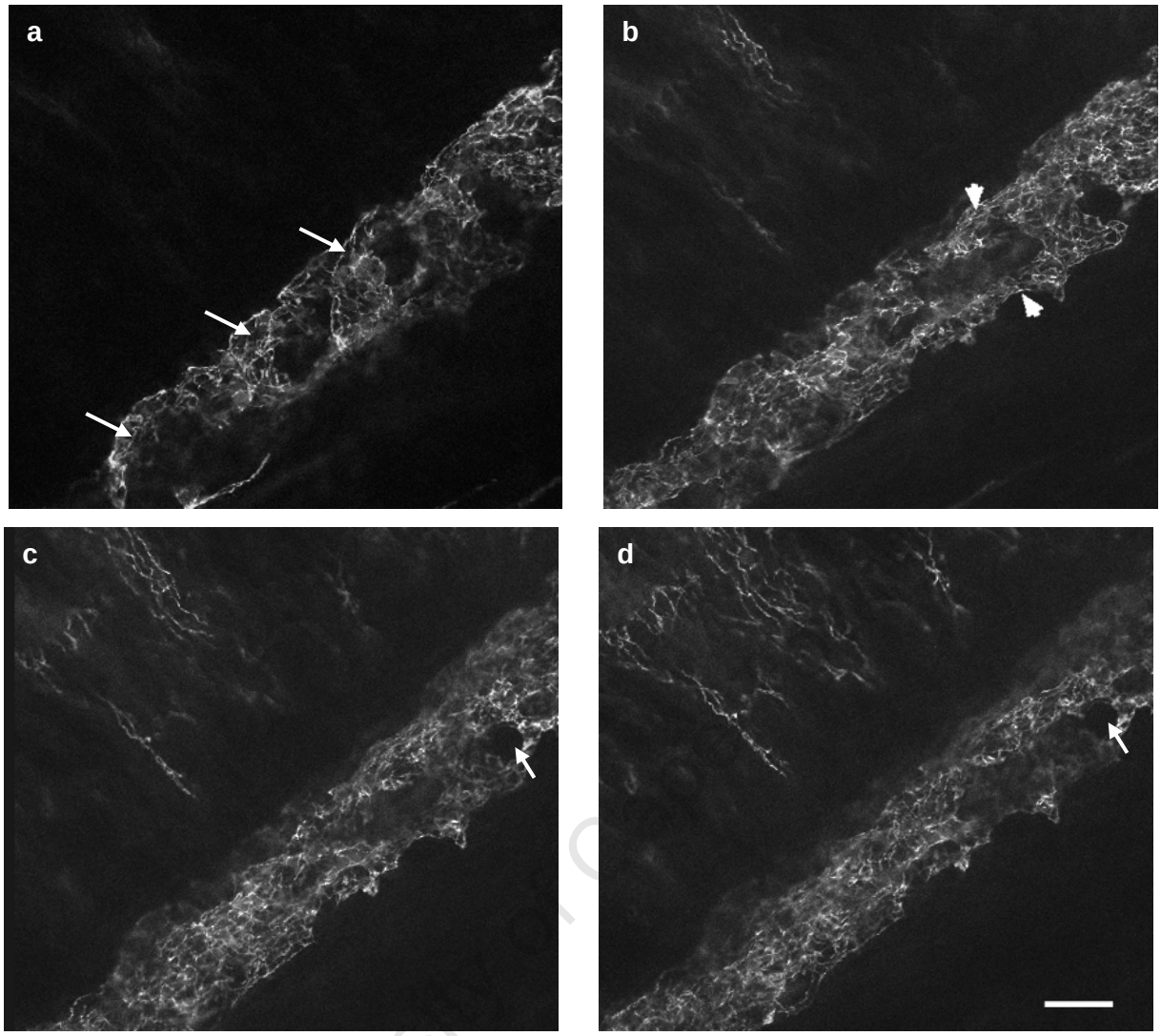

Figure 3.23: Optical sections of a z-stack of the putative Schlemm's canal at P8.

a) An optical plane above the outer wall of the putative Schlemm's canal shows a loose spiral-like formation of the penetrating limbal vessels that terminate in the canal (arrows).

b-d) Optical sections taken at consecutively deeper planes in the limbus show that the morphology of the putative Schlemm's is canal-like throughout its entire thickness and is similar to that of adult mice. Arrowheads indicate where the canal has spilt into two vessels. Short arrows (c, d) indicate the formation of a short plexus.

Bar = 50 µm

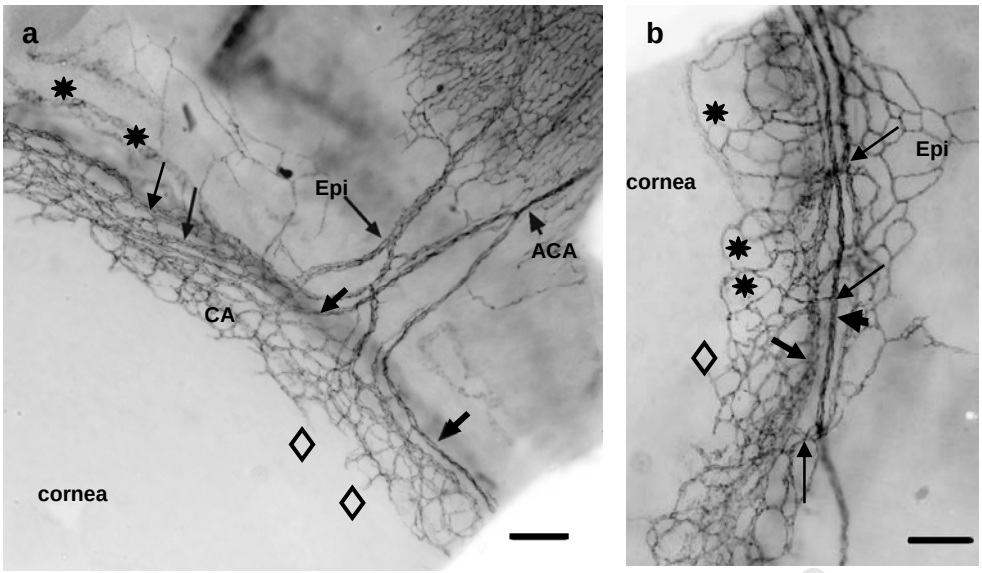

Figure 3.24: The superficial limbal plexus at P8.

Images have been inverted to illustrate a better contrast of the vasculature (dark) against a light background.

a) Veins (long arrow) and arteries (small arrows and arrowhead) vessels are morphologically distinguishable. The anterior ciliary artery (ACA) branches near the exterior ocular muscle plexus to give rise to the circular limbal arteries (small arrows). CA = corneal arcades; Diamonds = blind-ending vascular sprouts; Epi = episcleral veins. Stars indicate the episcleral lymphatic vessels. Bar = 100 µm

b) A single limbal artery (arrowhead) and perilimbal vein (small arrow) form anastomoses with the corneal arcades and episcleral plexus (Epi). Diamonds = blind-ending vascular sprouts. Stars indicate the corneal arcades. Bar = 100 µm

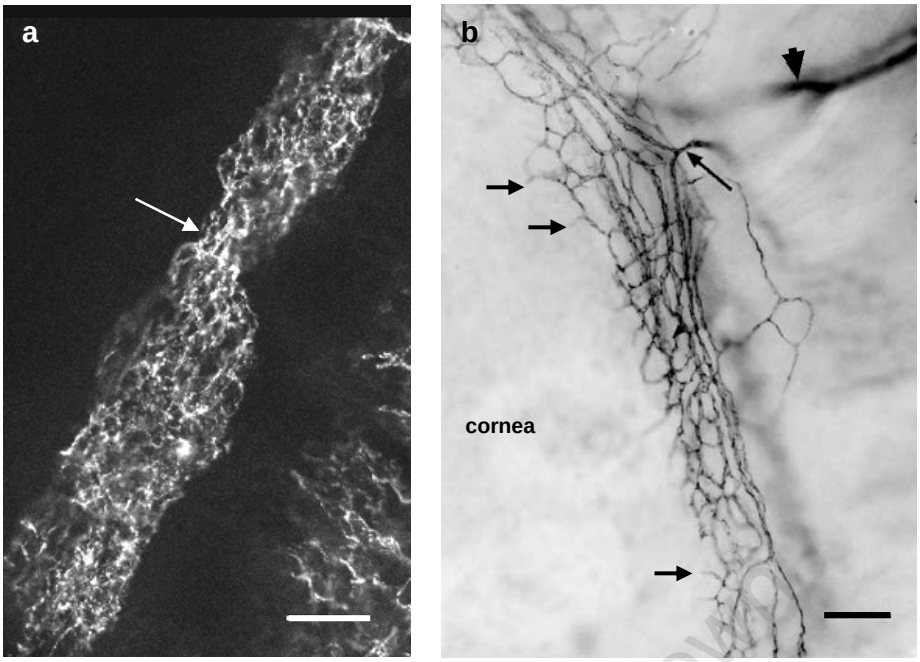

Figure 3.25: Schlemm's canal and the superficial limbal vasculature at P10.

a) The Schlemm's canal of adult-like morphology is shown. The optical section is approximately 50 µm below the superficial limbal plexus. Long arrow indicates a narrow segment of the canal. Bar = 50 µm

b) An inverted contrast image shows less dense packing of the superficial limbal plexus. Numerous branched blind-ending vessels arising from the corneal arcades are present (short arrows). Two branches of the circular limbal artery meet (long arrow) to penetrate the limbus in the vicinity of the branching long posterior artery (arrowhead). Bar = 100 µm

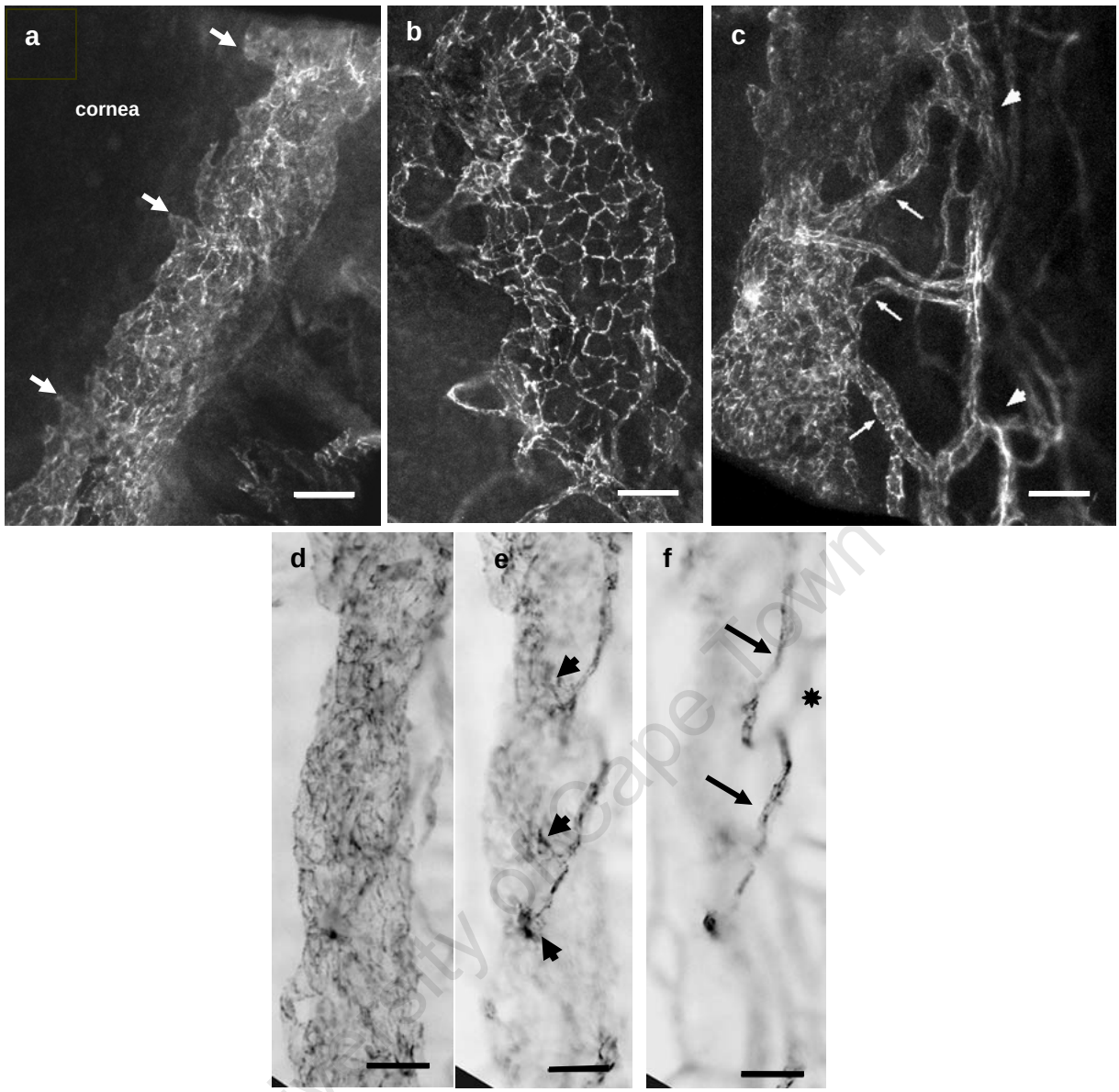

Figure 3.26: The morphology of Schlemm's canal at P12 and P14.

a-c) Extended focus images generated from optical sections through the deeper regions of the limbus and Schlemm's canal at P12. Bar = 50 µm

a) Schlemm's canal shows a mature morphology throughout the limbal circle. The anterior and posterior walls were often smooth with few small diverticuli (small arrows) emerging from the anterior wall.

b) PECAM-1 staining on the cell periphery shows a segment of the canal with large endothelial cells.

c) Numerous collector channels (long arrows) connect Schlemm's canal to the deep limbal plexus (arrowheads) just superficial to the canal. The endothelial cells are not enlarged in this region.

d-f) A series of optical sections of Schlemm's canal at P14. Bar = 50 µm. Inverted images.

d) The deepest optical plane shows a mature morphology of the canal.

e) Collector channels (arrowheads) arise from raised sections of the outer wall of the canal.

f) In an optical plane more superficial than that shown in (e), the narrow collector channels (arrows) can be seen travelling parallel to the canal. Star indicates vessels in the optical plane of the superficial limbus.

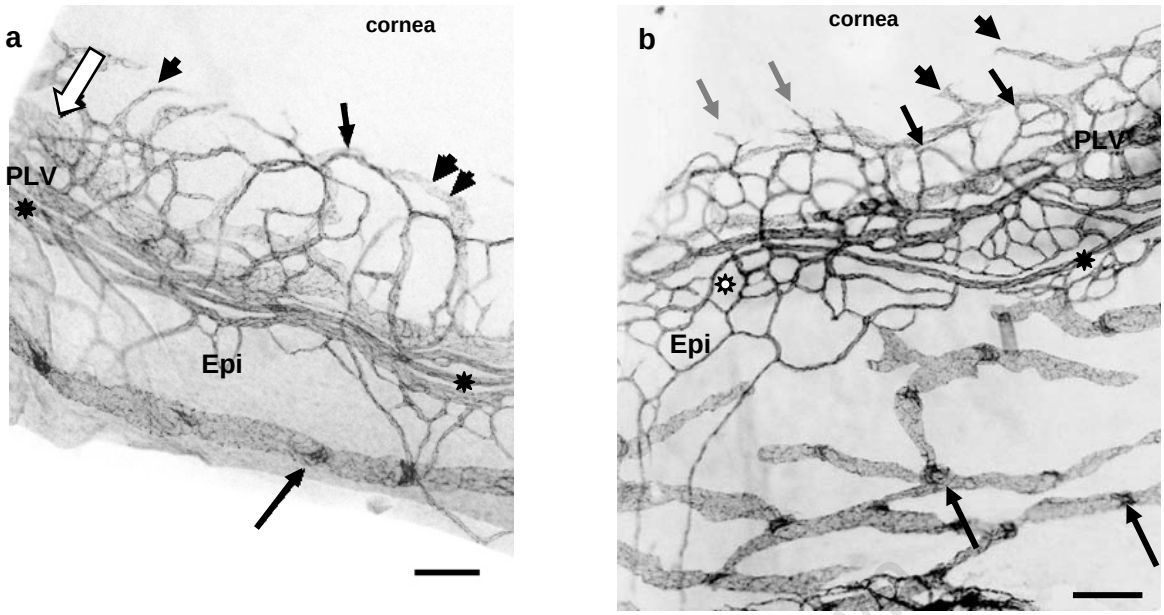

Figure 3.27: The superficial limbal vasculature at P12 and P14.

Images have been inverted to illustrate a better contrast of the vasculature (dark) against a light background.

a) P12: The corneal arcades (short arrow) are simple and penetrate deep into the cornea. Blind-ending lymphatic vessels (arrowheads) and lymphatic vessel arcades (double arrowhead) branch off the perilimbal lymphatic vessel that lies deeper in the limbus (open arrow). Long arrow indicates valve-like structure in the episcleral lymphatic vessel. Epi = a rudimentary episcleral plexus. The circular limbal artery (black stars) is continuous in this region. Bar = 100 µm

b) P14: Short arrows indicate the corneal arcades. Grey arrows indicate possible sites of vessel regression. Arrowhead shows blind-ending extensions of lymphatic vessels. Episcleral circumferential vessels have valve-like structures at points of branching and also at regular intervals along straight segments of the episcleral lymphatic vessels (long arrows). The plexus located on the posterior side of the perilimbal veins (Epi) does not show signs of vessel regression. The circular limbal artery (black star), terminates in the episcleral plexus as indicated by the black and white star. Bar = 100 µm

3.5 A quantitative analysis of the posttrabecular aqueous outflow pathway and the superficial limbal vasculature in normal (WT), *Foxc1*$^{+/-}$ and *Bmp4*$^{+/-}$ mice.

Having established a method for viewing wholemounts of the murine anterior ocular segment, and having described the three-dimensional anatomical organisation of the limbal vessels and Schlemm's canal, the next aim was to use this information to explore the effects of certain developmental genes on the overall micro architecture of the aqueous drainage vessels.

Abnormalities of Schlemm's canal, such as reduced width or total absence of the canal have previously been reported in *Foxc1*$^{+/-}$ and *Bmp4*$^{+/-}$ mice (Chang et al., 2001; Smith et al., 2000). These authors have reported that the severity of abnormalities of the canal and structures of the iridocorneal angle in *Foxc1*$^{+/-}$ and *Bmp4*$^{+/-}$ genotypes differed amongst mouse strains. However, because these observations were based on analysis of histological sections, the overall three-dimensional features of the canal and the anatomical relationships between the canal and limbal vessels could not be described. Therefore, in order to determine the full extent of differences in Schlemm's canal architecture and to plot the relationship to collector channels and the limbal vasculature in mice with different genotypes, a morphological comparison and statistical analysis was conducted. The genotypes included wildtype mice on two different backgrounds: C57BL/6Jx129 (pigmented animals) and ICR (albino) mouse strains; *Foxc1*$^{+/-}$ mice on both backgrounds, and *Bmp4*$^{+/-}$ mice on the ICR background. Most wildtype and *Foxc1*$^{+/-}$ and *Bmp4*$^{+/-}$ mice used in this study were old breeders that were no longer required for the breeding programme at the animal unit, UCT. Mice were categorized into the following age groups: 6-8 months, 10-12 months and 15 months. Unfortunately it was not possible to obtain both strains and genotypes for all three of the above age groups. The mouse strains and genotypes, and, the number of eyes used in each age group are indicated in below.

Age group (months)	Strain	Genotype	Number of eyes (n)
6-8	ICR	Wildtype (WT)	12
6-8	C57BL/6Jx129	Wildtype (WT)	10
6-8	C57BL/6Jx129	*Foxc1*$^{+/-}$	18
10-12	ICR	Wildtype (WT)	14
10-12	ICR	*Bmp4*$^{+/-}$	12
10-12	ICR	*Foxc1*$^{+/-}$	16
10-12	C57BL/6Jx129	Wildtype (WT)	16
10-12	C57BL/6Jx129	*Foxc1*$^{+/-}$	8
15	C57BL/6Jx129	*Foxc1*$^{+/-}$	12

Anterior segments were immunostained with rat anti-murine PECAM-1 and anti-rat Alexa 488 secondary antibodies. Images of the entire circumference of Schlemm's canal were captured (see section **2.3**), processed (see section **2.4**), and the width of the canal was measured at regular intervals using a morphometric grid overlay (see section **2.5**). For the analysis of the perilimbal/episcleral plexus, images were captured and processed as above, and the penetration of the corneal arcades into the cornea, and the complexity of the arcade plexuses were measured (see section **3.5.2**). Collector channels were counted and the total per mouse eye recorded (see sections **2.3** and **3.5.5.4**). In order to test for significance, the raw data from all the above measurements were subjected to analysis of variance (ANOVA) (see section **2.6)**. For the purpose of clarity, the data from the measurements of the width of Schlemm's canal (**SC width**), the number of collector channels, the distance penetrated into the cornea by the corneal arcades (**CA length**) and the number of vascular loops formed in the corneal arcade plexus (**complexity**) are presented in the following formats:

- In bar charts representing the means (or medians) and standard error of the means (SEM) in C57BL/6Jx129 mice (yellow-orange bar cluster) and in ICR mice (blue bar cluster) (Figures 3.28, 3.32, 3.34 and 3.35).
- In Tables 1-3, where the number of eyes studied (n (eyes)), the means, SEM, and significance (p-values) determined by ANOVA are listed. For **SC width** and **CA length**, the total number of measurements per group (n (data points) is given in the tables. The different age groups, strains and genotypes are assigned to different columns.

In order to establish whether the effects determined by ANOVA are significant, further analysis was done to test for differences as follows:

- age and genotype within the C57Bl/6Jx129 (C57) strain (**pink** cells in Tables 1-3)
- age within the C57 strain and *Foxc1*$^{+/-}$ genotype (**dark green** cells in Tables 1-3)
- genotype within the 10-12 month age group of the ICR strain (**blue** cells in Tables 1-3)
- age (excluding the 15 month age group) and strain within the wild type (WT) genotype (**yellow** cells in Tables 1-3), and,
- strain and genotype (*Foxc1*$^{+/-}$) within the 10-12 month age group (**pale green** cells in Tables 1-3).

The above categories are listed in column 1 in Tables 1-3 and the significance determined between groups (columns 2-9) is compared in cells of the same colour code in the row of that category. In each of the above categories, p-values are followed by either *, ** or ***. These p-values relate to the significance between groups containing the corresponding *, **, or *** in the same colour-coded cells on the same row. P-values which are significant are stated in the text that follows below and in

red font in Tables 1-3, whereas those values that are not significant are only stated in black font in Tables 1 -3. For the remainder of the text below, the C57BL/6Jx129 mouse strain will be referred to as C57.

3.5.1 A quantitative analysis of the aqueous vessels in normal (WT), *Foxc1*$^{+/-}$ and *Bmp4*$^{+/-}$ mice.

3.5.1.1 The width of Schlemm's canal in normal (WT), *Foxc1*$^{+/-}$ and *Bmp4*$^{+/-}$ mice.

The overall impression seen in Figure 3.28 is that the *Foxc1*$^{+/-}$ mice (yellow and blue brick-patterned bars) and *Bmp4*$^{+/-}$ (darker blue speckled bar) have narrower mean widths of Schlemm's canal compared to wildtype (WT) mice (plain yellow and blue bars). What is not clear is whether strain and age have an effect on the mean SC width. ANOVA, performed on the entire data set where all coefficients of effects were taken into account (looking at the whole model), showed that the interactions of strain and age, and genotype were significant ($p > 0.0001$). In order to determine where these effects were significant, further analysis was done to test for differences between the mean SC widths within the above designated groups: Although the mean SC width was slightly higher in left eyes (69.58 µm) compared to right eyes (67.72 µm), ANOVA showed that the mean SC width between left and right eyes was not significantly different ($p= 0.4007$). Therefore, the means stated in Table 1 reflect the combined means of left and right eyes.

In C57 mice (yellow-orange coloured bar cluster – Figure 3.28), *Foxc1*$^{+/-}$ mice (brick-patterned bars) had lower mean SC widths in than that of WT mice (plain yellow coloured bars). ANOVA showed that within this strain, the interaction of age (6-8 and 10-12 month) and genotype (WT and *Foxc1*$^{+/-}$) was not significant. However, genotype alone had a significant effect on the width of Schlemm's canal in C57 mice. WT mice had significantly higher mean SC widths (77.44 µm and 74.59 µm) than *Foxc1*$^{+/-}$ mice (58.69 µm and 63.97) ($p = 0.0000$* compared to * respectively - see pink cells in Table 1). Within each genotype (WT or *Foxc1*$^{+/-}$), age had no effect on the mean SC width in this strain (see pink and dark green cells in Table 1). The above trend of a narrower canal in *Foxc1*$^{+/-}$ mice on this background is similar to that reported on other mouse strains (Chang et al., 2001; Smith et al., 2000).

In contrast, the trend shown by ICR mice (blue bar cluster – Figure 3.28) was less clear. Whilst the mean width of the canal in 6-8 month wild type mice (pale plain blue bar) was the highest of all groups in this study (84.98 µm), that of the10-12 month WT group (plain darker blue bar) was

markedly lower (56.59 µm) than in *Bmp4*$^{+/-}$ (70.76 µm - darker blue speckled bar) and *Foxc1*$^{+/-}$ (68.55 µm - darker blue brick-patterned bar) mice in the same age group. Within the ICR strain, there were no age-matched *Foxc1*$^{+/-}$ and *Bmp4*$^{+/-}$ genotypes for the 6-8 month group. Therefore the 6-8 month group was excluded from the ANOVA when testing for the effect of genotype on the mean SC width. Here WT mice had a significantly lower mean SC width compared to the ICR *Bmp4*$^{+/-}$ mice (p = 0.0309* and * respectively – bright blue cells in Table 1) whereas *Foxc1*$^{+/-}$ and *Bmp4*$^{+/-}$ genotypes were not significantly different (see bright blue cells in Table1). This finding is in contrast to the trend shown in C57 mice. Since the relative change in width of the canal between 6-8 month old ICR WT and 10-12 month old ICR *Foxc1*$^{+/-}$ was similar to that seen in C57 mice, it is possible that the 10-12 month old ICR WT mice are outliers in this study. This anomaly was also observed in the number of collector channels (Figure 3.33) in these two groups and is discussed in Chapter 4. If, however, the 10-12 month ICT WT age group is excluded from the analysis, or assumed not to be significantly different to the 8-10 month group (as seen in the C57 mice), then, it can be deduced that the overall effect of *Foxc1*$^{+/-}$ is a reduced mean SC width and therefore its effect is similar in both strains. Therefore, for the rest of the analysis on the number of collector channels, the length and complexity of the corneal arcades (see sections **3.5.1.4, 3.5.2.1; 3.5.2.3**) within the 10-12 month ICR WT group, it will be assumed that because age has no effect on the C57 strain, that this is similarly true for the ICR mice.

The relative severity of the effect of *Foxc1*$^{+/-}$ on each strain was not revealed in the above analysis. In order to determine whether the mean SC width differed between strains, and, to test for differences on the effect of genotype in the 10-12 month age group between each strain, ANOVA was performed to test for differences between WT mice in the C57 and ICR strains. The mean SC width in ICR WT mice (6-8 months) was significantly higher than that in all other WT mice (p = 0.0001** compare to ** - yellow cells in Table 1). On the other hand, the mean SC width of ICR WT mice of 10-12 month age was significantly lower than that in all other WT mice (p = 0.0000** compare to ** - yellow cells in Table1). Again the anomalous 10-12 month ICR WT group is the cause of the age effect between strains. If this group is excluded, or assumed to be not significantly different to the 6-8 month ICR WT mice, then the overall effect of strain is observed where ICR WT mice have a higher mean SC width than that of the C57 WT mice (p = 0.00367 – Student's T-Test).

When testing for differences between the mean SC widths by strain (C57 vs ICR) and genotype (*Foxc1*$^{+/-}$ vs WT) within the 10-12 month age group, the effect of the genotype was significant within each strain (p = 0.0174). The mean SC width was significantly lower in ICR WT mice (56.59 µm)

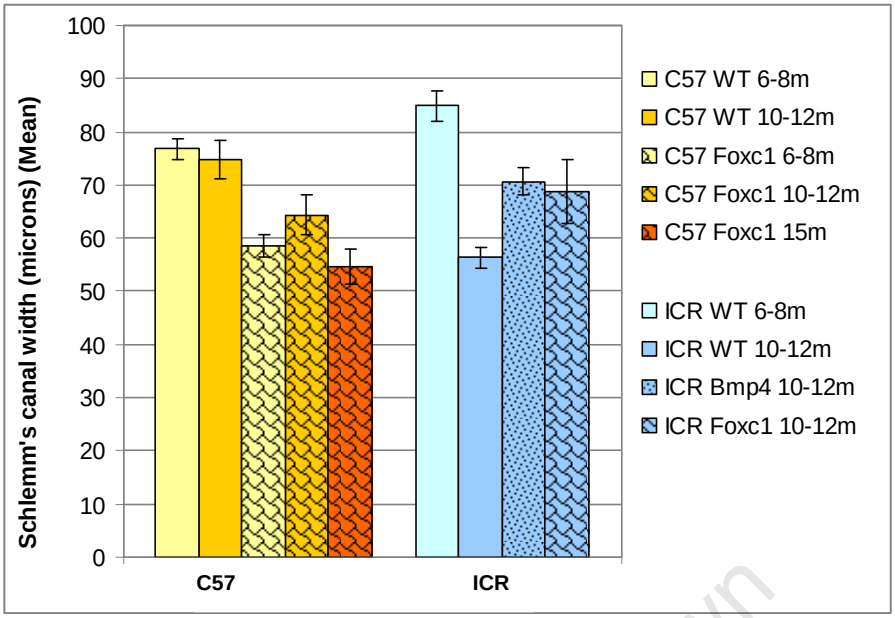

Figure 3.28: Schlemm's canal width in normal (WT), *Foxc1*$^{+/-}$ and *Bmp4*$^{+/-}$ mice.

Bar chart showing the mean width of Schlemm's canal (in microns) for each group. Error bars represent the standard error of the mean.

C57 = C57BL/6Jx129 mouse strain (yellow-orange shaded bars); ICR = ICR mouse strain (blue shaded bars); WT = normal (wildtype) mice (plain coloured bars); *Foxc1*$^{+/-}$ genotype (brick patterned bars); *Bmp4*$^{+/-}$ genotype (fine speckled patterned bar). 6-8 month age group = pale yellow or pale blue background colour; 10-12 month age group = dark yellow and darker blue background colour; 15 month age group = orange background colour.

compared to that in ICR *Foxc1*$^{+/-}$ mice (68.55 µm) ((p = 0.0174** compared to ** - pale green cells in Table 1). By contrast, the mean SC width was marginally higher in C57 WT (74.59 µm) compared to and C57 *Foxc1*$^{+/-}$ mice (63.97 µm), although not significant in this age group (p = 0.1359* and * respectively - pale green cells in Table 1). Based on the fact that age has no significant effect within genotype, and if this function is collapsed and the 10-12 month ICR WT mice are excluded (or assumed not significantly different to the 8-10 month ICR WT mice), then the overall effect of *Foxc1*$^{+/-}$ is not significantly different between the ICR and C57 mice (p = 0.6664 - not shown in Table1).

3.5.1.2 The frequency of variation in the width of Schlemm's canal in normal (WT), *Foxc1*$^{+/-}$ and *Bmp4*$^{+/-}$ mice.

During the analysis of Schlemm's canal, there were indications that there were differences in the overall shape or pattern of the canal around the limbus between the two strains and genotypes. Since the measurements of the canal were taken in series (see section **2.2.3**) it was possible to plot these and then determine whether the width of the canal showed variations that might reveal a pattern that

may be typical to the strain and genotype. Plotted line graphs depicting the SC widths from individual mouse eyes whose mean SC widths were similar to that of the group mean are shown in Figures 3.29a-h. In order to smooth the graph, a trendline (red line) was generated using a moving average of 5 points around each measurement. The x-axes indicate all points measured throughout the length of the canal and the y axes indicate the width of each point in microns. In order to establish the usefulness of this method, the trends shown in the graphs were compared to composite images of segments of Schlemm's canal, representing approximately 25% of its total length around the limbus (indicated by the green bar in Figures 3.29a-h). (The images shown in Figures 3.30 and 3.31 were not from the same mice from which the plots were generated, but would also have had a similar mean SC width to the group mean).

Although the width of Schlemm's canal varied at different points along its length, segments where the width showed little variation or a gradual change were more frequently seen in the 6-8 month and 10-12 month C57 WT mice than in the *Foxc1*$^{+/-}$ groups (Compare Figures 3.29 a, b with d, e). A composite image (produced from 4-6 sequential images) shows a segment (approximately 25%) of the limbus in a 6-8 month old C57 WT mouse eye (Figure 3.30a). This image displays a morphological trend that is represented by the green line in the plotted data (compare figures 3.28b and 3.30a). This trend shows that within 25% of the length of the canal, the change in width of the canal is gradual. The morphology of Schlemm's canal from a 10-12 month old C57 WT mouse eye is seemingly different and wider than at 6-8 months (Figure 3.30b). However, although the width of the canal appears to be stable, small bifurcations, split segments (short arrows – Figure 3.30b) or constricted regions (long arrows – Figure 3.30b) within the canal would account for a smaller measurement in these regions, and would thus account for the higher variability in the plot (compare Figures 3.29b and 3.30b). In contrast, changes in the width of Schlemm's canal in C57 *Foxc1*$^{+/-}$ mice were more gradual and reflected an undulating pattern throughout the limbus (Figure 3.29c, d). This morphological pattern was also evident in the composite images representing 25% of the total length of the canal (Figure 3.30c, d - variations in widths are indicated between arrow heads).

On the other hand, 6-8 month old ICR WT mice displayed broad segments of the canal showing little variability in width. Such segments formed substantial sections of the canal and were more frequently observed in this group compared to C57 mice and other genotype groups within the ICR strain (Figure 3.28f and 3.31a). Slight fluctuations in the SC width are due to measurements that may have been captured at the points indicated by short arrows in Figure 3.31a. The canal in 10-12 month

SCHLEMM'S CANAL WIDTH	C57 WT 6-8m	C57 WT 10-12m	C57 *Foxc1* +/- 6-8m	C57 *Foxc1* +/- 10-12m	C57 *Foxc1* +/- 15m	ICR WT 6-8m	ICR WT 10-12m	ICR *Bmp4* +/- 10-12m	ICR *Foxc1* +/- 10-12m
n (eyes)	10	16	18	8	12	12	14	12	16
n (data points)	788	1230	1295	595	829	901	1049	1018	1196
Mean SC width (microns)	77.44	74.59	58.69	63.97	54.97	84.98	56.59	70.76	68.55
SEM	1.95	3.66	2.06	3.7	3.29	2.92	1.91	2.67	5.95
Signicance: ANOVA - effects of									
Age and *Foxc1*+/- in the C57 strain	**0.0000***		*						
	0. 7537**	**	0. 7537***	***					
Age within the C57 strain and *Foxc1*$^{+/-}$ genotype				*					
			0.2296*	**	0.0601**				
Genotype in 10-12m group in ICR strain							**0.0309***	*	
								**	0.7206**
Age and strain within WT genotype	0.4998*	*				**0.0000****	**		
	** , ***					**0.0001*****	***		
Strain and *Foxc1*+/- within 10-12m		0.1359*		*			**0.0174****		**

Table 1: The means, standard error of the mean and P values for the width of Schlemm's canal in normal (WT), *Foxc1*$^{+/-}$ and *Bmp4*$^{+/-}$ mice.

The data are grouped according to strain (C57BL/6Jx129, or ICR), genotype (normal, *Foxc1*$^{+/-}$ or *Bmp4*$^{+/-}$) and age (6-8, 10-12 or 15 month old mice). C57 = C57BL/6Jx129; WT = normal mouse eyes; n (eyes) = the number of mouse eyes per group; n (data points) = the total number of measurements made in each group; SEM = standard error of the mean. Significance was determined by ANOVA that tested for the effects of strain, age, and/or genotype in the different groups listed in the 1st column and the associated p-values appear in the colour-coded blocks. Significance (or no significance) is compared between groups where p-values are followed by (*, ** or ***) and groups with the corresponding (*. ** or ***) in the cells coded with the same colour. P- values indicating significance are in red font.. The mean values are in blue text.

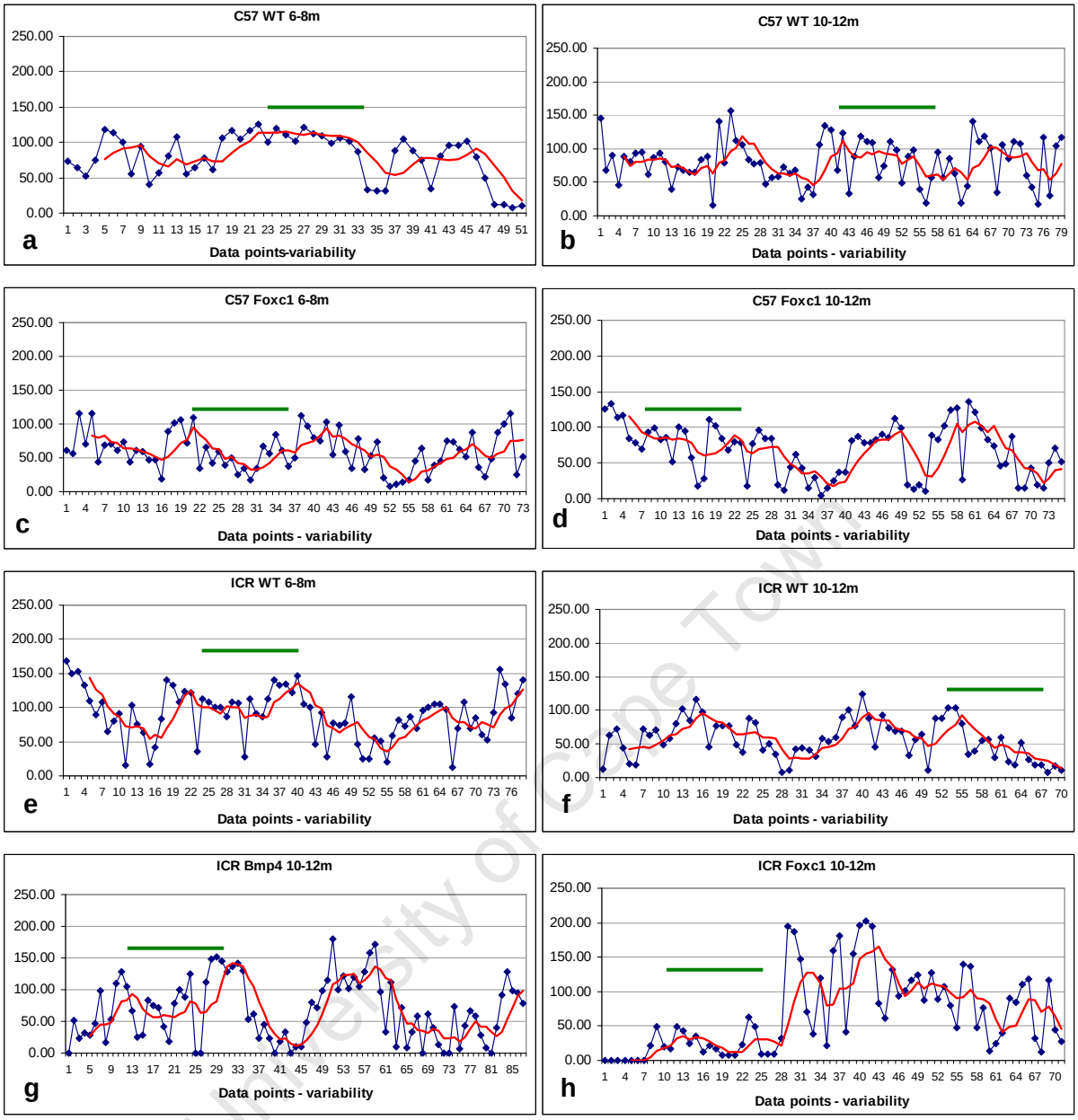

Figure 3.29: The frequency of variability in the width of Schlemm's canal in normal (WT), *Foxc1*$^{+/-}$ and *Bmp4*$^{+/-}$ mice.

a – h) Line charts showing individual measurements (in microns) of Schlemm's canal taken sequentially along the entire length of the canal (at points on the grid overlay (see section 2.2.4) from one mouse eye in each group. The x- axis indicates the number of points measured along the entire Schlemm's canal in one mouse eye. The Y axis indicates the measured width of Schlemm's canal (in microns) at each data point (blue line). A trendline (red line) was generated based on a moving average of 5 points to smooth the data and show possible variations in the patterning/shape of Schlemm's canal over its length around the limbus. The green bar indicates the region represented in the composite images of Schlemm's canal from the same group in Figures 3.30 and 3.31. C57 = C57BL/6Jx129 mouse strain; ICR = ICR mouse strain; WT = normal (wildtype) mice; Foxc1 = *Foxc1*$^{+/-}$ genotype; Bmp4 = *Bmp4*$^{+/-}$genotype; 6-8m = 6-8 month age group, 10-12m = 10-12 month age group.

a) 6-8 month old C57 WT mouse eye:
b) 10-12 month old C57 WT mouse eye:
c) 6-8 month old C57 *Foxc1*$^{+/-}$ mouse eye:
d) 10-12 month old C57 *Foxc1*$^{+/-}$ mouse eye:
e) 6-8 month old ICR WT mouse eye:
f) 10-12 month old ICR WT mouse eye:
g) 10-12 month old ICR *Bmp4*$^{+/-}$mouse eye:
h) 10-12 month old ICR *Foxc1*$^{+/-}$ mouse eye:

ICR WT mice was markedly different and displayed substantial segments showing gradual changes in the width which were separated by shorter narrower segments (Figures 3.29f and 3.31b – short arrows). The marked variability seen in the data points along the canal in ICR *Bmp4*$^{+/-}$ mice (Figure 3.29g) is seen in abrupt and frequent changes of its width and shape (Figure 3.31c - short arrows). The canal in ICR *Foxc1*$^{+/-}$ mice often displayed segments where the width of the canal changed gradually to form long narrow segments (Figure 3.29h and 3.31d - short arrows).

The above findings demonstrate that to a certain extent, there is a correlation between the plotted sequential measurements of the width of Schlemm's canal and its morphology. Since the plotted sequential widths of Schlemm's canal shown in Figure 3.29 and the images representing the corresponding groups shown in Figures 3.30 and 3.31 were not necessarily from the same mouse eye, these findings suggest that the overall pattern/shape of the canal may be characteristic of strains and genotype.

3.5.1.3 Morphological analysis of Schlemm's canal in normal (WT), *Foxc1*$^{+/-}$ and *Bmp4*$^{+/-}$ mice.

The above mean SC width and the trend shown by the sequential measurements of the canal, reflect its relative variability and average width around the limbus. Schlemm's canal is also known to take on various forms such as splitting into two vessels and forming a plexus (Ashton, 1953), and has previously reported to be absent in *Foxc1*$^{+/-}$ and *Bmp4*$^{+/-}$ mouse eyes (Chang et al., 2001; Smith et al., 2000). Since there were indications that the overall shape of the canal may be affected by strain and genotype, the question arose as to whether these factors also influence the overall morphology of the vessel. Since the above analyses of width and variability would not reflect these morphological changes, the presence of specific morphological features (see section **2.2.5**) was quantified at every 2nd grid line which intercepted with the canal. In the case of the canal being absent in some regions, this "feature" was counted at every 2nd grid line in this region of the limbus. The proportion of the different morphological features was calculated for each mouse eye and determined for each group.

In all groups, most of the canal formed a single tube / vessel (Figure 3.32). With the exception of the 10-12 month old C57 WT which displayed 25% bifurcations in the canal, less than 10% of the canal showed this feature in the other groups. These findings suggested that neither strain nor genotype accounted for any change in the proportion of the canal showing bifurcations. Likewise, the presence of a plexus also accounted for less than 10% of the canal with no strain or genotype effects seen. In contrast, a fragmented or absent canal was only detected in *Foxc1*$^{+/-}$ and *Bmp4*$^{+/-}$

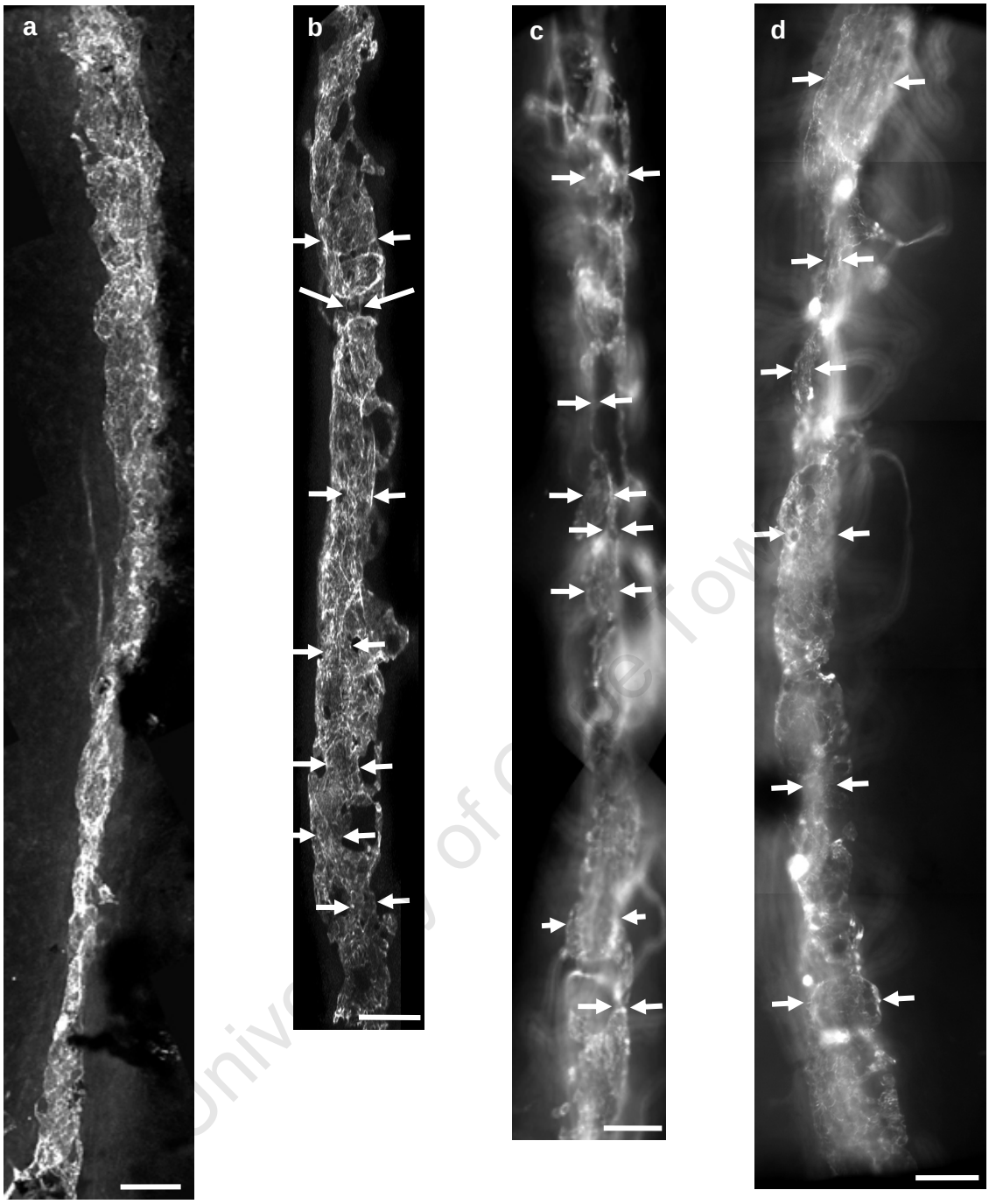

Figure 3.30: Composite images of long segments of Schlemm's canal in normal (WT), *Bmp4*$^{+/-}$ and *Foxc1*$^{+/-}$ C57BL/6Jx129 mice.

a) WT mouse eye at 6 months: The width of Schlemm's canal gradually diminishes over approximately ¼ of the limbus. Bar = 100 µm

b) WT mouse eye at 12 months: The overall width of Schlemm's canal appears regular. However, the presence of plexus-like/split regions (short arrows) and short constricted segments (long arrows) would account for the variability in the measurements seen in Figure 3.29. Bar = 100 µm

c) *Foxc1*$^{+/-}$ mouse eyes at 8 months: Schlemm's canal shows larger variations in shape and width (indicated between arrows) compared to that seen in WT mice shown in a and b. Bar = 100 um

d) The variations in width and shape in *Foxc1*$^{+/-}$ mouse eyes at 12 months are similar to that seen at 6-8 months. Bar = 100 µm

mouse eyes (see "fragmented" section in Figure 3.32). Within each of these groups, an absent Schlemm's canal was noted in only a small proportion of mouse eyes (2-3 eyes per group, each Since the number of plexuses, bifurcations and single vessel morphology do not appear to be genotype or strain dependant, there may be limited benefit of using this analysis to determine other genetic effects on the morphology of Schlemm's canal. This analysis also revealed regions in the limbus where the canal was not detected. However, these regions would be allocated a value of zero when measuring the width of the canal and therefore would be revealed as a series of zero values in the line graphs of the sequential measurements of SC width.

3.5.1.4 A quantitative assessment of collector channels in normal (WT), *Foxc1*$^{+/-}$ and *Bmp4*$^{+/-}$ mice.

Collector channels are aqueous vessels lined by vascular endothelium that drain the aqueous humour from Schlemm's canal into the perilimbal superficial/episcleral vascular plexus. As seen in Figures 3.4, 3.5 and 3.6d, these vessels were revealed by PECAM-1 immunostaining and could be traced from the episcleral plexus through the limbus to Schlemm's canal in wholemount preparations. The total number of collector channels was determined for each eye as described in section **2.5** and the effects of strain and genotype and age on the number of collector channels was determined by ANOVA and linear regression.

Figure 3.33 shows a bar chart representing the mean of the total number of collector channels per eye for each group and the standard error of the mean (SEM). The means, SEM and the number of eyes analysed in each group are listed in Table 2. The general trend shown in Figure 3.33 shows that the mean number of collector channels per eye is markedly lower in *Foxc1*$^{+/-}$ mice (brick-patterned yellow-orange and blue bars) compared to WT mice (plain coloured bars - Figure 3.33). ANOVA showed that the effect of strain and genotype, and, strain and age were significant ($p < 0.001$) therefore further analysis was done to test for differences between the number of collector channels within the specific groups as for determining significance in mean SC width (see **3.5.1** in SC width analysis).

Within the C57 strain, ANOVA showed that the <u>interaction</u> of age and genotype had a significant effect on the number of collector channels ($p = 0.0145$). The mean number of collector channels in 6-8 and 10-12 month WT mice (19.4 and 22.06 respectively - Table 2) was significantly higher than that of the 6-8 and 10-12 month *Foxc1*$^{+/-}$ mice (17.44 and 13.63 respectively - Table 2) ($p = 0.000$* compared to * - pink cells in Table 2). However, age had no significant effect on the number of collector channels within WT or *Foxc1*$^{+/-}$ genotypes in the C57 strain (see pink and

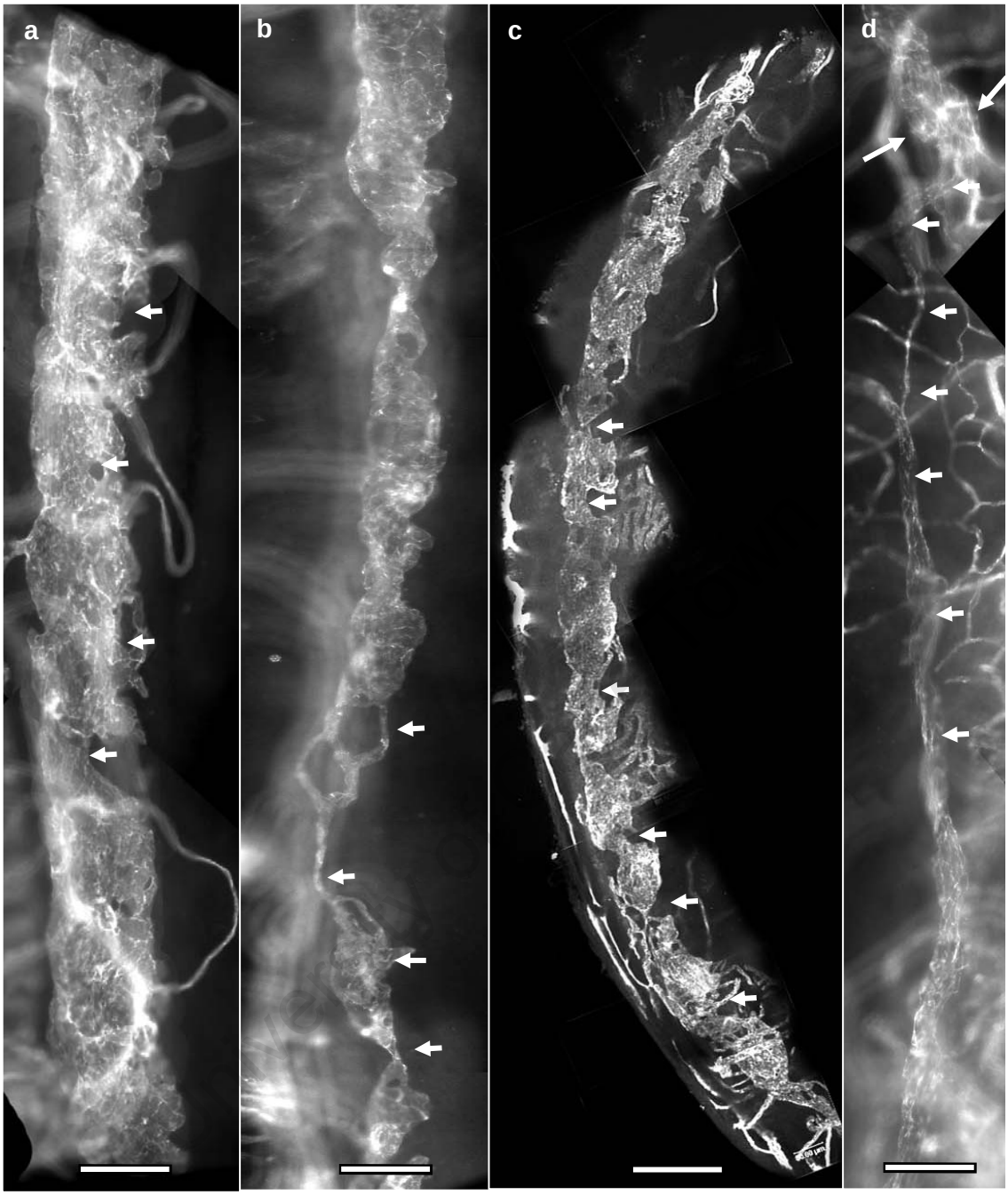

Figure 3.31: Composite images of long segments of Schlemm's canal in normal (WT), *Bmp4*$^{+/-}$ and *Foxc1*$^{+/-}$ ICR mice.

a) WT mouse eye at 6-8 months: Schlemm's canal shows a consistent width with few narrow regions (short arrows). Bar = 100 µm

b) WT mouse eye at 10-12 months: A wide Schlemm's canal (top of image) narrows progressively and gives way to large variations in shape (small arrows). Bar = 100 µm

c) Schlemm's canal in a *Bmp4*$^{+/-}$ mouse eye shows large and frequent variations in width (small arrows) and form. Bar = 100 µm

d) A narrow segment of Schlemm's canal in a *Foxc1* $^{+/-}$ mouse eye shows a relatively smooth contour (short arrows) over a long segment of the limbus and gives way abruptly to a wide canal (long arrows). The plexus in view is located deeper in the wholemount and is associated with the iris vasculature. Bar = 100 µm

dark green cells - Table 2). from different mice). In the 10-12 month old C57 *Foxc1*$^{+/-}$ group, only one eye (n=8) showed 12 % of the limbus where Schlemm's canal was absent. A more severe phenotype was seen the 15 month old C57 *Foxc1*$^{+/-}$ group where in 4 mouse eyes (n=12), Schlemm's canal was not present in 15-30% of the limbus. In three eyes from the ICR *Bmp4*$^{+/-}$ group (n=12) and two eyes from the ICR *Foxc1*$^{+/-}$ group (n=16), Schlemm's canal was absent in 10-17% of the limbus. In the most severe case, almost 25% of a continuous section around the limbus was devoid of the canal. In the less severe cases, Schlemm's canal was absent in a few short regions of the limbus. PECAM-1 staining was generally located at the cell periphery with up to 20% of the canal (in some mice) showing some dispersion of the stain in all groups (data not shown). An exception was the 15 month old C57 *Foxc1*$^{+/-}$ group which displayed a higher proportion of dispersed PECAM-1 (44%).

The mean number of collector channels in the 6-8 month old ICR mice (26.33 - Table 2) (pale blue bar - Figure 3.33) was markedly higher than all other groups (yellow and blue bar clusters in Figure 3.33, - see also means in Table 2). On the other hand, the number of collector channels in the 10-12 month old ICR WT mice (plain darker blue bar) were markedly less (14.17) than all other WT mice (plain coloured bars - Figure 3.33 and blue text in Table 2). This unexpected finding is in keeping with the surprisingly narrow width of Schlemm's canal in this group, and is further addressed in Chapter 4: Discussion. ANOVA showed that genotype had no significant effect on the ICR strain (see bright blue cells in Table 2). However, if the 10-12 month age group is excluded, then the overall effect of *Foxc1*$^{+/-}$ or *Bmp4*$^{+/-}$ is a reduction in the number of collector channels compared to WT mice, and thus follows a similar trend shown in the C57 strain.

In order to determine whether there are strain effects on the number of collector channels, ANOVA tested for differences between WT mice in the C57 and ICR strains, and, for differences on the effect of genotype in the 10-12 month age group between each strain. Within the WT genotype, ANOVA showed that the interaction of age and strain had a significant effect on the number of collector channels (p =0.0000). The mean number of collector channels was significantly different between 6-8 month C57 and ICR WT mice (19.4 and 26.33 respectively), and, between 10-12 month old C57 and ICR WT mice (22.96 and 13.86 respectively) (p = 0.0000* compare to * - yellow cells in Table 2). Again age had no significant effect on the number of collector channels in C57 mice, whereas the converse was true for ICR mice. This difference is most likely to be due to the unusual 10-12 month ICR WT group.

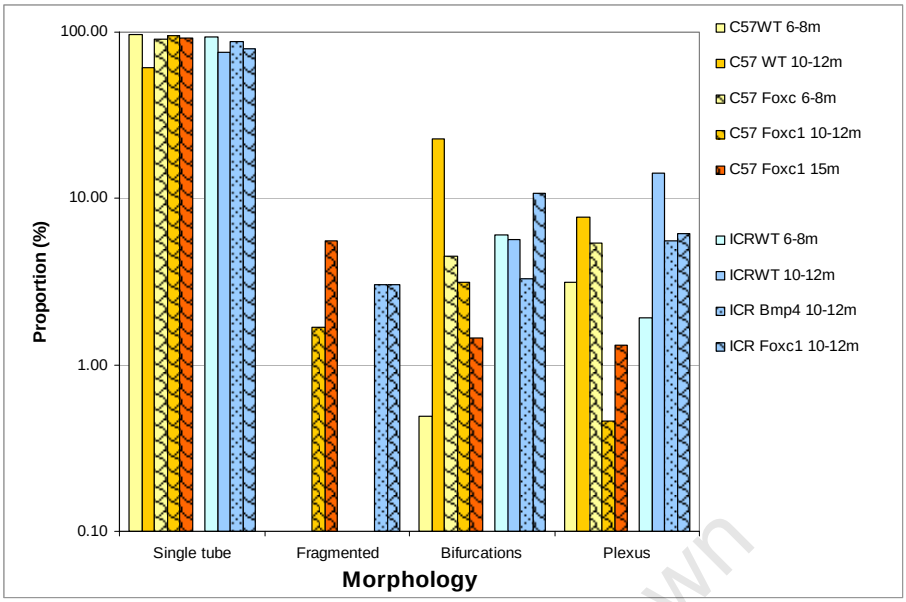

Figure 3.32: Quantitative analysis of morphological features displayed by Schlemm's canal in normal (WT), *Foxc1*$^{+/-}$ and *Bmp4*$^{+/-}$ mice.

a) Bar graphs indicate the proportion of morphological features detected in Schlemm's canal in normal (WT), *Foxc1*$^{+/-}$ and *Bmp4*$^{+/-}$ mice. The different morphological features are indicated on the x-axis and the proportion is shown on a logarithmic scale on the y axis.

C57 = C57BL/6Jx129 mouse strain (yellow-orange shaded bars); ICR = ICR mouse strain (blue shaded bars); 6-8 month age group = pale yellow or pale blue background colour; 10-12 month age group = dark yellow and darker blue background colour; 15 month age group = orange background colour. WT = normal (wildtype) mice (plain yellow and blue shaded bars); *Foxc1*$^{+/-}$ genotype (brick patterned bars); *Bmp4*$^{+/-}$ genotype (fine speckled patterned bar).

Within the 10-12 month age group, the effect of *Foxc1*$^{+/-}$ on the mean number of collector channels on the C57 strain was significant (p = 0.0000*** compare to *** - pale green cells Table 2), with WT mice showing a higher mean than *Foxc1*$^{+/-}$ mice (22.06 and 13.63 respectively). Conversely, the mean number of collector channels is not significantly different between ICR *Foxc1*$^{+/-}$ and ICR 10-12 month old WT mice (pale green cells Table 2). However, if 10-12 month old WT group is excluded and the data from the 6-8 month ICR WT mice is used, then *Foxc1*$^{+/-}$ (and *Bmp4*$^{+/-}$) mice have significantly fewer collector channels (11.44 and 14.17 respectively) than WT mice (26.33) (p = 0.0000 - Student's T test).

In summary, *Foxc1*$^{+/-}$ mice have fewer collector channels than WT mice in both C57 and ICR strains. However, due to the peculiar findings of the 10-12 month ICR WT mice, it is difficult to unequivocally state that strain (and genotype within the ICR strain) have a significant effect on the number of collector channels. If the 10-12 month old ICR WT data are excluded, or assumed not

significantly different to the 8-10 month old mice, then strain shows an effect on the number of collector channels. Furthermore, *Foxc1*$^{+/-}$ has a greater effect on the number of collector channels within the ICR strain (from 26.33 (WT) to 11.44) than on the number of collector channels in C57 mice (from 21.03 (WT) to 16.23). If the above is true, then the *Bmp4*$^{+/-}$ genotype also has a significant effect on the on the number of collector channels.

3.5.2 A quantitative analysis of the superficial perilimbal plexus in normal (WT), *Foxc1*$^{+/-}$ and *Bmp4*$^{+/-}$ mice.

Genetic background (strain) is known to affect the density of the normal limbal vasculature and its angiogenic response in corneal angiogenic assays (Chan et al., 2004). However, it is not known to what extent the overall architecture of the superficial limbal vasculature is affected by *Bmp4* and *Foxc1* haploinsufficiency on the C57 and ICR strains. In order to study the three dimensional architecture of the perilmbal vasculature, images of the superficial vasculature in immunostained anterior segments were captured in sequence throughout the limbus (see section **2.2.5**) and subjected to two forms of analysis. One was to determine the mean distance (**CA length**) the corneal arcades extended into the cornea, and, the other was to determine the complexity of the plexus formed by the corneal arcades. For the former, the distance between the most distal capillary loops of the corneal arcades and the most distally located perilimbal vein was measured using a morphometric grid overlay as described in Section **2.5**. In order to ensure randomisation, measurements were taken at every 2nd grid line that crossed/intercepted with a capillary of the corneal arcades.

3.5.2.1 The CA lengths in normal (WT), *Foxc1*$^{+/-}$ and *Bmp4*$^{+/-}$ mice.

Analysis of the raw data of the individual measurements representing the distance of penetration into the cornea by the corneal arcades (**CA length**) and the sum of the capillary loops per eye (**Complexity**) revealed that neither data sets followed a normal distribution (Shapiro-Wilk's test). Therefore, the median values and the range in each group are shown in the bar charts in Figures 3.34 and 3.35. Because ANOVA uses the mean to determine significance, the means for CA length and complexity are stated in blue text in Table 3. The number of eyes studied (n (eyes)), total number of CA length measurements per group (n (data points)), SEM values, and, significance (p-values) determined by ANOVA are stated in Table 3.

The overall impression from Figure 3.34 is that *Foxc1* and *Bmp4* haploinsufficiency (blue speckled and brick-patterned bars) have a markedly greater effect on the mean CA lengths in the

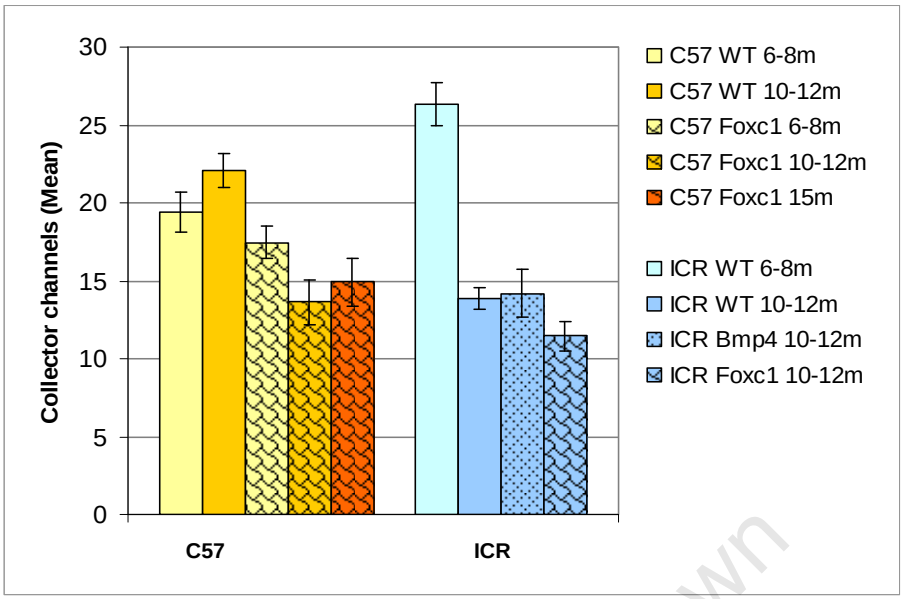

Figure 3.33: The number of collector channels in normal (WT), *Foxc1*$^{+/-}$ and *Bmp4*$^{+/-}$ mice.

Bar chart showing the group mean (Y axis) of the total number of collector channels per mouse eye in normal (WT), *Foxc1*$^{+/-}$ and *Bmp4*$^{+/-}$ mice. Error bars represent the standard error of the mean.

C57 = C57BL/6Jx129 mouse strain (yellow-orange shaded bars); ICR = ICR mouse strain (blue shaded bars); 6-8 month age group = pale yellow or pale blue background colour; 10-12 month age group = dark yellow and darker blue background colour; 15 month age group = orange background colour. WT = normal (wildtype) mice (plain yellow and blue shaded bars); *Foxc1*$^{+/-}$ genotype (brick patterned bars); *Bmp4*$^{+/-}$ genotype (fine speckled patterned bar).

ICR strain (blue bar cluster) than in the C57 mice (yellow-orange coloured bar cluster). ANOVA indicated that the interaction of strain and genotype was significant (p = 0.0000).

Within the C57 strain, WT mice had significantly lower mean CA lengths (101.65 µm and 96.41 µm for 6-8 and 10-12 month groups respectively) than *Foxc1*$^{+/-}$ mice (139.57 µm and 109.36 µm for 6-8 and 10-12 month groups respectively) (p = 0.0061* compare to * - pink cells in Table 3-a). The effect of age on the mean CA length in *Foxc1*$^{+/-}$ mice was not significant in this strain (compare bright green cells in Table 3-a).

Within the ICR strain, genotype has a significant effect where the mean CA lengths were significantly lower in WT mice (113.94 and 48.2 µm) compared to *Bmp4*$^{+/-}$ mice (230.66 µm) (p = 0.0154* and * respectively - Table 3-a) and *Foxc1*$^{+/-}$ mice (557.09 µm) (p = 0.0000** compared to ** - bright blue cells in Table 3-a). The upper limit of the range shown in the ICR *Foxc1*$^{+/-}$ group (darker blue brick-patterned bar - Figure 3.34) was due to one particular eye that showed

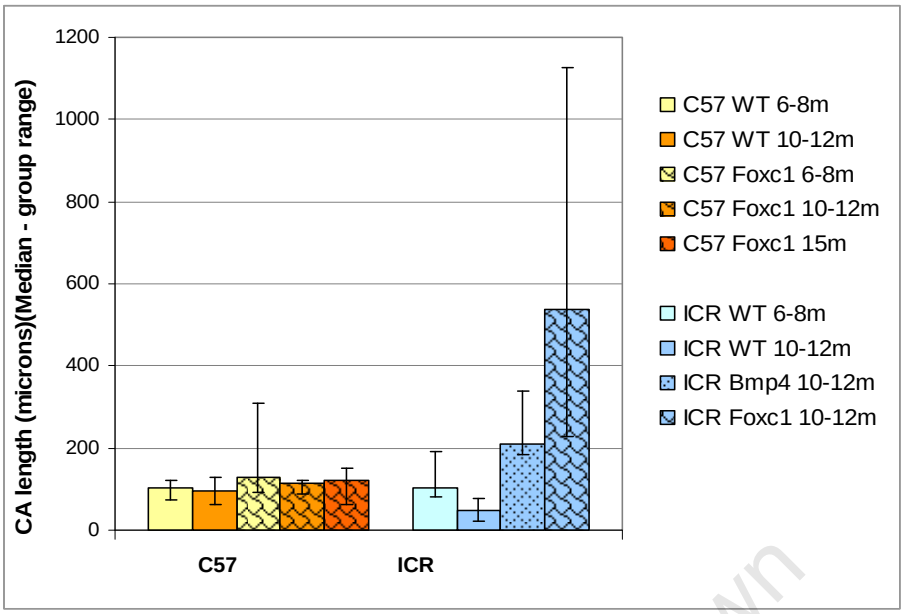

Figure 3.34: The CA lengths in normal (WT), *Foxc1*$^{+/-}$ and *Bmp4*$^{+/-}$ mice.

Bar chart shows the group median values (Y axis) of the CA lengths (in microns). Error bars represent the range of the medians for individual mouse eyes in each group.

C57 = C57BL/6Jx129 mouse strain (yellow-orange shaded bars); ICR = ICR mouse strain (blue shaded bars); 6-8 month age group = pale yellow or pale blue background colour; 10-12 month age group = dark yellow and darker blue background colour; 15 month age group = orange background colour. WT = normal (wildtype) mice (plain yellow and blue shaded bars); *Foxc1*$^{+/-}$ genotype (brick patterned bars); *Bmp4*$^{+/-}$ genotype (fine speckled patterned bar).

severe anterior segment dysgenesis and extreme neovascularisation. However, exclusion of this data point made little difference in the significant effect of *Foxc1*$^{+/-}$ on the CA length in ICR mice.

In order to determine whether the mean CA lengths differed between strains, ANOVA tested for differences between WT mice in the C57 and ICR strains. Age had no effect on the mean CA length in the C57 strain (see yellow cells in Table 3-a), whereas 10-12 month old ICR WT mice had significantly shorter mean CA lengths compared to the 6-8 month ICR WT group (p = 0.0000** compare ** - yellow cells in Table 3-a). However, due to the previous irregularities shown by the 10-12 month ICR WT mice, and that age has no effect in C57 mice, it can thus be assumed that age has no effect in the ICR strain. If the 10-12 month ICR WT is excluded (or assumed not to be significantly different to the 6-10 month old mice), then the mean CA length in ICR WT mice (113.94) is not significantly different to that of the all C57 WT mice (97.04) (p = 0.0622*, * - Student's T test for independent samples). ANOVA determined that the effect of genotype was different within strains in the 10-12 age group. In C57 WT mice, *Foxc1* haploinsufficiency had no significant effect on CA lengths pale green cells Table 2a), whereas ICR *Foxc1*$^{+/-}$ mice had a significantly higher mean CA length (575.09) than in ICR WT mice

COLLECTOR CHANNELS	C57 WT 6-8m	C57 WT 10-12m	C57 *Foxc1* +/- 6-8m	C57 *Foxc1* +/- 10-12m	*Foxc1* +/- 15m	ICR WT 6-8m	ICR WT 10-12m	ICR *Bmp4* +/- 10-12m	ICR *Foxc1* +/- 10-12m
n (eyes)	10	16	18	8	12	12	14	12	16
Total number of collector channels/ eye (Group mean)	19.4	22.06	17.44	13.63	14.91	26.33	13.86	14.17	11.44
SEM	1.32	1.1	1.03	1.45	1.55	1.38	0.69	1.54	0.91
Signicance: ANOVA - effects of									
Age and *Foxc1*+/- in the C57 strain	0.0000*		*						
	0.0460***	***	0.0460**	**					
Age within the C57 strain and *Foxc1*$^{+/-}$ genotype			0.1346	0.1346	1.1346				
Genotype in 10-12m group in ICR strain							0.8398*	*	
								**	0.0722**
Age and strain within WT genotype	*					0.0000*			
	0.1109**	**				0.0000***	***		
Strain and *Foxc1*+/- within 10-12m		** & 0.0000***		***			0.0060**		0.1776***

Table 2: The means, standard error of the mean and P values for the number of collector channels in normal (WT), *Foxc1*$^{+/-}$ and *Bmp4*$^{+/-}$ mice.

The data are grouped according to strain (C57BL/6Jx129, or ICR), genotype (normal, *Foxc1*$^{+/-}$ or *Bmp4*$^{+/-}$) and age (6-8, 10-12 or 15 month old mice). C57 = C57BL/6Jx129; WT = normal mouse eyes; n (eyes) = the number of mouse eyes per group; SEM = standard error of the mean. Significance was determined by ANOVA that tested for the effects of strain, age, and/or genotype in the different groups listed in the 1st column and the associated p-values appear in the colour-coded blocks. Significance (or no significance) is compared between groups where p-values are followed by (*, ** or ***) and groups with the corresponding (*. ** or ***) in the cells coded with the same colour. P- values indicating significance are in red font.. The mean values are in blue text.

a) CORNEAL ARCADES: PENETRATION	C57 WT 6-8m	C57 WT 10-12m	C57 Foxc1 6-8m	C57 Foxc1 10-12m	C57 Foxc1 15m	ICR WT 6-8m	ICR WT 10-12m	ICR Bmp4 10-12m	ICR Foxc1 10-12m
n (eyes)	10	16	18	8	12	12	14	10	16
n (data points)	312	572	568	279	419	465	522	429	540
Mean CA length (microns)	101.65	94.41	139.57	109.36	118	113.94	48.2	230.66	575.09
SEM	5.06	4.76	11.79	4.51	7.97	10.58	4.28	16.38	66.79
Signicance ANOVA - effects of									
Age and *Foxc1*+/- in the C57 strain	0.0061*		*						
			0.1351*	* & **	0.1351**				
Age within the C57 strain and *Foxc1*$^{+/-}$ genotype							0.0154*	** *	0.0000**
Genotype in 10-12m group in ICR strain	0.4441*	*				0.0000**	**		
Age and strain within WT genotype		0.8153*		*			0.0000**		**
b) CORNEAL ARCADES: COMPLEXITY	C57 WT 6-8m	C57 WT 10-12m	C57 Foxc1 6-8m	C57 Foxc1 10-12m	C57 Foxc1 15m	ICR WT 6-8m	ICR WT 10-12m	ICR Bmp4 10-12m	ICR Foxc1 10-12m
n (eyes)	10	16	18	8	12	12	14	10	16
Total number of loops /eye (Group mean)	86.8	82.93	119.66	114.37	84.58	55.16	26.71	178.8	118.5
SEM	7.35	6.68	7.25	12.24	6.64	5.67	2.29	12.98	34.95
Signicance ANOVA - effects of									
Age and *Foxc1*+/- in the C57 strain	0.0003*		*						
	0.5898**	**	0.5898***	***					
			*		0.0331*				
			0.6747**	**					
Age within the C57 strain and *Foxc1*$^{+/-}$ genotype							0.0003*	* **	0.1109**
Genotype in 10-12m group in ICR strain	*					0.0205*			
	0.6527***	***				0.0000**	**		
Age and strain within WT genotype		0.0044**		*** **			0.0044*		0.1701*** *

Table 3: The means, standard error of the mean and P values for CA lengths (a), and the complexity of the corneal arcades (b) in normal (WT), *Foxc1*$^{+/-}$ and *Bmp4*$^{+/-}$ mice.

The data are grouped according to strain (C57BL/6Jx129, or ICR), genotype (normal, *Foxc1*$^{+/-}$ or *Bmp4*$^{+/-}$) and age (6-8, 10-12 or 15 month old mice). C57 = C57BL/6Jx129; WT = normal mouse eyes; n (eyes) = the number of mouse eyes per group; n (data points) = the total number of measurements made in each group; SEM = standard error of the mean. Significance was determined by ANOVA that tested for the effects of strain, age, and/or genotype in the different groups listed in the 1st column and the associated p-values appear in the colour-coded blocks. Significance (or no significance) is compared between groups where p-values are followed by (*, ** or ***) and groups with the corresponding (*. ** or ***) in the cells coded with the same colour. P- values indicating significance are in red font.. The mean values are in blue text.

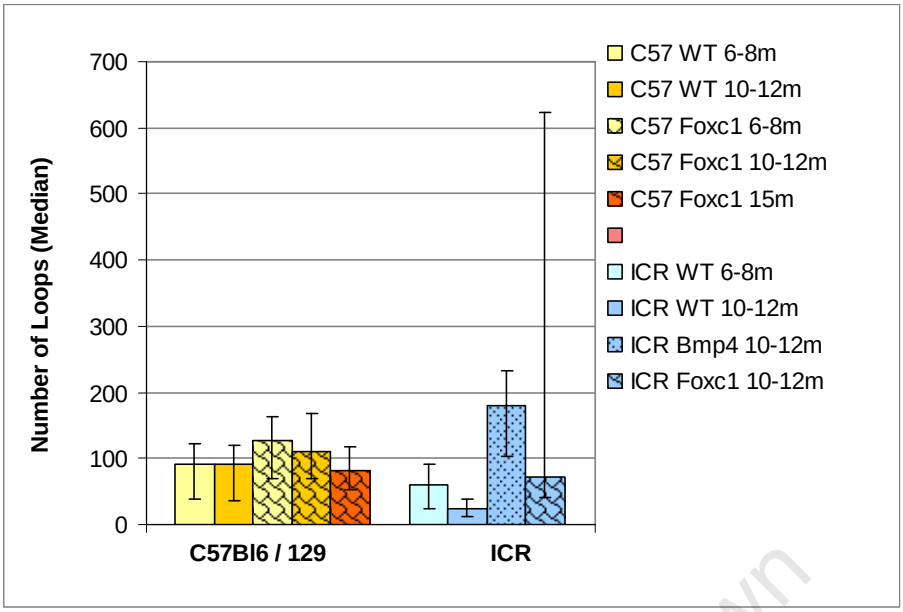

Figure 3.35: The complexity of the corneal arcades in normal (WT), *Foxc1*$^{+/-}$ and *Bmp4*$^{+/-}$ mice.

b) Bar chart showing the group median values (Y-axis) of the total number of loops (complexity) formed by the plexus of the corneal arcades. Error bars represent the range of the medians for individual mouse eyes in each group.

C57 = C57BL/6Jx129 mouse strain (yellow-orange shaded bars); ICR = ICR mouse strain (blue shaded bars); 6-8 month age group = pale yellow or pale blue background colour; 10-12 month age group = dark yellow and darker blue background colour; 15 month age group = orange background colour. WT = normal (wildtype) mice (plain yellow and blue shaded bars); *Foxc1*$^{+/-}$ genotype (brick patterned bars); *Bmp4*$^{+/-}$ genotype (fine speckled patterned bar).

(48.2)(p = 0.000** compared to ** - pale green cell in Table 3-a). Even if the mean CA length of 8-10 month old ICR WT mice is considered, it can thus be concluded that overall, *Foxc1*$^{+/-}$ has a significantly greater effect on the mean CA length in ICR mice than that in the C57 strain.

3.5.2.2 The complexity of the corneal arcade vessels in normal (WT), *Foxc1*$^{+/-}$ and *Bmp4*$^{+/-}$ mice:

The above section has shown that the extent to which capillaries of the corneal arcades penetrate into the cornea is both strain and genotype dependant. Others have reported that the number of primary and secondary branches per unit area of the limbal vasculature is also strain dependant (Chan et al., 2004). Although neovascularisation was observed in *Bmp4*$^{+/-}$ and *Foxc1*$^{+/-}$ / *Foxc2*$^{+/-}$ mouse eyes, the extent of in-growth into the cornea and the complexity of the perilimbal plexus in these genotypes are not known (Chang et al., 2001; Smith et al., 2000). In the present study, the depth of penetration of the corneal arcades into the cornea (CA length) in ICR WT mice was not necessarily accompanied by an excessive number of secondary and tertiary capillary loops within

the longer corneal arcade loops (CA in Figure 3.8b, c), whereas these were present in shorter corneal arcades in C57 WT mice (CA in Figure 3.8d, f). Since both size and complexity are architectural features of a plexus, the aim of the following analysis was to determine to what extent the complexity of the perilimbal plexus was affected by strain, genotype and age. In order to determine the complexity of the plexus throughout the limbus, each capillary loop of the corneal arcades was counted and the sum of the loops recorded for each eye (see section **2.2.5** and Figure 2.5). Since the area covered by the corneal arcades was not measured in this study, the vessel density (i.e. number of vessels per unit area) was not calculated.

3.5.2.3 An analysis of the complexity of the corneal arcades in normal (WT), *Foxc1*$^{+/-}$ and *Bmp4*$^{+/-}$ mice:

In the bar chart shown in Figure 3.35, the corneal arcades in WT mice (plain yellow or plain blue bars) are less complex than *Foxc1*$^{+/-}$ mice in the corresponding age groups (yellow or blue brick-patterned bars). ANOVA showed that strain and genotype had a significant effect on the complexity of the corneal arcades ($p < 0.01$). Within the C57 strain, the complexity of the arcades was significantly less in WT mice (86.8 and 82.93) than in *Foxc1*$^{+/-}$ mice (119.66 and 114.37) ($p = 0.0003$* compared to * - pink cells in Table 3-b). In *Foxc1*$^{+/-}$ mice, only the 15 month old animals had significantly less complex corneal arcades compared to younger mice (see dark green cells and pink cells in Table 3b).

Within the ICR strain, WT mice appear to have less complex corneal arcades than *Foxc1*$^{+/-}$ and *Bmp4*$^{+/-}$mice (compare plain coloured bars to speckled and brick-patterned bars in Figure 3.35). ANOVA showed that the overall mean complexity was significantly less in ICR WT mice (26.71) compared to that in *Bmp4*$^{+/-}$ mice (178.8), whereas *Bmp4*$^{+/-}$ mice were not significantly different to *Foxc1*$^{+/-}$ mice (118.5) ($p = 0.0003$* compare to * - bright blue cells in Table 3-b). The upper range of complexity shown in the ICR *Foxc1*$^{+/-}$ group was also caused by the same eye that showed the upper range in CA length. However, exclusion of this data point did not change the significance.

The effect of strain and genotype on the mean complexity of the corneal arcades was significant. Complexity was significantly less in ICR WT mice (55.16 and 26.71) compared to C57 mice (86.8 and 82.93) ($p = 0.0205$* compare to * - yellow cells in Table 3-b). *Foxc1*$^{+/-}$ showed a significant effect on the complexity in both mouse strains ($p = 0.0044$*,** - compare with *,** - pale green cells in Table 3-b), with similar values in each strain. However, because ICR WT mice had lower

complexity values than C57 WT mice, it can be concluded that the effect of *Foxc1*$^{+/-}$ on the complexity of the corneal arcades is greater in ICR than in the C57 strains.

3.5.2.4 Comparative morphology of the perilimbal veins in normal (WT), *Foxc1*$^{+/-}$ and *Bmp4*$^{+/-}$ mice.

The above statistical findings that show significant differences in the CA length and complexity between WT and *Foxc1*$^{+/-}$ groups are not obvious in C57 mice when viewing the morphology of the corneal arcades (Figures 3.36a-c). Here, it was difficult to distinguish between any differences in the complexity of the corneal arcades in 6-8 month C57 WT, 10-12 month C57 WT and 10-12 month *Foxc1*$^{+/-}$ mice (Figure 3.36a, b and c respectively). However, subtle differences in morphology were detected statistically by the method of analysis used in the present study. In contrast, clear differences in penetration of the arcades into the cornea and the level of complexity of the capillary loops are seen between ICR WT and C57 WT strains (compare Figures 3.36a, d). Figure 3.36 d shows a typical example of the simple organisation of the corneal arcades that were frequently seen in the 10-12 month WT group. The penetration of the capillary arcades into the cornea was substantially less (small arrow - Figure 3.36d) than that seen in the C57 strain (Figure 3.36a, b). A marked difference in the complexity and size of the corneal arcade plexus was observed in ICR *Bmp4*$^{+/-}$ and ICR *Foxc1*$^{+/-}$ mice compared to that in the ICR WT mice (Figures 3.36e, f). The arcades extend deep into the cornea and show multiple levels of capillary loops (long arrow Figure 3.36e). Blind-ending lymphatic vessels had also penetrated deep into the cornea in these mice (long arrow – Figure 3.36f). In many cases, the large and highly complex corneal arcades did not completely surround the limbus, but were observed in segments between which a normal or less aberrant morphology was found.

Since neovascularisation in *Foxc1*$^{+/-}$ and *Bmp4*$^{+/-}$ mice may occur during the development of the superficial limbal plexus, it was expected that the angioarchitecture of the perilimbal veins and circular limbal artery may also be aberrant in these mice. Despite the presence of severe neovascularisation in some *Foxc1*$^{+/-}$ and *Bmp4*$^{+/-}$ mice, the angioarchitecture of the perilimbal veins and circular limbal artery in was similar to that seen in normal mice (Figure 3.36). Typically, C57Bl/6Jx129 mice often had two perilimbal veins running in parallel which formed anastomoses at regular intervals (stars in Figures 3.36a-c) with circular limbal artery (open arrow - Figures 3.36b, c) generally located between the two perilimbal veins. On the other hand, as described in section **3.4** and shown in Figure 3.8, the organisation of the perilimbal veins in WT mice was clearly different with a single perilimbal vein and segmented circular limbal artery in the ICR strain (stars and open arrow in Figure 3.36d respectively).

Figure 3.36: The relative size and complexity of the superficial perilimbal plexus in normal (WT), *Foxc1*$^{+/-}$ and *Bmp4*$^{+/-}$ mice.

a) WT C57BL/6Jx129 mouse eye in 6-8 month age group: The corneal arcades form primary (short white arrow) and secondary capillary loops (long white arrow) that form anastomoses with the single circular limbal artery (open arrow) and branched perilimbal vein (star). Bar = 100 µm

b) WT C57BL/6Jx129 mouse eye in 10-12 month age group: The corneal arcades are similar in size and complexity to that seen in Figure 3.14 a. The double perilimbal veins (stars) are typical of the C57Bl6 strain (see also Figures 3.8 d and f). Open arrow indicates the circular limbal artery. Bar = 100 µm

c) C57BL/6Jx129 *Foxc1*$^{+/-}$ mouse eye in 15m age group: The size and complexity of the corneal arcades and vascular organisation of the perilimbal veins (stars), circular limbal artery (open arrow) and lymphatic vessels (long arrow) are similar to that seen in normal mouse eyes. Bar = 100 µm

d) WT ICR mouse eye in 10-12 month age group: The corneal arcades are markedly less in number and than that seen in the C57 strain. The arcades anastomose with a singular perilimbal vein (star) and circular limbal artery (open arrow). Long arrow indicates a blind-ending lymphatic vessel in the cornea. (Also see Figures 3.8 a, b, c, and e). Bar = 100 µm

e) ICR *Bmp4*$^{+/-}$ mouse eye in 10-12 month age group: The corneal arcades show extensive branching (complexity) and a marked penetration into the cornea compared to the normal ICR mouse eye. The perilimbal vein (star) and circular limbal artery (open arrow) appear normal in these mice. The long arrow indicates a tertiary capillary loop. Bar = 100 µm

f) ICR *Foxc1*$^{+/-}$ mouse eye in the 10-12 month age group. The complexity of the corneal arcade plexus is very extensive and penetrates deep into the cornea. Blind ending lymphatic vessels (long arrow) have also penetrated the cornea. Open arrow indicates the circular limbal artery. Star indicates the single perilimbal vein. Bar = 100 µm

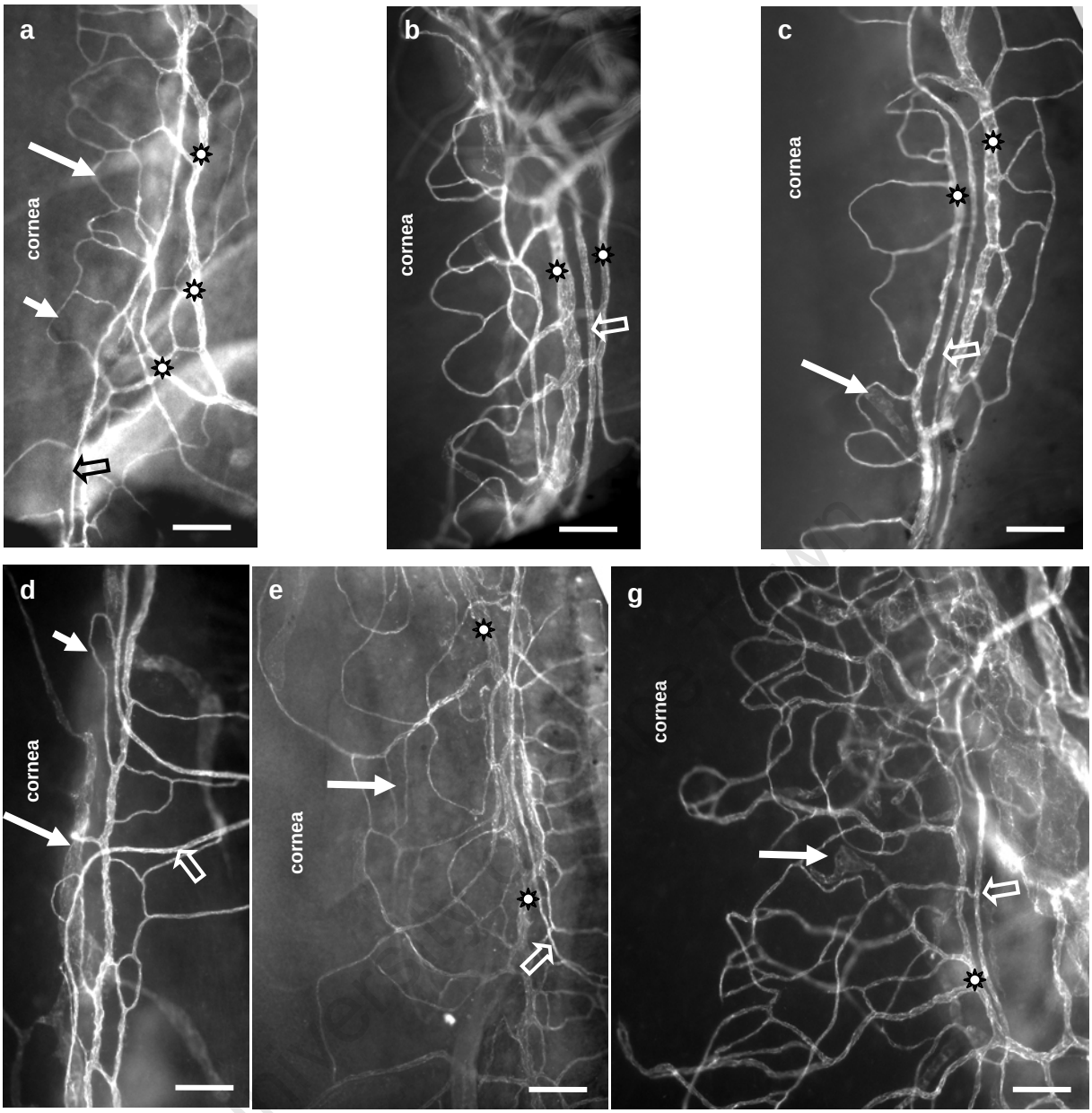

Figure 3.36: The relative size and complexity of the superficial perilimbal plexus in normal (WT), *Foxc1*$^{+/-}$ and *Bmp4*$^{+/-}$ mice

CHAPTER 4

Discussion

Anterior segment dysgenesis (ASD) is a developmental syndrome arising from one or more defective genes that negatively influence the development of the trabecular meshwork and Schlemm's canal, thus increasing the risk of IOP and predisposing the individual to glaucoma. The aetiology of ASD is poorly understood and knowledge of the normal development of the aqueous vessels is incomplete. The mouse has been extensively used as a model to study the effect of genes implicated in anterior segment dysgenesis. Previous studies of the murine aqueous outflow pathway have been limited to scrutiny of histological sections. The three-dimensional imaging in this study reveals the full extent of Schlemm's canal, its morphological features and peculiarities, and provides details of the anatomical organisation and development of all the aqueous outflow vessels and limbal vasculature. Of particular value to this study was the application of the wholemount PECAM-1 immunofluorescent labelling technique that enabled the unequivocal discrimination between the different vessel phenotypes.

Haploinsuffiency of *Foxc1* and *Bmp4* in mice results in anterior segment dysgenesis, (Chang et al., 2001; Smith et al., 2000). Immunofluorescent imaging enabled analysis and reconstruction of the outflow vessels in *Foxc1* and *Bmp4* heterozygous mice bred on the C57BL/6Jx129 and ICR backgrounds. This approach has provided further clues about the role of these genes in ocular development.

PECAM-1 is a suitable marker for all limbal vessels.

In order to conduct a detailed study of the entire posttrabecular outflow pathway, the organisation of aqueous vessels and limbal vasculature had to be viewed in three dimensions throughout the entire limbus. The pan-endothelial cell marker PECAM-1 has previously been shown to be expressed by all blood and lymphatic vessels, as well as by the endothelium of Schlemm's canal in humans (Heimark et al., 2002; Read et al., 2007). This study confirmed that this antibody could also be used to detect Schlemm's canal in mouse eyes. Positive identification of Schlemm's canal was achieved by comparing the location of PECAM-1 immunostained vessels in frozen sections with the corresponding blood vessels and Schlemm's canal in toluidine blue or haematoxylin and eosin-stained histological sections. (The results also demonstrated that methanol fixation of the tissues yielded the best signal intensity with the lowest background fluorescence. This technical achievement was important because if the background had not been successfully lowered, it would

not have been possible to easily/clearly visualise Schlemm's canal. This is because it lies deep and underneath the superficial perilimbal vessels).

Having shown that PECAM-1 stains Schlemm's canal in cryosections, the next objective was to identify Schlemm's canal and the related limbal vasculature in wholemounts of the anterior segment using PECAM-1 antisera. To achieve this, arteries, veins, lymphatic vessels and Schlemm's canal needed to be morphologically distinctive so that each vessel could be identified, and so that a reconstruction of the three-dimensional organisation of the vessels of the aqueous outflow pathway could be completed. The PECAM-1 staining revealed a complex network of limbal vessels with different widths, contours (e.g. smooth, varicose, irregular, and branching) and staining intensities. Importantly, the different sizes and shapes of the endothelial cells lining the various limbal vessels were clearly delineated by peripheral PECAM-1 distribution. At the onset of this study, there were no known studies of murine blood vessels stained by PECAM-1 that clearly defined the different vascular phenotypes. Therefore, identification of arteries, veins and lymphatic vessels in the mouse limbus was reliant on the morphological features of these different vessel phenotypes reported in similar wholemount studies of other tissues (Ezaki et al., 2001; Gale et al., 2002; Baluk et al., 2004, 2004a; Murfee et al., 2007; Baluk and McDonald,, 2008). Lymphatic vessels were specifically identified since they were LYVE-1 positive. It was not possible, however, to use the above comparative approach to identify the murine Schlemm's canal. Instead, Schlemm's canal was identified by synthesis of two-dimensional and three-dimensional information. Firstly, as shown in this study and that by others (Chang et al., 2001; Smith et al., 2001, 2001a; Libby et al., 2003), in histological sections, Schlemm's canal in normal mice is always broad and flattened, and is always located deep in the limbus, at least 50-60 μm below the superficial limbal vessels. This depth and shape information was used to direct the analysis of images arising from the 3-D optical sectioning. The most important identification feature of Schlemm's canal was the evidence of vessels (collector channels) linking the canal to the superficial (venous) vasculature.

Thus, as shown in Table 4, the combination of phenotype identification described above, the specific shape and size of the endothelial cells in the different vessels and the staining intensity and distribution of PECAM-1, enabled the construction of a detailed map of the posttrabecular outflow pathway and limbal vasculature.

	Vessel morphology	Endothelial cell morphology	PECAM-1 staining intensity
Arteries arterioles	"rigid" vessels of uniform width along unbranched segments	Relatively short cells with fusiform shape, Cell borders are straight	Very intense staining at cell borders
veins	More flexuous / sinuous vessels with small variations in width	Slightly larger cells than seen in arteries. Cell borders are straight	Intense staining at cell borders
capillaries	Narrow vessels (7-10 um in width)	Narrow fusiform cells. Cell borders not easily distinguished.	Intense staining
Lymphatic vessels	Moderately large varicose (sac-like) vessels with blind-ending extensions protruding into the cornea. Valve-like structures present at regular intervals and at bifurcations within the vessel.	Large squamous cells with ruffled cell borders.	Moderate to weak PECAM-1 staining. Intense staining with LYVE-1 antibodies.
Schlemm's canal	Mainly a single vessel of uneven width with intermittent splitting into two short parallel vessels and occasional plexuses.	Outer wall of the canal is lined with large endothelial cells. Cells lining the inner wall are smaller and more variable in size. Possible intercellular pores are visible in the endothelium lining the inner wall. .	Weakest PECAM-1 signal relative to other vessels. Does not express LYVE-1.
Collector channels	Different vessel phenotypes. Long capillary-like vessels that travel obliquely through to the superficial limbus. Short, vein-like vessels that form a perpendicular path from the canal to the superficial limbus. All collectors display dilatations (putative ostea) where they insert into the outer wall of the canal. No dilatations are present at points of anastomoses with the superficial limbal vessels.	Similar to veins in wider collectors, and to capillaries in narrow collectors.	Intense staining

Table 4: Comparative morphological features of the murine limbal vessels.

The anatomical organisation of the posttrabcular aqueous outflow pathway and limbal vasculature in the normal mouse eye.

This study describes the detailed anatomical organisation of the aqueous outflow vessels and the limbal vasculature in the normal mouse eye. An overall view is shown in a composite image that was generated from images captured in sequence around the limbus (Figure 4.1). By comparing the relative location of the identified vessels to that reported in the limbus of other species (Morrison et al., 1995; Bron et al., 1997, Selbach et al., 1998), it was then possible to name the various vessels. The superficial perilimbal vasculature receives arterial blood from the lateral and medial long posterior ciliary arteries (LPCA) and two anterior ciliary arteries (ACA) that arise from the inferior and superior extraocular muscle vascular beds. Each ACA and LPCA feeds into separate arterial segments (four segments in total) that make up the circular limbal artery (CLA 1-4 in Figure 4.1). Each CLA segment traverses approximately 25% of the limbus and drains into the perilimbal veins (PLV). By contrast, the perilimbal veins (either a single vein or two interconnected veins in ICR and C57BL/6Jx129 mice respectively) form a continuous ring around the limbus. These veins anastomose with the corneal arcades (CA), episcleral capillary plexuses (Epi) and the distal ends of the circular limbal arterial segments. There are few arteriovenous anastomoses (AVA) which connect the anterior ciliary arteries and episcleral veins (EPI veins). AVAs act as shunts between arteries/arterioles and veins/venules and provide a mechanism that

exerts resistance to flow. AVAs are thought to play a role in regulating the outflow of aqueous humour and are numerous in human, primate, rabbit and rat eyes (Bron et al., 1997; Selbach et al., 1998, 2005). However, the low number of AVAs in the mouse eye suggests that these do not play a significant role in regulating the outflow of aqueous into the circulatory system in this species.

The organisation of the corneal arcades was visibly different in ICR and C57BL/6Jx129 mice. In both strains, the penetration of the corneal arcades into the cornea was ~105 μm. On the other hand, the number of branches and anastomoses in the corneal arcades ("complexity") was ~50% greater in C57BL/6Jx129 than in ICR mice. These findings support the notion of heterogeneity of the superficial limbal vessels between mouse strains and extend those reported by Chan et al. (2004). The significance of these differences will be discussed later in this chapter.

The anatomical organisation of the superficial limbal vasculature shown in this study differs somewhat to that reported by Ninomyia et al. (2006). For instance, these authors describe two iridociliary ring arteries; one that is supplied by the anterior ciliary arteries and the other by the long posterior ciliary arteries. The former "ring" artery supplies the ciliary body whereas the latter "ring" artery supplies the iris. The present study confirms the presence of a "ring" artery that supplies the iris (here referred to as the major arterial circle of the iris). However, no other branches off the anterior ciliary artery, other than the circular limbal arterial segments, were seen in this study. Thus it can be concluded that the ciliary body receives blood via branches off the major arterial circle of the iris and/or the long posterior ciliary arteries. Whilst these authors report that the conjunctiva is supplied by the anterior ciliary arteries, it is not clear how the superficial limbal vasculature is supplied or drained. This is reflected in Figure 3 in Ninomiya et al. (2006) which shows an unbranched vessel (artery) that traverses above the perilimbal plexus. This artery penetrates the limbus and comes to lie under (internal to) the iridial vessels. However, there is clearly no anatomical similarity between this artery and the circular limbal arteries seen in the present study. By contrast, the vascular organisation, the arterial supply to and, the venous drainage of the limbus reported in the rat is virtually identical to that shown in the present study with the exception that in the rat, the circular limbal artery appears to completely encircle the limbus and the capillary bed of the corneal arcades is more complex (Morrison et al., 1995).

This study shows that extending from the perilimbal veins (and occasionally from the venous side of the corneal arcades) into the deep limbus are several collector channels (CC – Figure 4.1) of different widths and lengths that connect to Schlemm's canal. [Some of these channels displayed a hook-shape as shown in the aqueous veins in the human eye (Dvorak-Theobald, 1934, 1955;

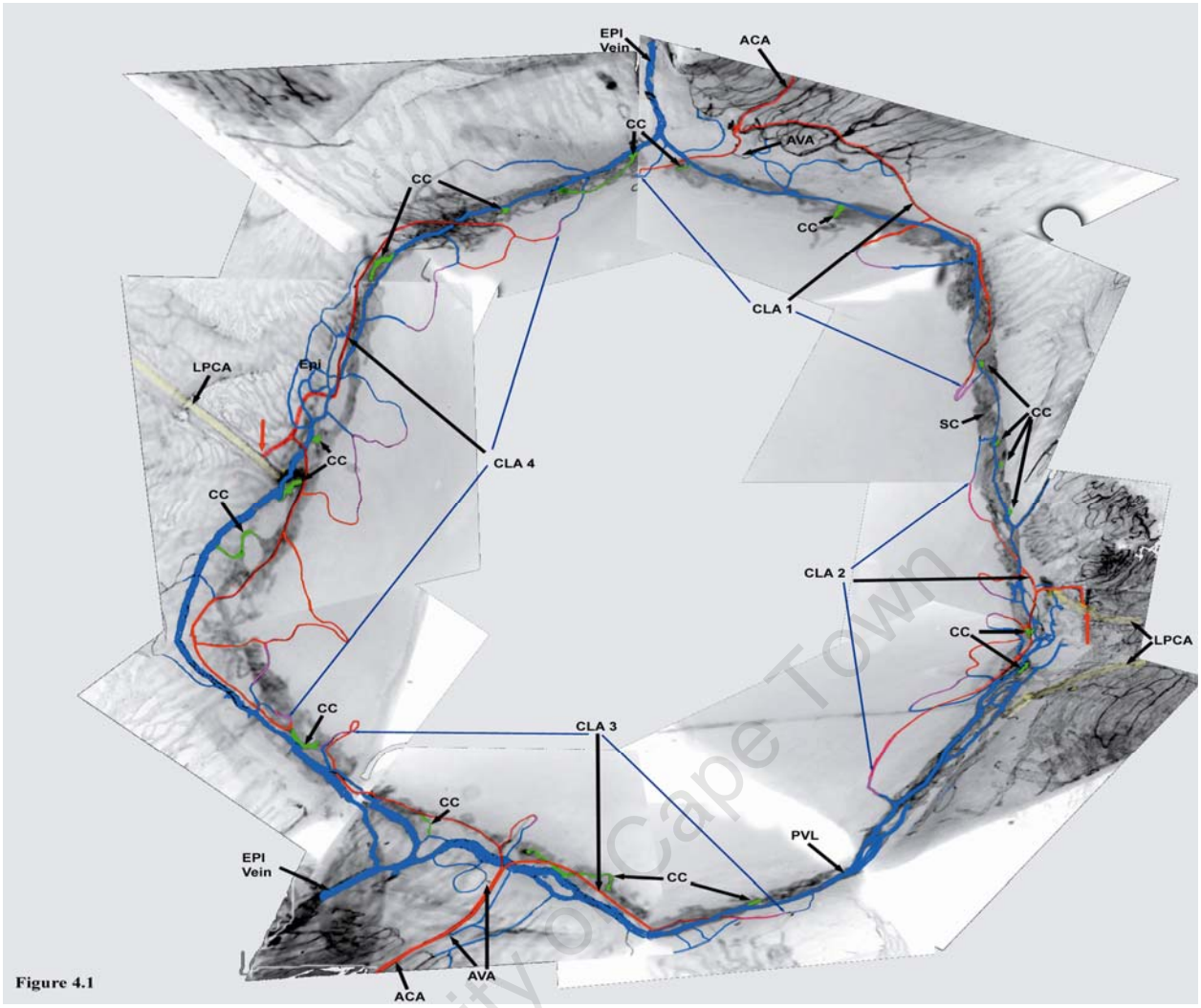

Figure 4.1: Three-dimensional organisation of the limbal vasculature in the normal mouse eye (ICR strain).

ACA = anterior ciliary artery, AVA = arteriovenous anastomoses, CA = corneal arcades, CC = collector channels, CLA 1-4 = different segments of the circular limbal artery – blue arrows indicate boundaries of each segment. EPI vein = episcleral vein, Epi = episcleral plexus, LPCA = long posterior ciliary artery, SC = Schlemm's canal (large grey vessels located in the deeper optical plane). Red arrows indicate the point where the LPCA branches to feed the CLA

Ashton, 1952)] The distribution of collector channels around the limbus appears to be random,, but generally there are more channels located closer to the main venous outflow routes from the limbus (these were generally associated with four extraocular muscles). Overall, ICR mice had ~20% more collector channels than the C57BL/6Jx129 mice. However, the number of collector channels varied considerably within each strain and between eyes from individual mice. In ~85% of wildtype mice, the difference in the number of channels was less than 25% between eyes. However, in a few mice, this difference could be as much as 30 to 40%. This apparent randomness was also reflected by the statistical analysis which showed that overall there were no significant differences between left and right eyes.

Thus in mice, the aqueous outflow pathway that links Schlemm's canal to the circulatory system is simple and direct. These findings support and extend that reported by Smith et al. (2002). This is in contrast to humans and primates where most collector channels link to a deep scleral plexus from which veins communicate with the episcleral veins (Dvorak-Theobald, 1934, 1955; Ashton, 1951; Jocson and Sears, 1968, 1969; Bron et al., 1997).

The three dimensional imaging in this study provided a particularly revealing picture of Schlemm's canal in the mouse. Of all the vessels in the limbus, Schlemm's canal was generally the broadest. As can be seen in Figure 4.1, the width and morphology of the canal varies considerably throughout the limbus. The single broad, canal-like vessel was interspersed with regions displaying large varicosities (alternating wide and narrow segments). In addition, short diverticuli extended anteriorly. Sometimes the canal bifurcated into two or more vessels forming a "plait-like" plexus. Overall, the morphology of the murine Schlemm's canal was found to be similar to that shown by microcorrosion casts of the human and rat eyes (Ashton, 1951, 1952; Ashton and Smith 1953; Morrison et al., 1995). The mean width of Schlemm's canal was ~10% wider in the ICR (85 μm) than in the C57BL/6Jx129 mice (~75 μm). In both strains, the height of the canal was ~10-15 μm. Within an individual mouse, the width of the canal could be as narrow as 10 μm and as wide as 260 μm in rare instances. The measurement of the average width however, is not particularly useful when very extreme variations in widths occur. Therefore, to derive more revealing information about the overall "pattern/shape" of the canal, an analysis of the variability of width was done. This revealed that in normal mice, the frequency of width changes along substantial portions of Schlemm's canal was relatively low.

This study shows that the morphological features of the murine Schlemm's canal are also similar to lymphatic vessels. These include the variable shape of the canal as well as a weaker PECAM-1

staining intensity compared to that seen in veins and arteries. This latter finding supports that reported by Heimark et al. (2002). It has been proposed that the inner wall of Schlemm's canal has properties displayed by blood vessels in some instances and by lymphatic vessels in other instances. In addition, the levels of expression of a few endothelial cell markers are more typical of lymphatic endothelial cells than those in blood vessels (Ramos et al., 2007). This dual phenotype is also seen in the endothelial cells lining the hepatic sinusoids which, like lymphatic vessels and the inner wall of Schlemm's canal, also lie on a discontinuous basement membrane devoid of pericytes (Ramos et al., 2007). LYVE-1 is expressed by endothelial cells lining the hepatic sinusoids in mice (Mouta Carreira et al., 2001), but it is not yet known if this is true for Schlemm's canal (Ramos et al., 2007). LYVE-1 was not detected in the murine Schlemm's canal. This study also clearly showed that there was no anatomical relationship between Schlemm's canal and LYVE-1 positive lymphatic vessels in the limbus. Lymphatic vessels were locate internal to the superficial limbal blood vessels and formed a discontinuous perilimbal ring from which blind-ending vessels extended into the cornea. The discontinuous perilimbal lymphatic vessels drain into a network of episcleral lymphatic vessels in which structural formations resembling secondary valves were observed. No connections between these lymphatic vessels and other blood vessels were observed in this study.

The sequence and timing of the development of the posttrabecular aqueous outflow vessels and superficial limbal vasculature.

The development of the post-trabecular aqueous outflow vessels in the mouse eye is not yet fully understood. Although some studies have shown the time points during which the primitive Schlemm's canal becomes evident, the origin/source of the canal is not yet known (Vanden Hoek et al., 1987; Smith et al., 2001).

Morphogenesis of Schlemm's canal

During the course of the present study, the following specific issues were considered:

- Does the murine Schlemm's canal develop *de novo* as suggested by the findings of Ramírez et al. (2004)? If the canal forms *de novo*, then does it form by vasculogenesis or haemovasculogenesis?

  OR

- Does the murine Schlemm's canal develop by an angiogenic process from downgrowths of the limbal vasculature as proposed by Smelser and Ozaniks (1971) and Hamanaka et al., (1992)? If the canal forms by angiogenesis, then from which vascular bed is the canal derived (i.e. from the superficial limbal vasculature or the uveal vasculature)?

In order to establish how, or from where the murine Schlemm's canal develops, it was necessary to determine when the Schlemm's canal was/is first evident, then to examine earlier time-points in order to obtain information about the preceding events. The approach, therefore, was to first examine the older postnatal mice (when Schlemm's canal was expected to be present as described previously (Smith et al. 2001)), then progressively move to earlier time points until a recognizable canal or complete "vascular" ring could not be seen in the deep limbus. It was found that this time-point was between P2 and P3. However, one of the major challenges in examining the P2 stage was to definitively identify the primitive Schlemm's canal. Since structures other than PECAM-1 positive vessels in the wholemounts of the limbus were not stained, it was difficult to relate the position of the vessels deeper in the limbus to any particular structure, for example to the trabecular meshwork Therefore, indirect criteria were used to identify the primitive Schlemm's canal at P2 as follows.

The first criterion was that vessels or vascular segments that could be considered as the primitive Schlemm's canal would be expected to be circumferentially arranged in the deep limbus. At P2, short vascular sprouts and rudimentary sprouting vascular segments orientated in the circumferential plane were indeed seen arising from the terminal ends of penetrating intralimbal vessels (red vessels and segments 1-4 in Figure 4.2a, see also Figures 3.12-3.15). Based on the circumferential orientation of these vascular segments, it could be concluded that these were either 1) the anlagen of Schlemm's canal, or 2) a primitive intrascleral vascular plexus. If these vascular segments were the anlagen of Schlemm's canal, then one would expect that these vessels would remodel at later postnatal ages to form a recognisable Schlemm's canal. If, however, these segments were not destined to be Schlemm's canal, but were to become an intrascleral plexus, then one would expect to see yet another set of PECAM-1 stained vessels deeper in the limbus at later postnatal ages representing the Schlemm's canal anlagen. Since the latter was never seen, this provided (indirect) evidence that these vessels were the anlagen of Schlemm's canal.

The second criterion was that if the circumferentially arranged vessels or vascular segments were precursors of Schlemm's canal, then they would lie deep in the limbus and thus closer to the choroidal and ciliary body vasculature. At all postnatal stages, these circumferentially orientated vascular segments were located between the superficial perilimbal plexus and the choroidal vasculature, lying deep in the limbus, close to the latter vascular bed. This was deduced from the distance in the Z-plane between these vessels and the superficial limbal vessels and the choroidal vasculature. This difference is also evident by the long (red) and short (blue) vessels that link the

Figure 4.2: Three-dimensional reconstruction of the morphogenesis of the posttrabecular aqueous outflow vessels in the mouse.

a) The organisation of limbal vessels at P2 as viewed from within the limbus: Unbranched blind-ending vessels (green) terminate in the mid limbus. In the deep limbus, branching vessels (red) give rise to vascular sprouts (1, 2). A vascular segment (3) is connected via two or more vessels to the superficial perilimbal plexus. Another segment (4) shows the connection of the vascular segment to the superficial limbal and uveal vasculature (via the red and blue vessel respectively).

b) A plasticine model depicts the anlagen of Schlemm's canal at P2-P3: SC = the putative Schlemm's canal (green structure) has formed from the fusion of two vascular sprouts arising from two collector channels (blue structures). Primary sprouts (yellow structures) emerge in all directions of the putative canal.

c) A plasticine model depicts the early formation of the primitive plexus of the putative Schlemm's canal at P3-4: The distal ends of the longer vascular sprouts (yellow structures) have fused with the "central" vessel (green structure - SC) to form a primary plexus. Secondary sprouts (pale orange structures) emerge from the primary plexus (yellow structures).

d) A plasticine model depicts the early expansion of the putative Schlemm's canal at P6: The fusion of the former primary plexus in (c) with the "core" vessel causes this vessel to increase in diameter/width. New tertiary sprouts (pale orange structures emerge predominantly from the lateral and exterior (upper) surfaces of the plexus of the primitive Schlemm's canal. A secondary plexus is formed from the "secondary" sprouts in (c).

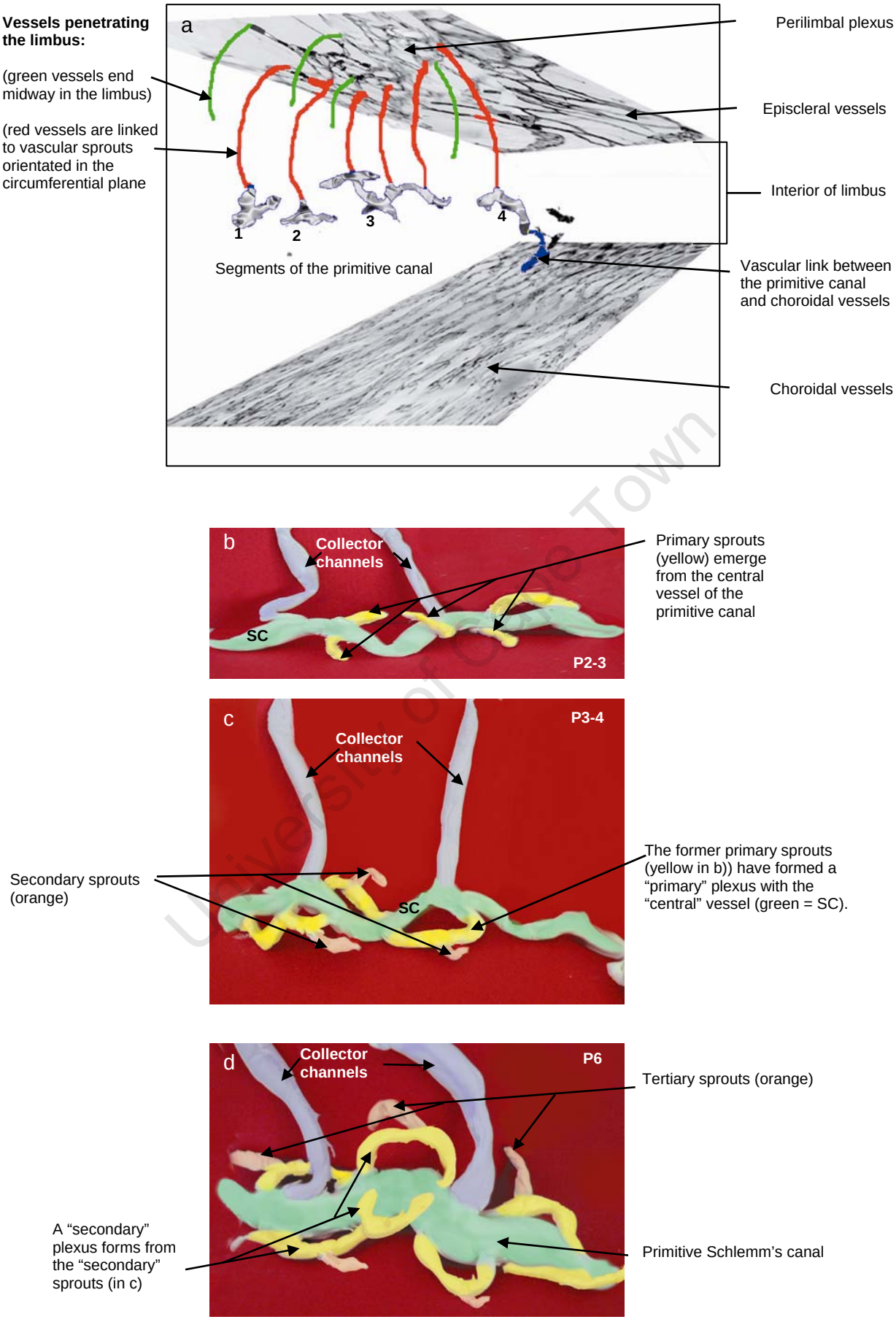

Figure 4.2: Three-dimensional reconstruction of the morphogenesis of the posttrabecular aqueous outflow vessels in the mouse.

circumferential vessels to the superficial limbal vessels and choroidal vessels respectively (Figure 4.2a). These vascular segments contained erythrocytes and were located posterior to the vasculature of the ciliary processes. This is in keeping with the location of the primitive Schlemm's canal (seen as blood vessels) reported in histological sections (Smith et al., 2001). Other vascular structures were not observed between these circumferentially orientated vascular segments and the choroidal or the superficial limbal vasculature at all postnatal ages. Therefore, based on these findings it was concluded that the primitive vascular segments seen at P2 were indeed the anlagen of Schlemm's canal.

The above two lines of evidence also enabled one to answer the question of whether the Schlemm's canal develops *de novo* or by angiogenesis. The presence of blind-ending vessels that penetrate the interior of limbus, strongly suggests that these are the precursors of the collector channels, and it is from these that the circumferential Schlemm's canal anlagen emerge. It is recognised that this is insufficient evidence on its own, and that it is theoretically possible, that these blind-ending vessels could connect to the "anlagen of Schlemm's canal" which had formed de novo. In this case, one would expect to see at least some isolated segments of the primitive Schlemm's canal (that were not connected to any other vessels). This scenario was never observed. In conclusion, at this stage, the evidence is in favour of the angiogenic model. Finally, further supportive evidence is the presence of erythrocytes in the "Schlemm's canal segments" that were connected to the vasculature (circulatory system) at two or more points thus enabling blood flow.

The next question is from which vascular bed is Schlemm's canal derived? Connectivity was seen between the anlagen of the canal and choroidal vessels and the superficial limbal vessels with a greater number of connections between the latter vascular bed. If the anlagen of Schlemm's canal are associated with vessels arising from the choroidal vasculature, then one would expect to find some circumferentially orientated vascular segments solely connected to the choroidal vessels. This was never seen. Instead, several vascular segments were connected only to the superficial limbal vasculature. Thus it can be concluded that the origin of the murine Schlemm's canal is from vessels arising solely from the superficial limbal vasculature.

Further morphological changes to these anlagen were then studied at postnatal ages from P3 through to P14 at which stage the typical canal-like morphology was present throughout the deep limbus. Up to the age where the "adult-like" form of Schlemm's canal occupied the entire limbus (P12), various levels of "maturation" were seen in different segments of the developing canal.

The morphological features that reflect the most mature forms which also formed a substantial portion of the developing Schlemm's canal from P3 to P12 are summarised as follows: At P3 sprouting vascular segments were longer and more complex than that seen at P2 with plait-like loops surrounding a central vessel (compare Figures 4.2b and c). The first evidence that the rudimentary plexus of the primitive Schlemm's canal had completely encircled the limbus was seen at P4. This deep perilimbal vascular ring consisted of a wider region of sprouting peripheral vessels that spiralled around closely-knit vessels that surrounded the thicker "core" vessel (Figure 4.2c). At this stage erythrocytes were sparse in the primitive Schlemm's canal but were not detected in the canal beyond P4.

A canal-like morphology first emerged at P8 in portions of the primitive Schlemm's canal. At subsequent postnatal ages, progressively greater portions of Schlemm's canal showed this canal-like morphology, and by P14, much of the canal appeared to be similar to that seen in adult mice. At this stage, the width of the primitive Schlemm's canal had increased approximately three-fold above that at the onset of its morphogenesis. Between P10 and P14, there was a progressive increase in the size of the endothelial cells lining Schlemm's canal. The timing of this change to the size of the endothelial cells correlates with the presence of "giant" vacuoles seen at P14 reported by Smith et al. (2001), and suggests that aqueous fluid is being transported into the canal. Throughout all stages of development, Schlemm's canal remained linked to the superficial limbal vessels via the numerous putative collector channels first seen at P2. In contrast, connections to the choroidal vessels were very rarely observed beyond P3. The collector channels were substantially more numerous at P14 compared to the numbers seen in adult mice, suggesting that many of these regress at a later stage. This suggests that although "morphologically mature", the Schlemm's canal may not necessarily have reached functional maturity. This is in keeping with the report of more giant vacuoles in the inner wall endothelium of Schlemm's canal at P18-21 than at P14 (Smith et al., 2001).

Remodelling of the superficial limbal vasculature

At P2, the superficial limbal vessels were not morphologically distinguishable as arteries or veins (as seen in the adult mouse eye), but formed a planar / relatively flat dense perilimbal plexus. This plexus was connected via several morphologically indistinct vessels (putative episcleral veins and anterior ciliary arteries) to the vasculature of the exterior ocular muscles, thus indicating that it was connected to the circulatory system. The first evidence of an arterial phenotype (the presumptive circular limbal artery - CLA) was observed at P4 and was recognised as short unbranched vessels within the "undifferentiated" plexus. At successive postnatal ages, the density

and complexity of the plexus reduced as the presumptive CLA, perilimbal veins and corneal arcades became morphologically more distinct. Connectivity between the CLA and a now recognisable anterior ciliary artery and the posterior ciliary artery first became evident at P8. In contrast to Schlemm's canal which shows a mature morphology at P14 the superficial perilimbal plexus, although substantially remodelled, had not yet reached the same level of maturation seen in adult mice. This relative immaturity may be associated with the closed eyelids which generally open from P12-14. It is postulated that once the eyelids have opened, that the capacity to absorb oxygen from the atmosphere may induce more rapid remodelling of this plexus to its adult form. Further studies using 14 to 60 day old mice are required to reveal the temporal and architectural changes to the superficial perilimbal vasculature through to adulthood.

As stated above, the perilimbal lymphatic vessels were present at P2 and were linked to a network of lymphatic vessels in the episclera. At P3, putative secondary valves were seen points where these vessels branched, and at P4, these valves were also seen in the linear segments of the lymphatic vessels. Thereafter, no further morphological changes were evident. Importantly, there was no evidence of any connectivity between the lymphatic vessels and Schlemm's canal, or to other blood vessels in the portion of the anterior segment revealed in the PECAM-1 immunostained wholemounts.

From the findings in this study it can be seen that the three-dimensional imaging approach has extended the knowledge of the development and the anatomical organisation of the murine posttrabecular aqueous outflow pathway and associated superficial limbal vasculature. The next objective was to determine whether the same imaging approach could advance the understanding of the role of *Foxc1* and *Bmp4* on this pathway.

The effect of *Foxc1* haploinsufficiency on the posttrabecular aqueous outflow pathway and limbal vasculature.

The present study revealed that all components of the posttrabecular aqueous outflow pathway were abnormal in *Foxc1*$^{+/-}$ mice. Similar to that reported by Smith et al. (2001) for other mouse strains, abnormalities seen in Schlemm's canal included a significantly reduced mean width and fragmented or missing sections of the canal in both strains with ICR mice slightly more severely affected. Analysis of width variability showed that there were more frequent changes in width as compared to wild-type mice, and the changes were more substantial. The average reduction in width of 15-20% is less than the 50-60% reduction reported by Smith et al. (2001). These differences could be due to strain differences. However, a more likely possibility for these

differences is that Smith et al. (2001) did not view or analyse the entire canal, since these authors studied only representative sections.

This study has also revealed that the number of collector channels was reduced in *Foxc1*$^{+/-}$ mice as compared to wild-type mice, on both backgrounds with ~15% greater reduction in ICR mice compared to the C57BL/6Jx129 strain. One possibility is that the number of collector channels is reduced because portions of Schlemm's canal are absent. However, it was only in a few *Foxc1*$^{+/-}$ mice (less than 30%) that the canal was absent. The most likely possibility is that number of collector channels is determined during morphogenesis, and that the *Foxc1* gene plays a role in this process.

Foxc1$^{+/-}$ mice also showed no significant changes in the superficial limbal vasculature other than in the corneal arcades. These changes included an increase in the complexity as well as deeper penetration of this plexus into the corneas. These features are indicative of corneal neovascularisation. This deduction is supported by Kidson et al. (1999) who report that in *Foxc*$^{-/-}$ mice, there is an abnormal corneal stroma and evidence of corneal vascularisation. It is also in agreement with Smith et al. (2001) who show corneal neovascularisation in older heterozygous mice who have the spontaneous mutation for *Foxc1* (*Foxc*$^{ch/-}$). As seen with the other components of the aqueous outflow pathway, corneal neovascularisation was clearly more severe in ICR mice. Further discussion of the possible role of *Foxc1* in the corneal neovascularisation will follow after the next section.

The effect of *Bmp4* haploinsufficiency on the posttrabecular aqueous outflow pathway and limbal vasculature.

Similar to that seen in *Foxc1*$^{+/-}$ ICR mice, haploinsufficiency of *Bmp4* had a significant effect on the morphology of the aqueous outflow pathway. This included a reduction in the width of Schlemm's canal and in the number of collector channels. Moreover, the increase in complexity and penetration of corneal arcades in *Bmp4*$^{+/-}$ mice provides evidence of corneal neovascularisation. These findings support and extend those reported by Chang et al. (2001). Compared to *Foxc1*$^{+/-}$ mice, the penetration of the corneal arcades was not as extensive. This suggests that Bmp4 and Foxc1 act on different targets in the cornea, and a reduction in the dosage of each of these genes regulates corneal neovascularisation in different ways.

The effect of *Foxc1*$^{+/-}$ and *Bmp4*$^{+/-}$ on corneal neovascularisation.

There are a number of possible causes as to why the complexity of corneal arcades and penetration of these vessels into the cornea occurs in *Foxc1*$^{+/-}$ and *Bmp4*$^{+/-}$ mice. One cause is that structural aberrations of the corneal stroma results in larger interfibrillar spaces, improper hydration and alteration of the extracellular matrix thus allowing the ingrowth of vessels (Azar, 2006). Indeed, disruption of the collagen fibres and accompanying corneal neovascularisation has been reported in *Bmp4*$^{+/-}$ adult mice (Chang et al., 2001) and observed in *Foxc*$^{-/-}$ embryos (Kidson et al., 1999). Neovascularisation has been observed in *Foxc2*$^{+/-}$ and aged *Foxc1*$^{ch/+}$ mice and the corneal stroma appears abnormal (see Figure 3g, h in Smith et al., 2000). Although the corneal stroma was not evaluated in the present study, the above studies and the findings of the present study suggest that haploinsufficiency of *Bmp4* and *Foxc1* primarily affects the development of the corneal stroma. Therefore, during development of the perilimbal plexus, the blood vessels penetrate further into the interfibrillar spaces of the abnormal corneal stroma.

Another cause of neovascularisation could be an imbalance of the resident angiogenic factors in the cornea with the balance in favour of the proangiogenic factors (for example, VEGF, FGF, TGFα and TGFβ amongst others), or a reduction in antiangiogenic factors (e.g. endostatin, angiostatin, soluble VEGF receptor-1) (Chang et al, 2001a; Ambati et al., 2006, 2007). The corneal epithelium is the main source of the soluble VEGR receptor-1 (sVEGFR-1) which binds VEGF secreted by the corneal epithelium and stromal cells (Ambati et al., 2006, 2007). This receptor is not expressed in the corneal epithelium of *Corn-1*$^{+/-}$ mice resulting in corneal vascularisation in these mice (Ambati et al., 2007). An abnormal corneal epithelium with accompanying corneal vascularisation is also present in *Foxc1* mutants (Kidson et al., 1999) and *Foxc1*$^{+/-}$ *Foxc2*$^{+/-}$ mice (Smith et al., 2000). This suggests that *Foxc1*$^{+/-}$ may directly or indirectly influence the concentration of sVEGFR-1. Indeed, the present study reveals that neovascularisation was more severe in *Foxc1*$^{+/-}$ mice. Therefore, it is hypothesised that in addition to the influence of abnormal stroma on vessel penetration, a lower dosage of sVEGFR-1 further enhances corneal vascularisation in *Foxc1*$^{+/-}$ mice.

The effect of strain on the limbal vasculature.

Although the strains used in the present study are not closely related, it was interesting to note that *Foxc1*$^{+/-}$ mice on the non-pigmented ICR background displayed a more severe "morphological phenotype" than that shown by the pigmented C57BL/6Jx129 strain, particularly with regard to the corneal neovascularisation. A possible cause is that the genes involved in melanin synthesis (i.e. tyrosinase or tyrosine hydroxylase) can modify the expression of *Foxc1* as reported by Libby

et al. (2003) and Gould et al. (2004). Another possible cause is that there are modifier genes that are inherent to particular strains that result in a specific limbal vascular organisation and density. This is shown by a single or two perilimbal veins in ICR and C57Bl/6J mice respectively, as well as the different complexity of the corneal arcades in these strains. This heterogeneity is also reflected in the aqueous outflow vessels and thus support and extend the findings of Chan at al. (2004).

This study further extends the notion of heterogeneity within strain by the unusually low measurements of all parameters analysed in the 10-12 month ICR wildtype mice. Since these animals originated from the same litter, it is likely that there is a dominant effect of a carrier gene from the parental line that limits/partially suppresses the growth of the aqueous outflow vessels and the superficial limbal vasculature. As proposed by John et al. (1999); in order to avoid the above effects of modifier genes, wildtype and heterozygous animals should originate from the same litter. However, it was not possible to obtain wildtype littermates for the *Foxc1*$^{+/-}$ and *Bmp4*$^{+/-}$ mice as the animals used for this study were older breeders whose littermates had been discarded prior to the onset of this study. It was also not possible to obtain more mice in the 10-12 month age category as there was no ready supply of older animals during the latter part of this study. . [It is recognised that the number of mice in each group is relatively small. Nevertheless, it is felt that the greater number of data points in this study and the more thorough analysis obtained for each eye makes this acceptable to provide a meaningful statistical outcome. Indeed, the for the most part, the statistical analysis was able to detect significant differences between genotypes using the current sample size, and the data showed a similar trend in the reduced width of Schlemm's canal reported previously in *Foxc1*$^{+/-}$ and *Bmp4*$^{+/-}$ mice (Smith et al., 2000; Chang et al., 2001).]

Further evidence of heterogeneity within strains is seen by each eye having a "unique" profile based on the combination of all the parameters (i.e. width of Schlemm's canal, the number of collector channels, the depth of penetration by corneal arcades into the cornea, and the complexity of the corneal arcade plexus) analysed (Figure 4.3a). The difference in profiles between eyes and mice become more striking in *Foxc1* and *Bmp4* haploinsufficiency (Figure 4.3b, c) and provides further support for the difference in the severity of dysgenesis between eyes and animals in *Foxc1*$^{+/-}$ and *Bmp4*$^{+/-}$ (Chang et al., 2001; Smith et al., 2000). From these "unique" profiles, it is clear that the aqueous outflow vessels and corneal arcades are affected in most eyes in *Foxc1*$^{+/-}$ and *Bmp4*$^{+/-}$ mice which suggests that the penetrance of these genes may be high. Previous studies on *Foxc1*$^{+/-}$ and *Bmp4*$^{+/-}$ mice included clinical parameters that showed high penetrance in

certain strains (Chang et al., 2001; Smith et al., 2000). Since slit-lamp microscopy and ophthalmoscopic equipment were unavailable for this study, assessment of clinical phenotype and penetrance cannot be determined with certainty on the ICR and C57BL/6Jx129 backgrounds. Nevertheless, obvious synechiae were observed only in a small proportion of mouse eyes in which the canal was incomplete, and only one eye showed a displaced pupil. Based on these "clinical" features, one can therefore assume that the penetrance of *Foxc1* and *Bmp4* haploinsufficiency is low in the ICR and C57BL/6Jx129 strains.

The analysis of the aqueous outflow vessels in *Foxc1*$^{+/-}$ and *Bmp4*$^{+/-}$ mice and the observations of how these vessels develop in mice suggest that sprouting angiogenesis from the perilimbal plexus is a the key factor that eventually leads to the completeness of development of Schlemm's canal. Based on the observations of the growth patterns of the collector channels, Schlemm's canal and the superficial perilimbal vessels, the role of likely angiogenic factors and FOXC1 and BMP4 in the morphogenesis of the posttrabecular aqueous outflow pathway is proposed.

Morphogenesis of the aqueous outflow vessels: a working model.

The first component of the aqueous outflow pathway that forms is the putative collector channels. These arise by sprouting angiogenesis from the superficial perilimbal plexus in response to signals arising from the deep limbus. One of the major angiogenic factors is vascular endothelial growth factor VEGF. There are several isoforms of VEGF, some that are freely diffusible (e.g. VEGF120) and others, such as VEGF164 and VEGF189, that have affinity for the matrix and tend to set up moderate to steep gradients in the extracellular matrix (Holderfield et al., 2008). It is hypothesised that hypoxic conditions in the deep limbus arise because of growth of the eye, and it is these hypoxic conditions that trigger the initial outgrowth of the anlagen of the collector channels. Hypoxia is known to upregulate the expression of the hypoxia inducible factor (HIF-1α) which induces the expression and secretion of vascular endothelial growth factor (VEGF) (by the stromal cells in the deep limbus or by the presumptive trabecular meshwork Treins et al., 2005). The growth of the limbus may also alter the stiffness (density) of the extracellular matrix which is known to induce the expression of the VEGF receptor (VEGFR-2) in endothelial cells (Mammoto et al., 2009). In addition, the expression VEGF in the deep limbus or primitive trabecular meshwork may also be induced by Bmp4/BMP4 since it is known to upregulate VEGF expression and also stimulate angiogenesis in zebrafish, murine osteoblasts and human endothelial cells (Deckers et al., 2002; He et al., 2005; Zhou et al., 2007). At P2, the aqueous humour contains Bmp4 secreted from the ciliary body (Chang et al., 2001), and this could diffuse through the cornea and limbal stroma, stimulating VEGF expression. The detection of the phosphorylated

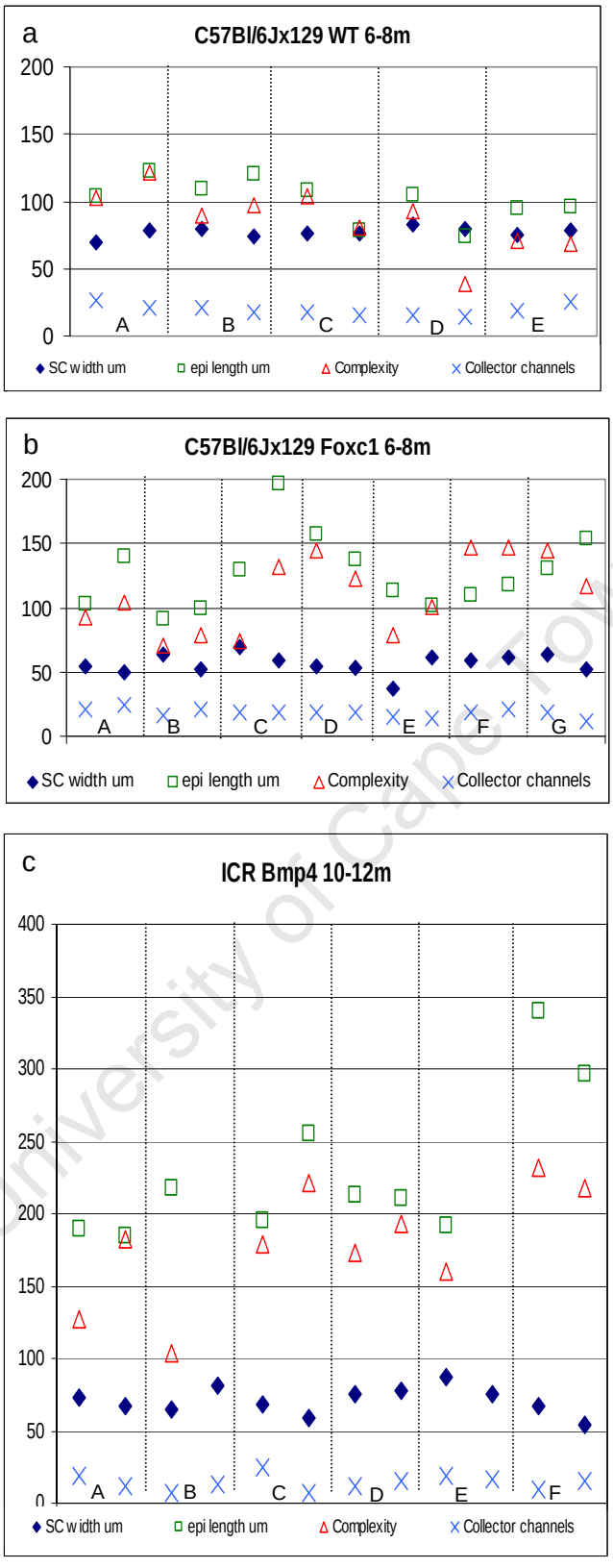

Figure 4.3: Morphological profiles of individual mouse eyes:

Profiles are based on the mean widths of Schlemm's canal, the total number of collector channels, the mean length of the corneal arcades and the total number of loops (complexity)
Individual mice are indicated (A-E in a) (A-G in b), (A-F in c) and left and right data sets represent the profiles of the left and right eyes respectively.

form of Smad1 (pSmad1) in the limbal stroma at postnatal ages (P1-P7) (Zhao et al., 2002) provides support for this hypothesis. This milieu encourages sprouting angiogenesis from the perilimbal plexus and attract the growing vessels inwards towards the increasing concentrations of VEGF.

Questions arise as to what determines the sites of sprouting and what factors guide the growing putative collector channels. Firstly, the site of sprouting may be selected or controlled by pericytes that are known to associate with primitive ("undifferentiatied") plexuses (Gerhardt and Betsholtz, 2003). It is therefore likely that pericytes are present in the primitive superficial perilimbal plexus and these may trigger sprouting from specific sites within this plexus. Secondly, since pericytes are known to be associated with the perilimbal vasculature and collector channels in the adult human eye (de Kater et al., 1990), it is possible that pericytes also accompany the downgrowing primitive collector channels as noted in other vessels (Gerhardt and Betsholtz, 2003). Thirdly, pericytes originate from neural crest cells that express *Foxc1* (Etchevers et al., 2001; Gage et al., 2005). Cells expressing *Foxc1* are present in the periocular mesenchyme at 11.5 dpc (Kidson et al., 1999; Gage et al., 2005) and therefore Foxc1 may play a role in the specification of progenitor cells that later differentiate into pericytes. Fourthly, in hypoxic conditions, HIF-1α is expressed by pericytes. This induces the expression of chordin-like 1(CHL-1) (as shown in human retinal vessels (Kane et al., 2008)) which binds to BMP4. This binding prevents the antiangiogenic effect of BMP4 and allows the endothelial cells to respond to VEGF. As stated above, a possible source of Bmp4 in the mouse eye is the ciliary body (Chang et al., 2001). In this way, pericytes may play a central role in guiding the primitive collector channels as they progress deeper into the limbus. Fifthly, neural guidance molecules expressed by the stromal cells or peripheral nerves may direct the path of the putative collector channels as shown in other blood vessels (Carmeliet and Tessier-Lavigne, 2005). In adult rats, the perilimbal plexus contains a network of nerve fibres which are structurally and functionally associated with the limbal vasculature (Selbach et al., 1998). If, in the mouse such a neural network is present, then it is possible that angiogenesis of these vessels can be triggered by angiogenic signals (i.e. VEGF) secreted by peripheral nerves (Mukouyama et al., 2002) and guided by neural guidance molecules such as netrins and semaphorins (Carmeliet and Tessier-Lavigne, 2005). Netrins and semaphorins are secreted by stromal and neurons respectively and receptors for these signalling molecules (i.e. Unc5, neuropilin and) are known to be expressed by endothelial cells at the tip of the growing vessels (Carmeliet and Tessier-Lavigne, 2005). Thus, factors that initiate sprouting angiogenesis from the superficial perilimbal plexus may be derived from one or several of the above sources. Thereafter, the growing primitive collector channels can be guided through the limbus by

pericytes, neural guidance molecules and a VEGF gradient established by the deep limbal stromal cells or mesenchymal cells of the primitive trabecular meshwork.

The next phase in the formation of the aqueous outflow pathway is the development of the anlagen of Schlemm's canal. Once the putative collector channels have reached the dense mesenchyme of the primitive trabecular meshwork reported at this stage (Smith et al., 2001), they branch perpendicularly and grow along the circumferential plane (Figure 4.2a). These initial sprouting vessels are the "core" or primary vessels that form the anlagen of Schlemm's canal. A number of questions that concern the formation of the anlagen of Schlemm's canal spring to mind.
The first question is why do the putative collector channels branch next to and not penetrate the primitive trabecular meshwork? One possible cause is that the dense packing of mesenchymal cells (Smith et al., 2001) does not provide an easy passage for the growing vessels. A second possible cause is that antiangiogenic factors may be expressed in this region at this stage. Although the expression of endostatin, a potent antiangiogenic factor, has only been reported in the human trabecular meshwork (Ohlmann et al., 2005), if it expressed in the mouse at this stage, it would provide a suitable mechanism for inhibiting the growth of the putative collector channels into the primitive trabecular meshwork. A third possibility is that Bmp4 signalling in this region may antagonise any VEGF secretion by the mesenchymal cells of the primitive trabecular meshwork. Indeed, the phosphorylated form of Smad1 (pSmad1) is reported to be present in this region during early postnatal ages (P1-P7) (Zhao et al., 2002) which suggests that Bmp4 signalling is active.

The next question is what causes the anlagen of Schlemm's canal to specifically grow in the circumferential plane. It is possible that the location of stromal cells secreting angiogenic factors may guide the growing vessels. Alternatively, the underlying mesenchymal cells of the primitive trabecular meshwork may play a role in this endeavour. To answer these questions, structural features of the developing trabecular meshwork shown in other studies were correlated with the growth pattern of the primitive Schlemm's canal at the corresponding postnatal ages. Shortly before P2, the mesenchyme of the primitive trabecular meshwork is condensed and the cell nuclei are not as elongated as at P4 as seen in histological sections (Smith et al., 2001). This suggests that prior to P2, these cells may be orientated in the circumferential plane as noted in the human foetus and thus are aligned along the same plane as the fibres of the extracellular matrix which they secrete (Hamanaka et al., 1992). This circumferential orientation of the matrix fibres may therefore provide guidance cues for the anlagen of Schlemm's canal. This notion is suggested by Hamanaka et al., (1992) and is supported by studies that show that the orientation of fibres in the

extracellular matrix defines the direction of cell division (Théry et al., 2005). At P4 when the primitive canal has completely encircled the limbus, the primitive trabecular meshwork shows signs of differentiation with the cell nuclei orientated in the anterior posterior plane (i.e. at perpendicular to the circumferential plane) (Smith et al., 2001). These findings suggest that the extracellular matrix and antiangiogenic signals produced by the trabecular meshwork play a pivotal role in the formation of and preferential orientation of the anlagen of Schlemm's canal.

The next step in the development of the aqueous vessels is the growth in width of and modelling of Schlemm's canal. One way this could be regulated is by signals from the trabecular meshwork. With the primitive Schlemm's canal now fully encircling the deep limbus, and closely associated with the future trabecular meshwork, the possibility arises that reciprocal signals between the growing canal and the trabecular meshwork will direct for development and differentiation. It has been suggested that the vasculature (particularly the role of signals from endothelial cells) has a profound effect on the differentiation of tissues during organogenesis as shown in other organs systems such as the liver, pancreas, kidney, lung, bone, and the central nervous system (Crivellato et al., 2007). Support in favour of the role of endothelial cells in inducing differentiation of the trabecular meshwork in the mouse eye, is provided by the present study which shows that the primitive canal is formed several days (6 days) before clear signs of differentiation of the trabecular meshwork are evident as reported by Smith et al. (2001). Further support for this notion is the presence of blood vessels near the undifferentiated trabecular meshwork reported in the rat, cat and human eye, (Remé et al., 1983a, b; Richardson et al., 1985; Hamanaka et al., 1992). Thus the endothelial cells in the anlagen of Schlemm's canal may induce the differentiation of the primitive trabecular meshwork that lies directly below the vessels. Thereafter, newly differentiated cells of the trabecular meshwork could provide signals that stimulate sprouting from the peripheral vessels of the primitive Schlemm's canal. Thus in this way, reciprocal signalling between these two compartments may define the final width of the canal and trabecular meshwork.

Modelling of the primitive plexus into a canal may occur as a result of changes in the flow dynamics in the limbal vasculature (Risau, 1997). At P2-P3, short vascular segments are often connected to the perilimbal vasculature by two or more putative collector channels or to the uveal vasculature (Figure 4.2a, b), and evidence of blood flow is seen in these segments (see Figure 3.11b). Between P3 and P4, the primary sprouts have fused with the central "core" vessels and have formed a plexus (Figure 4.2c). Since it appears that "bulk" flow of aqueous humour into the canal only occurs later (at P14 - in Smith et al. (2001)), it is likely that the initial modelling of

Schlemm's canal is governed by haemodynamics. Accordingly, blood flow through the primitive Schlemm's canal may increase shear forces on these vessels and drive the process of peripheral sprouting and coalescence which results in an increase in size of the "core" vessel. Evidence in favour of this is seen by the emergence of the arterial phenotype in the superficial perilimbal plexus at P4 once the primitive Schlemm's canal has encircled the limbus.

What governs the expression of the vessel phenotypes in the perilimbal plexus? The specific patterning of the perilimbal arteries and veins may lie in certain components of the vascular plexus that are destined to become arteries. Molecular markers for arteries and veins are already expressed during the early development of vessels prior to the differentiation of the vessel wall and a morphological phenotype (reviewed in le Noble et al., 2004). Foxc1, in conjunction with VEGF, specifies the arterial phenotype via the Notch1/4 signalling pathway (Hayashi and Kume, 2008). In the mouse eye, this specification could take place as early as 11.5 dpc when *Foxc1* is expressed in the cells of mesodermal origin (Gage et al., 2005), which may form progenitor endothelial cells that incorporate into the primitive perilimbal plexus which develops prenatally. Later, these predetermined vessels in the primitive perilimbal plexus become morphologically distinct as arteries as the flow dynamics changes due to the increased vascular bed provided by the developing Schlemm's canal and by the connectivity to the uveal vasculature.

The above model has proposed the role of factors that, in combination, control the development of the posttrabecular aqueous outflow pathway. Each stage of this process appears to be exquisitely regulated by the spatial and temporal expression of proangiogenic factors, the organisation of the extracellular matrix and the reciprocal signalling between the primitive trabecular meshwork and developing Schlemm's canal. Where then in the proposed model would haploinsufficiency of *Bmp4* and *Foxc1* have their affects? This and other studies have shown that haploinsufficiency of these genes can result in reduced width of Schlemm's canal and even cause its absence in some regions around the limbus.

In *Foxc1*$^{+/-}$ mice, there is sustained expression of *Foxc1* in the corneal and limbal stroma (Kidson et al., 1999). Therefore, in combination with other modifier genes, haploinsufficiency of *Foxc1* may result in the incorrect specification of pericyte progenitors in a portion of stromal cells. This may result in the absence of sprouting from the perilimbal plexus and/or guidance of collector channels in certain regions in the limbus. Subsequently, the absence of putative collector channels will lead to incomplete segments of the primitive canal. *Foxc1* is expressed in the angle mesenchyme shortly before birth, and its haploinsufficiency affects the differentiation of the

trabecular meshwork and the formation of Schlemm's canal (Smith et al., 2001). In *Foxc*$^{+/-}$ mice, the width of Schlemm's canal and underlying trabecular meshwork are similarly reduced and in areas where Schlemm's canal is absent, the trabecular meshwork is poorly differentiated or absent (see Figure 2 in Smith et al. (2001)). This provides support for the reciprocal signalling between the developing Schlemm's canal and trabecular meshwork as suggested above. Therefore, Foxc1 may initiate a cascade of events that allows the stepwise control of 1) the angiogenic signals that attract the downgrowing putative collector channels, 2) the preferential alignment of mesenchymal cells and extracellular matrix fibres in the circumferential plane to guide the anlagen of Schlemm's canal, and 3) the competency of the differentiating trabecular cells to respond to signals from the developing Schlemm's canal. If BMP4 stimulates VEGF expression in the primitive trabecular meshwork, then a reduced gene dosage and subsequent lower concentration in the aqueous humour could account for the lack of VEGF expression in some regions of the primitive trabecular meshwork, thus leading to missing or poorly formed segments of Schlemm's canal.

Conclusion.

This descriptive and genetic study has provided new and detailed information on the posttrabecular aqueous outflow vessels in mice and has provided novel insights into the development of this pathway and its relationship to the superficial limbal vasculature. It provides a platform for future studies that will focus on the spatial and temporal expression of vascular guidance cues that may play a role in the development of the murine posttrabecular aqueous outflow pathway. For example, the postulated relationship between the peripheral nerves or pericytes and the developing aqueous outflow pathway will be explored using multiple immunolabelling to detect blood and aqueous vessels, nerve fibres and pericytes using antibodies to PECAM-1, neurofilament protein and smooth muscle actin respectively. Further studies will examine the spatial and temporal expression of angiogenic factors such as VEGF or bFGF in the limbus to determine if they are expressed by the developing trabecular meshwork or specific cells such as the pericytes or peripheral nerves. Importantly, the roles of Foxc1 and Bmp4 in the growth and guidance of the aqueous outflow vessels need to be further explored. One means of pursuing this would be to use *Bmp4*$^{+/-}$ *Foxc1*$^{+/-}$ double heterozygous mice which will determine whether these genes act synergistically to govern the morphogenesis of the aqueous outflow pathway. If embryonic lethal, then one or both genes could be downregulated perinatally using conditional knockout *Bmp4*$^{+/-}$ *Foxc1*$^{+/-}$ double heterozygous mice. The above multiple immunolabelling approach can then be used to study the developing aqueous vessels and the spatial and temporal expression of angiogenic factors in the limbus in these mice.

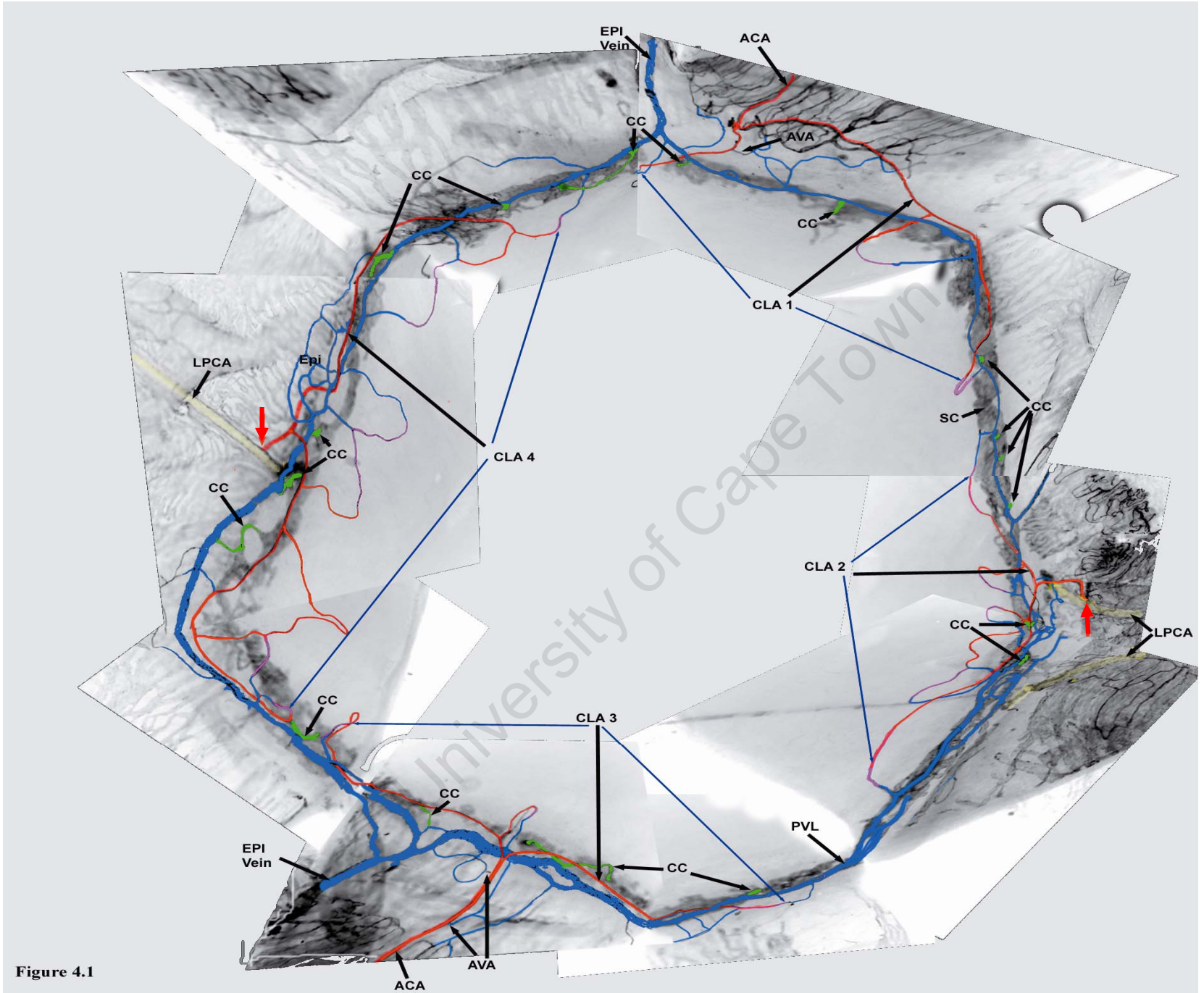

Figure 4.1: Three-dimensional organisation of the limbal vasculature in the normal mouse eye (ICR strain).
ACA = anterior ciliary artery, AVA = arteriovenous anastomoses, CA = corneal arcades, CC = collector channels, CLA 1-4 = different segments of the circular limbal artery – blue arrows indicate boundaries of each segment. EPI vein = episcleral vein, Epi = episcleral plexus, LPCA = long posterior ciliary artery, SC = Schlemm's canal (large grey vessels located in the deeper optical plane). Red arrows indicate the point where the LPCA branches to feed the CLA.

REFERENCES

Aihara, M., Lindsey, J. D. and Weinreb, R. N. (2003). Aqueous humor dynamics in mice. *Invest. Ophthalmol. Vis. Sci.* **44**, 5168-73.

Albelda, S. M., Muller, W. A., Buck, C. A. and Newman, P. J. (1991). Molecular and cellular properties of PECAM-1 (endoCAM/CD31): a novel vascular cell-cell adhesion molecule. *J.Cell Biol.* **114**, 1059-68.

Albelda, S. M., Oliver, P. D., Romer, L. H. and Buck, C. A. (1990). EndoCAM: a novel endothelial cell-cell adhesion molecule. *J.Cell Biol.* **110**, 1227-37.

Allingham, R. R., Damjii, K., Freedman, S., Moroi, S. and Shafranov, G. (2005). Shield's Textbook of Glaucoma, (ed. R. R. Allingham K. Damjii S. Freedman S. Moroi and G. Shafranov). Philadelphia: Lippincott Williams and Wilkens.

Alvarez, Y., Cederlund, M. L., Cottell, D. C., Bill, B. R., Ekker, S. C., Torres-Vazquez, J., Weinstein, B. M., Hyde, D. R., Vihtelic, T. S. and Kennedy, B. N. (2007). Genetic determinants of hyaloid and retinal vasculature in zebrafish. *BMC. Dev. Biol.* **7**, 114.

Ambati, B. K., Joussen, A. M., Ambati, J., Moromizato, Y., Guha, C., Javaherian, K., Gillies, S., O'Reilly, M. S. and Adamis, A. P. (2002). Angiostatin inhibits and regresses corneal neovascularization. *Arch. Ophthalmol.* **120**, 1063-8.

Ambati, B. K., Nozaki, M., Singh, N., Takeda, A., Jani, P. D., Suthar, T., Albuquerque, R. J., Richter, E., Sakurai, E., Newcomb, M. T. et al. (2006). Corneal avascularity is due to soluble VEGF receptor-1. *Nature* **443**, 993-7.

Ambati, B. K., Patterson, E., Jani, P., Jenkins, C., Higgins, E., Singh, N., Suthar, T., Vira, N., Smith, K. and Caldwell, R. (2007). Soluble vascular endothelial growth factor receptor-1 contributes to the corneal antiangiogenic barrier. *Br. J. Opthalmol.* **91**, 505-8.

Asai-Coakwell, M., Backhouse, C., Casey, R. J., Gage, P. J. and Lehmann, O. J. (2006). Reduced human and murine corneal thickness in an Axenfeld-Rieger syndrome subtype. *Invest. Ophthalmol. Vis. Sci.* **47**, 4905-9.

Ashton, N. (1951). Anatomical study of Schlemm's canal and aqueous veins by means of neoprene casts. Part I. Aqueous veins. *Br. J. Opthalmol.* **35**, 291-303.

Ashton, N. (1952). Anatomical study of Schlemm's canal and aqueous veins by means of neoprene casts. II. Aqueous veins. *Br. J. Opthalmol.* **36**, 265-7; contd.

Ashton, N. and Smith, R. (1953). Anatomical study of Schlemm's canal and aqueous veins by means of neoprene casts. III. Arterial relations of Schlemm's canal. *Br. J. Opthalmol.* **37**, 577-86.

Attisano, L. and Wrana, J. L. (2000). Smads as transcriptional co-modulators. *Curr. Opin. Cell Biol.* **12**, 235-43.

Austin, B. A., Coulon, C., Liu, C. Y., Kao, W. W. and Rada, J. A. (2002). Altered collagen fibril formation in the sclera of lumican-deficient mice. *Invest. Ophthalmol. Vis. Sci.* **43**, 1695-701.

Ayalon, O., Sabanai, H., Lampugnani, M. G., Dejana, E. and Geiger, B. (1994). Spatial and temporal relationships between cadherins and PECAM-1 in cell-cell junctions of human endothelial cells. *J. Cell Biol.* **126**, 247-58.

Azar, D. T. (2006). Corneal angiogenic privilege: angiogenic and antiangiogenic factors in corneal avascularity, vasculogenesis, and wound healing (an American Ophthalmological Society thesis). *Trans.*

Am. Ophthalmol. **104**, 264-302.

Babu, A. N., Murakawa, T., Thurman, J. M., Miller, E. J., Henson, P. M., Zamora, M. R., Voelkel, N. F. and Nicolls, M. R. (2007). Microvascular destruction identifies murine allografts that cannot be rescued from airway fibrosis. *J. Clin. Invest.* **117**, 3774-85.

Balazs, E. A., Toth, L. Z. and Ozanics, V. (1980). Cytological studies on the developing vitreous as related to the hyaloid vessel system. *Albrecht Von Graefes Arch. Klin. Exp. Ophthalmol.* **213**, 71-85. (Abstact only)

Baldwin, H. S., Shen, H. M., Yan, H. C., DeLisser, H. M., Chung, A., Mickanin, C., Trask, T., Kirschbaum, N. E., Newman, P. J., Albelda, S. M. et al. (1994). Platelet endothelial cell adhesion molecule-1 (PECAM-1/CD31): alternatively spliced, functionally distinct isoforms expressed during mammalian cardiovascular development. *Development* **120**, 2539-2553.

Baluk, P., Lee, C. G., Link, H., Ator, E., Haskell, A., Elias, J. A. and McDonald, D. M. (2004). Regulated angiogenesis and vascular regression in mice overexpressing vascular endothelial growth factor in airways. *Am. J. Pathol.* **165**, 1071-85.

Baluk, P. and McDonald, D. M. (2008). Markers for microscopic imaging of lymphangiogenesis and angiogenesis. *Ann. N. Y. Acad. Sci.***1131**, 1-12.

Baluk, P., Raymond, W. W., Ator, E., Coussens, L. M., McDonald, D. M. and Caughey, G. H. (2004a). Matrix metalloproteinase-2 and -9 expression increases in Mycoplasma-infected airways but is not required for microvascular remodeling. *Am. J. Physiol. Lung Cell. Mol. Physiol.* **287**, L307-17.

Banerji, S., Ni, J., Wang, S. X., Clasper, S., Su, J., Tammi, R., Jones, M. and Jackson, D. G. (1999). LYVE-1, a new homologue of the CD44 glycoprotein, is a lymph-specific receptor for hyaluronan. *J.Cell Biol.* **144**, 789-801.

Barishak, Y. R. (2003). Development of the angle of the anterior chamber in human and vertebrate animals' eyes. *Vet. Ophthalmol.* **6**, 1-2.

Battista, S. A., Lu, Z., Hofmann, S., Freddo, T., Overby, D. R. and Gong, H. (2008). Reduction of the available area for aqueous humor outflow and increase in meshwork herniations into collector channels following acute IOP elevation in bovine eyes. *Invest. Ophthalmol. Vis. Sci.* **49**, 5346-52.

Bernd, A. S., Aihara, M., Lindsey, J. D. and Weinreb, R. N. (2004). Influence of molecular weight on intracameral dextran movement to the posterior segment of the mouse eye. *Invest. Ophthalmol. Vis. Sci.* **45**, 480-484.

Berry, F. B., Lines, M. A., Oas, J. M., Footz, T., Underhill, D. A., Gage, P. J. and Walter, M. A. (2006). Functional interactions between FOXC1 and PITX2 underlie the sensitivity to *FOXC1* gene dose in Axenfeld-Rieger syndrome and anterior segment dysgenesis. *Hum. Mol. Genet.***15**, 905-19.

Bhutto, I. A. and Amemiya, T. (2001). Microvascular architecture of the rat choroid: Corrosion cast study. *Anat. Rec.* **264**, 63-71.

Bill, A. (1993). Some aspects of aqueous humour drainage. *Eye* **7**, 14-19.

Billinton, N. and Knight, A. W. (2001). Seeing the wood through the trees: a review of techniques for distinguishing green fluorescent protein from endogenous autofluorescence. *Anals. Biochem.* **291**, 175-97.

Brandt, J. D. and O'Donnell, M. E. (1999). How does the trabecular meshwork regulate outflow? Clues from the vascular endothelium. *J. Glaucoma* **8**, 328-339.

Bron, A. J., Tripathi, R. C. and Tripathis, B. J. (1997). Wolff's Anatomy of the Eye and Orbit. London:

Chapman and Hall.

Burger, P. C., Chandler, D. B., Fryczkowski, A. W. and Klintworth, G. K. (1987). Scanning electron microscopy of microcorrosion casts: applications in ophthalmologic research. *Scanning Microsc.* **1**, 223-31.

Burns-Bellhorn, M. S., Bellhorn, R. W. and Benjamin, J. V. (1978). Anterior segment permeability to fluorescein-labeled dextrans in the rat. *Invest. Ophthalmol. Vis. Sci.* **17**, 857-62.

Campos, M., Amaral, J., Becerra, S. P. and Fariss, R. N. (2006). A novel imaging technique for experimental choroidal neovascularization. *Invest. Ophthalmol. Vis. Sci.* **47**, 5163-70.

Carmeliet, P. and Tessier-Lavigne, M. (2005). Common mechanisms of nerve and blood vessel wiring. *Nature* **436**, 193-200.

Chan, C. K., Pham, L. N., Chinn, C., Spee, C., Ryan, S. J., Akhurst, R. J. and Hinton, D. R. (2004). Mouse strain-dependent heterogeneity of resting limbal vasculature. *Invest. Ophthalmol. Vis. Sci.* **45**, 441-447.

Chang, B., Smith, R. S., Peters, M., Savinova, O. V., Hawes, N. L., Zabaleta, A., Nusinowitz, S., Martin, J. E., Davisson, M. L., Cepko, C. L. et al. (2001). Haploinsufficient *Bmp4* ocular phenotypes include anterior segment dysgenesis with elevated intraocular pressure. *BMC. Genetics* **2:18. Epub;%2001 Nov 6.**, 18.

Chang, J. H., Gabison, E. E., Kato, T. and Azar, D. T. (2001a). Corneal neovascularization. *Curr.Opin.Ophthalmol.* **12**, 242-249.

Chan-Ling, T., McLeod, D. S., Hughes, S., Baxter, L., Chu, Y., Hasegawa, T. and Lutty, G. A. (2004). Astrocyte-endothelial cell relationships during human retinal vascular development. *Invest. Ophthalmol. Vis. Sci.* **45**, 2020-32.

Chen, L., Cursiefen, C., Barabino, S., Zhang, Q. and Dana, M. R. (2005). Novel expression and characterization of lymphatic vessel endothelial hyaluronate receptor 1 (LYVE-1) by conjunctival cells. *Invest. Ophthalmol. Vis. Sci.* **46**, 4536-4540.

Cook, C. S. and Sulik, K. K. (1986). Sequential scanning electron microscopic analyses of normal and spontaneously occurring abnormal ocular development in C57B1/6J mice. *Scan. Electron. Microsc.*, 1215-1227.

Craig, L. E., Spelman, J. P., Strandberg, J. D. and Zink, M. C. (1998). Endothelial cells from diverse tissues exhibit differences in growth and morphology. *Microvasc. Res.* **55**, 65-76.

Creuzet, S., Vincent, C. and Couly, G. R. (2005). Neural crest derivatives in ocular and periocular structures. *Int. J. Dev. Biol.* **49**, 161-171.

Crivellato, E., Nico, B. and Ribatti, D. (2007). Contribution of endothelial cells to organogenesis: a modern reappraisal of an old Aristotelian concept. *J. Anat.* **211**, 415-27.

Cursiefen, C., Ikeda, S., Nishina, P. M., Smith, R. S., Ikeda, A., Jackson, D., Mo, J. S., Chen, L., Dana, M. R., Pytowski, B. et al. (2005). Spontaneous corneal hem- and lymphangiogenesis in mice with destrin-mutation depend on VEGFR3 signaling. *Am. J. Pathol.* **166**, 1367-77.

Cursiefen, C., Schlotzer-Schrehardt, U., Kuchle, M., Sorokin, L., Breiteneder-Geleff, S., Alitalo, K. and Jackson, D. (2002). Lymphatic vessels in vascularized human corneas: Immunohistochemical investigation using LYVE-1 and podoplanin. *Invest. Ophthalmol. Vis. Sci.* **43**, 2127-2135.

Cvekl, A. and Tamm, E. R. (2004). Anterior eye development and ocular mesenchyme: new insights from mouse models and human diseases. *Bioessays* **26**, 374-86.

Davis-Silberman, N. and Ashery-Padan, R. (2005). Iris development in vertebrates; genetic and molecular considerations. *Brain Res.* **20**, 20-32.

de Kater, A. W., Shahsafaei, A. and Epstein, D. L. (1992). Localization of smooth muscle and nonmuscle actin isoforms in the human aqueous outflow pathway. *Invest. Ophthalmol. Vis. Sci.* **33**, 424-9.

de Kater, A. W., Spurr-Michaud, S. J. and Gipson, I. K. (1990). Localization of smooth muscle myosin-containing cells in the aqueous outflow pathway. *Invest. Ophthalmol. Vis. Sci.* **31**, 347-53.

Deckers, M. M., van Bezooijen, R. L., van der Horst, G., Hoogendam, J., van Der Bent, C., Papapoulos, S. E. and Lowik, C. W. (2002). Bone morphogenetic proteins stimulate angiogenesis through osteoblast-derived vascular endothelial growth factor A. *Endocrinology* **143**, 1545-53.

DeLisser, H. M., Chilkotowsky, J., Yan, H. C., Daise, M. L., Buck, C. A. and Albelda, S. M. (1994a). Deletions in the cytoplasmic domain of platelet-endothelial cell adhesion molecule-1 (PECAM-1, CD31) result in changes in ligand binding properties. *J.Cell Biol.* **124**, 195-203.

DeLisser, H. M., Newman, P. J. and Albelda, S. M. (1994). Molecular and functional aspects of PECAM-1/CD31. *Immunology Today* **15**, 490-5.

Dell, S., Peters, S., Muther, P., Kociok, N. and Joussen, A. M. (2006). The role of PDGF receptor inhibitors and PI3-kinase signaling in the pathogenesis of corneal neovascularization *Invest. Ophthalmol. Vis. Sci.* **47**, 1928-37.

Dvorak-Theobald, G. (1934). Schlemm's Canal: Its Anastomoses and Anatomic Relations. *Trans. Am. Ophthalmol. Soc.*. **32**, 574-95.
Dvorak-Theobald, G. (1955). Further studies on the canal of Schlemm. *Am. J. Ophthalmol.* **39**, 65-89.

Ebata, N., Sawa, Y., Nodasaka, Y., Yamaoka, Y., Yoshida, S. and Totsuka, Y. (2001). Immunoelectron microscopic study of PECAM-1 expression on lymphatic endothelium of the human tongue. *Tissue Cell* **33**, 211-8.

Eichmann, A., Pardanaud, L., Yuan, L. and Moyon, D. (2002). Vasculogenesis and the search for the hemangioblast. *J. Hematother. Stem. Cell Res.* **11**, 207-14.

Eichmann, A., Yuan, L., Moyon, D., Lenoble, F., Pardanaud, L. and Breant, C. (2005). Vascular development: from precursor cells to branched arterial and venous networks. *Int. J. Dev. Biol.* **49**, 259-67.

Epstein, D. L. and Rohen, J. W. (1991). Morphology of the trabecular meshwork and inner-wall endothelium after cationized ferritin perfusion in the monkey eye. *Invest. Ophthalmol. Vis. Sci.* **32**, 160-71.

Erhard, H., Rietveld, F. J., Brocker, E. B., de Waal, R. M. and Ruiter, D. J. (1996). Phenotype of normal cutaneous microvasculature. Immunoelectron microscopic observations with emphasis on the differences between blood vessels and lymphatics. *J Invest. Dermatol.* **106**, 135-40.

Erickson-Lamy, K., Rohen, J. W. and Grant, W. M. (1991). Outflow facility studies in the perfused human ocular anterior segment. *Exp. Eye Res.* **52**, 723-31.

Etchevers, H. C., Vincent, C., Le Douarin, N. M. and Couly, G. F. (2001). The cephalic neural crest provides pericytes and smooth muscle cells to all blood vessels of the face and forebrain. *Development* **128**, 1059-68.

Ethier, C. R. (2002). The inner wall of Schlemm's canal. *Exp. Eye Res.* **74**, 161-172.

Evans, A. L. and Gage, P. J. (2005). Expression of the homeobox gene *Pitx2* in neural crest is required for optic stalk and ocular anterior segment development. *Hum. Mol. Genet.* **14**, 3347-3359.

Ezaki, T., Baluk, P., Thurston, G., La Barbara, A., Woo, C. and McDonald, D. M. (2001). Time course of endothelial cell proliferation and microvascular remodeling in chronic inflammation. *Am. J. Pathol.* **158**, 2043-55.

Feng, D., Nagy, J. A., Pyne, K., Dvorak, H. F. and Dvorak, A. M. (2004). Ultrastructural localization of platelet endothelial cell adhesion molecule (PECAM-1, CD31) in vascular endothelium. *J. Histochem. Cytochem.* **52**, 87-101.

Feng, J. Q., Chen, D., Cooney, A. J., Tsai, M. J., Harris, M. A., Tsai, S. Y., Feng, M., Mundy, G. R. and Harris, S. E. (1995). The mouse bone morphogenetic protein-4 gene. Analysis of promoter utilization in fetal rat calvarial osteoblasts and regulation by COUP-TFI orphan receptor. *J Biol Chem* **270**, 28364-73.

Fruttiger, M. (2002). Development of the mouse retinal vasculature: angiogenesis versus vasculogenesis. *Invest. Ophthalmol. Vis. Sci.* **43**, 522-7.

Furuta, Y. and Hogan, B. L. (1998). BMP4 is essential for lens induction in the mouse embryo. *Genes Dev.* **12**, 3764-75.

Gaasterland, D. E., Jocson, V. L. and Sears, M. L. (1970). Channels of aqueous outflow and related blood vessels. 3. Episcleral arteriovenous anastomoses in the rhesus monkey eye (Macaca mulatta). *Arch. Ophthalmol.* **84**, 770-5.

Gage, P. J., Rhoades, W., Prucka, S. K. and Hjalt, T. (2005). Fate maps of neural crest and mesoderm in the mammalian eye. *Invest. Ophthalmol. Vis. Sci.* **46**, 4200-8.

Gage, P. J., Suh, H. and Camper, S. A. (1999). Dosage requirement of *Pitx2* for development of multiple organs. *Development* **126**, 4643-51.

Gale, N. W., Thurston, G., Hackett, S. F., Renard, R., Wang, Q., McClain, J., Martin, C., Witte, C., Witte, M. H., Jackson, D. et al. (2002). Angiopoietin-2 is required for postnatal angiogenesis and lymphatic patterning, and only the latter role is rescued by angiopoietin-1. *Dev. Cell* **3**, 411-423.

Galkina, E. and Ley, K. (2007). Vascular adhesion molecules in atherosclerosis. *Arterioscler. Thromb. Vasc. Biol.* **27**, 2292-301.

Gerhardt, H. and Betsholtz, C. (2003). Endothelial-pericyte interactions in angiogenesis. *Cell Tissue Res.* **314**, 15-23.

Gould, D. B. and John, S. W. M. (2002). Anterior segment dysgenesis and the developmental glaucomas are complex traits. *Hum. Mole. Genet.* **11**, 1185-1193.

Gould, D. B., Smith, R. S. and John, S. W. M. (2004). Anterior segment development relevant to glaucoma. *Int. J. Dev. Biol.* **48**, 1015-1029.

Graesser, D., Solowiej, A., Bruckner, M., Osterweil, E., Juedes, A., Davis, S., Ruddle, N. H., Engelhardt, B. and Madri, J. A. (2002). Altered vascular permeability and early onset of experimental autoimmune encephalomyelitis in PECAM-1-deficient mice. *J. Clin. Invest.* **109**, 383-92.

Hamanaka, T., Bill, A., Ichinohasama, R. and Ishida, T. (1992). Aspects of the development of Schlemm's canal. *Exp. Eye Res.* **55**, 479-488.

Hamid, S. A., Ferguson, L. E., McGavigan, C. J., Howe, D. C. and Campbell, S. (2006). Observing three-dimensional human microvascular and myogenic architecture using conventional fluorescence microscopy. *Micron* **37**, 134-8.

Hamrah, P., Chen, L., Cursiefen, C., Zhang, Q., Joyce, N. C. and Dana, M. R. (2004). Expression of vascular endothelial growth factor receptor-3 (VEGFR-3) on monocytic bone marrow-derived cells in the

conjunctiva. *Exp. Eye Res.* **79**, 553-61.

Hamrah, P., Liu, Y., Zhang, Q. and Dana, M. R. (2003). The corneal stroma is endowed with a significant number of resident dendritic cells. *Invest. Ophthalmol. Vis. Sci.* **44**, 581-9.

Harris, M. J. and Juriloff, D. M. (1998). Nonallelic noncomplementation models in mice: the first arch and lidgap-Gates mutations. *Genome* **41**, 789-96.

Hasegawa, T., McLeod, D. S., Bhutto, I. A., Prow, T., Merges, C. A., Grebe, R. and Lutty, G. A. (2007). The embryonic human choriocapillaris develops by hemo-vasculogenesis. *Dev. Dyn.* **236**, 2089-100.

Hawes, N. L., Smith, R. S., Chang, B., Davisson, M., Heckenlively, J. R. and John, S. W. M. (1999). Mouse fundus photography and angiography: A catalogue of normal and mutant phenotypes. *Mol. Vis.* **5**, U1-U8.

Hayashi, H. and Kume, T. (2008). Foxc transcription factors directly regulate Dll4 and Hey2 expression by interacting with the VEGF-Notch signaling pathways in endothelial cells. *PLoS ONE* **3**, e2401.

Heimark, R. L., Kaochar, S. and Stamer, W. D. (2002). Human Schlemm's canal cells express the endothelial adherens proteins, VE-cadherin and PECAM-1. *Curr. Eye Res.* **25**, 299-308.

Hiemisch, H., Schutz, G. and Kaestner, K. H. (1998). The mouse *Fkh1/Mf1* gene: cDNA sequence, chromosomal localization and expression in adult tissues. *Gene* **220**, 77-82.

Hoar, R. M. (1982). Embryology of the eye. *Environ. Health Perspect.* **44**, 31-4.

Hogan, B. L. (1996). Bone morphogenetic proteins in development. *Curr. Opin. Genet. Dev.* **6**, 432-8.

Hogan, B. L. (1996a). Bone morphogenetic proteins: multifunctional regulators of vertebrate development. *Genes Dev.* **10**, 1580-94.

Holderfield, M. T. and Hughes, C. C. (2008). Crosstalk between vascular endothelial growth factor, notch, and transforming growth factor-beta in vascular morphogenesis. *Circ. Res.* **102**, 637-52.

Hong, H. K., Lass, J. H. and Chakravarti, A. (1999). Pleiotropic skeletal and ocular phenotypes of the mouse mutation congenital hydrocephalus (*ch/Mf1*) arise from a winged helix forkhead transcription factor gene. *Hum. Mol. Genet.* **8**, 625-637.

Hong, Y.-K., Harvey, N., Noh, Y.-H., Schacht, V., Hirakawa, S., Detmar, M. and Oliver, G. (2002). *Prox1* is a master control gene in the program specifying lymphatic endothelial cell fate. *Dev. Dyn.* **225**, 351-7.

Hyldahl, L. (1985). Factor VIII expression in the human embryonic eye. Differences between endothelial cells of different origin. *Ophthalmologica* **191**, 184-7.

Idrees, F., Vaideanu, D., Fraser, S. G., Sowden, J. C. and Khaw, P. T. (2006). A review of anterior segment dysgeneses. *Surv. Ophthalmol.* **51**, 213-31.

Iida, K., Koseki, H., Kakinuma, H., Kato, N., Mizutani-Koseki, Y., Ohuchi, H., Yoshioka, H., Noji, S., Kawamura, K., Kataoka, Y. et al. (1997). Essential roles of the winged helix transcription factor MFH-1 in aortic arch patterning and skeletogenesis. *Development* **124**, 4627-38.

Ittner, L. M., Wurdak, H., Schwerdtfeger, K., Kunz, T., Ille, F., Leveen, P., Hjalt, T. A., Suter, U., Karlsson, S., Hafezi, F. et al. (2005). Compound developmental eye disorders following inactivation of TGF beta signaling in neural-crest stem cells. *J. Biol.* **4**, 11.

Iwao, K., Inatani, M., Okinami, S. and Tanihara, H. (2008). Fate mapping of neural crest cells during eye development using a protein 0 promoter-driven transgenic technique. *Graefes Arch. Clin. Exp. Ophthalmol.* **246**, 1117-22.

Janes, R. G. and Bounds, G. W., Jr. (1955). The blood vessels of the rat's eye. *Am. J. Anat.* **96**, 357-73.

Jocson, V. L. and Sears, M. L. (1968). Channels of aqueous outflow and related blood vessels. I. Macaca mulatta (rhesus). *Arch. Ophthalmol.* **80**, 104-14.

Jocson, V. L. and Sears, M. L. (1969). Channels of aqueous outflow and related blood vessels. II. Cercopithecus ethiops (Ethiopian green or green vervet). *Arch. Ophthalmol.* **81**, 244-53.

John, S. W., Hagaman, J. R., MacTaggart, T. E., Peng, L. and Smithes, O. (1997). Intraocular pressure in inbred mouse strains. *Invest. Ophthalmol. Vis. Sci.* **38**, 249-53.

John, S. W. M., Anderson, M. G. and Smith, R. S. (1999). Mouse genetics: A tool to help unlock the mechanisms of glaucoma. *J. Glaucoma* **8**, 400-412.

Johnson, M. (2006). 'What controls aqueous humour outflow resistance?' *Exp. Eye Res.* **82**, 545-57.

Johnson, M. C. and Kamm, R. D. (1983). The role of Schlemm's canal in aqueous outflow from the human eye. *Invest. Ophthalmol. Vis. Sci.* **24**, 320-5.

Johnstone, M. A. (2004). The aqueous outflow system as a mechanical pump: evidence from examination of tissue and aqueous movement in human and non-human primates. *J. Glaucoma* **13**, 421-38.

Johnstone, M.A. (2006). A new model describes an aqueous outflow pump and explores causes of pump failure in glaucoma. In Essentials of Ophthalmology: Glaucoma (eds Grehn, F. Weinreb, R.N), pp 3-34, Berlin, Springer.

Joussen, A. M., Beecken, W. D., Moromizato, Y., Schwartz, A., Kirchhof, B. and Poulaki, V. (2001). Inhibition of inflammatory corneal angiogenesis by TNP-470. *Invest. Ophthalmol. Vis. Sci.* **42**, 2510-6.

Kane, R., Godson, C. and O'Brien, C. (2008). Chordin-like 1, a bone morphogenetic protein-4 antagonist, is upregulated by hypoxia in human retinal pericytes and plays a role in regulating angiogenesis. *Mol. Vis.* **14**, 1138-48.

Kidson, S. H., Kume, T., Deng, K. Y., Winfrey, V. and Hogan, B. L. M. (1999). The forkhead/winged-helix gene, *Mf1*, is necessary for the normal development of the cornea and formation of the anterior chamber in the mouse eye. *Dev. Biol.* **211**, 306-322.

Kitamura, K., Miura, H., Miyagawa-Tomita, S., Yanazawa, M., Katoh-Fukui, Y., Suzuki, R., Ohuchi, H., Suehiro, A., Motegi, Y., Nakahara, Y. et al. (1999). Mouse Pitx2 deficiency leads to anomalies of the ventral body wall, heart, extra- and periocular mesoderm and right pulmonary isomerism. *Development* **126**, 5749-58.

Kiyono, M. and Shibuya, M. (2003). Bone morphogenetic protein 4 mediates apoptosis of capillary endothelial cells during rat pupillary membrane regression. *Molecular and Cellular Biology* **23**, 4627-4636.

Komai, Y. and Ushiki, T. (1991). The three-dimensional organization of collagen fibrils in the human cornea and sclera. *Invest. Ophthalmol. Vis. Sci.* **32**, 2244-58.

Krohn, J. (1999). Expression of factor VIII-related antigen in human aqueous drainage channels. *Acta Ophthalmol Scand* **77**, 9-12.

Krohn, J. and Bertelsen, T. (1998). Light microscopy of uveoscleral drainage routes after gelatine injections into the suprachoroidal space. *Acta Ophthalmol Scand* **76**, 521-7.

Krupin, T (1996) The Glaucomas, vol. 1 (ed. R. Rich M. B. Shields and T. Krupin). Missouri, USA: Mosby Year Book Inc.

Kurihara, T., Kitamura, K., Takaoka, K. and Nakazato, H. (1993). Murine bone morphogenetic protein-4 gene: existence of multiple promoters and exons for the 5'-untranslated region. *Biochem. Biophys. Res. Comm.* **192**, 1049-56.

Kume, T., Deng, K. Y., Winfrey, V., Gould, D. B., Walter, M. A. and Hogan, B. L. M. (1998). The forkhead/winged helix gene *Mf1* is disrupted in the pleiotropic mouse mutation congenital hydrocephalus. *Cell* **93**, 985-996.

Kure, T., Chang, J. H., Kato, T., Hernandez-Quintela, E., Ye, H., Lu, P. C., Matrisian, L. M., Gatinel, D., Shapiro, S., Gosheh, F. et al. (2003). Corneal neovascularization after excimer keratectomy wounds in matrilysin-deficient mice. *Invest. Ophthalmol. Vis. Sci.* **44**, 137-44.

Kurihara, T., Kitamura, K., Takaoka, K. and Nakazato, H. (1993). Murine bone morphogenetic protein-4 gene: existence of multiple promoters and exons for the 5'-untranslated region. *Biochem. Biophys. Res. Comm.* .**192**, 1049-56.

Lahvis, G. P., Lindell, S. L., Thomas, R. S., McCuskey, R. S., Murphy, C., Glover, E., Bentz, M., Southard, J. and Bradfield, C. A. (2000). Portosystemic shunting and persistent fetal vascular structures in aryl hydrocarbon receptor-deficient mice. *Proc. the Nat. Acad. Sci. USA* **97**, 10442-7.

Lametschwandtner, A., Lametschwandtner, U. and Weiger, T. (1984). Scanning electron microscopy of vascular corrosion casts--technique and applications. *Scan. Electron. Microsc.*, 663-95.

Lametschwandtner, A. and Lametschwandtner, U. (1992). Historical review and technical survey of vascular casting and scanning electron microscopy. In Scanning Electron Microscopy of Vascular Casts: Methods and Applications (Electron Microscopy in Biology and Medicine), (ed. P. M. Motta T. Murakami and H. Fujita). Dordrecht, Kluwer Academic Publishers.

Lang, R. A. (2004). Pathways regulating lens induction in the mouse. *Int. J. Dev. Biol.* **48**, 783-91.

Lawson, K. A., Dunn, N. R., Roelen, B. A., Zeinstra, L. M., Davis, A. M., Wright, C. V., Korving, J. P. and Hogan, B. L. (1999). *Bmp4* is required for the generation of primordial germ cells in the mouse embryo. *Genes Dev.* **13**, 424-36.

le Noble, F., Moyon, D., Pardanaud, L., Yuan, L., Djonov, V., Matthijsen, R., Breant, C., Fleury, V. and Eichmann, A. (2004). Flow regulates arterial-venous differentiation in the chick embryo yolk sac. *Development* **131**, 361-75.

Lee, P. P., Walt, J. W., Rosenblatt, L. C., Siegartel, L. R. and Stern, L. S. (2007). Association between intraocular pressure variation and glaucoma progression: data from a United States chart review. *Am. J. Ophthalmol.* **144**, 901-907.

Libby, R. T., Smith, R. S., Savinova, O. V., Zabaleta, A., Martin, J. E., Gonzalez, F. J. and John, S. W. M. (2003). Modification of ocular defects in mouse developmental glaucoma models by tyrosinase. *Science* **299**, 1578-1581.

Lindsey, J. D. and Weinreb, R. N. (2002). Identification of the mouse uveoscleral outflow pathway using fluorescent dextran. *Invest. Ophthalmol. Vis. Sci.* **43**, 2201-2205.

Liu, W., Lagutin, O. V., Mende, M., Streit, A. and Oliver, G. (2006). Six3 activation of *Pax6* expression is essential for mammalian lens induction and specification. *EMBO J.* **25**, 5383-95.

Llobet, A., Gasull, X. and Gual, A. (2003). Understanding trabecular meshwork physiology: a key to the control of intraocular pressure? *News Physiol Sci* **18**, 205-9.

Lütjen-Drecoll, E. (1998). Functional morphology of the trabecular meshwork in primate eyes. *Prog. Retin. Eye Res.***18**, 91-119.

Majji, A. B., Cao, J. T., Chang, K. Y., Hayashi, A., Aggarwal, S., Grebe, R. R. and de Juan, E. (2000). Age-related retinal pigment epithelium and Bruch's membrane degeneration in senescence-accelerated mouse. *Invest. Ophthalmol. Vis. Sci.* **41**, 3936-3942.

Mamdouh, Z., Chen, X., Pierini, L. M., Maxfield, F. R. and Muller, W. A. (2003). Targeted recycling of PECAM from endothelial surface-connected compartments during diapedesis. *Nature* **421**, 748-53.

Maruyama, K., Li, M., Cursiefen, C., Jackson, D. G., Keino, H., Tomita, M., Van Rooijen, N., Takenaka, H., D'Amore, P. A., Stein-Streilein, J. et al. (2005). Inflammation-induced lymphangiogenesis in the cornea arises from CD11 b-positive macrophages. *J. Clin. Invest.* **115**, 2363-2372.

Matsumoto, M., Tanaka, T., Yamamoto, T., Noiri, E., Miyata, T., Inagi, R., Fujita, T. and Nangaku, M. (2004). Hypoperfusion of peritubular capillaries induces chronic hypoxia before progression of tubulointerstitial injury in a progressive model of rat glomerulonephritis. *J. Am. Soc. Nephrol*.**15**, 1574-81.

McLeod, D. S., Hasegawa, T., Prow, T., Merges, C. and Lutty, G. (2006). The initial fetal human retinal vasculature develops by vasculogenesis. *Dev. Dyn.* **235**, 3336-47.

McMenamin, P. G. (1989). Human fetal iridocorneal angle: a light and scanning electron microscopic study. *Br. J. Opthalmol.* **73**, 871-9.

McMenamin, P. G. (2000). Optimal methods for preparation and immunostaining of iris, ciliary body, and choroidal wholemounts. *Invest. Ophthalmol. Vis. Sci.* **41**, 3043-3048.

McMenamin, P. G. and al-Shakarchi, M. J. (1989). The effect of various levels of intraocular pressure on the rat aqueous outflow system. *J. Anat.* **162**, 67-82.

Mears, A. J., Jordan, T., Mirzayans, F., Dubois, S., Kume, P., Parlee, M., Ritch, R., Koop, B., Kuo, W. L., Collins, C. et al. (1998). Mutations of the forkhead/winged-helix gene, *FKHL7*, in patients with Axenfeld-Rieger anomaly. *Am. J. Hum. Genet.* **63**, 1316-1328.

Meyer, P. A. R. and Watson, P. G. (1987). Low dose fluorescein angiography of the conjunctiva and episclera. *Br. J. Opthalmol.*, **71**, 2-10.

Miller, S. A., Dykes, D. D. and Polesky, H. F. (1988). A simple salting out procedure for extracting DNA from human nucleated cells. *Nucleic Acids Res.* **16**, 1215.

Mitchell, C. A., Risau, W. and Drexler, H. C. (1998). Regression of vessels in the tunica vasculosa lentis is initiated by coordinated endothelial apoptosis: a role for vascular endothelial growth factor as a survival factor for endothelium. *Dev. Dyn.* **213**, 322-33.

Mitchell, C. H., Fleischhauer, J. C., Stamer, W. D., Peterson-Yantorno, K. and Civan, M. M. (2002). Human trabecular meshwork cell volume regulation. *Am. J. Physiol. Cell Physiol.* **283**, C315-26.

Mohan, R. R., Kim, W. J., Chen, L. and Wilson, S. E. (1998). Bone morphogenic proteins 2 and 4 and their receptors in the adult human cornea. *Invest. Ophthalmol. Vis. Sci.* **39**, 2626-36.

Morisada, T., Oike, Y., Yamada, Y., Urano, T., Akao, M., Kubota, Y., Maekawa, H., Kimura, Y., Ohmura, M., Miyamoto, T. et al. (2005). Angiopoietin-1 promotes LYVE-1-positive lymphatic vessel formation. *Blood* **105**, 4649-4656.

Moromizato, Y., Stechschulte, S., Miyamoto, K., Murata, T., Tsujikawa, A., Joussen, A. M. and Adamis, A. P. (2000). CD18 and ICAM-1-dependent corneal neovascularization and inflammation after

limbal injury. *Am. J. Pathol.* **157**, 1277-81.

Morrison, J. C., Fraunfelder, F. W., Milne, S. T. and Moore, C. G. (1995). Limbal microvasculature of the rat eye. *Invest. Ophthalmol. Vis. Sci.* **36**, 751-6.

Moseley, G. W. and Jackson, D. E. (2004). The Multiple Functions of PECAM-1. *Australian Biochemist* **35**, 9-12.

Moses, R. A. (1981). The conventional outflow resistances. *Am. J. Ophthalmol.* **92**, 804-10.

Mouta Carreira, C., Nasser, S. M., di Tomaso, E., Padera, T. P., Boucher, Y., Tomarev, S. I. and Jain, R. K. (2001). LYVE-1 is not restricted to the lymph vessels: expression in normal liver blood sinusoids and down-regulation in human liver cancer and cirrhosis. *Cancer Res.* **61**, 8079-84.

Mukouyama, Y. S., Shin, D., Britsch, S., Taniguchi, M. and Anderson, D. J. (2002). Sensory nerves determine the pattern of arterial differentiation and blood vessel branching in the skin. *Cell* **109**, 693-705.

Murfee, W. L., Rappleye, J. W., Ceballos, M. and Schmid-Schonbein, G. W. (2007). Discontinuous expression of endothelial cell adhesion molecules along initial lymphatic vessels in mesentery: the primary valve structure. *Lymphat. Res. Biol.* **5**, 81-9.

Murphy, T. J., Thurston, G., Ezaki, T. and McDonald, D. M. (1999). Endothelial cell heterogeneity in venules of mouse airways induced by polarized inflammatory stimulus. *Am. J. Pathol.* **155**, 93-103.

Napier, H. R. (2005) Ontogenesis of the cornea and ciliary body: A morphological and molecular study. Doctoral Thesis, University of Cape Town.

Napier, H. R. and Kidson, S. H. (2005). Proliferation and cell shape changes during ciliary body morphogenesis in the mouse. *Dev. Dyn.* **233**, 213-23.

Newman, P. J. (1997). The biology of PECAM-1. *J. Clin. Invest.* **99**, 3-8.

Newman, P. J., Berndt, M. C., Gorski, J., White, G. C., 2nd, Lyman, S., Paddock, C. and Muller, W. A. (1990). PECAM-1 (CD31) cloning and relation to adhesion molecules of the immunoglobulin gene superfamily. *Science* **247**, 1219-22.

Ninomiya, H. and Inomata, T. (2005). Microvasculature of the hamster eye: scanning electron microscopy of vascular corrosion casts. *Vet. Ophthalmol* **8**, 7-12.

Ninomiya, H. and Inomata, T. (2006). Microvasculature of the mouse eye: Scanning electron microscopy of vascular corrosion casts. *J. Exp. Anim. Sci.* **43**, 129-159.

Ninomiya, H., Inomata, T. and Kanemaki, N. (2005). Microvasculature of the retina, ciliary processes and choroid in the North American raccoon (Procyon lotor) eye: A scanning electron microscopic study of corrosion casts. *J. Vet. Med. Sci.* **67**, 547-554.

Ninomiya, H. and Kuno, H. (2001). Microvasculature of the rat eye: scanning electron microscopy of vascular corrosion casts. *Vet. Ophthalmol.* **4**, 55-59.

Novotny, H. R. and Alvis, D. L. (1961). A method of photographing fluorescence in circulating blood in the human retina. *Circulation* **24**, 82-6.

O'Ceallaigh, S., Herrick, S. E., Bluff, J. E., McGrouther, D. A. and Ferguson, M. W. (2006). Quantification of total and perfused blood vessels in murine skin autografts using a fluorescent double-labeling technique. *Plast. Reconstr. Surg.* **117**, 140-51.

Ohlmann, A. V., Ohlmann, A., Welge-Lussen, U. and May, C. A. (2005). Localization of collagen

XVIII and endostatin in the human eye. *Cur.r Eye Res.* **30**, 27-34.

Ohto, H., Maeda, H., Shibata, Y., Chen, R. F., Ozaki, Y., Higashihara, M., Takeuchi, A. and Tohyama, H. (1985). A novel leukocyte differentiation antigen: two monoclonal antibodies TM2 and TM3 define a 120-kd molecule present on neutrophils, monocytes, platelets, and activated lymphoblasts. *Blood* **66**, 873-81.

Oliver, G. and Harvey, N. (2002). A stepwise model of the development of lymphatic vasculature. *Ann. N. Y. Acad. Sci.* **979**, 159-65; discussion 188-96.

Parc, C. E., Johnson, D. H. and Brilakis, H. S. (2000). Giant vacuoles are found preferentially near collector channels. *Invest. Ophthalmol. Vis. Sci.* **41**, 2984-2990.

Pederson, J. E. and Toris, C. B. (1987). Uveoscleral outflow: diffusion or flow? *Invest. Ophthalmol. Vis. Sci.* **28**, 1022-4.

Pei, Y. F. and Rhodin, J. A. (1970). The prenatal development of the mouse eye. *Anat. Rec.* **168**, 105-125.

Pressman, C. L., Chen, H. X. and Johnson, R. L. (2000). LMX1b, a LIM homeodomain class transcription factor, is necessary for normal development of multiple tissues in the anterior segment of the murine eye. *Genesis* **26**, 15-25.

Quantock, A. J., Dennis, S., Adachi, W., Kinoshita, S., Boote, C., Meek, K. M., Matsushima, Y. and Tachibana, M. (2003). Annulus of collagen fibrils in mouse cornea and structural matrix alterations in a murine-specific keratopathy. *Invest. Ophthalmol. Vis. Sci.* **44**, 1906-11.

Ramírez, J. M., Ramírez, A. I., Salazar, J. J., Rojas, B., De Hoz, R. and Trivino, A. (2004). Schlemm's canal and the collector channels at different developmental stages in the human eye. *Cells Tissues Organs* **178**, 180-185.

Ramos, R. F., Hoying, J. B., Witte, M. H. and Daniel Stamer, W. (2007). Schlemm's canal endothelia, lymphatic, or blood vasculature? *J. Glaucoma* **16**, 391-405.

Read, A. T., Chan, D. W. and Ethier, C. R. (2007). Actin structure in the outflow tract of normal and glaucomatous eyes. *Exp. Eye Res.* **84**, 214-26.

Remé, C., Urner, U. and Aeberhard, B. (1983). The development of the chamber angle in the rat eye. Morphological characteristics of developmental stages. *Graefes Arc.h Clin. Exp. Ophthalmo.l* **220**, 139-53.

Remé, C., Urner, U. and Aeberhard, B. (1983a). The occurrence of cell death during the remodelling of the chamber angle recess in the developing rat eye. *Graefes Arch. Clin. Exp. Ophthalmol.* **221**, 113-21.

Richardson, T. M., Marks, M. S., Ausprunk, D. H. and Miller, M. (1985). A morphologic and morphometric analysis of the aqueous outflow system of the developing cat eye. *Exp. Eye Res.* **41**, 31-51.

Risau, W. (1997). Mechanisms of angiogenesis. *Nature* **386**, 671-4.

Rich, R., Shields, M.B. and Krupin, T. (1996). The Glaucomas. St Louis, Mosby Year Book Inc.

Ritter, M. R., Aguilar, E., Banin, E., Scheppke, L., Uusitalo-Jarvinen, H. and Friedlander, M. (2005). Three-dimensional in vivo imaging of the mouse intraocular vasculature during development and disease. *Invest. Ophthalmol. Vis. Sci.* **46**, 3021-3026.

Ritter, M. R., Banin, E., Moreno, S. K., Aguilar, E., Dorrell, M. I. and Friedlander, M. (2006). Myeloid progenitors differentiate into microglia and promote vascular repair in a model of ischemic retinopathy. *J. Clin. Invest.* **116**, 3266-3276.

Runnels, J. M., Zamiri, P., Spencer, J. A., Veilleux, I., Wei, X., Bogdanov, A. and Lin, C. P. (2006). Imaging molecular expression on vascular endothelial cells by in vivo immunofluorescence microscopy. *Mol. Imaging* **5**, 31-40.

Saika, S., Liu, C. Y., Azhar, M., Sanford, L. P., Doetschman, T., Gendron, R. L., Kao, C. W. C. and Kao, W. W. Y. (2001). TGF beta 2 in corneal morphogenesis during mouse embryonic development. *Dev. Biol.* **240**, 419-432.

Saint-Geniez, M. and D'Amore, P. A. (2004). Development and pathology of the hyaloid, choroidal and retinal vasculature. *Int. J. Dev. Biol.* **48**, 1045-1058.

Saint-Geniez, M., Maldonado, A. E. and D'Amore, P. A. (2006). VEGF expression and receptor activation in the choroid during development and in the adult. *Invest. Ophthalmol. Vis. Sci.* **47**, 3135-42.

Sambrook, J., Fritsch, E. F. and Maniatis, T. (1989). Molecular Cloning: A laboratory manual, (ed. J. Sambrook E. F. Fritsch and T. Maniatis). USA: Cold Spring Harbor Laboratory Press.

Sauter, B., Foedinger, D., Sterniczky, B., Wolff, K. and Rappersberger, K. (1998). Immunoelectron Microscopic Characterization of Human Dermal Lymphatic Microvascular Endothelial Cells: Differential Expression of CD31, CD34, and Type IV Collagen with Lymphatic Endothelial Cells vs Blood Capillary Endothelial Cells in Normal Human Skin, Lymphangioma, and Hemangioma In Situ. *J. Histochem. Cytochem.* **46**, 165-176.

Savinova, O. V., Sugiyama, F., Martin, J. E., Tomarev, S. I., Paigen, B. J., Smith, R. S. and John, S. W. (2001). Intraocular pressure in genetically distinct mice: an update and strain survey. *BMC.Genet.* **2:12. Epub;%2001 Aug 9.**, 12.

Selbach, J. M., Buschnack, S. H., Steuhl, K. P., Kremmer, S. and Muth-Selbach, U. (2005). Substance P and opioid peptidergic innervation of the anterior eye segment of the rat: an immunohistochemical study. *J. Anat.* **206**, 237-42.

Selbach, J. M., Schonfelder, U. and Funk, R. H. W. (1998). Arteriovenous anastomoses of the episcleral vasculature in the rabbit and rat eye. *J. Glaucoma* **7**, 50-57.

Seo, S., Fujita, H., Nakano, A., Kang, M., Duarte, A. and Kume, T. (2006). The forkhead transcription factors, Foxc1 and Foxc2, are required for arterial specification and lymphatic sprouting during vascular development. *Dev. Biol.* **294**, 458-470.

Sequeira Lopez, M. L., Chernavvsky, D. R., Nomasa, T., Wall, L., Yanagisawa, M. and Gomez, R. A. (2003). The embryo makes red blood cell progenitors in every tissue simultaneously with blood vessel morphogenesis. *Am. J. Physiol. Regul. Integr. Comp. Physiol.* **284**, R1126-37.

Sevel, D. and Isaacs, R. (1988). A re-evaluation of corneal development. *Trans Am Ophthalmol Soc* **86**, 178-207.

Silverman, M. D., Zamora, D. O., Pan, Y., Texeira, P. V., Planck, S. R. and Rosenbaum, J. T. (2001). Cell adhesion molecule expression in cultured human iris endothelial cells. *Invest. Ophthalmol. Vis. Sci.* **42**, 2861-6.

Simmons, S. T., Bernstein, P. and Hollander, D. A. (2008). A comparison of long-term intraocular pressure fluctuation in patients treated with bimatoprost or latanoprost. *Am. J. Ophthalmol.* **146**, 473-7.

Sit, A. J., Coloma, F. M., Ethier, C. R. and Johnson, M. (1997). Factors affecting the pores of the inner wall endothelium of Schlemm's canal. *Invest. Ophthalmol. Vis. Sci.* **38**, 1517-1525.

Smelser, G. K. and Ozanics, V. (1971). The development of the trabecular meshwork in primate eyes. *Am.J.Ophthalmol.* **1**, 366-385.

Smith, R. S., Korb, D. and John, S. W. M. (2002). A goniolens for clinical monitoring of the mouse iridocorneal angle and optic nerve. *Molecular Vision* **8**, 26-31.

Smith, R.S., John, S.W.M. and Nishina, P.M. (2001b) The posterior segment and orbit. In Systematic evaluation of the mouse eye: Anatomy, Pathology and Biomethods. (eds R.S. Smith, S.W.M. John, P.M. Nishina, and J.P. Sundberg, J.P.), pp 25-44. *CRC Press*

Smith, R.S., Sundberg, J.P. and **John, S.W.M.** (2001a). The anterior segment and ocular adnexae. In Systematic evaluation of the mouse eye: Anatomy, Pathology and Biomethods. (eds R.S. Smith, S.W.M. John, P.M. Nishina, and J.P. Sundberg, J.P.), pp 3-24. *CRC Press.*

Smith, R. S., Zabaleta, A., Kume, T., Savinova, O. V., Kidson, S. H., Martin, J. E., Nishimura, D. Y., Alward, W. L., Hogan, B. L. and John, S. W. (2000). Haploinsufficiency of the transcription factors FOXC1 and FOXC2 results in aberrant ocular development. *Hum. Mol. Genet.* **9**, 1021-1032.

Smith, R. S., Zabaleta, A., Savinova, O. V. and John, S. W. (2001). The mouse anterior chamber angle and trabecular meshwork develop without cell death. *BMC. Dev. Biol.* **1:3. Epub;%2001 Feb 14.**, 3.

Snowden, J. C. (2007). Molecular and developmental mechanisms of anterior segment dysgenes. *Eye* **21**, 1310-18.

Sommer, P., Napier, H. R., Hogan, B. L. and Kidson, S. H. (2006). Identification of *Tgf beta1i4* as a downstream target of *Foxc1*. *Dev. Growth Differ.* **48**, 297-308.

Sulik, K. K., Dehart, D. B., Johnson, C. S., Ellis, S. L., Chen, S. Y., Dunty, W. C., Jr. and Zucker, R. M. (2001). Programmed cell death in extraocular muscle tendon/sclera precursors. *Mol. Vis.* **7**, 184-91.

Sun, J., Paddock, C., Shubert, J., Zhang, H. B., Amin, K., Newman, P. J. and Albelda, S. M. (2000). Contributions of the extracellular and cytoplasmic domains of platelet-endothelial cell adhesion molecule-1 (PECAM-1/CD31) in regulating cell-cell localization. *J. Cell Sci.***113**, 1459-1469.

Théry, M., Racine, V., Pepin, A., Piel, M., Chen, Y., Sibarita, J. B. and Bornens, M. (2005). The extracellular matrix guides the orientation of the cell division axis. *Nat. Cell Biol.* **7**, 947-53.

Thurston, G., Baluk, P. and McDonald, D. M. (2000). Determinants of endothelial cell phenotype in venules. *Microcirculation* **7**, 67-80.

Toris, C. B., Gregerson, D. S. and Pederson, J. E. (1987). Uveoscleral outflow using different-sized fluorescent tracers in normal and inflamed eyes. *Exp. Eye Res.* **45**, 525-32.

Treins, C., Giorgetti-Peraldi, S., Murdaca, J., Monthouel-Kartmann, M. N. and Van Obberghen, E. (2005). Regulation of hypoxia-inducible factor (HIF)-1 activity and expression of HIF hydroxylases in response to insulin-like growth factor I. *Mol. Endocrinol.* **19**, 1304-17.

Tripathi, R. C. (1968). Ultrastructure of Schlemm's canal in relation to aqueous outflow. *Exp. Eye Res.* **7**, 335-341.

Tripathi, R. C. (1971). Mechanism of the aqueous outflow across the trabecular wall of Schlemm's canal. *Exp. Eye Res.* **11**, 116-121.

Tripathi, R. C. and Tripathi, B. J. (1972). The mechanism of aqueous outflow in lower mammals. *Exp. Eye Res.* **14**, 73-79.

Tripathi, R. C. and Tripathi, B. J. (1973). The mechanism of aqueous outflow in birds. I. An ultrastructural study of normal eyes. *Exp. Eye Res.* **15**, 409-23.

Tripathi, R. C. and Tripathi, B. J. (1973). The mechanism of aqueous outflow in birds. II. An

ultrastructural study of perfused eyes. *Exp. Eye Res.* **15**, 425-34.

Trousse, F., Esteve, P. and Bovolenta, P. (2001). BMP4 mediates apoptotic cell death in the developing chick eye. *J. Neurosci.* **21**, 1292-1301.

Ujiie, K. and Bill, A. (1984). The drainage routes for aqueous humor in monkeys as revealed by scanning electron microscopy of corrosion casts. *Scan. Electron. Microsc.*, 849-56.

Vallien, G., Langley, R., Jennings, S., Specian, R. and Granger, D. N. (2000). Expression of endothelial cell adhesion molecules in neovascularized tissue. *Microcirc.* **7**, 249-258.

Van Buskirk, E. M. (1979). The canine eye: the vessels of aqueous drainage. *Invest. Ophthalmol. Vis. Sci.* **18**, 223-30.

van Mourik, J. A., Leeksma, O. C., Reinders, J. H., de Groot, P. G. and Zandbergen-Spaargaren, J. (1985). Vascular endothelial cells synthesize a plasma membrane protein indistinguishable from the platelet membrane glycoprotein IIa. *J. Biol. Chem.* **260**, 11300-6.

van Wijngaarden, P., Coster, D. J., Brereton, H. M., Gibbins, I. L. and Williams, K. A. (2005). Strain-dependent differences in oxygen-induced retinopathy in the inbred rat. *Invest. Ophthalmol. Vis. Sci.* **46**, 1445-52.

Vanden Hoek, T. L., Goossens, W. and Knepper, P. A. (1987). Fluorescence-labeled lectins, glycoconjugates, and the development of the mouse AOP. *Invest. Ophthalmol. Vis. Sci.* **28**, 451-8.

Vecchi, A., Garlanda, C., Lampugnani, M. G., Resnati, M., Matteucci, C., Stoppacciaro, A., Schnurch, H., Risau, W., Ruco, L., Mantovani, A. et al. (1994). Monoclonal antibodies specific for endothelial cells of mouse blood vessels. Their application in the identification of adult and embryonic endothelium. *European J. Cell Biol.* **63**, 247-54.

Wagner, D. D., Olmsted, J. B. and Marder, V. J. (1982). Immunolocalization of von Willebrand protein in Weibel-Palade bodies of human endothelial cells. *J. Cell Biol.* **95**, 355-60.

Warwick, R. (1976). Eugene Wolff's Anatomy of the eye and orbit. London. H.K Lewis & Co. LTD.

Winnier, G., Blessing, M., Labosky, P. A. and Hogan, B. L. (1995). Bone morphogenetic protein-4 is required for mesoderm formation and patterning in the mouse. *Genes Dev.* **9**, 2105-16.

Wong, C. W., Wiedle, G., Ballestrem, C., Wehrle-Haller, B., Etteldorf, S., Bruckner, M., Engelhardt, B., Gisler, R. H. and Imhof, B. A. (2000). PECAM-1/CD31 trans-homophilic binding at the intercellular junctions is independent of its cytoplasmic domain; evidence for heterophilic interaction with integrin alphavbeta3 in Cis. *Mol. Bio. Cell* **11**, 3109-21.

Wordinger, R., Agarwal, R., Talati, M., Fuller, J., Lambert, W. and Clark, A. (2002). Expression of bone morphogenetic proteins (BMP), BMP receptors, and BMP associated proteins in human trabecular meshwork and optic nerve head cells and tissues. *Mol. Vis.* **8**, 241-250.

Yamashita, T., Takahashi, A. and Honjin, R. (1980). Spatial aspect of the mouse orbital venous sinus. *Okajimas Folia Anat. Jpn.* **56**, 329-336.

Ye, W., Gong, H. Y., Sit, A., Johnson, M. and Freddo, T. F. (1997). Interendothelial junctions in normal human Schlemm's canal respond to changes in pressure. *Invest. Ophthalmol. Vis. Sci.* **38**, 2460-2468.

You, L., Kruse, F. E., Pohl, J. and Volcker, H. E. (1999). Bone morphogenetic proteins and growth and differentiation factors in the human cornea. *Invest. Ophthalmol. Vis. Sci.* **40**, 296-311.

Zhao, S., Chen, Q., Hung, F. C. and Overbeek, P. A. (2002). BMP signaling is required for development

of the ciliary body. *Development* **129**, 4435-42.

Zhou, Q., Heinke, J., Vargas, A., Winnik, S., Krauss, T., Bode, C., Patterson, C. and Moser, M. (2007). ERK signaling is a central regulator for BMP-4 dependent capillary sprouting. *Cardiovasc. Res.* **76**, 390-9.